Claude Pascal Weiss

Fault Tolerant Switched Reluctance Machines with Distributed Inverters - Modeling and Control -

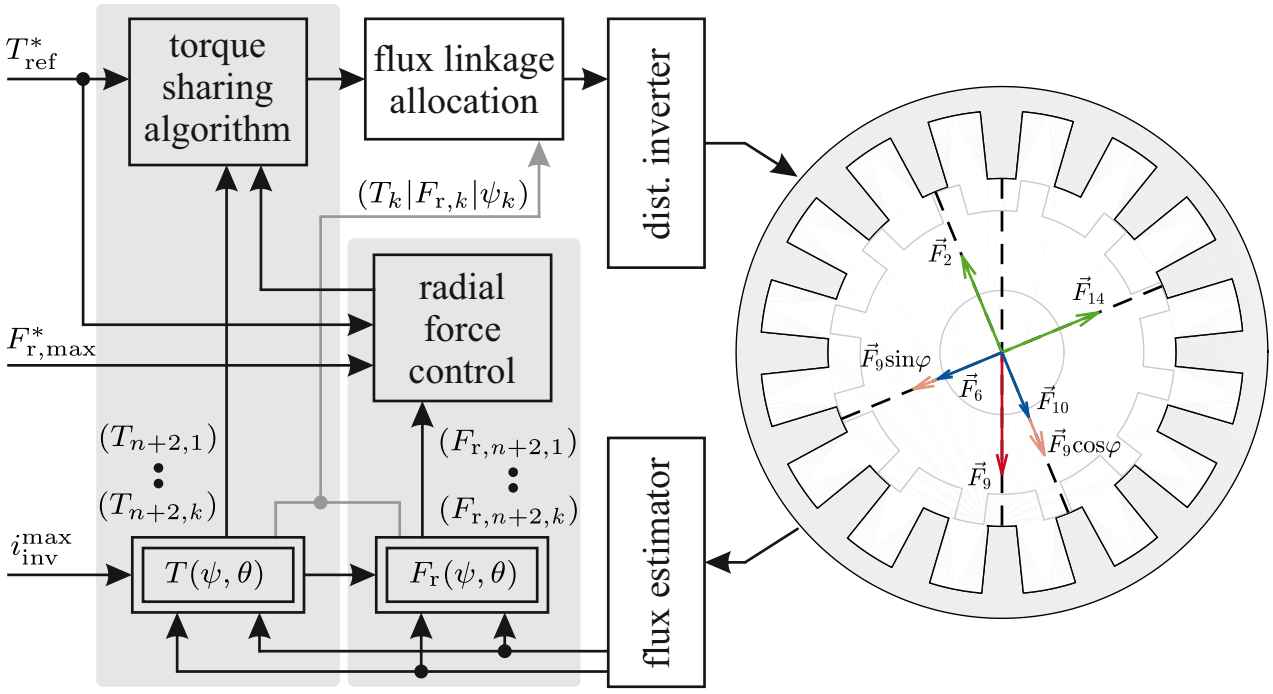

Aachener Beiträge des ISEA Band 145

Fault Tolerant Switched Reluctance Machines with Distributed Inverters - Modeling and Control -

Von der Fakultät für Elektrotechnik und Informationstechnik der Rheinisch-Westfälischen Technischen Hochschule Aachen zur Erlangung des akademischen Grades eines Doktors der Ingenieurwissenschaften genehmigte Dissertation

vorgelegt von
Diplom-Ingenieur, Diplom-Wirtschaftsingenieur
Claude Pascal Weiss
aus Johannesburg, Südafrika

Berichter:
Univ.-Prof. Dr.-Ir. Dr.-h. c. Rik W. De Doncker
Univ.-Prof. Dr.-Ing. Wilfried Hofmann

Tag der mündlichen Prüfung: 24. April 2020

Claude Pascal Weiss

Fault Tolerant Switched Reluctance Machines with Distributed Inverters - Modeling and Control -

AACHENER BEITRÄGE DES ISEA
Vol. 145

Editor:
Univ.-Prof. Dr. ir. h. c. Rik W. De Doncker
Director of the Institute for Power Electronics and Electrical Drives (ISEA)
RWTH Aachen University

ISSN 1437-675X

Institute for Power Electronics and Electrical Drives (ISEA)
RWTH Aachen University
Jägerstr. 17/19 • 52066 Aachen • Germany
Tel: +49 (0)241 80-96920
Fax: +49 (0)241 80-92203
post@isea.rwth-aachen.de

Preface

Diese Arbeit entstand im Rahmen meiner Tätigkeit als wissenschaftlicher Mitarbeiter am Institut für Stromrichtertechnik und Elektrische Antriebe (ISEA) der RWTH Aachen University. Zuerst möchte ich mich bei meinem Doktorvater Herrn Prof. Rik W. De Doncker für die Möglichkeit am ISEA zu promovieren bedanken, sowie für das stets entgegengebrachte Vertrauen. Herrn Prof. Wilfried Hofmann danke ich für die Übernahme des Korreferats.

Mein Dank für viele fruchtbare Diskussionen und Austausch (fachlich und nicht-ganz-fachlich) gilt meinen langjährigen Bürokollegen Bernhard Burkhart, Ilyia Ralev, Tetsuya Kojima, Annegret Klein-Heßling und Tobias Lange. Für die Korrektur der Arbeit und Ihren wertvollen Input möchte ich mich bei Johann Wichern und Bernhard Burkhart bedanken. Des Weiteren bedanke ich mich bei den zahlreichen Studenten, die meine Arbeit in Form von Bachelor- und Masterarbeiten bereichert haben und mich als wissenschaftliche Hilfskräfte tatkräftig unterstützt haben. Für die gute gemeinsame Projektarbeit und Unterstützung bei den Mengen an benötigten Umrichtermodule möchte ich mich bei Georges Engelmann bedanken.

Für die kollegiale Zeit und das außerordentliche positive Arbeitsklima am ISEA möchte ich mich bei allen beteiligten bedanken, vor allem der Antriebsgruppe für ihren guten Teamgeist und die vielen unterhaltsamen Antriebstreffen.

Bei meinen Eltern bedanke ich mich dafür, dass sie mich stets gefördert haben, mir das studieren im Ausland ermöglicht haben und mich immer bei allen meinen Tätigkeiten und Vorhaben unterstützt haben. Mein weiterer Dank gilt allen Freunden die immer wieder für die nötige Ablenkung neben der Dissertation gesorgt haben und mir das Leben ausserhalb des Instituts gezeigt haben. Vor allem gilt mein besonderer Dank meiner lieben Frau Anna, die während der gesamten ISEA und Dissertationszeit zu mir stand und mir vor allem in der Schreibphase den Rücken frei gehalten hat. Danke!

Aachen, im September 2020 *Claude Weiss*

Contents

1 Introduction

High reliability, safety- and operations-critical applications, where injury, environmental hazard and financial loss has to be evaded requires fault tolerant drive systems [1, 2]. The increasing number of more electric aircrafts and autonomous vehicles being developed all set a high standard for the reliability of electric drives [3–5]. In such safety critical applications, failure of the drive system usually results in fatal injuries, which has to be avoided at all costs. In operations-critical applications, such as the medical and chemical industry, failure of for example electric pumps can result in personal and environmental disaster. Also in the mining industry operation downtime, due to drive failure, is extremely costly and thus, has to be avoided [6]. For such applications a reliable, fault tolerant electrical drive, which can operate in harsh conditions is necessary. The switched reluctance machine (SRM) may offer such a solution.

Even though the first basic concept of reluctance machines was introduced in 1839 by W.H. Taylor [7], only with the advances in power electronics in the 1980's the control of this type of machine became feasible and its benefits could be harnessed [8]. Since then SRMs have been investigated and proposed for many different applications. Their simple and robust mechanical design, consisting only of a salient rotor and stator iron sheet structure (double salient) with no rotor windings or magnets, makes the SRM an inherently reliable machine. Its simplistic construction, furthermore, is interesting for high-speed applications and applications operating in harsh environmental conditions such as high temperatures as found in aircraft turbines [3, 9].

The SRM's small short-circuit current and open-circuit voltage during fault condition adds to its inherent fault tolerance by reducing the probability of an electrical induced fire in the application [10]. The SRM's generally low magnetic phase coupling and its electrically independent phases strengthens its operability during fault [11, 12]. Furthermore, the fairly independent control of tangential and radial force makes the SRM an appropriate candidate to implement fault tolerant control (FTC) strategies [13, 14]. Especially, SRMs with distributed inverters, i.e. connecting an inverter to each stator tooth coil, allow for an individual radial pole force control to minimize the unbalanced magnetic pull (UMP) existing during single pole faults.

1.1 Aim of This Work

This thesis addresses three main SRM topics concerning fault tolerant applications. Firstly, a streamlined implemented direct instantaneous torque control is the base requirement. Secondly, a holistic machine design, to enable low torque ripple and fault tolerant control strategies, for the required operation range is necessary. Finally, an efficient control to reduce unbalanced magnetic pull during fault condition has to be implemented.

The model dependency of direct instantaneous torque control (DITC) used during normal, fault-free operation is investigated. The objective is to reduce the control complexity by reducing the necessary number of lookup tables resembling the machine characteristics, exploiting the parallel processing capability of the field programmable gate array (FPGA). Therefore, a DITC control structure with only one lookup table (LUT) is proposed. The saved memory space can then be used to add LUTs modeling mutual pole coupling and radial pole forces, required for fault tolerant control strategies.

From a system level perspective, independent of whether fault-free or fault tolerant operation is used, the SRM should be designed with its application specific control in mind. Thus, a generalized methodology for designing SRMs with a planned statistical approach, known as design of experiments (DOE), is proposed. In contrast to previous approaches, the control algorithm used for the machine is part of the design process. In addition, this approach allows the engineer to understand interactions between the design variables and decide on the trade-offs from contradicting optimization criteria found in machine design, while immensely reducing and simplifying the overall process.

Fault tolerant SRM operation with a distributed inverter during single pole fault is investigated. This fault condition is the most probable cause in such a drive configuration. Thereby, the goal is to minimize torque ripple during fault, while also to minimize the radial unbalanced magnetic pull (UMP). Thus, a combination of DITC and a radial force minimization control (RFMC) is proposed. Simulation and experimental results are presented for two implemented fault control strategies.

1.2 Outline

This thesis is organized in seven chapters, which are briefly introduced in this section.

Chapter 2: Fundamentals

This chapter provides a compact overview on the operating principle and mathematical equations describing the switched reluctance machine (SRM), followed by an introduction on the concept of distributed inverters and their benefits. Thereafter, the basic SRM control algorithms, hysteresis current control (HCC), direct average torque control (DATC) and direct instantaneous torque control (DITC) are presented. Finally, the different SRMs investigated within the scope of this thesis are introduced.

Chapter 3: Modeling Switched Reluctance Machines

The third chapter presents different modeling approaches of SRMs depending on which effect should be incorporated in the system simulation. The difference between phase-based modeling, which is commonly used for fault-free SRM operation, and models necessary for fault operation are discussed.

Chapter 4: DITC Control Improvement - Fault-Free Operation

Chapter 4 investigates the model dependency of DITC on the control quality. Furthermore, a DITC control structure with only one LUT is proposed. The reduction of control complexity enables online adaptive tuning algorithms to minimize torque ripple during fault-free operation. A further method to reduce torque ripple is by machine design. A machine design methodology, incorporating the used control strategy, based on design of experiments (DOE) is proposed. An exemplary 1 kW three-phase machine design is executed to demonstrate the effectiveness of this approach.

Chapter 5: Control of Distributed Inverters - Fault Tolerant Control

Chapter 5 introduces the possibilities given by a distributed inverter in respect to fault tolerant control strategies. Different new radial force minimization controls (RFMCs) in conjunction with direct instantaneous torque control (DITC) are proposed. The impact of each control on torque, radial pole forces, unbalanced magnetic pull and current loading is investigated. The operation boundaries for different SRM configurations are presented.

Chapter 6: Experimental Results and Analysis: SRM-16/12

The experimental test-bench setup used and measurement results from a 1 kW laboratory SRM are presented in chapter 6. Thereby, the previously proposed control strategies are verified and analyzed. Effects of machine asymmetries and magnetic pole coupling observed in the measurements are discussed.

Chapter 7: Conclusions and Outlook

The final chapter summarizes all key findings from the thesis and provides an outlook on related future research topics.

2 Fundamentals

The following chapter introduces the fundamentals of switched reluctance machines as well as showing an overview of the machine configurations investigated in this thesis. The required inverter topologies and employed control techniques are introduced, followed by the concept of distributed inverters.

2.1 Switched Reluctance Machines

This section presents the operating principle as well as the electrical and magnetic machine equation representation of the SRM.

2.1.1 Operating Principle

In contrast to rotating field machines, such as the induction machine (IM) and permanent magnet synchronous machine (PMSM), which produce their torque based on the Lorentz principle, a switched reluctance machine's (SRM) torque production is based on the reluctance force. Reluctance describes the magnetic resistance experienced by a magnetic field in non-magnetic material such as electrical steel and air. Figure 2.1 shows an iron core with a coil winding, an air gap and a movable iron bar. The coil winding is excited by a current i flowing through the windings N_w resulting in an induced magnetic flux ϕ which follows the path of least resistance as indicated in figure 2.1a.

The flux path causes an exerting reluctance force on the movable bar in the air gap. The force indicated in figure 2.1a shows a tangential component F_tan and a radial component F_r in reference to the air gap and resulting movement of the iron bar. Allowing the movement of the iron bar between figure 2.1a and figure 2.1b, the effective air gap seen by the flux is reduced and, therefore, the energy within the system is minimized. Figure 2.1b shows the energetic stable condition, as in this position the air-gap length and, therefore, the total reluctance is minimized resulting in only a remaining radial force on the iron bar.

This principle of attracting forces between two components traversed by a magnetic flux is used in the SRM. SRMs typically consist of a double salient geometry as shown for

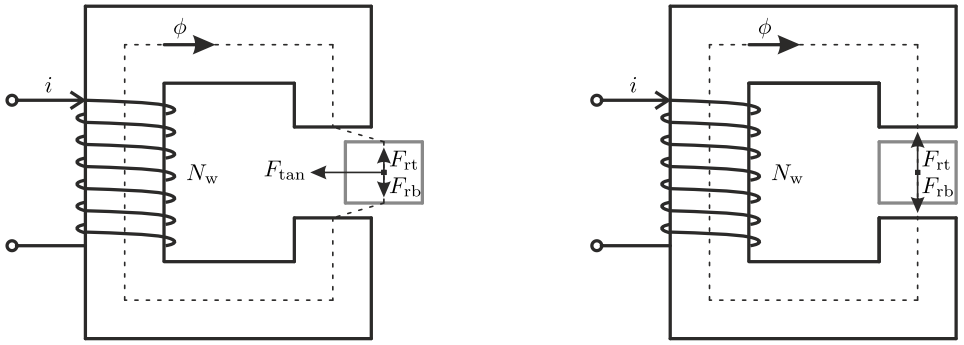

(a) Unstable condition (b) Stable condition

Figure 2.1: Coil winding with iron core exerting reluctance force

a 16/12 configuration in figure 2.2a, i.e. the machine consists of 16 stator and 12 rotor teeth.

In figure 2.2a and figure 2.2b the unaligned and aligned rotor positions in respect to phase 1 (pole 1.1) are illustrated. These two rotor positions are defined in terms of their electrical rotor position θ_{el} as 0° and 180° respectively and are used throughout the thesis. The naming convention for each stator tooth and, therefore, for each pole within a machine is also shown in figure 2.2a. Thereby, a mathematically positive numbering direction is used. The first number represents the phase number, while the second number is the pole number. Thus, the shown machine has four phases with 16 poles. The pole numbers 1, 5, 9 and 13 belong to phase number 1.

The electrical angle is calculated from the mechanical rotor position θ_m using equation (2.1).

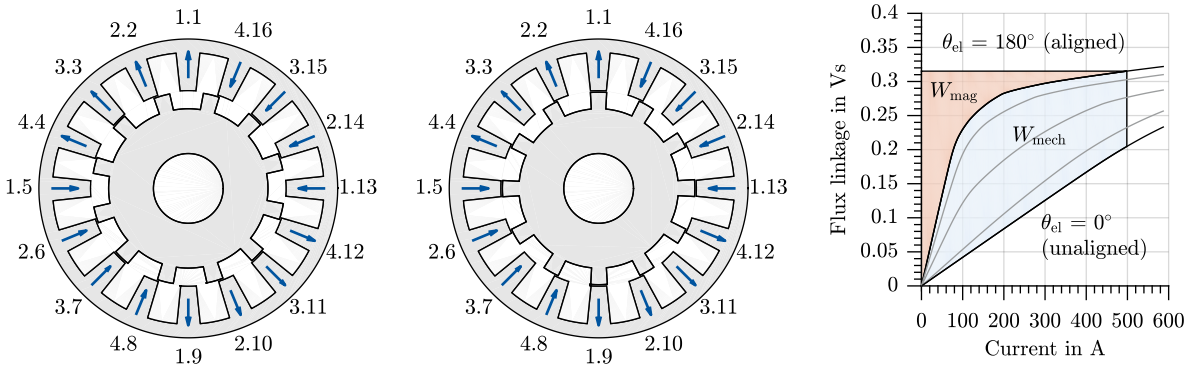

(a) Unaligned rotor position (b) Aligned rotor position (c) Co-energy loop

Figure 2.2: Characteristic SRM rotor positions in respect to phase 1 (pole 1.1) and its respective co-energy loop

$$\theta_{\mathrm{el}} = N_{\mathrm{r}} \cdot \theta_{\mathrm{m}} \tag{2.1}$$

The necessary stator number N_{s} and rotor number N_{r} defining the SRM's configuration depends on the phase number N_{ph} and pole pair number p, and can be expressed by equation (2.2) and equation (2.3).

$$N_{\mathrm{s}} = 2 \cdot N_{\mathrm{ph}} \cdot p \tag{2.2}$$

$$N_{\mathrm{r}} = 2 \cdot (N_{\mathrm{ph}} - 1) \tag{2.3}$$

The most commonly used configurations are listed in table 2.1. The configurations shown in bold are used and investigated within this thesis and are introduced in section 2.4.

Table 2.1: Common SRM configurations (configurations in bold are used in this thesis)

No. of phases	2		**3**			**4**		**5**	
No. of pole pairs	1	2	1	**2**	**3**	1	**2**	1	**2**
Configuration: $N_{\mathrm{s}}/N_{\mathrm{r}}$	4/2	8/4	6/4	**12/8**	**18/12**	8/6	**16/12**	10/8	**20/16**

2.1.2 Machine Equations

Electrical Description

An SRM's electrical behavior is described by its stator voltage equation (2.4).

$$v_{\mathrm{ph}}(t) = R_{\mathrm{ph}} \cdot i_{\mathrm{ph}}(t) + \frac{\mathrm{d}\psi_{\mathrm{ph}}(t)}{\mathrm{d}t} \tag{2.4}$$

In equation (2.4) v_{ph} is the phase voltage, R_{ph} represents the total phase winding resistance during operation, i_{ph} is the phase current and ψ_{ph} is the phase flux linkage. The flux linkage ψ_{ph} can be expressed in terms of its phase inductance L_{ph} and current i_{ph}. Furthermore, the flux linkage and inductance are either time-variant or specifically for SRMs the time variants are described as a dependence on phase current i_{ph} and rotor position θ as shown in equation (2.5).

$$\psi_{\mathrm{ph}}(i_{\mathrm{ph}},\theta) = L_{\mathrm{ph}}(i_{\mathrm{ph}},\theta) \cdot i_{\mathrm{ph}} \tag{2.5}$$

Expanding equation (2.4) with equation (2.5), the stator voltage equation is rewritten as equation (2.6). Thus, the general machine equation consists of the applied voltage v_{ph}, voltage drop across the windings, the phase- and incremental inductances and the speed

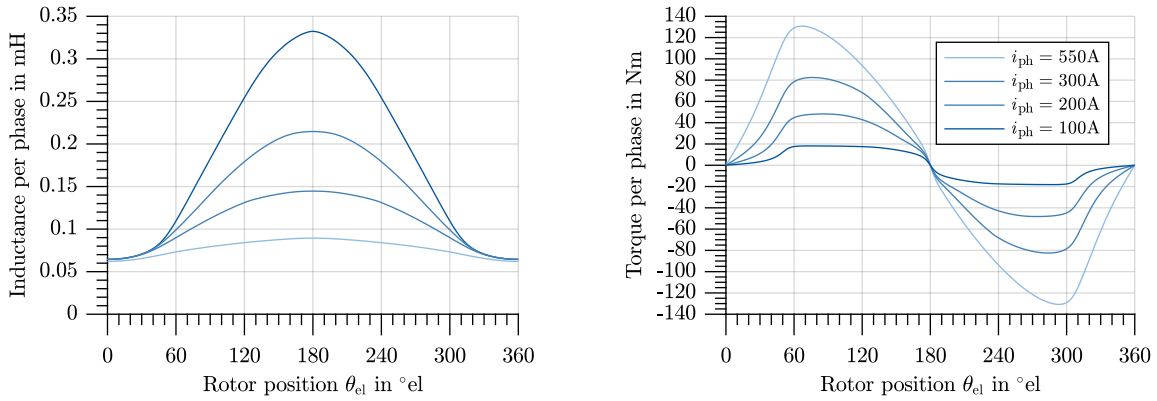

(a) Inductance profile

(b) Torque profile

Figure 2.3: Exemplary inductance and torque profile versus rotor position and current

dependent back electromotive force (EMF).

$$v_{ph} = \underbrace{R_{ph} \cdot i_{ph}}_{\text{ohmic voltage drop}} + \underbrace{\left(L_{ph}(i_{ph},\theta) + i_{ph}\frac{\partial L_{ph}(i_{ph},\theta)}{\partial i_{ph}} \right)\frac{\mathrm{d}i_{ph}}{\mathrm{d}t}}_{\text{incremental inductance } l(i_{ph},\theta)} + \underbrace{i_{ph}\frac{\partial L_{ph}(i_{ph},\theta)}{\partial \theta}\frac{\mathrm{d}\theta}{\mathrm{d}t}}_{\text{back EMF}} \tag{2.6}$$

The introduced inductance in equation (2.5) represents a non-linear function of both phase current i_{ph} and rotor position θ. The current dependency arises from the SRM's operation in material saturation to increase its energy conversion efficiency and, therefore, reduce the power rating of the converter [8, 10, 15]. An exemplary inductance profile is shown in figure 2.3a for various current values. As the current increases, the inductance value at the aligned rotor position ($\theta_{el} = 180°$) saturates and, therefore, decreases. A corresponding static torque profile is shown in figure 2.3b. With increasing phase current i_{ph}, the torque production increases. Furthermore, a SRM produces positive torque when its phase is excited before $\theta_{el} < 180°$, while negative torque is produced when the phase is excited between 180° and 360° independent of the current's direction in the coils.

Torque production, when the machine is not operated in saturation, can be expressed by the phase current i_{ph} and phase inductance L_{ph} as shown in equation (2.7)

$$T(i_{ph},\theta) = \frac{1}{2} i_{ph}^2 \frac{\mathrm{d}L_{ph}}{\mathrm{d}\theta} \tag{2.7}$$

However, when considering saturation for the torque calculation, the co-energy W_{co} and respective transferred mechanical energy W_{mech} have to be used. The co-energy is calculated from the integration over the flux linkage as in equation (2.8).

$$W_{\mathrm{co}} = \int \psi_{\mathrm{ph}}(i_{\mathrm{ph}},\theta)\mathrm{d}i_{\mathrm{ph}} \tag{2.8}$$

The mechanical energy W_{mech} is expressed by equation (2.9), which results from calculating the co-energy integration over an entire electrical period. The area enclosed by this co-energy loop is shown exemplary in figure 2.2c as W_{mech}.

$$W_{\mathrm{mech}} = \oint \psi_{\mathrm{ph}}(i_{\mathrm{ph}},\theta)\mathrm{d}i_{\mathrm{ph}} \tag{2.9}$$

The SRM torque is determined from the derivative of the co-energy as in equation (2.10).

$$T = \frac{\partial W_{\mathrm{co}}}{\partial \theta} \tag{2.10}$$

The SRM's average torque $\overline{T}_{\mathrm{avg}}$ is expressed by equation (2.11), which is calculated from the mechanical energy W_{mech} during one electrical period multiplied by the number of phases N_{ph} and rotor teeth N_{r}.

$$\overline{T}_{\mathrm{avg}} = \frac{N_{\mathrm{ph}} \cdot N_{\mathrm{r}}}{2\pi} \cdot W_{\mathrm{mech}} \tag{2.11}$$

Magnetic Description

In contrast to the electrical description, SRMs can be described as a magnetic circuit. The coil shown in figure 2.1 is expressed as an equivalent source as in equation (2.12).

$$\Theta_{\mathrm{MMF}} = \oint H\mathrm{d}l = N_{\mathrm{w}} i = R_{\mathrm{m}}\phi \tag{2.12}$$

The path along the iron core is divided into steel reluctances $R_{\mathrm{m}}^{\mathrm{fe}}$ and air-gap reluctances $R_{\mathrm{m}}^{\mathrm{ag}}$. The reluctance describes a flux tube using equation (2.13).

$$R_{\mathrm{m}} = \frac{l}{\mu_0 \mu_{\mathrm{r}} A} \tag{2.13}$$

Thereby, l is the flux tube length, A corresponds to the cross-sectional area orthogonal to the magnetic flux ϕ, $\mu_0 = 4\pi \cdot 10^{-7}$ H/m is the constant permeability in vacuum and μ_{r} is the relative permeability of the material used. While in air $\mu_{\mathrm{r}} = 1$, for all other materials μ_{r} depends on the magnetic saturation characteristic of the respective material. Figure 2.4 depicts characteristic permeability μ values versus magnetic field strength H

for common electrical steel. Furthermore, the relationship between the flux density B and magnetic field strength H in electrical steel is shown in the figure. These two quantities are coupled by the material permeability μ as in equation (2.14).

$$B = \mu H \tag{2.14}$$

The magnetic flux ϕ in figure 2.1 can also be determined by the surface integral of the normal component of the magnetic flux density B through the cross section A as in equation (2.15).

$$\phi = \int_A B \cdot \mathrm{d}A \tag{2.15}$$

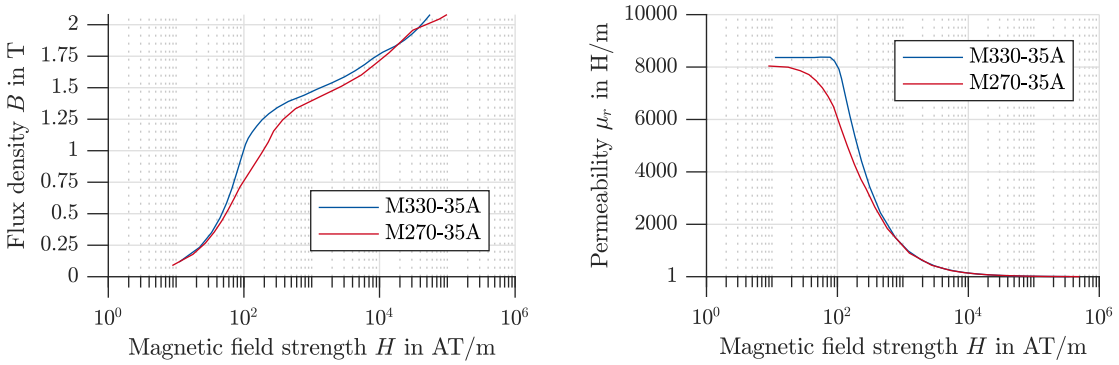

Figure 2.4: Exemplary permeability curves for common electrical steel materials

2.2 Distributed Inverters

In this section, the power electronics necessary to drive switched reluctance machines are presented. Furthermore, the concept and benefit of installing distributed inverters is discussed.

2.2.1 Topology

The two most common inverter topologies used for SRMs are either the full bridge topology or the asymmetric half bridge topology. A discussion on further topologies has been presented in [16, 17]. The full bridge is shown schematically for one machine phase in figure 2.5a and is used for synchronous and induction machines. The phase current can either be controlled in a positive or negative direction. In contrast to synchronous and induction machines, switched reluctance machines only require current flow in one direction to produce torque (see equation (2.7)), therefore, the inverter for SRMs can be

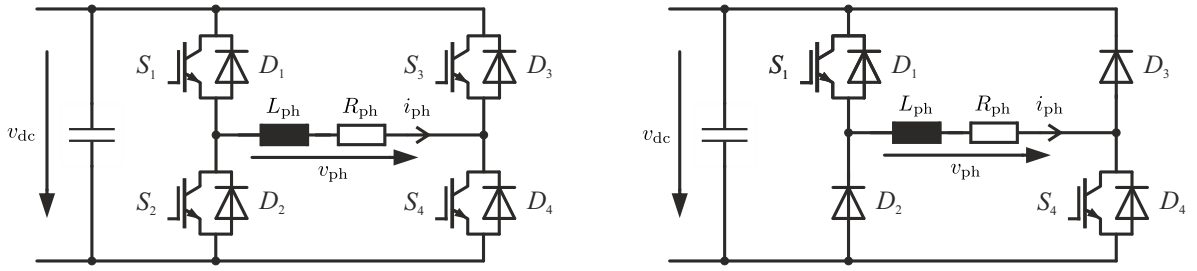

(a) Full bridge

(b) Asymmetric half bridge

Figure 2.5: Inverter topologies used for switched reluctance machines (shown only for one phase)

reduced in complexity and part count by using an asymmetric half bridge as is shown in figure 2.5b. This is also the most common topology used for switched reluctance machines, even though currently not readily available on the market as off-the shelf modules. A further benefit of the asymmetric half bridge is its inherent ability in case of a diode or switch shoot-through not to short circuit the dc-link, thereby increasing its fault tolerance capability.

To control the phase current i_{ph} the switching states shown in table 2.2 are selected by the control algorithm. Thereby, the *magnetization* state results in the dc-link voltage reduced by the voltage drop across the switches S_1 and S_4 to be applied to the machine phase resulting in a positive current gradient ($\Delta i_{ph} > 0$) as long as the back EMF is lower than the applied voltage. During the *demagnetization* state a negative dc-link voltage reduced by the voltage drop across the diodes D_2 and D_3, is applied resulting in a negative current gradient ($\Delta i_{ph} < 0$). The two remaining zero voltage states are referred to as *free-wheeling* states. These two states apply a near zero voltage to the machine phase resulting in an approximately constant current ($\Delta i_{ph} \approx 0$) and, therefore, flux linkage. The phase current i_{ph} reduces due to the back EMF, ohmic voltage drop and the voltage drop across one switch and one diode. However, if the back EMF is larger than the losses, i.e. during generating operation, the phase current i_{ph} increases instead of decreasing.

Table 2.2: Switching and conduction states for SRM inverters

		S_1	S_4	D_2	D_3
Magnetisation	$\Delta i_{ph} > 0$	1	1	0	0
Demagnetisation	$\Delta i_{ph} < 0$	0	0	1	1
Free-wheeling 1	$\Delta i_{ph} \approx 0$	1	0	0	1
Free-wheeling 2	$\Delta i_{ph} \approx 0$	0	1	1	0

2.2.2 Benefits of Distributed Inverters

Normally SRM inverters are built-up on a phase-based level. Each machine phase has one controllable inverter half-bridge or at least each machine phase is individually controllable, as also found in the shared-leg or Miller circuit topologies [18, 19]. However, to increase redundancy and fault tolerant operation, the number of inverter modules per phase can be increased, as has been proposed as a decoupled dual-channel SRM for aerospace in [3, 20]. The dual-channel SRM increases the overall drive reliability in respect to inverter and machine phase faults. Ding et. al. propose a 12/8 SRM containing two separate three-phase winding systems and two inverters operating the machine as two independent 6/4 SRMs. Thus, in case of a fault half of the machine can still be operated.

The number of inverter modules can further be increased until the current of each stator tooth is individually controllable [21]. Such a concept, where the inverter module is directly connected to the end-windings of the stator tooth, is presented and implemented for SRM-20/16 in [14]. The focus has been on integrating a distributed inverter into a direct-drive application to reduce overall drive volume and increase the drive's fault tolerance capability.

By adding intelligence (microelectronics) to the stator module the concepts of a *smart stator tooth* becomes viable. The smart tooth, as implemented for a PMSM with concentrated windings in [22, 23], has the ability to self-sufficiently control its stator tooth current even when communication to the central control digital signal processor (DSP) unit is lost. Therefore, the decentralization of control in case of a fault allows each tooth to operate autonomously and thus, ride through the fault.

Distributed inverters lead to three main advantages, namely, an optimal power electronics *integration* into the overall drive train, a focus on *modular design* of the power stage leading to economies of scale and an increased *fault tolerant operability*, resulting in control freedom during drive faults.

Integration

The current trend throughout industry to increase drive system power density has led to volume reduction of components by overall system integration. Thereby, considering the entire electric drivetrain as one component from the design stage up to production has led to overall system optimizations instead of individual component optimization. Furthermore, integration reduces the overall volume by elimination of separate housing and cooling for all components and connections between components.

The holistic design approach has further enabled system cost reduction and increased system efficiency. Distributed inverters allow the distribution of the entire power amongst

multiple smaller power devices and dc-link capacitors leading to a miniaturization of individual components, while also resulting in a distribution of the heat producing components [24, 25]. This miniaturization is further accelerated by wide-bandgap (WBG) power semiconductor switches with their reduced losses and thus smaller housing and cooling area. The close proximity of loss producing switching devices and the stator end-windings necessitates a well-designed cooling concept, filter design and electromagnetic noise suppression [26, 27].

For various PMSM configurations for electric vehicle applications different power electronic integration concepts are presented in literature [28–30].

Modular Design

In distributed inverter systems, each inverter module is identical resulting in a modularization at the component level, leading to a reduction in system cost due to economies of scale during manufacturing. A single control unit can, furthermore, be combined with various power stages resulting in a customizability to a certain extent, while retaining the benefits of mass production [2].

Fault Tolerant Operability and Control

A system is defined as fault tolerant (FT) if after a fault this system is still operational or at least operational with reduced performance, also known as *limp home* capability. Fault tolerant operability is usually achieved by incorporating redundancy in the system and applying specific control strategies, which react to individual short-circuit or open-circuit failures [2].

A distributed inverter, where each stator tooth has its dedicated power stage, increases the operability of the drive during fault, as only one pole is rendered non-functional during a fault and not the entire machine phase. Thus, an inherent *limp home* capability is given by the hardware allowing fault tolerant control strategies.

2.2.3 Faults, Detection and Reliability

When discussing fault tolerant operability, it is also necessary to discuss inverter and machine faults, possibilities to detect these faults, as well as the reliability of the distributed inverter system compared to a standard asymmetric half-bridge inverter.

Classifications of SRM faults, their effect on drive performance and possible remedies to

avoid a complete failure of the drive has been discussed in literature [31]. This section is a short overview of the most prominent faults in regard to using a distributed inverter. A more detailed examination of faults and reliability of a distributed inverter is found in [32]. The most common failures in inverters, besides the capacitor, are either short circuit or open circuit of the switches [33]. The most common failures in the electrical machines, besides bearing failure, are winding isolation short-circuit or open-circuit faults [34–36].

Short-circuit faults are usually more critical than open-circuit faults, especially in regard to drive operation after a fault. Short-circuit failures often lead to high currents in the inverter or machine, especially, when only a small number of turns in the machine coil are shorted [37]. However, with adequate fault detection methods these high currents can be suppressed or avoided by switching off the faulty inverter module [11]. Only a short-circuit in the dc-link (e.g. capacitor) or in the machine coil can not be influenced by actively switching off the pole module. In case of a shorted dc-link or capacitor the entire drive has to be stopped, except if a redundant power supply is implemented [38]. A short-circuit in the machine windings causes induced currents in the windings, which should be small enough not to cause a thermal overheating of the machine [11]. However, the circulating currents will cause additional torque ripple and vibration. As long as the machine stays thermally stable its operation can be continued, similar to an open-circuit fault. An open-circuit fault in the distributed capacitor would cause a loss of $1/N_\mathrm{s}$ capacitance, which would only increase the voltage ripple during operation. In case of an open-circuit fault in one of the switches the SRM can still be partly operated as suggested for a phase-based inverter by [31], or as in this thesis, the entire pole is switched off and not used during the fault operation. Similarly, an open-circuit fault in the machine coil renders the entire pole unusable. If one of the diodes fails, no free-wheeling path for the current exists forcing the current to zero resulting in a sharp increase in voltage, which could destroy the corresponding switch in the inverter. The destroyed switch then again would result in an open-circuit fault.

To actively switch off a faulty pole, either a fault detection method is implemented or a fuse can be used. To realize fault tolerant control strategies, which can react to a fault, the control algorithm needs to know which component of the pole is defective to react appropriately [32]. Once the faulty component and, thus, the faulty inverter module has been isolated, the faulty machine pole acts as an open-circuit fault to the control. Therefore, the most probable fault case for a fault tolerant control (FTC) to react to is a single pole open-circuit fault.

Even though a distributed inverter has more components than a standard asymmetrical half-bridge inverter its reliability, in regard to the failure of a complete phase, is considerably higher due to the largely increased redundancy of the individual switching components. The increase in reliability for distributed inverters is presented for SRM-20/16 in [32].

2.3 Control Overview

The following section is a short summary on commonly used control algorithms for switched reluctance machines. These algorithms are the fundamentals for the control adaptations introduced in chapter 4 and chapter 5.

2.3.1 Hysteresis Current Control and Average Torque Control

The basic method to operate an SRM is by hysteresis current control (HCC). Thereby, a positive voltage is applied to the machine phase at the turn-on angle θ_{on} and a negative voltage is applied to the machine at the turn-off angle θ_{off}. In between these two angles the current is controlled to follow the reference current i^*_{ref} within a hysteresis current band Δi by using the free-wheeling switching state, i.e. near zero voltage as shown in figure 2.7a.

In figure 2.6 a schematic overview of the control structure for hysteresis current control (HCC) is shown. To control machine torque with HCC a LUT is necessary where, for a given machine, depending on torque T and speed n the optimal switching angles θ_{on} and θ_{off} as well as the reference current i_{ref} are stored. The switching frequency is variable and determined by the width of the used hysteresis band Δi. Investigations regarding the influence of different switching angles on control, drive performance and acoustic behaviour are found in [39–41].

The resulting torque waveform and co-energy loop for hysteresis current control is shown in figure 2.7b and figure 2.7c. By applying correct turn-on θ_{on} and turn-off θ_{off} angles and by using the correct reference current i_{ref} for the hysteresis band, the average output

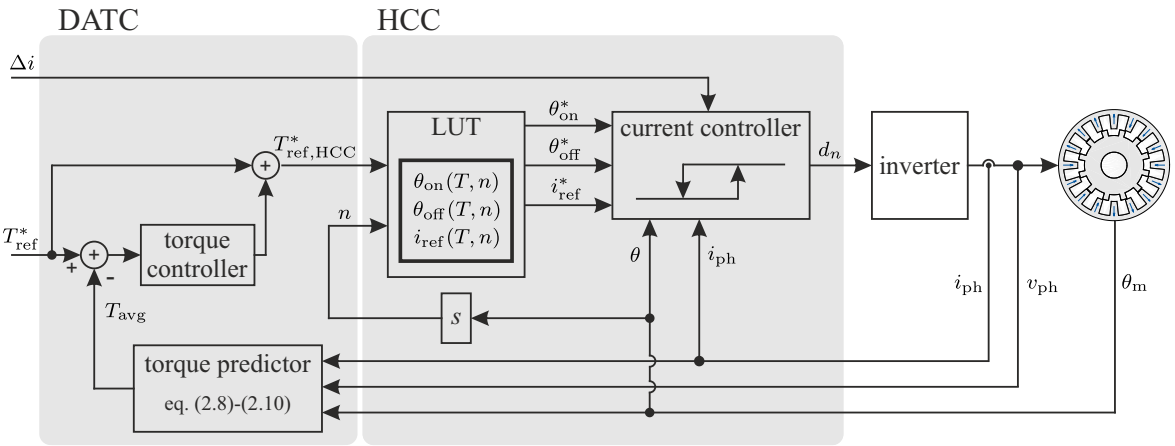

Figure 2.6: Schematic control overview of Hysteresis Current Control (HCC) and Direct Average Torque Control (DATC)

torque of the SRM is set.

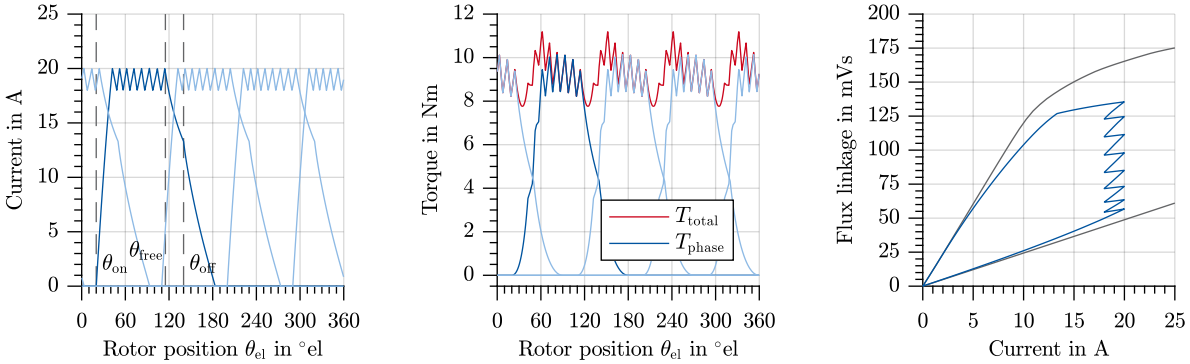

(a) Phase current (b) Phase & total torque (c) Phase co-energy loop

Figure 2.7: Characteristic Hysteresis Current Control (HCC) waveforms during pulsed operation of a four-phase machine

As the rotational speed of the machine increases, so does the back EMF, reducing the effective voltage across the machine phase. This reduces the current gradient during magnetizing state and can cause the phase current not to reach the desired reference current i^*_{ref}. During such an operation, the half-bridge inverter only switches once during each electrical period resulting in a so-called single pulse operation. The resulting current, torque and co-energy trajectories are displayed in figure 2.8. Single pulse operation allows switched reluctance machines to operate in a vast speed range, which enables one of its strength. Furthermore, the overall operational efficiency of the machine and especially of its inverter is improved due to reduced switching. The trade-off, however, is no active control over torque ripple. Therefore, during single pulse operation the torque ripple can become excessive.

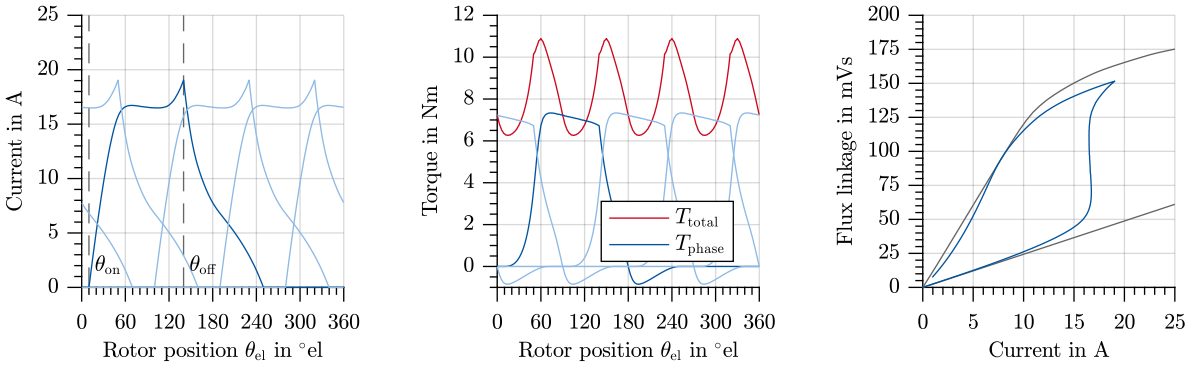

(a) Phase current (b) Phase & total torque (c) Phase co-energy loop

Figure 2.8: Characteristic Hysteresis Current Control (HCC) waveforms during single pulse operation of a four-phase machine

The HCC algorithm can be extended by an average torque predictor functioning as a feedback loop and a PI-controller, as is the case in direct average torque control (DATC) [42]. Figure 2.6 shows how DATC is added to the HCC algorithm. The torque predictor is either realized by a $T_{\mathrm{ph}}(i_{\mathrm{ph}},\theta_{\mathrm{el}})$-LUT or calculated from the terminal quantities using equation (2.8) and equation (2.11). Thereby, the switched reluctance machine is operated in average torque control over a wide operating range, with the drawback that the torque ripple is not directly influenced in this control method. The choice of HCC parameters (θ_{on}, θ_{off}, i_{ref}), which lead to an efficient optimal torque production is normally done in offline calculations. These parameters are then stored in torque and speed dependent LUTs on the control hardware.

2.3.2 Direct Instantaneous Torque Control

To overcome torque ripple and to obtain a smooth output torque in SRMs, the DITC algorithm was developed. This algorithm is based on an online calculation of the machine flux linkage from measured phase quantities and using the non-linear machine characteristics to estimate the current phase torque. The algorithm is either implemented hysteresis based as originally introduced on analogue circuits [43, 44], or as used in this thesis, based on pulse width modulation (PWM) [45, 46].

The structure of the pulse width modulation based predictive direct instantaneous torque control (PWM-DITC) algorithm is schematically shown in figure 2.9. The input variables are the reference torque T^*_{ref} to be set by the control and the maximum allowable machine phase current i_{max}. Furthermore, the electrical rotor position θ_{el}, phase current i_{ph} and effective phase voltage v_{ph} are necessary to determine the actual flux linkage ψ_n and phase torque T_n.

The electrical rotor position can either be determined from measuring the absolute mechanical rotor position θ_{m} with a resolver or by using sensorless position detection methods

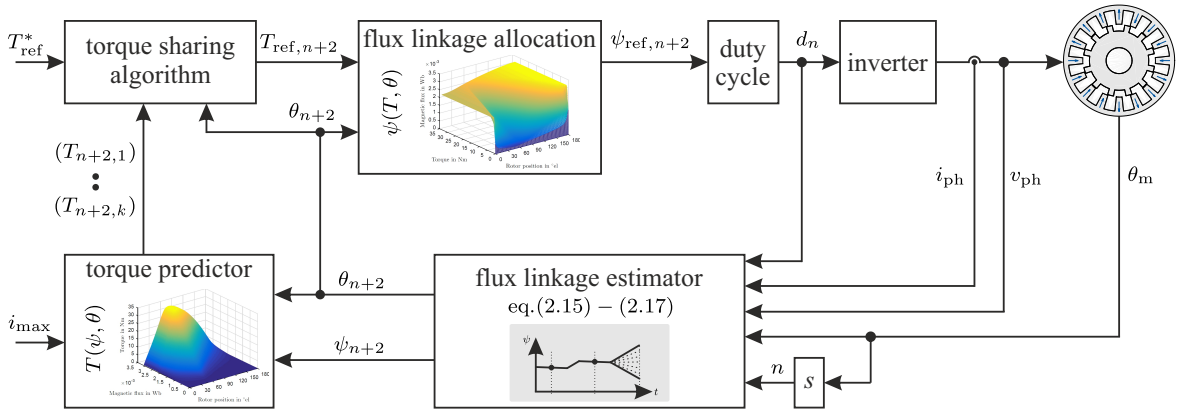

Figure 2.9: Schematic overview of predictive PWM based DITC control structure

as discussed in [47, 48]. The effective phase voltage v_{ph} is either measured from the machine terminals, or calculated according to equation (2.16) from the measured dc-link voltage v_{dc} and applied duty cycle d_n. Thereby, the dc-link voltage v_{dc} is measured while the respective current dependent voltage drop across inverter switches $v_{\mathrm{switch}}(i)$ and diodes $v_{\mathrm{diode}}(i)$ are subtracted to obtain an effective dc-link voltage $v_{\mathrm{dc,eff}}$.

$$v_{\mathrm{ph}} = d_n \cdot v_{\mathrm{dc,eff}} = d_n \cdot (v_{\mathrm{dc}} - v_{\mathrm{switch}}(i) - v_{\mathrm{diode}}(i)) \tag{2.16}$$

The current phase flux linkage ψ_n is either estimated from a $\psi(i,\theta)$-LUT or by integrating the voltage equation (2.4) as presented in discrete form in equation (2.17). This flux linkage ψ_{n+1} available in the machine is used to estimate the minimum and maximum flux linkage values ψ_{n+2} attainable in the following switching period. According to equation (2.18) these flux linkage values $\psi_{n+2}^{\mathrm{min}}$ and $\psi_{n+2}^{\mathrm{max}}$ are attained by applying a negative $-v_{\mathrm{dc,eff}}$ or positive $v_{\mathrm{dc,eff}}$ voltage to the phase for an entire switching period respectively.

$$\psi_{n+1} = \psi_n + (d_n \cdot v_{\mathrm{dc,eff}} - R_{\mathrm{ph}} \cdot i_{\mathrm{ph}})\Delta t \tag{2.17}$$

$$\psi_{n+2} = \psi_{n+1} \pm (v_{\mathrm{dc,eff}} \mp R_{\mathrm{ph}} \cdot i_{\mathrm{ph}})\Delta t \tag{2.18}$$

These two values ($\psi_{n+2}^{\mathrm{min}}$ and $\psi_{n+2}^{\mathrm{max}}$) represent the boundary flux linkages, which are used by the algorithm to allocate torque to each phase. The maximum allowed flux linkage $\psi_{\mathrm{lim}}^{\mathrm{max}}$ is limited by the maximum allowed phase current given by the value i_{max}. This prediction algorithm is shown schematically in figure 4.6 whereby k has to be set to 2 to represent the basic flux predictor used in DITC. The variable k, as introduced in section 4.1.2.2, describes the number of different flux linkage values predicted for one phase. In its base case only two flux linkages, the minimum and maximum, are predicted, i.e. $k = 2$.

The machine's phase torque $T_{n+2,k}$ is estimated by using the non-linear characteristics of the SRM stored in a $T_{\mathrm{ph}}(\psi_{\mathrm{ph}},\theta_{\mathrm{el}})$-LUT. With rotor position and the boundary flux linkage values, the minimum and maximum phase torque for the period $n + 2$ is determined. Thereafter, the multiphase torque sharing algorithm creates a priority list (phase priority stack) of all phases according to their torque producing capability and shares the reference torque amongst all phases [49]. Thus, each phase is allocated a reference torque $T_{\mathrm{ref},n+2}$. The duty cycle d_n set by the inverter is calculated from the reference flux linkage $\psi_{\mathrm{ref},n+2}$, which is determined by using a $\psi_{\mathrm{ph}}(T_{\mathrm{ph}},\theta_{\mathrm{el}})$-LUT. Thus, the PWM-DITC algorithm is based on at least two lookup tables used as the inverse machine model.

Figure 2.10 shows exemplary waveforms of phase current, phase torque and the co-energy loop when using the PWM-DITC algorithm. In comparison to the previously presented control types, the value of current is not directly controlled, but is a result of the machine dynamics (EMF) and the controlled flux linkage and torque reference.

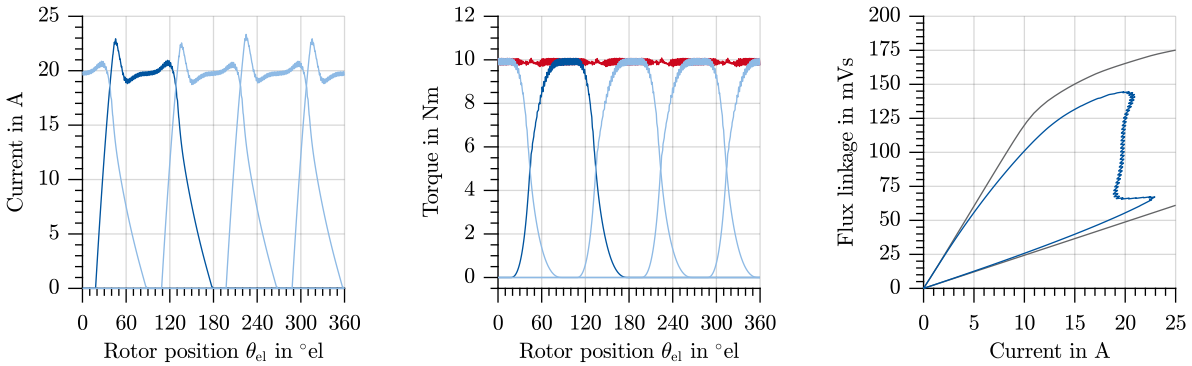

(a) Phase current (b) Phase & total torque (c) Phase co-energy loop

Figure 2.10: Characteristic PWM direct instantaneous torque control waveforms of a four-phase machine

2.4 Investigated SRM Configurations

The discussion and analysis in this thesis is based on four different investigated switched reluctance machines. The four machine cross sections are shown in figure 2.11 and are referred to as SRM-12/8, SRM-18/12, SRM-16/12 and SRM-20/16 respectively (see table 2.1).

Table 2.3 presents the machine data of the investigated SRMs. Thereby, the maximum values of speed and power $n^{\max}$ and $P^{\max}$ are short term maximum values for each machine, while the nominal values n^{nom} and P^{nom} represent continuous operation for the design control strategy. As the machines SRM-18/12 and SRM-16/12 are designed for HCC a reduced speed and power range $n^{\text{nom}}_{\text{DITC}}$ and $P^{\text{nom}}_{\text{DITC}}$ respectively are given for operation with DITC control. The reduced speed range is due to the necessary voltage reserve for DITC, while derating in power is due to the change of current waveform and an inherent increase in root mean square (RMS) current density.

SRM-12/8

SRM-12/8 is a 1 kW inner-rotor SRM with three phases and two pole pairs. The machine is designed to operate with DITC at its nominal operating point of 1 kW at 1500 rpm and a current density of 6.6 A/mm^2 (air ventilated cooling). The design procedure for this machine is presented in section 4.2. Especially the stator and rotor tooth geometry and number of windings are designed for DITC operation.

Table 2.3: Machine data of investigated SRMs

		SRM-12/8	SRM-18/12	SRM-16/12	SRM-20/16
No. of phases	N_{ph}	3	3	4	5
No. of pole pairs	p	2	3	2	2
Max. power	P^{max}	1 kW	70 kW	1 kW	67 kW
Max. speed	n^{max}	1500 rpm	23 krpm	1500 rpm	700 rpm
Nom. power	P^{nom}	-	35 kW	1 kW	-
Nom. speed	n^{nom}	-	6000 rpm	1000 rpm	-
Nom. power (DITC)	$P^{\mathrm{nom}}_{\mathrm{DITC}}$	1 kW	27 kW	400 W	56 kW
Nom. speed (DITC)	$n^{\mathrm{nom}}_{\mathrm{DITC}}$	1500 rpm	6000 rpm	400 rpm	300 rpm
Max. MMF/pole	$\Theta_{\mathrm{MMF,pl}}$	750 AT	3000 AT	1400 AT	14 500 AT
Switching frequency	f_{PWM}	10 kHz	20/40 kHz	10/20 kHz	10 kHz
DC-link voltage	v_{dc}	48 V	345 V	60 V	400 V
Outer radius	r_3	62.5 mm	97 mm	60 mm	320 mm
Active stack length	l_{stk}	80 mm	120 mm	115 mm	150 mm
Air-gap length	δ_{ag}	0.35 mm	0.5 mm	0.25 mm	1.5 mm
No. of windings	N_{w}	40	26	117	160
Wire diameter	d_{cu}	1.3 mm	1.6 mm	0.72 mm	1.5 mm
Current density	J_{RMS}	6.6 A/mm^2	12.5 A/mm^2	6.5 A/mm^2	7 A/mm^2
Designed control		DITC	HCC/DITC	HCC	DITC

SRM-18/12

SRM-18/12 is a three phase high-speed machine designed for a small electric vehicle with a maximum power rating of 70 kW and a maximum speed of 23 krpm [50]. The machine is designed to operate with hysteresis current control and single pulse operation at high speeds, while at speeds below $n^{\mathrm{nom}}_{\mathrm{DITC}} = 6$ krpm it can be operated with DITC. The nominal operating power $P^{\mathrm{nom}}_{\mathrm{DITC}}$ of SRM-18/12 is 27 kW at the design current density J_{RMS} of 12.5 A/mm^2. This machine has a water jacket cooling resulting in the higher allowable current density compared to the other three machines [51]. This machine too, is the only investigated machine with three pole pairs. Compared to the other machines, SRM-18/12 has a relatively low inductance to allow the high-speed operation. Therefore, to reduce current and torque ripple while using DITC a high switching frequency is used.

SRM-16/12

SRM-16/12 is a 1 kW SRM with four phases and two pole pairs. This machine is designed to operate with HCC up to $n^{\mathrm{nom}} = 1000$ rpm and with DITC up to 400 rpm. The machine has self-ventilated cooling with a current density of 6.5 A/mm^2. SRM-16/12 has the ability to connect inverter modules to each stator tooth and is, therefore, used to investigate

different fault tolerant control strategies on the test bench. The test bench is described in section 6.1.

SRM-20/16

SRM-20/16 is an outer-rotor SRM direct drive for railway traction applications with a nominal speed of 300 rpm and a torque of 1800 Nm. The machine is designed with focus on fault tolerant operation, hence a five phase design with four poles per phase is chosen [14, 32]. Furthermore, the drive is operated with DITC up to its nominal speed and power level at a current density of 7 A/mm^2 (air cooled).

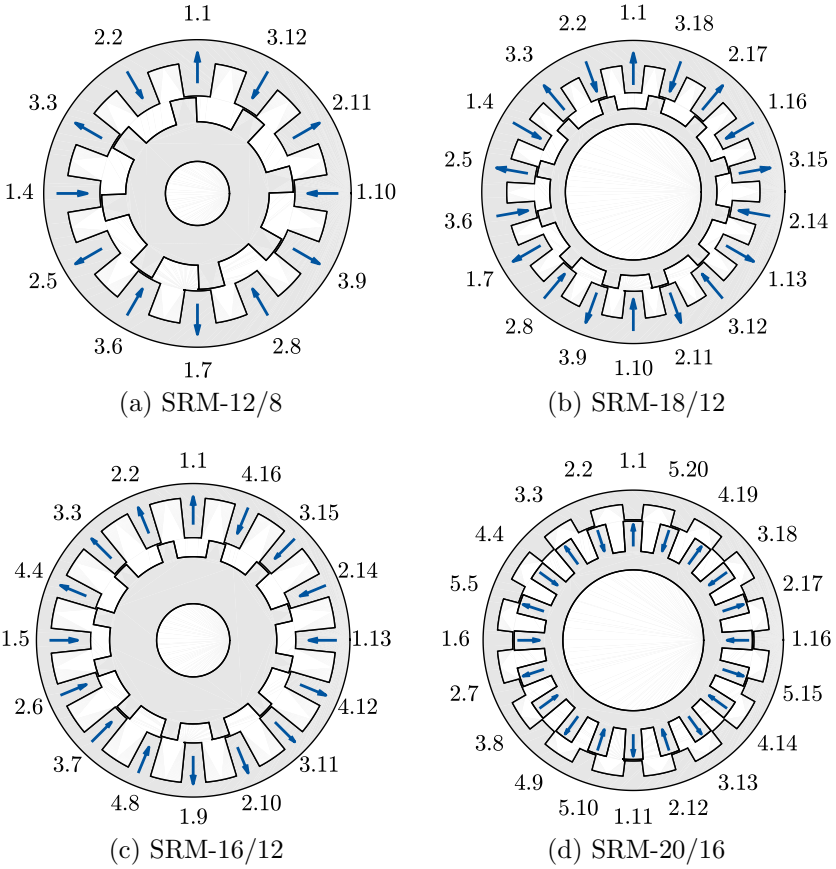

(a) SRM-12/8 (b) SRM-18/12

(c) SRM-16/12 (d) SRM-20/16

Figure 2.11: Cross section of investigated switched reluctance machines

3 Modeling Switched Reluctance Machines

The following chapter introduces different models used in this thesis. The models have specific advantages depending on the effects to be simulated in the SRM. At first, a short model overview is presented, followed by the introduction of the *Symmetric Phase Model*, which is normally used in literature. The SRM is represented only by one phase assuming electrical and electromagnetic symmetry on a phase level. Thereafter, an *Asymmetric Pole Model* is presented, which is used when information of each SRM pole is necessary. This is the case when rotor eccentricities should be accounted for. The asymmetric pole model, however, does not consider electromagnetic coupling between phases or poles. To consider mutual phase or pole coupling a *Mutual Coupling Model* is presented at the end of the chapter. The final and most accurate model type is the finite element analysis based *FEA Coupled Model*.

3.1 Overview

Machine models in simulation are necessary during the machine design and control algorithm development process. Such models used in an overall system simulation are referred to as *offline models*. The models are distinguished by their accuracy resembling the machine characteristics and their computational effort, i.e. execution speed. They range from simple linear equations to complex finite element analysis (FEA) or multi-physics based models.

Furthermore, machine models are used in control algorithms to operate the drive. These models are referred to as *online models*. Thereby, the focus when creating such models lies in their ability to be executed in real-time (within a switching period), while being as accurate as possible. For direct instantaneous torque control (DITC) these online models in their earliest form consisted of analog circuitry, followed by control algorithms implemented in digital signal processors (DSP), i.e. sequential code execution as with PWM-DITC. Today, ever more field programmable gate arrays (FPGA) with their fast parallel execution capability are used.

SRM models are classified by their main state variable and are either flux-linkage or inductance based. The common task of all machine models is to describe the relationship between flux linkage or current in the machine and its produced output torque or radial force.

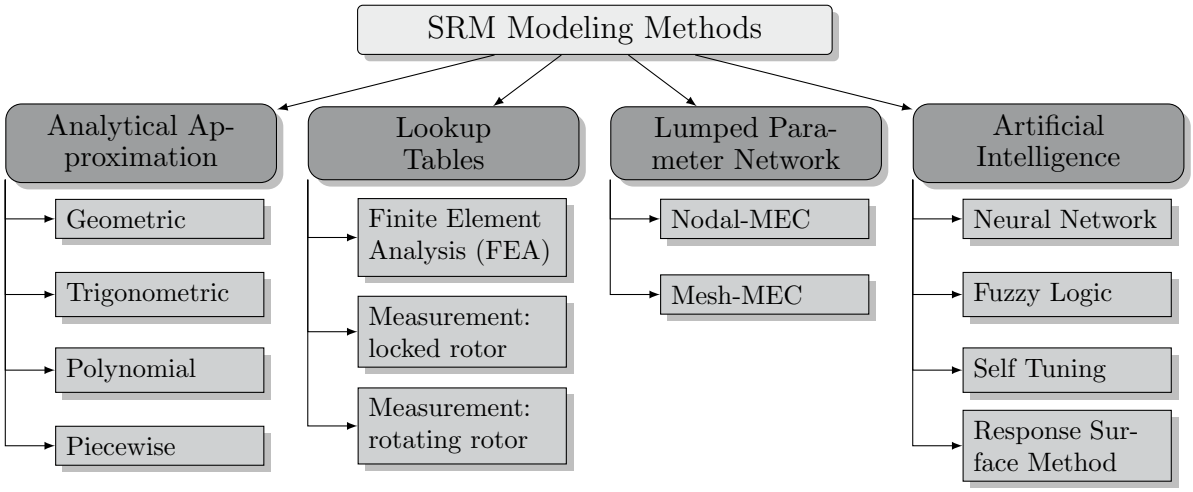

Figure 3.1: Overview of SRM modeling techniques

The models are either of a linear or non-linear type. The former, assumes a linear relationship between flux linkage and current, which causes the flux linkage and phase inductance to be only rotor position dependent, i.e. $\psi(\theta)$ and $L(\theta)$. The non-linear model additionally considers effects such as magnetic saturation of the iron material. As modern SRMs are usually operated in deep material saturation only non-linear models are of interest here. This leads to the flux linkage $\psi_{\mathrm{ph}}(i_{\mathrm{ph}},\theta_{\mathrm{el}})$ and phase inductance $L_{\mathrm{ph}}(i_{\mathrm{ph}},\theta_{\mathrm{el}})$ being dependent on rotor position θ_{el} and phase current i_{ph}.

In figure 3.1 an overview of different categories of models found in literature is shown. The models are divided into four main categories, which are shortly described in the following. A general overview of different modeling types and their advantages and disadvantages is presented in [52, 53].

Analytical Approximation

The simplest SRM model is based on analytical equations, whereby the geometry of the machine is used to describe the flux path in the machine and, thus, its characteristics (inductance, torque profile, etc.) are determined [54–57]. A further method is by approximating the iron material saturation or directly approximating the SRM characteristic by polynomials or piecewise continuous functions [52, 58, 59]. The simplistic formulation and reduced computational burden to solve the equations in real time are the main benefit using analytical equations [60]. However, this comes at the risk of oversimplification, which can lead to reduced accuracy. Therefore, in literature the models are often verified by finite element analysis (FEA) based models and measurements.

As online models, the analytical approach is commonly used in form of a torque sharing function (TSF) or current profiling to set continuous output torque. The TSF as

such determines the flux linkage or current to be set at each rotor position. Thus, it inherently encompasses the machine model and the control. The equation parameters for the torque sharing function, which are normally calculated offline and stored in tables, depend on each machine individually and, therefore, describe the machine's own characteristics. Thereby, different optimization goals such as torque ripple minimization [61–63] or efficiency optimization [59, 64, 65] have been pursued.

Lookup Tables

The majority of SRM models depend on some kind of lookup table (LUT) due to its ease and accuracy to model the different two-dimensional nonlinearities present in the reluctance machine. The drawback of LUTs are their resource intensive implementation in hardware compared to the analytical approach, and the necessity to simulate (by FEA) or measure the tables. The fundamental models consist of LUTs directly describing the machine's flux linkage and torque characteristics [66]. Another method to store and model SRM characteristics is by means of Miller's *gauge curves* as introduced in [58, 67]. The lookup tables are either generated from finite element analysis offline calculations [68] or can be constructed from test bench measurements. Test bench measurements can further be divided into locked rotor [66, 69] and rotating rotor measurement [70, 71]. In both measurement types, the machine's phase is excited with voltage pulses at various rotor positions to construct the LUTs. In the first measurement type, the rotor is clamped at fixed positions with a torque transducer to measure static torque, while in the second measurement type the rotor is rotated at low speed.

Lumped Parameter Network

Instead of using analytical equations to describe the flux distribution, a magnetic lumped parameter network (LPN) can be used [72]. Thereby, reluctances describe the main flux paths in the machine in form of flux tubes according to equation (2.13) [73]. The reluctance is dependent on the length l and relative permeability μ_r. The air-gap reluctance $R_\mathrm{m}^\mathrm{ag}(\theta)$, connecting stator and rotor teeth for example, is dependent on the rotor position θ_el, because the distance between rotor and stator teeth varies with rotor position. Reluctances representing the paths in iron sheet material $R_\mathrm{m}^\mathrm{fe}(\phi)$ are dependent on the change in relative permeability $\mu_\mathrm{r}(\phi)$ due to available magnetic flux ϕ. Therefore, the saturation effects present in SRMs is incorporated in this model [14]. These reluctances are combined to a magnetic equivalent circuit (MEC) depicting the entire machine. Solutions are either node or mesh based comparable to Kirchhoff's current and voltage law [74]. The benefit of such a LPN is the reproduction of phase and pole coupling when asymmetries in the machine need to be accounted for [52, 75].

The LPN is a performant solution, especially for offline models. Its drawback is solving

the non-linear matrices, which is currently still a challenge to do in real-time on a DSP or field programmable gate array (FPGA) [76]. The increasing computational power of microelectronics and more efficient solving algorithms will enable future LPN models to run in real-time and then be effectively used in the machine control.

Artificial Intelligence

In contrast to *analytical approximation*, where an explicit mathematical equation is formulated, artificial intelligence is based on a general model formulation which is trained by appropriate data sets to represent the non-linear SRM flux linkage characteristic. This type of modeling can achieve a high accuracy, however, the model training requires large data sets and high computational capability if to be done online [53]. The model formulations differ depending on the artificial technique used. Common SRM models found in literature are based on artificial neural network (ANN) [21, 77] or fuzzy logic [78].

Another method is using self tuning models, whereby, flux linkage is expressed as a function of phase current, rotor position and a number of coefficients. In [79], a online (on the DSP) linear recursive least-squares identification is used to determine the corresponding coefficients according to current measurements taken from the operating machine. This enables the machine model to be tuned according to the real machine.

3.2 Symmetric Phase Model

Lookup-table Model

Lookup-tables are the most common methods used to model switched reluctance machines. During the machine design stage FEA is used to predict the characteristics and performance of the final machine. Therefore, the machine tables are known and can be used to model the dynamic behavior of the SRM with its respective control and mechanical system (load). The LUTs account for the SRM's non-linear characteristics as shown in figure 3.3. Thereby, both material saturation along the magnetizing axis (flux linkage or current) and the rotor position dependent non-linear behavior are stored.

In figure 3.2 the fundamental flux linkage based phase model of an SRM according to its voltage equation (2.4) is depicted. The input variables are the applied phase voltage v_{ph} from the inverter and the electrical rotor position θ_{el}. The output variables are the phase current i_{ph}, tangential force $F_{\mathrm{tan,ph}}$ (or torque T_{ph}) per phase and if necessary radial force per pole $F_{\mathrm{rad,pl}}$.

This model in its elementary form requires two lookup tables $i_{\mathrm{ph}}(\psi_{\mathrm{ph}},\theta_{\mathrm{el}})$ and $F_{\mathrm{tan}}(\psi_{\mathrm{ph}},\theta_{\mathrm{el}})$

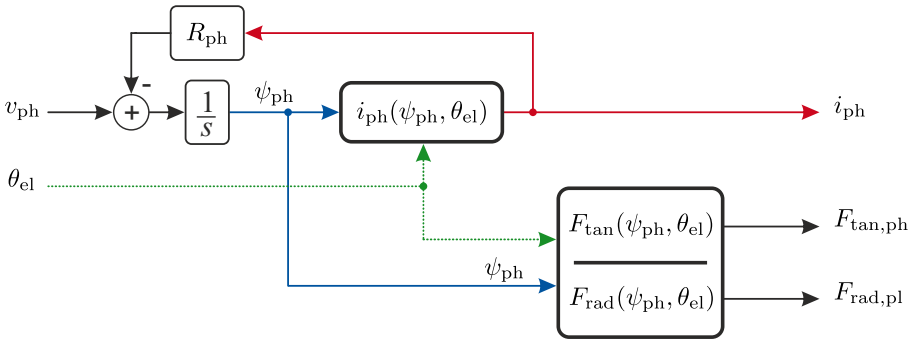

Figure 3.2: Phase based SRM model

(or $T_{\mathrm{ph}}(\psi_{\mathrm{ph}},\theta_{\mathrm{el}})$ for torque), which are shown for SRM-16/12 in figure 3.3a and figure 3.3b as an example. In figure 3.3c the corresponding radial force LUT per stator tooth is depicted. The fourth LUT $\psi_{\mathrm{ph}}(T_{\mathrm{ph}},\theta_{\mathrm{el}})$ shown in figure 3.3d is necessary to determine the reference flux linkage from reference torque in DITC as described in section 2.3.2.

The LUTs are either determined from FEA or from test bench measurements. During FEA modeling it is essential to consider manufacturing and material tolerances so that the calculated machine characteristics resemble those of the real machine.

From Measurement to FEA Characteristic

For SRM-16/12 test bench measurements (torque and flux linkage measurements with locked rotor) are taken and compared to the FLUX™2D FEA model. Besides deviations between the saturation characteristics of the FEA material and the real steel, modeling the stray flux in the air gap has a large effect on the saturation characteristic. The goal is to adapt the FEA model to minimize the error between the FEA characteristics and the ones retrieved from measurements. This is necessary as the LUT tables from FEA are used to develop the machine models and control algorithms.

The flux linkage trajectory as displayed in figure 3.4a at the aligned position ($\theta_{\mathrm{el}} = 180°$) is predominantly dependent on the air-gap reluctance and saturation in the yoke and tooth material. The difference in material saturation or the actual air-gap length in the prototype (measurement) to the FEA simulation is clearly visible. In contrast, the unaligned position ($\theta_{\mathrm{el}} = 0°$) is predominantly dependent on stray flux linkage between the stator and rotor. The position in between consist of a mixture of the two effects. Therefore, two arbitrary additional rotor positions 70° and 110° are shown.

A close up view of the corresponding FLUX™2D FEA model used for the simulation is depicted in figure 3.5. The air-gap length is 0.25 mm as given by the manufacturer and in machine data table 2.3.

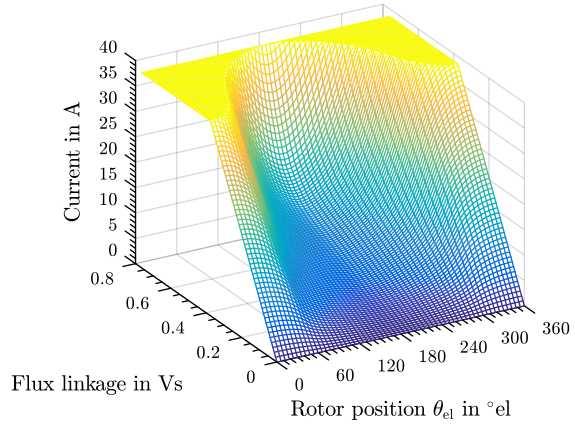

(a) $i_{ph}(\psi_{ph},\theta_{el})$

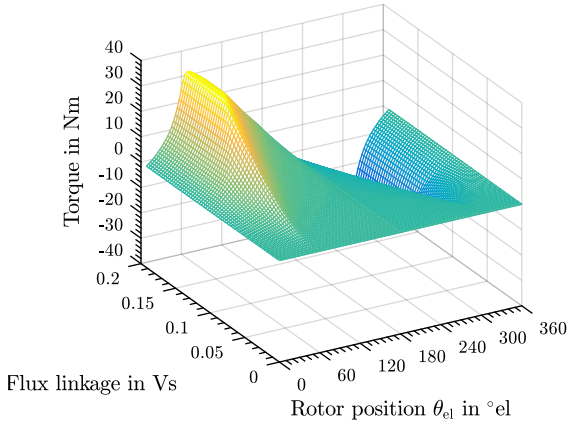

(b) $T_{ph}(\psi_{ph},\theta_{el})$

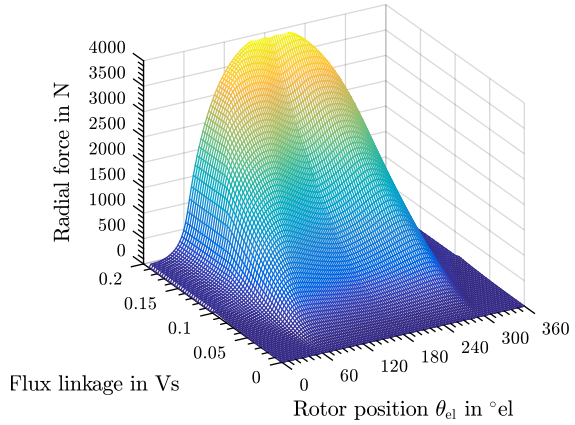

(c) $F_{rad}(\psi_{ph},\theta_{el})$

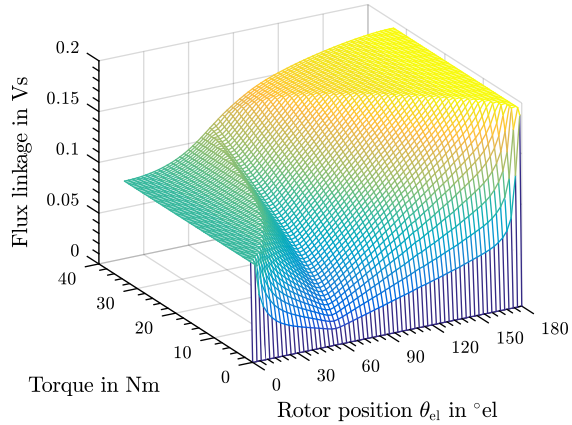

(d) $\psi_{ph}(T_{ph},\theta_{el})$

Figure 3.3: Characteristic lookup tables representing switched reluctance machines

The flux linkage trajectory after adjusting the FEA model to fit the manufactured machine is shown in figure 3.4b. The air-gap length is increased to 0.33 mm from 0.25 mm and a material with a saturation characteristic better matching the prototype material (from M330-35A to NO30) is chosen, to align the flux linkage curve at 180°. The second step is to align the curves at 0° by increasing the distance between the coil winding and the air gap to allow for more stray leakage flux between stator and rotor tooth tips.

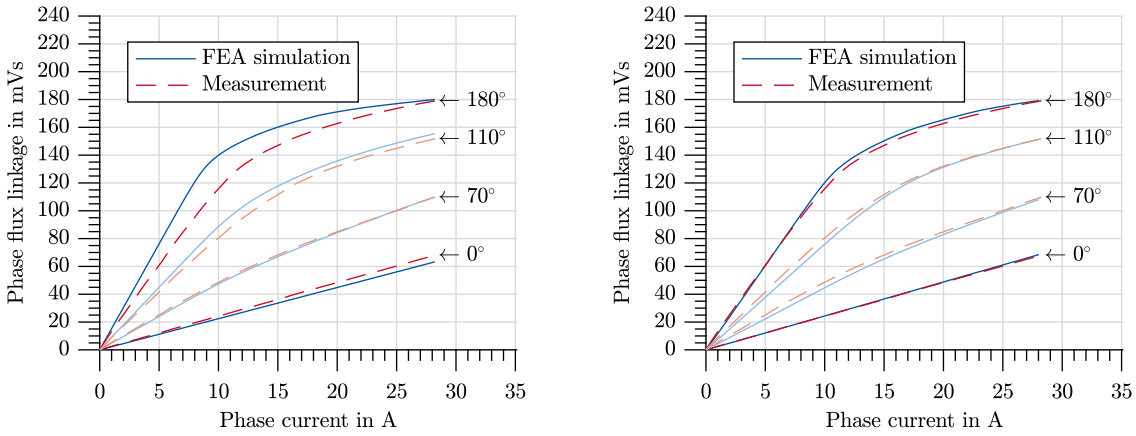

(a) Air-gap length: 0.25 mm, material: M330-35A

(b) Air-gap length: 0.33 mm, material: NO30 & reduced coil height

Figure 3.4: SRM-16/12: Comparison of measured and FEA simulated flux linkage trajectories

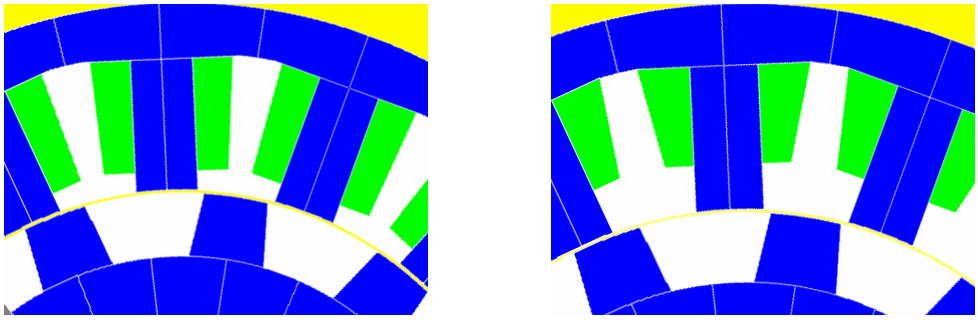

(a) Air-gap length: 0.25 mm

(b) Air-gap length: 0.33 mm & reduced coil height

Figure 3.5: SRM-16/12: Flux2D FEA cross sections with different coil modeling

3.3 Asymmetric Pole Model

The model from section 3.2 assumes all phases are symmetrical, however, if electrical or geometric asymmetries are of interest, a pole-based model is necessary. Such a model enables modeling of manufacturing asymmetries and resulting unbalanced magnetic pull (UMP) acting on the bearings [36]. The term asymmetry in such machines describes the fact that the air-gap length is not consistent along the rotor circumference. Either the rotor itself has a geometric asymmetry, while the bearings are placed centric to the stator (static eccentricity), or the bearings and, therefore, the entire rotor is not placed concentric to the stator (dynamic or rotating eccentricity). A dynamic eccentricity rotates with the rotor and, therefore, is periodic with the mechanical frequency. A static eccentricity interacts with each rotor tooth and, therefore, is periodic with the electrical frequency [80].

In figure 3.6, a LUT based asymmetric machine modeling approach is displayed. In contrast to the symmetric model presented in figure 3.2 each stator tooth is represented by an individual lookup table and all state variables are pole based [81]. Therefore, the number of LUTs required depends on the number of stator teeth N_s.

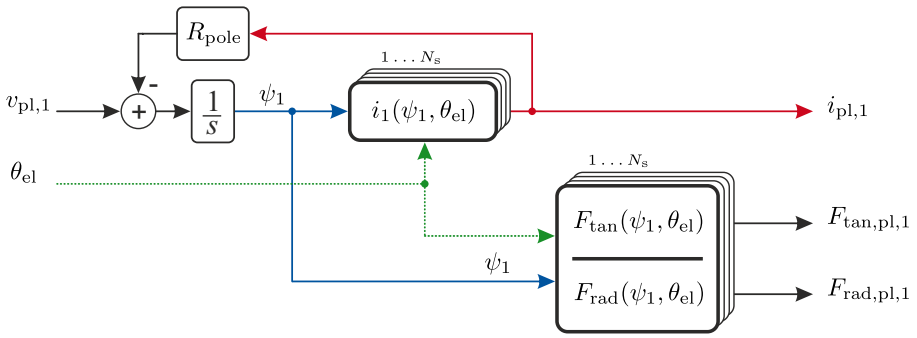

Figure 3.6: Pole based SRM model considering machine asymmetries

In a symmetric SRM the LUTs for each pole are identical. To model a static eccentricity, each pole has its own LUT representing the machine asymmetry in respect to the stator poles.

When a dynamic eccentricity is modeled the LUTs are shifted along the rotor circumference from tooth to tooth according to the mechanical rotor position [82]. An additional interpolation of values between the individual lookup tables along the position axis is used to achieve a smooth transition between neighboring tables. Thus, in contrast to static eccentricity where the LUTs are fixed to a stator tooth, during a dynamic eccentricity simulation, the LUTs become fixed to the rotor and the values for each stator tooth are calculated by cross LUT interpolation.

3.4 Mutual Coupling Model

The phases of SRMs are coupled electrically through the dc-link and electromagnetically by the machine's geometry and flux distribution. Furthermore, neighboring coil windings in a common slot are coupled through their individual changing electric fields when switched on and off. In contrast to rotating field machines, the electromagnetic coupling between phases in SRMs is relatively low and, therefore, the previously presented models usually suffice.

However, if the SRM is not operated in normal (healthy) condition and phase or pole faults are to be considered, a model is necessary, which considers asymmetric flux distribution and coupling between phases and poles.

In SRMs there are two possible coil arrangements, which are displayed in figure 3.7. The

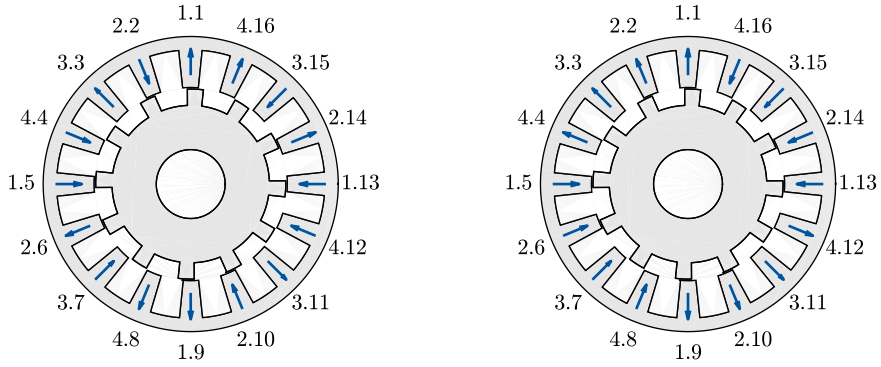

(a) Alternating phases (b) Non-alternating phases

Figure 3.7: Cross section of SRM-16/12 with two coil arrangements possible in SRMs shown by the arrows indicating the flux directions in each stator pole

coils are either connected as *alternating phases* (anti-parallel flux orientation) where each neighboring phase direction is opposite to the previous one, as in figure 3.7a, or the coils are connected as *non-alternating phases* (parallel flux orientation) resulting in a block wise connection in one direction as in figure 3.7b.

In machines with an odd number of phases, an alternating coil arrangement can be chosen resulting in all phases to couple in an alternating way. In even phase number machines, however, always both types of coupling will be present. This can be seen for SRM-16/12 in figure 3.7a and figure 3.7b where between poles 1.1 and 2.2 an *alternating* and between pole 1.1 and 4.16 a *non-alternating* flux direction is present independent of the coil arrangement.

During phase commutation, two consecutive phases are active, i.e. carrying current and producing flux in their phases. *Non-alternating* flux direction (parallel) in neighboring teeth usually causes a subtractive phase coupling reducing the overall flux, as the flux direction of both teeth oppose each other. In contrast *alternating* (anti-parallel) phase neighbors cause an additive flux, as both coupled teeth flux directions are the same. The influence of rotor position on the flux linkage for both coil arrangements and coupling influence due to phase excitation for SRM-16/12 and SRM-20/16 is shown in figure 3.8.

In figure 3.8 the *self flux linkage* ψ_{self} represents the trajectory when no coupling between neighboring phases is regarded. The flux linkages considering coupling between neighboring coils are $\psi_{\text{alternating}}$ for *alternating coupled flux* and $\psi_{\text{non-alt.}}$ for the *non-alternating* coil arrangement. The *non-alternating* (parallel) coil arrangement causes the flux linkage $\psi_{\text{non-alt.}}$ to experience a subtractive coupling effect, whereby the flux linkage is always lower than the self flux linkage ψ_{self}. All $\psi_{\text{non-alt.}}$ trajectories in figure 3.8 are lower than ψ_{self}. It can be observed how with increased phase current excitation the coupling effect increases resulting in a larger difference between the self flux and the non-alternating flux trajectory.

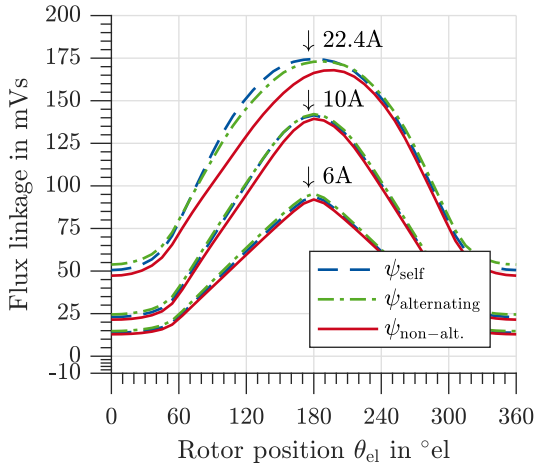

(a) SRM-16/12: Influence of rotor position on flux linkage [83]

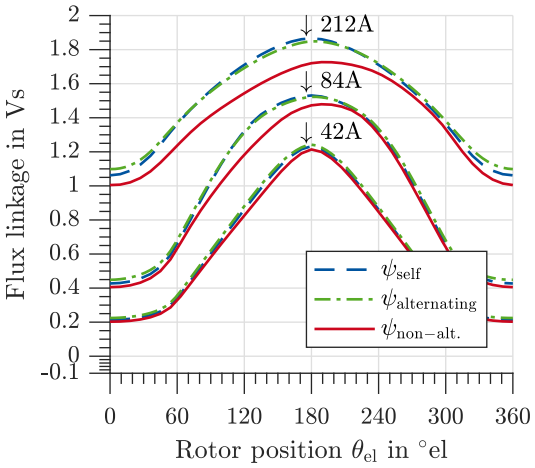

(b) SRM-20/16: Influence of rotor position on flux linkage

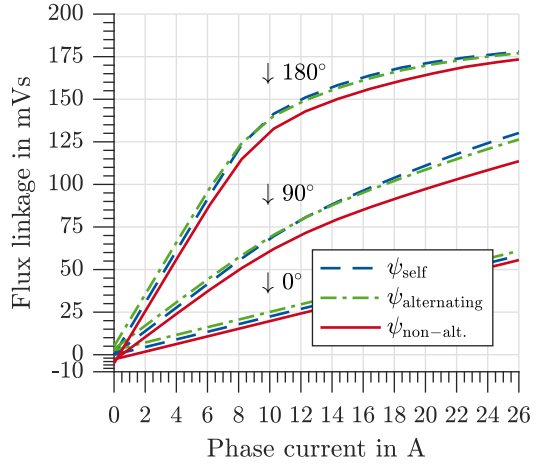

(c) SRM-16/12: Influence of phase current on flux linkage [83]

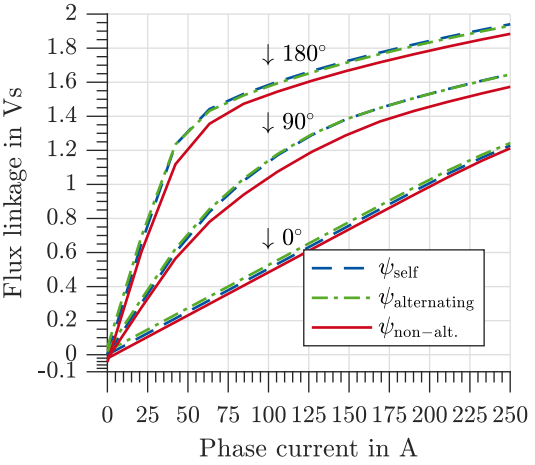

(d) SRM-20/16: Influence of phase current on flux linkage

Figure 3.8: Influence of coil arrangement on flux linkage for SRM-16/12 and SRM-20/16

Alternating (anti-parallel) flux direction causes an additive coupling increasing the flux linkage in the respective stator tooth. In figure 3.8c the trajectory for 0° shows higher values for $\psi_{alternating}$ compared to ψ_{self}. For $\theta = 90°$ and current values smaller than 10 A $\psi_{alternating}$ is larger than the self flux ψ_{self}. However, at higher current values or in figure 3.8a for $i_{ph} = 22.4\,A$ and $70° < \theta_{el} < 200°$ the alternating flux linkage trajectory reduces below that of the self flux linkage. This is contrary to the general theory. This effect can be accounted to excessive stator yoke saturation in SRM-16/12 as the yoke profile is relatively thin compared to the stator tooth width, resulting in an early saturation. The yoke saturation causes a negative subtractive effect on the overall flux linkage. In contrast, this excessive saturation effect is not as visible in figure 3.8b because the stator yoke of SRM-20/16 is large compared to the stator teeth, reducing the influence of yoke saturation. The larger phase overlap due to the higher number of phases in SRM-20/16

compared to SRM-16/12 is also visible in figure 3.8b.

Figure 3.9 shows the influence of coupling on the static torque profile. The superposition of phase 1 and 2 without coupling (superposition phase 1&2) is similar to the alternating coupled phase torque (coupled alternating). Non-alternating neighboring phases, however, deviate from the torque superposition. Therefore, when alternating coupled phases are present and a symmetric machine is modeled, as has been done here, simple torque superposition can be sufficient in predicting the torque. Thus, torque in machines with odd number of phases and only an alternating coil arrangement is sufficiently modeled by torque superposition of both commutating phases.

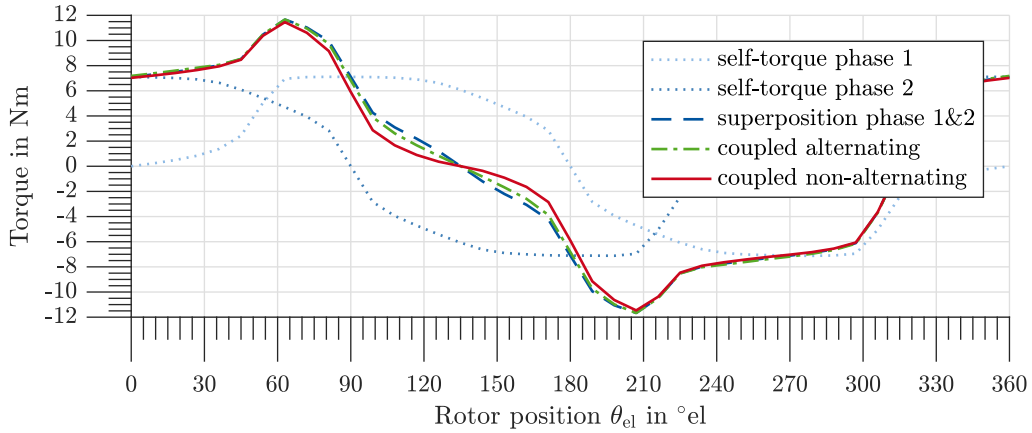

(a) SRM-16/12: Torque coupling at $i_{ph,1} = 14.3\,A$ and $i_{ph,2} = 14.3\,A$ [83]

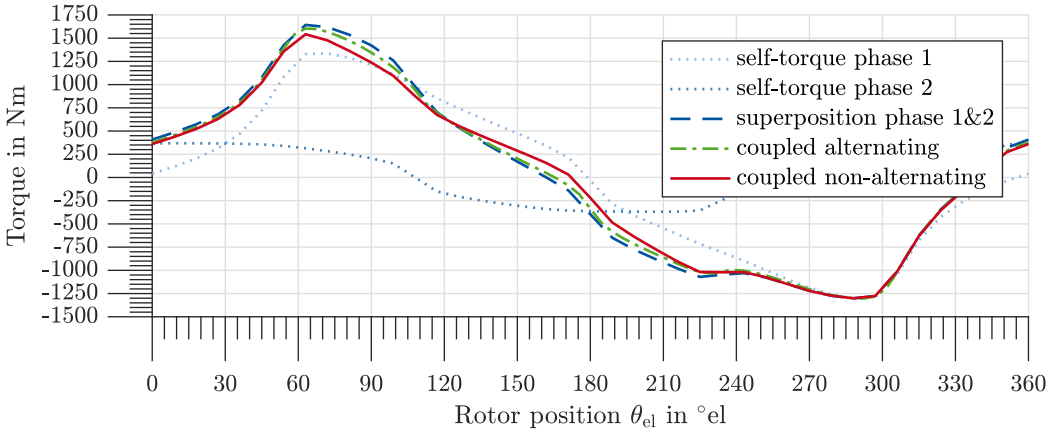

(b) SRM-20/16: Torque coupling at $i_{ph,1} = 148\,A$ and $i_{ph,2} = 63\,A$

Figure 3.9: Influence of coil arrangement on static torque production

An overview of the LUT-based model is shown only for phase 1 in figure 3.10 even though the whole model consists of two input phases 1 and 2. The modeling approach is similar to models presented in literature, where such models have effectively been used [43, 83–85].

In contrast to the models introduced in the previous sections, always both active phases

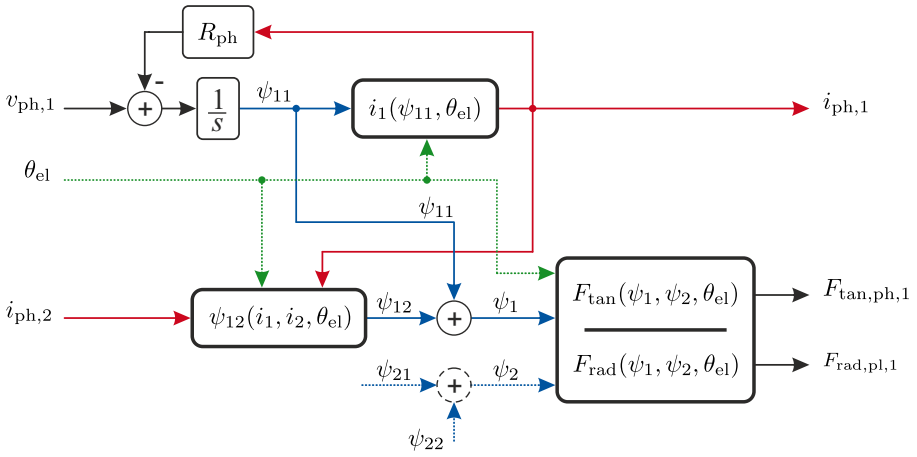

Figure 3.10: LUT based SRM model considering mutual coupling [83]

during phase commutation have to be represented in the SRM model because the coupling effect always influences both, the incoming and outgoing phase. The necessary LUTs are determined by simulating the machine in FEA for both phase currents i_1 and i_2 over the entire rotor position $\theta_{\mathrm{el}} = [0°, 360°]$.

From FEA the tables $\psi_{12}(i_1,i_2,\theta_{\mathrm{el}})$ and $\psi_{21}(i_1,i_2,\theta_{\mathrm{el}})$ for the coupling flux linkage from both currents are generated. Thereby, ψ_{12} represents the flux linkage influence from phase 2 onto phase 1, whereby ψ_{21} represents the opposite coupling flux linkage. In figure 3.11a an example graph for a fixed rotor position of phase 1 ($\theta_{\mathrm{el}} = 126°$) is shown. For clarity only a few phase 1 current values are shown. At current values $i_{\mathrm{ph},1} < 6.2\,\mathrm{A}$ the flux linkage ψ_{12} increases with increasing phase 2 current, while at higher phase 1 currents, the flux

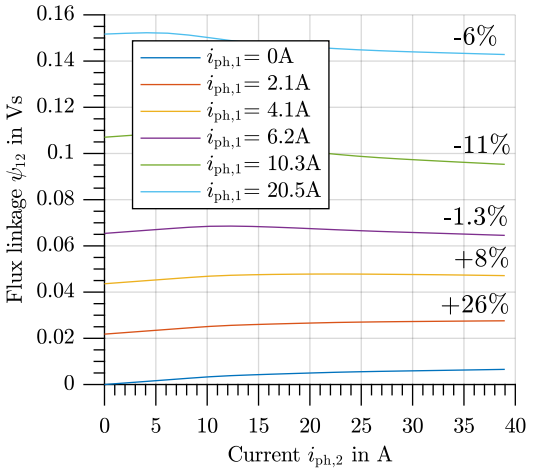

(a) $\psi_{12}(i_1,i_2,\theta_{\mathrm{el}})$: Influence of phase 2 on phase 1 at position $\theta_{\mathrm{el,ph1}} = 126°$

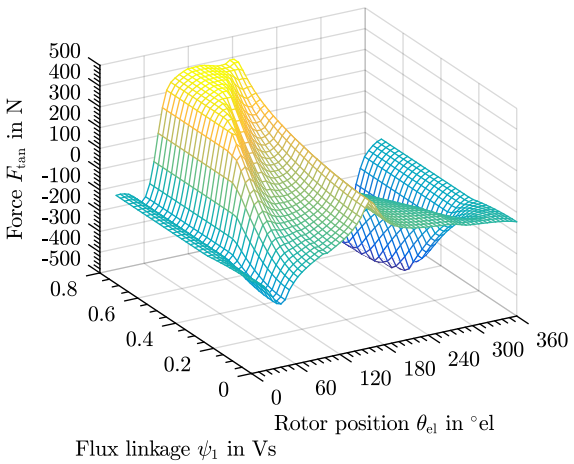

(b) $F_{\tan}(\psi_1,\psi_2,\theta_{\mathrm{el}})$: Influence of phase 2 on phase 1 at flux linkage $\psi_2 = 0.23\,\mathrm{Vs}$

Figure 3.11: Characteristic lookup tables representing mutual phase coupling

linkage decreases ψ_{12} due to increased saturation in the machine from both active phases. The change of flux linkage ψ_{12} is given as a percentage in the figure. Furthermore, LUTs for tangential force $F_{\tan}(\psi_1,\psi_2,\theta_{\mathrm{el}})$, shown in figure 3.11b, and radial force $F_{\mathrm{rad}}(\psi_1,\psi_2,\theta_{\mathrm{el}})$ have to be generated.

The LUT-based model in figure 3.10 can also be used to model mutual pole coupling during SRM single pole fault. Thereby, the LUTs are based on the participating and interacting poles as is discussed in detail in the experimental section in section 6.4.1.

3.5 FEA Coupled Model

An accurate and time consuming modeling method is the coupled FEA simulation. Thereby, the electric machine is represented by a 2-dimensional (2-D) or 3-dimensional (3-D) FEA model, while the machine control and inverter is modeled in another software such as MATLAB/Simulink. As the number of FEA solutions calculated is high, due to small time steps, the computational time to simulate a few periods is extensive, however, the benefit is that influences such as iron loss and eddy currents in the machine can be extracted [68, 86].

Figure 3.12 shows a simplified coupled modeling type. Thereby, MATLAB/Simulink is used to model the entire drive system including control, inverter, machine and load. To verify the correctness of the machine model, the current trajectories are taken from MATLAB/Simulink and passed to the FEA machine model. The flux linkage distribution, produced torque and radial forces are exported and compared to the MATLAB-system simulation model. This method allows a validation that the MATLAB/Simulink SRM model corresponds to the FEA model [87].

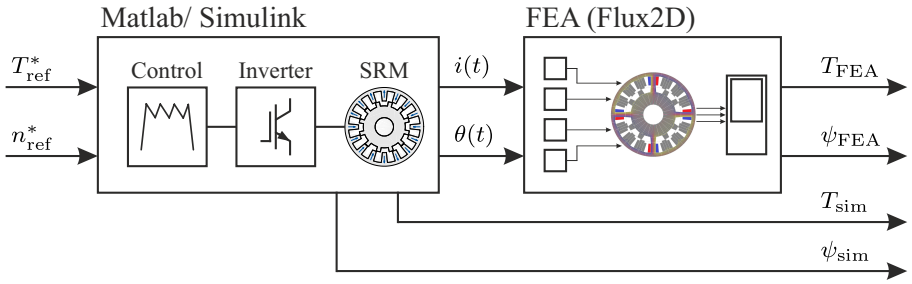

Figure 3.12: FEA coupled model

4 DITC Control Improvement - Fault-Free Operation

To minimize the inherent torque ripple present in switched reluctance machines, direct instantaneous torque algorithms are implemented. These are, independent of whether current profiling, torque sharing functions or DITC are used, highly dependent on the machine characteristic and machine modeling approaches, especially in regard to the used lookup tables. A DITC control structure with only one lookup table resembling the machine characteristic is proposed. The reduction of control complexity enables online adaptive tuning algorithms to minimize torque ripple during fault-free operation, as well as additional radial force LUTs required for fault tolerant control strategies which are introduced in chapter 5. Another method to reduce torque ripple is by machine design. A generalized methodology for designing switched reluctance machines with design of experiments (DOE) is presented. Thereby, the control algorithm used for the machine is considered during the design process.

4.1 Control Dependency on Machine Model

As SRMs are operated in high material saturation, their machine characteristics are highly non-linear. Independent of the SRM control an inverse machine model is necessary to determine the desired machine flux linkage and thus, the volt-second area to be applied by the inverter. This is the case with DATC for average torque control [42], DITC for instantaneous shaft torque [43, 45, 46], acoustic control such as DIFC for Mode-0 reduction [88, 89] or radial and tangential force control (DIT&FC) [13].

Especially in SRMs, the control quality essentially depends on the machine model quality as SRMs are operated by feed forward control algorithms [90]. Therefore, an overall goal when selecting and designing control algorithms has to be the model quality. Reducing either the dependence of the control algorithm on the model or the error between machine model and machine parameters is important. Furthermore, an overall attempt to minimize the hardware resources of the implemented control should be made.

In the following, the influence of LUT resolution used for PWM-DITC is analyzed with regard to the output torque ripple. Thereafter, different *flux linkage allocation* methods which can be used in DITC are proposed. The overall goal is to reduce the number of

lookup tables necessary by the control.

4.1.1 Lookup Table Resolution Reduction

The influence of lookup table resolution on the control quality is investigated for SRM-16/12, SRM-18/12 and SRM-20/16. These completely different machines show an equally different influence which the resolution of $T_{\mathrm{ph}}(\psi_{\mathrm{ph}},\theta_{\mathrm{el}})$ has on the resulting torque ripple. The following investigations have been done by a Simulink system simulation, whereby the SRM machine is modeled as a phase model (see section 3.2) with all characteristic lookup tables calculated from a finite element simulation (FLUX™2D) with an axis resolution stored using 8 bit, i.e. 256 values per axis while interpolation between all values is used. The resolution of the lookup tables used by the control algorithm varies in size.

In the following the control lookup table resolution is defined by a four-digit number describing the amount of bits used to represent each axis: current, rotor position, flux linkage and torque. For example, the number 6867 represents a control where the LUT axis current and flux linkage is represented by $2^6 = 64$ values, while the rotor position has a resolution of $2^8 = 256$ values between 0° and 180° and torque is represented by 128 values. In this section the rotor position is defined up to 180° because a symmetrical machine is assumed allowing the assumption of symmetry for all the characteristics.

As a quantity of control quality the torque ripple is used. Thereby, the torque ripple is determined by the rise and fall of torque during each switching period and is directly dependent on the torque gradient due to the physical drive parameters (inductance and dc-link voltage) and switching frequency of the inverter. Furthermore, the torque ripple is also dependent on the quality of phase commutation between two phases, i.e. how well the torque reference is shared amongst the conducting phases. Especially in low resolution tables, the phase commutation can determine the overall torque ripple.

The effects of the LUT resolution on torque with DITC is visible for SRM-18/12 in figure 4.1, for SRM-16/12 in figure 4.2 and for SRM-20/16 in figure 4.3.

For these results either linear interpolation (wInt) or no interpolation (nInt), i.e. nearest value is used in the $T_{\mathrm{ph}}(\psi_{\mathrm{ph}},\theta_{\mathrm{el}})$-LUT for the torque prediction lookup from the flux linkage estimator. For flux linkage allocation a high resolution (8 bit) $\psi_{\mathrm{ph}}(T_{\mathrm{ph}},\theta_{\mathrm{el}})$ table with interpolation is used. The lowest torque ripple values visible in figure 4.1 to figure 4.3 are for simulations using interpolation 8888wInt and 5555wInt at the highest frequency. Thus, when using interpolation in $T_{\mathrm{ph}}(\psi_{\mathrm{ph}},\theta_{\mathrm{el}})$ the error produced in the control is largely independent of the resolution used. When comparing figure 4.1a and figure 4.1b the main effect visible is due to the change in switching frequency, while the resolution as such does not have a significant influence. The resolution only causes a small variation between the results for the different resolutions. Furthermore, the constant decrease of torque ripple from 40 Nm upwards, results from a constant torque ripple independent of the produced

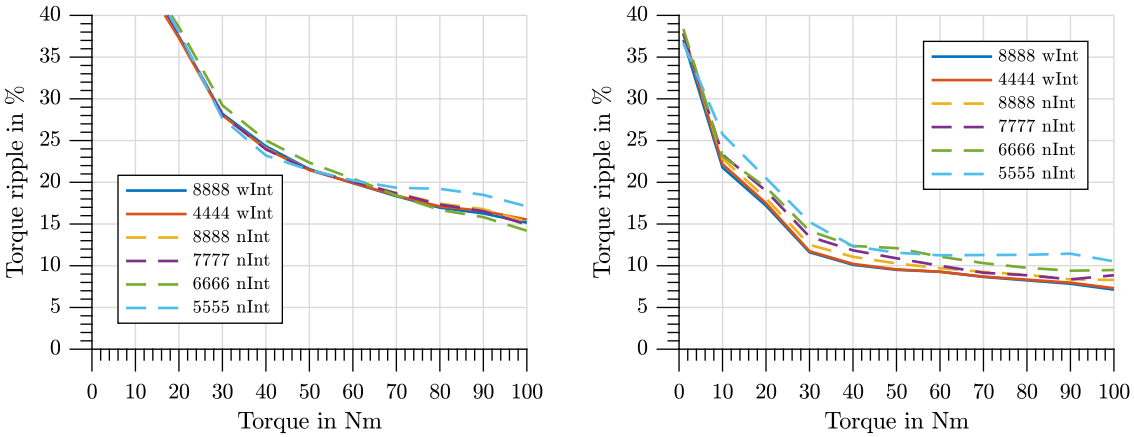

(a) $n = 1000\,\text{rpm}$ and $f_{\text{PWM}} = 20\,\text{kHz}$ (b) $n = 1000\,\text{rpm}$ and $f_{\text{PWM}} = 40\,\text{kHz}$ [90]

Figure 4.1: SRM-18/12: Comparison of $T_{\text{ph}}(\psi_{\text{ph}},\theta_{\text{el}})$-LUT resolutions with interpolation (wInt) and without interpolation (nInt)

torque. This constant ripple is produced during the phase commutation and suggests a torque sharing mismatch due to the predicted torque and flux values. The reduction in ripple due to resolution increase when no interpolation (nInt) is used is clearly visible at the higher torque values in figure 4.1b. An overall higher dependency of the torque ripple on LUT resolution at the higher switching frequencies is visible.

When comparing the 5555 bit torque ripple at $f_{\text{PWM}} = 10\,\text{kHz}$ in figure 4.2a and at $f_{\text{PWM}} = 20\,\text{kHz}$ in figure 4.2b an increase is visible, which at first is not expected. In all other simulations at higher LUT resolution, the torque ripple decrease with increasing switching frequency. In figure 4.2c the torque ripple results of a simulation at $T = 5\,\text{Nm}$ and $n = 100\,\text{rpm}$ for different LUT resolutions is shown. It is visible that the 6 bit and 7 bit trajectories are as expected and decrease with increasing switching frequency. The erratic trajectory of the 5 bit simulation is caused by too small changes in the flux linkage between switching period as an input to $T_{\text{ph}}(\psi_{\text{ph}},\theta_{\text{el}})$ resulting in wrong or no new update of the torque range and, therefore, reference torque. Thus, if the resolution is too low, PWM-DITC is not able to control the torque anymore and does not function. This only happens at extremely low resolutions. In the shown case of SRM-16/12 the 5 bit resolution results in a 6.2 mVs flux linkage resolution in $T_{\text{ph}}(\psi_{\text{ph}},\theta_{\text{el}})$ (equivalent to 1 Nm steps in $\psi_{\text{ph}}(T_{\text{ph}},\theta_{\text{el}})$), while 6 bit results in a 3 mVs and flux linkage step between lookup values.

In figure 4.2 and figure 4.3 the difference in torque ripple between 6666nInt and 7777nInt is due to quantization errors in the LUT. The torque ripple in these cases is caused by torque dips during phase commutation. The smaller resolution causes inaccuracy during torque estimation, which causes the torque sharing to cause steps instead of a smooth phase transition. In both machines SRM-16/12 and SRM-20/16 when 7 bit resolution is used, these steps are reduced to such an extent that resolution does not determine the torque ripple anymore.

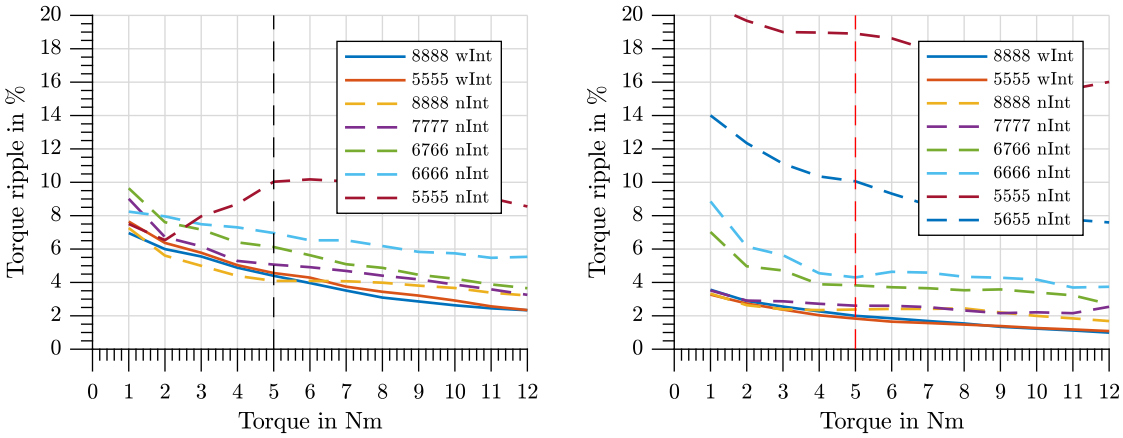

(a) $n = 100\,\text{rpm}$ and $f_{\text{PWM}} = 10\,\text{kHz}$ (b) $n = 100\,\text{rpm}$ and $f_{\text{PWM}} = 20\,\text{kHz}$ [90]

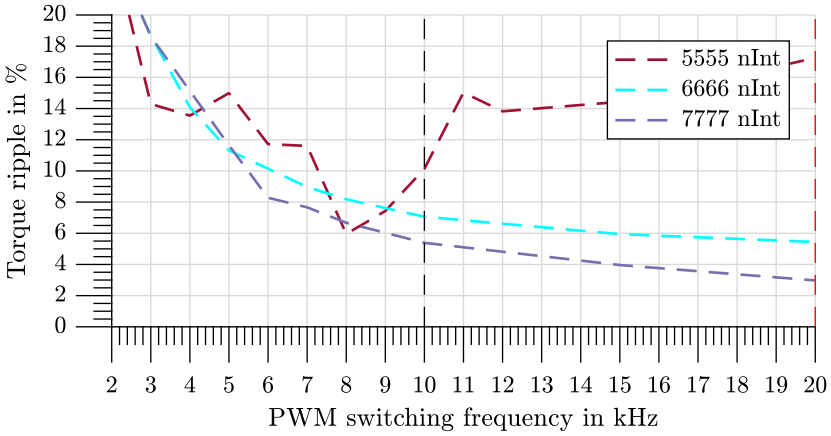

(c) Comparison of LUT resolution and f_{PWM} at $T = 5\,\text{Nm}$

Figure 4.2: SRM-16/12: Comparison of $T_{\text{ph}}(\psi_{\text{ph}},\theta_{\text{el}})$-LUT resolutions with interpolation (wInt) and without interpolation (nInt)

When no interpolation is used the smallest torque ripple is influenced by quantization errors from the resolution used. This is visible for 6666nInt and 7777nInt in figure 4.2b and figure 4.3b. Both simulations reach their own minimum values; however, these are higher than the values reached with interpolation. The quantization error is directly proportional to the table resolution. As an example to achieve similar results to the interpolated values, SRM-16/12 needs a 7 bit table (7777nInt) when no interpolation is used compared to a 5 bit table necessary when using interpolation (5555wInt). Similar, SRM-20/16 at $f_{\text{PWM}} = 16\,\text{kHz}$ needs a 8 bit table (8888nInt) when no interpolation is used compared to a 5 bit table necessary when using interpolation (5555wInt).

As $T_{\text{ph}}(\psi_{\text{ph}},\theta_{\text{el}})$ depends on ψ and $\theta_{\text{el.}}$ their resolution sensitivity is of considerable interest. In figure 4.2 when comparing 6766nInt and 6666nInt it is clearly visible that increasing the resolution of the rotor position the overall error can be reduced while only doubling the size of memory necessary for the LUT. A similar reduction can be observed when only

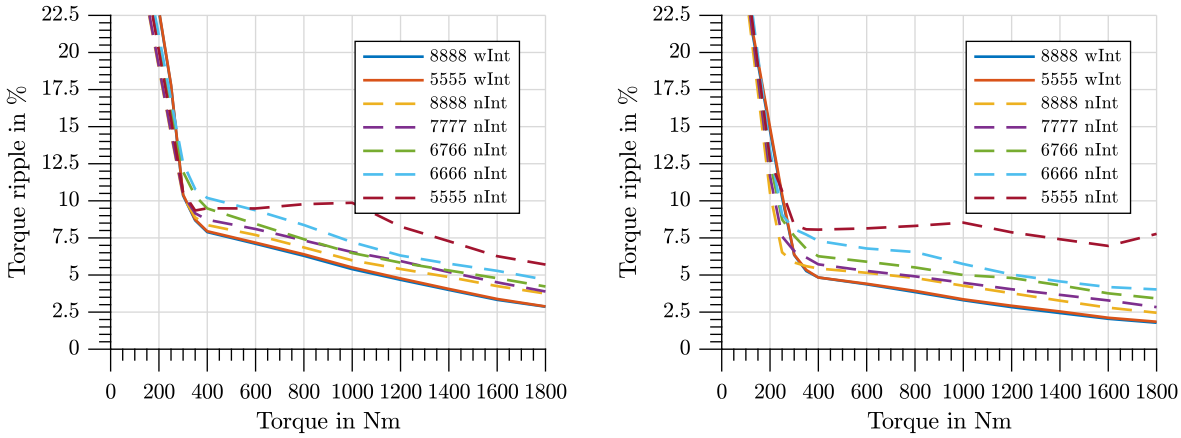

(a) $n = 100\,\text{rpm}$ and $f_{\text{PWM}} = 10\,\text{kHz}$ (b) $n = 100\,\text{rpm}$ and $f_{\text{PWM}} = 16\,\text{kHz}$

Figure 4.3: SRM-20/16: Comparison of $T_{\text{ph}}(\psi_{\text{ph}},\theta_{\text{el}})$-LUT resolutions with interpolation (wInt) and without interpolation (nInt)

reducing the resolution of the flux linkage axis in 6676nInt. As the control sensitivity for the rotor position is higher, it is preferred to use the highest feasible resolution for the rotor position. The figures, furthermore, show how using interpolation in the $T_{\text{ph}}(\psi_{\text{ph}},\theta_{\text{el}})$ lookup substantially reduces the necessary memory space on the FPGA as lower resolution are still adequate depending on the machine setup. Reducing the space needed for individual LUTs allows the introduction of more complex machine models considering mutual phase coupling [83, 85], rotor eccentricities [81, 82] or additional radial force characteristics for acoustic control [13, 89] or fault tolerant operation as introduced in chapter 5. Therefore, if the machine LUT values represent the actual physical machine then a relatively small resolution is sufficient to achieve a good control quality.

4.1.2 Omitting Torque-to-Flux Linkage Lookup Table

Figure 4.4 shows the overall predictive pulse width modulation (PWM) based DITC control structure, which in this thesis is executed on a FPGA. Different flux linkage allocation methods are discussed by introducing torque and flux linkage tuples $(T_{n+2,k}|\psi_{n+2,k})$ as state variables of the control. Thereby, n represents the current execution time step during which current measurement is taken and k the number of discrete flux linkage and torque states used by the control.

The common method in PWM-DITC for flux linkage allocation uses a $\psi_{\text{ph}}(T_{\text{ph}},\theta_{\text{el}})$-lookup table (figure 4.5a), as is presented in the fundamentals chapter (see section 2.3.2 and figure 2.9). The $\psi_{\text{ph}}(T_{\text{ph}},\theta_{\text{el}})$-LUT is determined from the $T_{\text{ph}}(i_{\text{ph}},\theta_{\text{el}})$ and $\psi_{\text{ph}}(i_{\text{ph}},\theta_{\text{el}})$ tables, which can be retrieved by simulation or measurement. Due to the generation of the inverse and steep gradients in the LUT, a relatively high resolution is necessary for $\psi_{\text{ph}}(T_{\text{ph}},\theta_{\text{el}})$ [89]. The $\psi_{\text{ph}}(T_{\text{ph}},\theta_{\text{el}})$-LUT is the inverse of the table $T_{\text{ph}}(\psi_{\text{ph}},\theta_{\text{el}})$, which

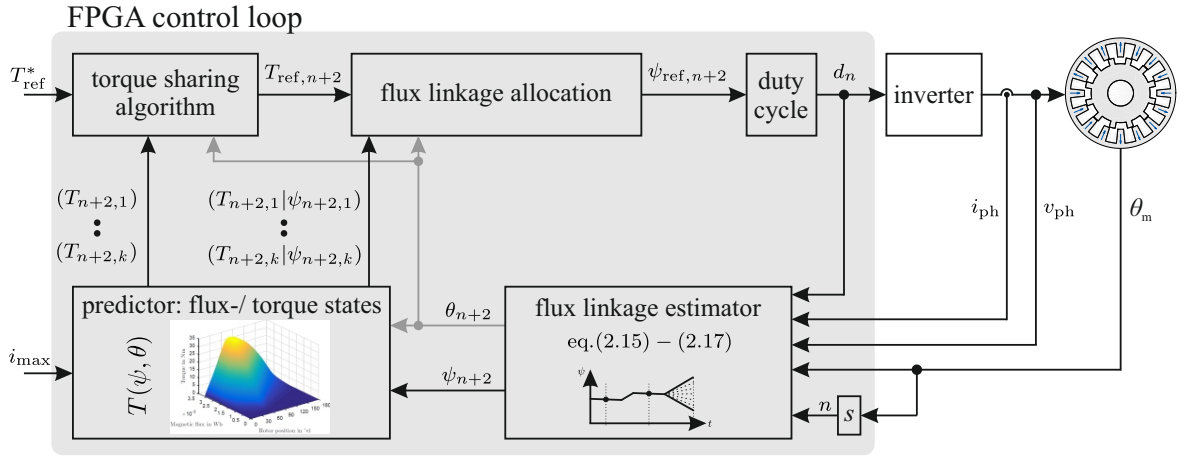

Figure 4.4: Schematic overview of predictive PWM based DITC control structure with flux linkage and torque state predictor [90]

already is used in DITC to predict the machine torque. It is proposed to store the corresponding flux linkage and torque values as $(T_{n+2,k}|\psi_{n+2,k})$ tuples from the $T_{\mathrm{ph}}(\psi_{\mathrm{ph}},\theta_{\mathrm{el}})$ torque prediction as shown in figure 4.6. This correlation and the FPGA's strength in parallel processing is used by implementing a parallel lookup of multiple flux linkage values between the estimated minimum $\psi_{n+2,1}$ and maximum $\psi_{n+2,k}$ value. The tuples are stored for the backwards calculation from the torque reference $T_{\mathrm{ref},n+2}$ back to the flux linkage reference $\psi_{\mathrm{ref},n+2}$ in the *flux linkage allocation* block in figure 4.4. For the $T_{n+2,k}|\psi_{n+2,k}$ tuples method there are three different approaches which can be used.

The first method shown in figure 4.5b uses only the predicted phase flux linkage range for the next period, i.e. minimum $\psi_{n+2,1}$ and maximum $\psi_{n+2,2}$ flux linkage values when a negative or positive duty cycle is applied to the entire switching period. The reference flux linkage is determined by interpolating between these two boundary values. This

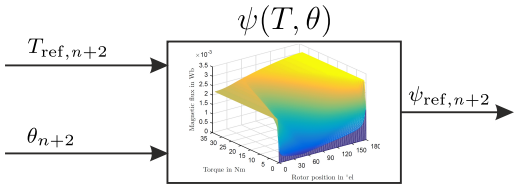

(a) $\psi_{\mathrm{ph}}(T_{\mathrm{ph}},\theta_{\mathrm{el}})$ lookup table

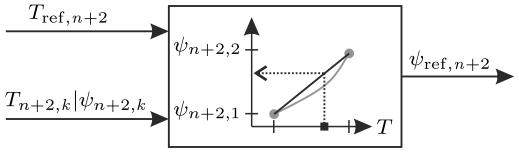

(b) 2 flux linkage states: interpolation

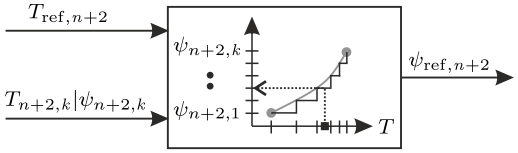

(c) k discrete flux linkage states: nearest

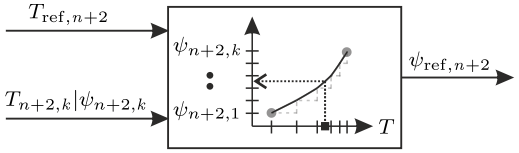

(d) k discrete flux linkage states: FLA interpolation

Figure 4.5: Different methods to implement flux linkage allocation in PWM-DITC [90]

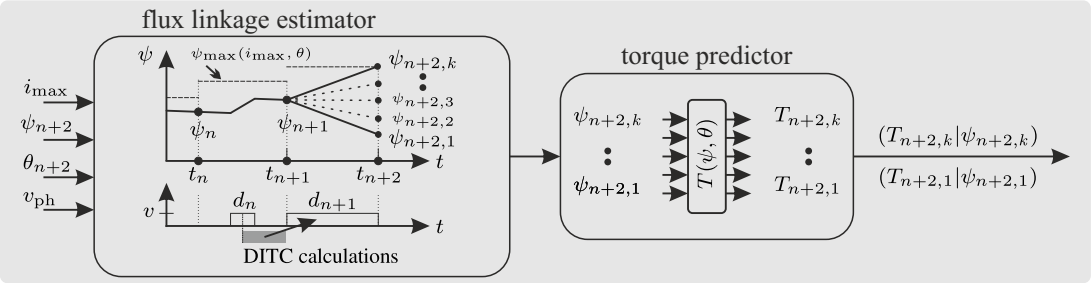

Figure 4.6: PWM based DITC flux linkage estimator and torque state predictor

allocation method approximates the trajectory between the minimum and maximum flux linkage values as a linear function. This method is discussed in section 4.1.2.1.

The second and third method visible in figure 4.5c and figure 4.5d, calculates multiple discrete flux linkage states from corresponding torque states. During the torque prediction in DITC not only the minimum and maximum values of each phase for the next period are determined, as in figure 4.5b, but an arbitrary number of k states between the minimum and maximum flux linkage predictions are calculated. The *flux linkage allocation* back calculation can either use the nearest solution as in figure 4.5c or an interpolation function is applied between the nearest tuples as in figure 4.5d. The interpolation allows a reduction in the amount of k states to be looked up, which is presented in section 4.1.2.2.

4.1.2.1 Two Flux Linkage and Torque States: Linear Interpolation

In this section the flux linkage allocation shown in figure 4.5b, where the amount of discrete lookup states k equals 2 is discussed. The linear approximation between the two boundary values, $T_{n+2,1}$ and $T_{n+2,2}$ causes an error between the actual flux linkage and the calculated flux linkage. The size of the interval between the boundary values is dependent on the applied volt-second area during each switching period. This results in a dependence on the inverter switching frequency, rotor position dependent phase inductance, machine speed (back emf) and dc-link voltage. In the following the accuracy of the flux linkage reference value $\psi_{\text{ref},n+2}$ is used as a merit to determine the quality of the control. The reference $\psi_{\text{ref},n+2}$ is compared to a reference determined by using a high resolution 8 bit $\psi_{\text{ph}}(T_{\text{ph}},\theta_{\text{el}})$ lookup table.

Figure 4.7a and figure 4.7b show the absolute and relative flux linkage error respectively for SRM-16/12 when using linear interpolation. The figures are plotted over arbitrary switching frequencies and three voltage levels surrounding the nominal machine design dc-link voltage of 60 V. Furthermore, two different operating points have been chosen, one at low torque level 2 Nm and 200 rpm and one operating point at a higher torque level 5 Nm and 200 rpm.

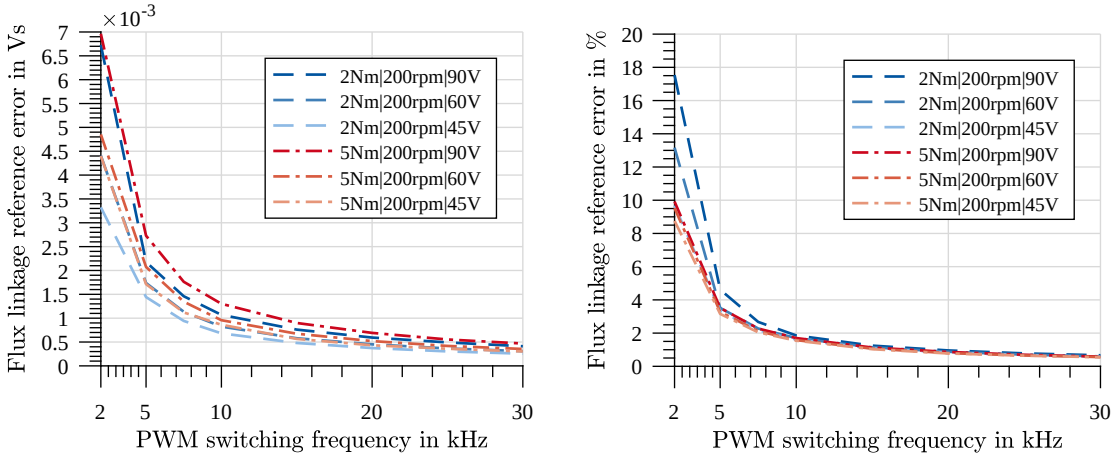

(a) Absolute error (b) Relative error

Figure 4.7: SRM-16/12: Comparison of various dc-link voltages, torque levels and switching frequencies on the flux linkage reference

In both figures the flux linkage error shows a strong dependency on the switching frequency, while only a small dependency on the different dc-link voltage and torque values. Figure 4.7b shows how the relative error increases at switching frequencies below 5 kHz and especially at the lower torque of 2 Nm. The graphs show that there is a switching frequency below which using a $\psi_{\mathrm{ph}}(T_{\mathrm{ph}},\theta_{\mathrm{el}})$-LUT is the better choice compared to the linear interpolation. For SRM-16/12, between 5 kHz and 2 kHz the relative flux linkage error increases from 5 % to well over 15 %. For switching frequencies above 10 kHz the flux linkage error becomes negligible and independent of the operating point. Thus, using interpolation between minimum and maximum flux linkage, instead of a $\psi_{\mathrm{ph}}(T_{\mathrm{ph}},\theta_{\mathrm{el}})$-LUT, is viable. To make the flux linkage allocation less dependent on the switching frequency of the machine the number of flux linkage and torque samples can be increased, which is investigated in the next section.

4.1.2.2 Discrete Flux Linkage and Torque States

By using the fast parallel calculation capability of FPGAs, multiple k discrete flux linkage states are computed simultaneously. Instead of using only two lookup values for the flux linkage allocation now k flux linkage and torque tuples are used (figure 4.5c). The maximum number of k flux linkage and torque tuples, which can be calculated in one switching period is determined by the computational capability of the FPGA used. The number of useful k states is limited by the given drive system, the resolution of the $T_{\mathrm{ph}}(\psi_{\mathrm{ph}},\theta_{\mathrm{el}})$ due to quantization errors and if interpolation is used or not as displayed in figure 4.8.

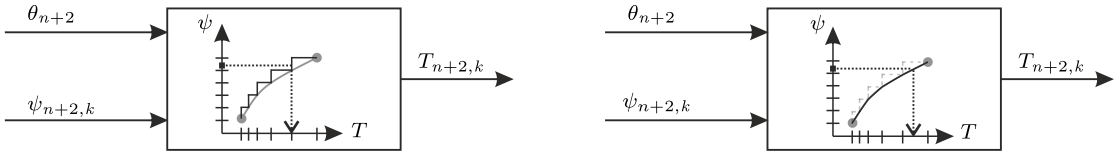

(a) $T_{\mathrm{ph}}(\psi_{\mathrm{ph}},\theta_{\mathrm{el}})$ no interpolation: nearest

(b) $T_{\mathrm{ph}}(\psi_{\mathrm{ph}},\theta_{\mathrm{el}})$ with interpolation

Figure 4.8: Torque predictor $T_{\mathrm{ph}}(\psi_{\mathrm{ph}},\theta_{\mathrm{el}})$ lookup either without interpolation (a) or with interpolation (b)

Without $T_{\mathrm{ph}}(\psi_{\mathrm{ph}},\theta_{\mathrm{el}})$ Interpolation

Figure 4.9 displays the torque states available during phase commutation of SRM-16/12 at 7 Nm and 100 rpm using an exemplary $k = 10$ states. Figure 4.9a shows a detailed view of phase commutation using a $T_{\mathrm{ph}}(\psi_{\mathrm{ph}},\theta_{\mathrm{el}})$-LUT with 6666 bit resolution (see section 4.1.1) and no interpolation when generating the $(T|\psi)$-tuples, but the nearest value is used. The number of available different states during each PWM period is not constant at $k = 10$ states. The actual number of different torque states is reduced due to quantization in the 5 bit LUT. Figure 4.9b shows a detailed view of the same phase commutation using linear interpolation in $T_{\mathrm{ph}}(\psi_{\mathrm{ph}},\theta_{\mathrm{el}})$-LUT when generating the $(T|\psi)$-tuples. Therefore, during each PWM period there are exactly $k = 10$ possible states DITC can choose from. T_{ref} in both figures is the reference phase torque selected by the torque sharing algorithm.

Not only the number of discrete states, but also the resolution of $T_{\mathrm{ph}}(\psi_{\mathrm{ph}},\theta_{\mathrm{el}})$ determines the effective usable states and resulting torque reference. Figure 4.9c compares different $T_{\mathrm{ph}}(\psi_{\mathrm{ph}},\theta_{\mathrm{el}})$-LUT resolutions and the resulting effective torque state distribution. Thus, if at the given operating point all 10 states should be usable a $T_{\mathrm{ph}}(\psi_{\mathrm{ph}},\theta_{\mathrm{el}})$ resolution of at least 8 bit is necessary, otherwise the number of effective flux linkage and torque states will be lower than expected. From figure 4.9c it is visible that with 6666 bit resolution 85 % of the time 5 states can be used (see figure 4.9a), while with a 7777 bit-LUT 80 % of the time 9 different states can be used by the controller.

From the simulation results shown for SRM-20/16 in figure 4.11c it is visible that for 5 bit resolution (figure 4.11a), fewer than 8 states can effectively be used. At 6 bit resolution mostly 9 - 15 states are available. Figure 4.12a shows a result where 20 states should be used, however, due to the resolution of 6 bit at most 15 states are available (see figure 4.11c). A similar result is shown in figure 4.12b with 7 bit and 20 states. From the state distribution in figure 4.11c it is visible that with 7 bit mostly 18 -25 states are available. Therefore, when choosing 20 states and a 7 bit-LUT these 20 states will nearly always be available to the control and not be limited by the LUT resolution.

In figure 4.10 a result for SRM-18/12 with a LUT resolution of 5555 bit and 20 states is shown. From the state distribution in figure 4.10c it is visible that for LUT resolutions of 5 bit mainly 14 states can be used. For this machine LUT resolutions higher than 6 bit

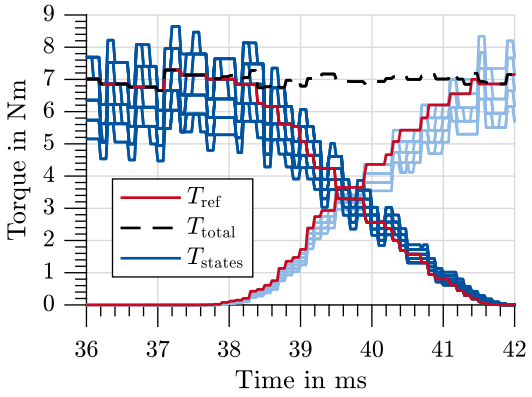

(a) 6666 bit resolution $T_{ph}(\psi_{ph},\theta_{el})$ without interpolation

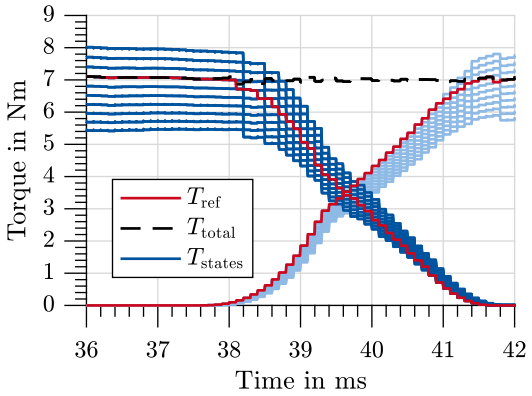

(b) 6666 bit resolution $T_{ph}(\psi_{ph},\theta_{el})$ with interpolation

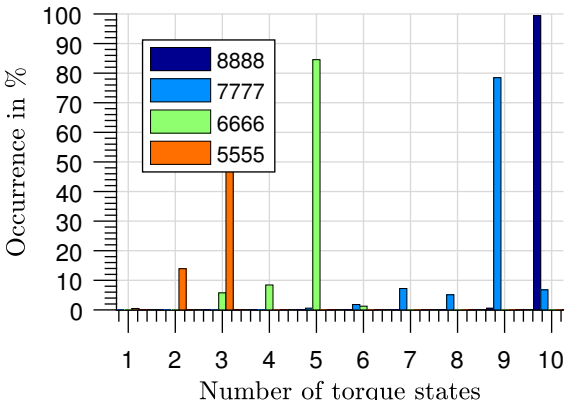

(c) Distribution of usable torque states depending on $T_{ph}(\psi_{ph},\theta_{el})$ resolution (4 to 8 bit) when no interpolation is used

Figure 4.9: SRM-16/12: Phase commutation with 10 torque states at 7 Nm, 100 rpm and $f_{PWM} = 10$ kHz

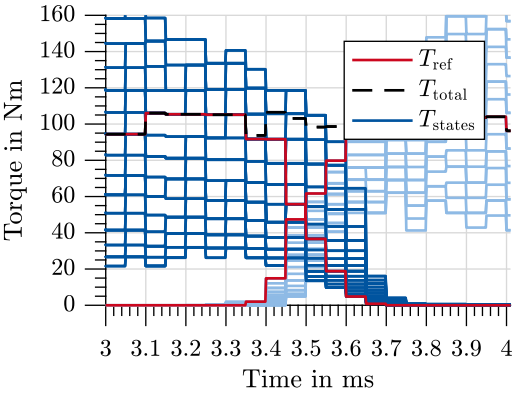

(a) 5555 bit resolution $T_{ph}(\psi_{ph},\theta_{el})$ without interpolation

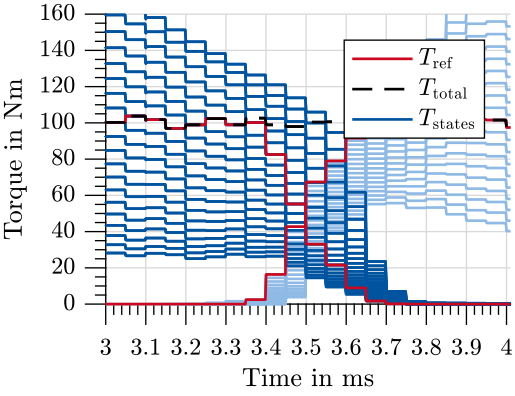

(b) 5555 bit resolution $T_{ph}(\psi_{ph},\theta_{el})$ with interpolation

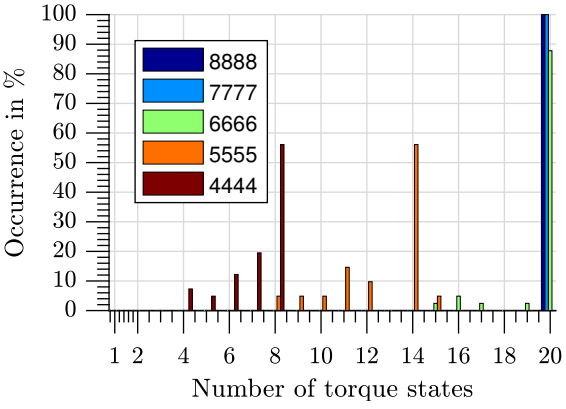

(c) Distribution of usable torque states depending on $T_{ph}(\psi_{ph},\theta_{el})$ resolution (4 to 8 bit) when no interpolation is used

Figure 4.10: SRM-18/12: Phase commutation with 20 torque states at 100 Nm, 1 krpm and $f_{PWM} = 20$ kHz [90]

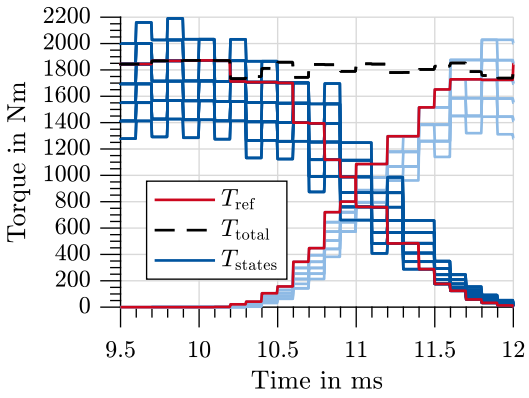

(a) 5555 bit resolution $T_{ph}(\psi_{ph},\theta_{el})$ without interpolation

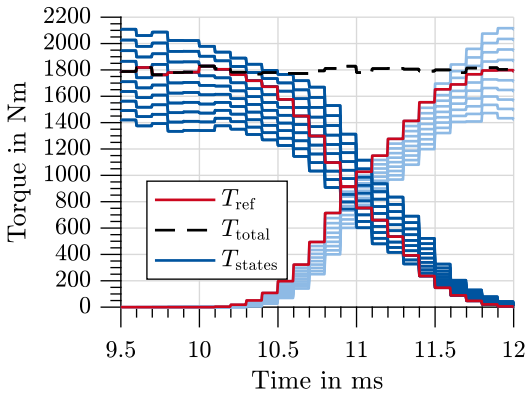

(b) 5555 bit resolution $T_{ph}(\psi_{ph},\theta_{el})$ with interpolation

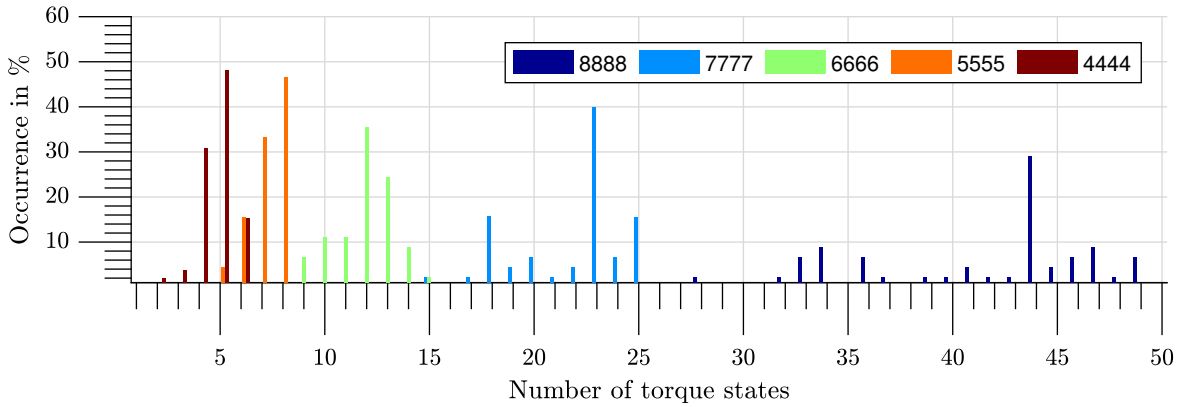

(c) Distribution of usable torque states depending on $T_{ph}(\psi_{ph},\theta_{el})$ resolution (4 to 8 bit) when no interpolation is used

Figure 4.11: SRM-20/16: Phase commutation with 10 torque states at 1800 Nm, 300 rpm and $f_{PWM} = 10$ kHz

result in nearly always 20 available states.

The number of available states depends on the effective applied volt-second area applied by the inverter, i.e dependent on switching frequency, dc-link voltage and machine speed, and the machine characteristics (inductance and flux linkage).

The maximum number of torque states available can be approximated by the given switching frequency f_{PWM} and effective phase voltage v_{ph} as in equation (4.1).

$$N_{states} = \frac{2 \cdot v_{ph}}{f_{PWM} \cdot d_{LUT,resolution}} \tag{4.1}$$

Thereby, $d_{LUT,resolution}$ represents the minimum distance between two consecutive flux linkage values in $T_{ph}(\psi_{ph},\theta_{el})$ lookup table. The minimum distance is dependent on the maximum machine flux linkage depicted in the LUT and which resolution is used for its

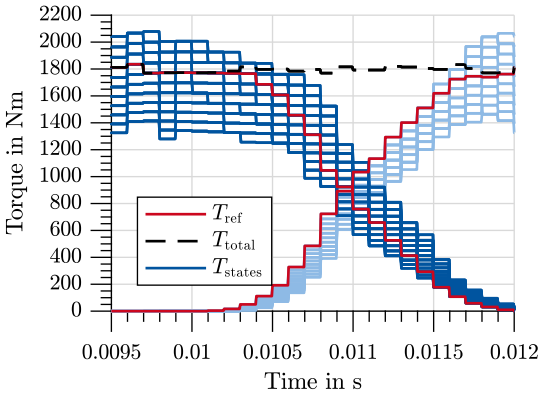

(a) 6666 bit resolution $T_{\text{ph}}(\psi_{\text{ph}},\theta_{\text{el}})$ without interpolation

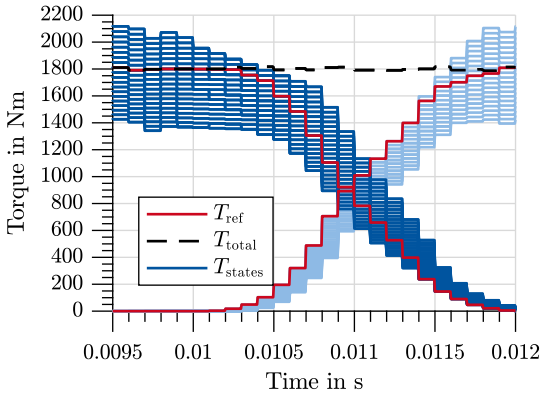

(b) 7777 bit resolution $T_{\text{ph}}(\psi_{\text{ph}},\theta_{\text{el}})$ without interpolation

Figure 4.12: SRM-20/16: Phase commutation with 20 torque states at 1800 Nm, 300 rpm and $f_{\text{PWM}} = 10\,\text{kHz}$

representation.

In figure 4.13, figure 4.14 and figure 4.15 simulation results for SRM-16/12, SRM-18/12 and SRM-20/16 are shown. The results are for two different switching frequencies and have been carried out without interpolation (nInt) in $T_{\text{ph}}(\psi_{\text{ph}},\theta_{\text{el}})$ for various LUT resolutions. It is clearly visible that the torque ripple reduction is dependent on the number of states used by the control. However, the LUT resolution also is determinate, suggesting that quantization error is the limiting factor. This is especially visible for SRM-16/12 in figure 4.13a, where the torque ripple does not significantly change when more than 10 states are used, however, the quantization influence of the resolution is strongly visible when changing from 5 bit to 6 bit, or from 6 bit to 8 bit. Similarly, this can be seen for

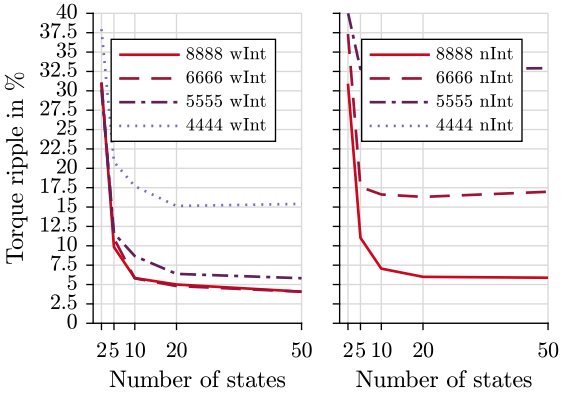

(a) At $f_{\text{PWM}} = 10\,\text{kHz}, 10\,\text{Nm}$ and 100 rpm

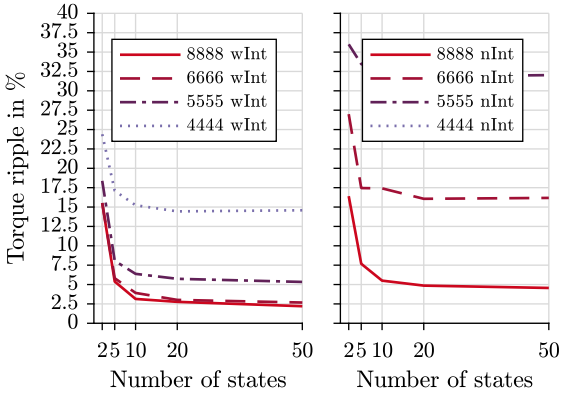

(b) At $f_{\text{PWM}} = 20\,\text{kHz}, 10\,\text{Nm}$ and 100 rpm

Figure 4.13: SRM-16/12: Torque ripple versus number of torque states with interpolation (wInt) and without interpolation using nearest values (nInt) during $T_{\text{ph}}(\psi_{\text{ph}},\theta_{\text{el}})$ lookup, flux linkage allocation uses nearest state value

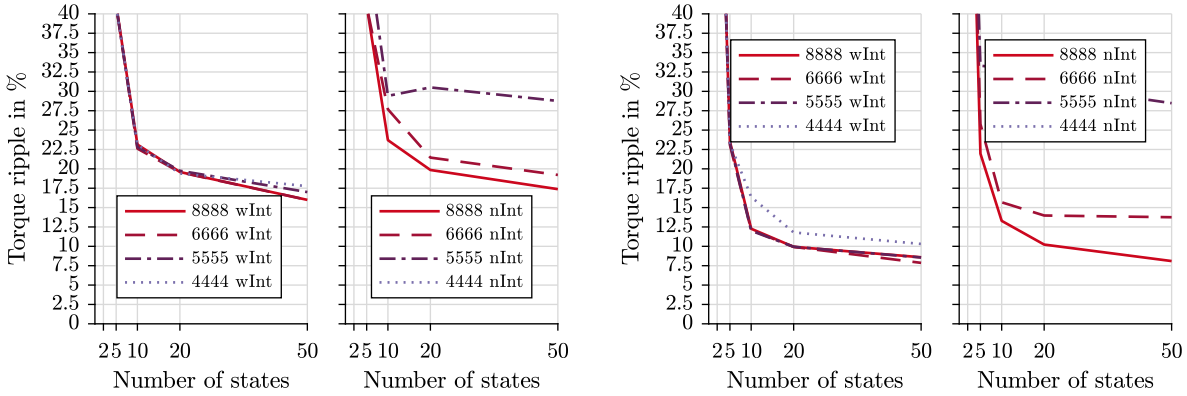

(a) At $f_{\mathrm{PWM}} = 20\,\mathrm{kHz}, 100\,\mathrm{Nm}$ and $1000\,\mathrm{rpm}$ (b) At $f_{\mathrm{PWM}} = 40\,\mathrm{kHz}, 100\,\mathrm{Nm}$ and $1000\,\mathrm{rpm}$

Figure 4.14: SRM-18/12: Torque ripple versus number of torque states with interpolation (wInt) and without interpolation using nearest values (nInt) during $T_{\mathrm{ph}}(\psi_{\mathrm{ph}},\theta_{\mathrm{el}})$ lookup, flux linkage allocation uses nearest state value

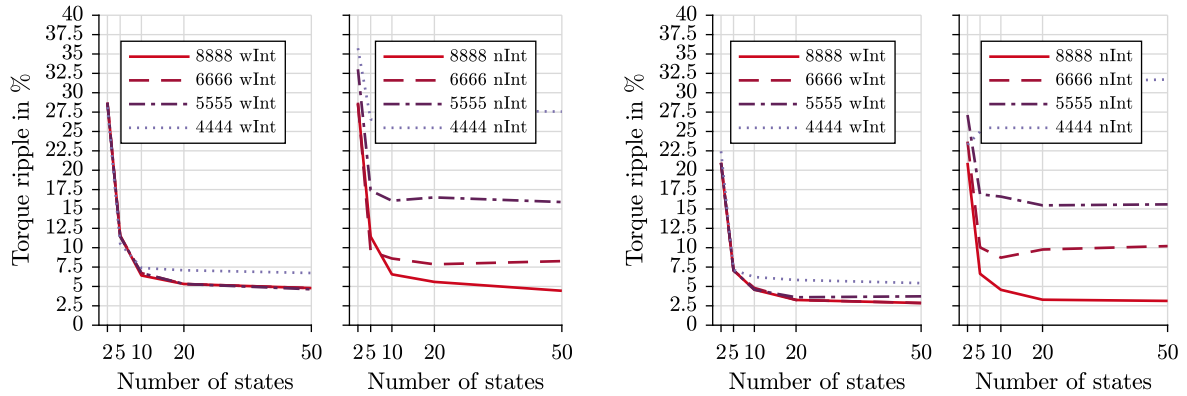

(a) At $f_{\mathrm{PWM}} = 10\,\mathrm{kHz}, 1800\,\mathrm{Nm}$ and $300\,\mathrm{rpm}$ (b) At $f_{\mathrm{PWM}} = 16\,\mathrm{kHz}, 1800\,\mathrm{Nm}$ and $300\,\mathrm{rpm}$

Figure 4.15: SRM-20/16: Torque ripple versus number of torque states with interpolation (wInt) and without interpolation using nearest values (nInt) during $T_{\mathrm{ph}}(\psi_{\mathrm{ph}},\theta_{\mathrm{el}})$ lookup, flux linkage allocation uses nearest state value

SRM-20/16 in figure 4.15. In contrast for SRM-18/12 (figure 4.14a) a higher number of torque states causes the torque ripple to reduce further. With SRM-18/12 even at 50 states a reduction in ripple is observed while not reaching a lower boundary. Concluding, if no interpolation in $T_{\mathrm{ph}}(\psi_{\mathrm{ph}},\theta_{\mathrm{el}})$ is used, the number of implemented discrete states k has to be selected in accordance to the LUT resolution implemented in the control.

With $T_{\mathrm{ph}}(\psi_{\mathrm{ph}},\theta_{\mathrm{el}})$ Interpolation

By adding interpolation in $T_{\mathrm{ph}}(\psi_{\mathrm{ph}},\theta_{\mathrm{el}})$ the usable (different) flux linkage and torque states are constant and defined by the number k. Thereby, the number of usable states is

independent of the $T_{\mathrm{ph}}(\psi_{\mathrm{ph}},\theta_{\mathrm{el}})$ table resolution, which causes the overall control quality to be less dependent on resolution. In figure 4.13, figure 4.14 and figure 4.15 simulation results with interpolation (wInt) are shown. It is visible that the control quality increases drastically especially when low resolutions (4 bit & 5 bit) are used. Therefore, adding a simple linear interpolation can be sufficient to reduce the necessary LUT resolution and therefore, the hardware memory requirement.

Torque ripple can further be decreased by increasing the number of used states, as before. The minimum ripple reached is again defined by the drive system. Similar as found without interpolation for SRM-16/12 and SRM-20/16 the simulated torque ripple decreases the most within the first 10 - 20 states. For these drive systems around 10 states are sufficient to achieve a good control quality. In contrast, again, SRM-18/12 shows a decrease in ripple even when 50 states are used. Therefore, in this drive system the more states are used the better. However, increasing the calculated states may become unreasonable as the hardware resources for all $(T|\psi)$-tuple calculations and storing for back calculation within one switching period may become too large. To overcome this large amount of necessary states, a linear interpolation algorithm is added to the *flux linkage allocation* calculation.

With Interpolation during Flux Linkage Allocation

To achieve the same control quality with largely reduced number of flux linkage states and therefore, with fewer parallel lookups, an interpolation is introduced during *flux linkage allocation* as shown in figure 4.5d. The reduction in necessary flux linkage states is visible

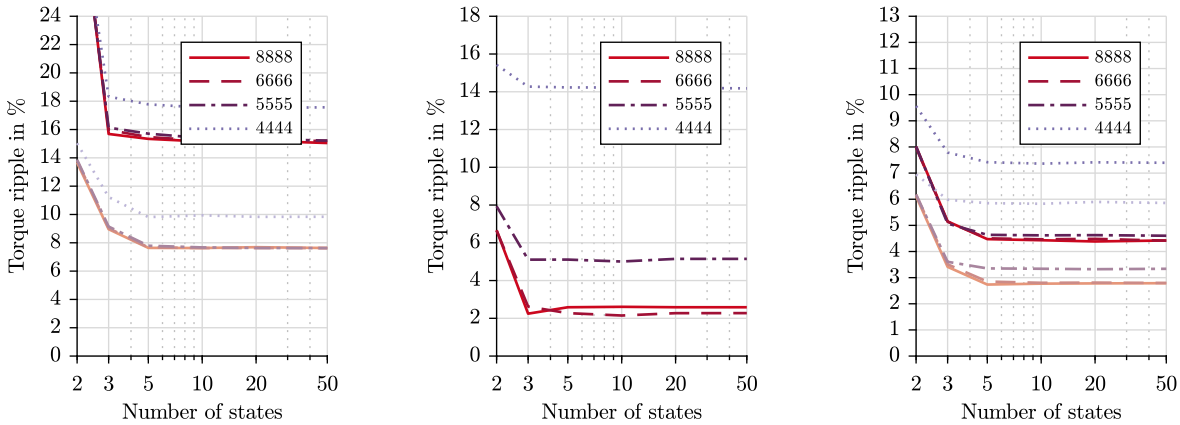

(a) SRM-18/12: 100 Nm, 1000 rpm, 20 kHz and 40 kHz (transparent)

(b) SRM-16/12: 10 Nm, 100 rpm, 20 kHz

(c) SRM-20/16: 1800 Nm, 300 rpm, 10 kHz and 16 kHz (transparent)

Figure 4.16: Comparison of torque ripple versus number of torque states with interpolation in $T_{\mathrm{ph}}(\psi_{\mathrm{ph}},\theta_{\mathrm{el}})$ and FLA interpolation

when comparing the results of figure 4.13 and figure 4.16b for SRM-16/12 and, figure 4.15 and figure 4.16c for SRM-20/16. The small machine SRM-16/12 shows that with its high switching frequency it is sufficient to use three flux linkage states, i.e. minimum, maximum and a center point (free-wheeling) of predicted flux linkage and then interpolate between these values during flux linkage allocation to achieve the same results as with a higher number of flux linkage states. However, the results for the larger two machines SRM-18/12 and SRM-20/16 show a distinct dependency of torque ripple on number of states for values smaller than five states.

For SRM-18/12 and SRM-20/16 thus using five states with interpolation during flux linkage allocation results in the same maximum DITC accuracy as when no interpolation and 20-50 states are used.

4.1.2.3 Outlook on Adaptive $T_{\mathrm{ph}}(\psi_{\mathrm{ph}},\theta_{\mathrm{el}})$ Tuning

The task of an adaptive $T_{\mathrm{ph}}(\psi_{\mathrm{ph}},\theta_{\mathrm{el}})$ tuning algorithm is to adapt the machine characteristics $T_{\mathrm{ph}}(\psi_{\mathrm{ph}},\theta_{\mathrm{el}})$ from measurements during machine operation. The reason for incorrect LUT values in the control may be due to manufacturing inaccuracies or aging of the machine causing a change of the physical machine quantities. Furthermore, in series production not all individual machine characteristics are measured, but a generalized $T_{\mathrm{ph}}(\psi_{\mathrm{ph}},\theta_{\mathrm{el}})$ characteristic may be used for the control of the entire series. Therefore, it can be advantageous to either use an identification run at start-up or an online adaption algorithm during operation to increase the control accuracy [48].

The previous section has shown that reducing the SRM characteristics for the control to only one LUT is a viable option. For an adaptive algorithm this results in only one characteristics which has to be tuned. Figure 4.17 presents a possible schematic overview for an adaptive algorithm. Thereby, the common PWM-DITC control structure from figure 4.4 is supplemented by a $T_{\mathrm{ph}}(\psi_{\mathrm{ph}},\theta_{\mathrm{el}})$-LUT tuning algorithm, which is divided into three parts, the *inductance estimator*, the *torque estimator* and the $T_{\mathrm{ph}}(\psi_{\mathrm{ph}},\theta_{\mathrm{el}})$ *table update*.

The tuning algorithm is based on the difference in measured/ estimated inductance compared to an inductance LUT $L_{\mathrm{ph}}(\psi_{\mathrm{ph}},\theta_{\mathrm{el}})$ in the control. The first step is to estimate the instantaneous inductance, which can be done by using the flux linkage as this is already calculated for DITC by the flux linkage estimator. The instantaneous phase inductance is calculated by rearranging equation (2.5) and dividing the flux linkage ψ_{ph} by the measured current i_{ph}. As this method requires a current value greater than zero, it can only estimate the inductance in an active phase. However, similar to methods found for sensorless SRM control, an algorithm for inactive phases could also be implemented [47].

Estimating the correct instantaneous torque in SRMs is a topic of ongoing research. Neural networks, analytical equations based on the SRM torque equation (2.7) or recursive

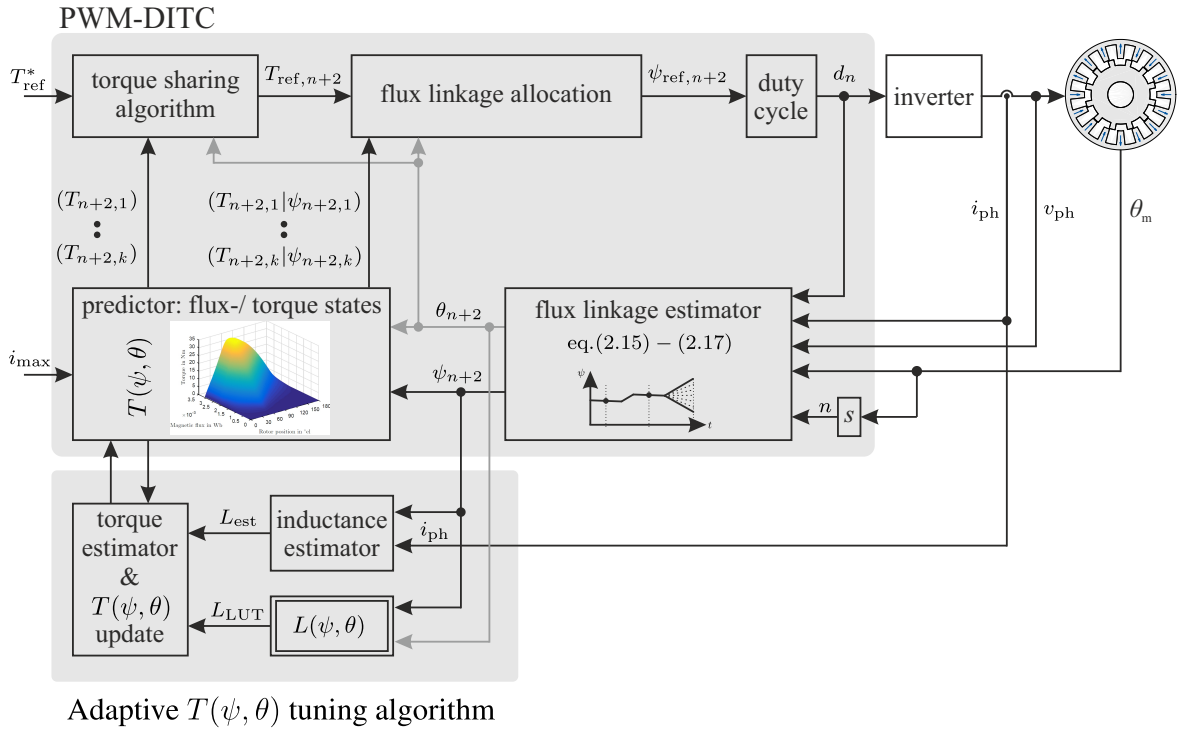

Figure 4.17: Schematic overview of predictive PWM based DITC control structure with adaptive $T_{\mathrm{ph}}(\psi_{\mathrm{ph}},\theta_{\mathrm{el}})$ tuning algorithm

least squares (RLS) algorithms have been suggested in literature [91, 92]. The two tasks of the torque estimator is to identify torque inaccuracies compared to the stored $T_{\mathrm{ph}}(\psi_{\mathrm{ph}},\theta_{\mathrm{el}})$-LUT and then to compensate for them. Once the correct instantaneous torque has been determined it is updated with a learning factor to the $T_{\mathrm{ph}}(\psi_{\mathrm{ph}},\theta_{\mathrm{el}})$ table at the location corresponding to the current flux linkage ψ_{n+1} and rotor position θ_{n+1}. To ensure a continuous smooth LUT surface, when updating individual entries, the surrounding entries in the table should also be updated accordingly.

The singular $T_{\mathrm{ph}}(\psi_{\mathrm{ph}},\theta_{\mathrm{el}})$-LUT in the control model allows for simple expansion of the PWM-DITC control structure, by either implementing new and improved tuning methods benefiting the fault-free operation quality of the SRM, or by adding control strategies for fault operation as introduced in chapter 5.

4.1.3 Conclusions

In section 4.1.1 it is shown that reducing the $T_{\mathrm{ph}}(\psi_{\mathrm{ph}},\theta_{\mathrm{el}})$-LUT resolution for PWM-DITC is a viable option when interpolation within this table is used. For the investigated machines SRM-16/12, SRM-18/12 and SRM-20/16 a 5 bit resolution is already sufficient, resulting in the minimum torque ripple for each considered drive, i.e. the LUT resolution does not add control inaccuracies during DITC. In comparison, when no interpolation is

used, the LUT resolution has to increase from 5 bit to 7 - 8 bit for similar torque ripple results.

The high resolution $\psi_{\mathrm{ph}}(T_{\mathrm{ph}},\theta_{\mathrm{el}})$-LUT previously necessary for PWM-DITC can be omitted by creating flux linkage and torque tuples $(T_{n+2,k}|\psi_{n+2,k})$ from the $T_{\mathrm{ph}}(\psi_{\mathrm{ph}},\theta_{\mathrm{el}})$ lookup. By using only two states (minimum and maximum predicted flux linkage) and using interpolation between these states during *flux linkage allocation* shows flux linkage errors of less than 2 % at high switching frequencies compared to using the $\psi_{\mathrm{ph}}(T_{\mathrm{ph}},\theta_{\mathrm{el}})$-LUT. For SRM-16/12 a switching frequency larger than 10 kHz means the LUT can be omitted, while for switching frequencies less than 5 kHz the flux linkage error rises above 15 % and thus, using $\psi_{\mathrm{ph}}(T_{\mathrm{ph}},\theta_{\mathrm{el}})$ remains the better option.

To reduce the effect of switching frequency on the flux linkage error and thus, on the output torque ripple, the number of flux linkage states are increased. Using 2 to 5 states shows an improvement in all three investigated machines by halving the output torque ripple, while again halving the torque ripple when further increasing the number of states to 10 as shown in figure 4.13 to figure 4.15.

Finally, linear interpolation is added to the *flux linkage allocation*. Thereby, the number of necessary flux linkage states can be reduced down to 3 up to 5 for all investigated machines, as then the physical minimum torque ripple for each machine is reached.

To use discrete flux linkage states within PWM-DITC effectively, a FPGA with the computational capability of calculating at least 5 reference lookup values and interpolating the result during *flux linkage allocation* within each switching period is necessary.

4.2 Machine Design Methodology Considering Control

Machine design has taken on various facets over the last few decades driven by ever changing demands in new applications and an ever increasing knowledge from experimental prototypes and computational capability [93]. As the applications change so does the focus regarding which criteria to optimize (e.g. efficiency, torque ripple, torque density, etc.). The idea of an optimal machine, regardless of the application, is replaced by the understanding that an *optimum machine design* is strictly linked to the requirements of an application with respect to the trade-offs given by the application. The increase in computational capacity enabling sophisticated machine models (complex multi-physics FEA) and modern optimization algorithms, allow for a much more competent approach towards the machine design process and its multi-objective optimization problem. However, the majority of SRM design literature focuses on the geometric machine cross-section, without incorporating the control used in the final application [56, 94, 95].

The geometric cross-section and electrical design of a SRM defines its characteristic be-

havior, especially in regard to its control performance. Therefore, it is essential to consider the control method used in the application already during the machine design process. The final machine geometry usually is an optimum consisting of often opposing multiple optimization criteria. Thus, a design method is helpful which enables the machine designer to optimize the machine cross-section according to his goals, while also enabling the designer to understand how trade-offs between different optimization criteria interact and how trade-offs are coupled to the design parameters. For this reason a machine design method based on the concept of design of experiments (DOE) is proposed [96–98].

4.2.1 Design of Experiments

Designing an electrical machine always incorporates multiple interacting input variables, which determine the final cross-section and electrical parameters. Optimizing all these variables simultaneously has brought about many different design approaches. To reduce the design complexity the amount of design variables are reduced, or only one optimization criteria is considered, for example, the machine efficiency, torque density or torque ripple. However, often the optimal machine for an application consists of a trade-off between the different optimization criteria. Population based iterative optimization algorithms searching for a pareto front depending on the optimization goals is one method to reduce the time to find an optimum [98]. Another is by using a cost function with appropriate weighting factors for the different optimization goals [94]. However, choosing the weighting factors is not always trivial and can cause the design to become a single solution optimization according to the selected weighting factors.

Finding the different pareto fronts for the machine optimization usually requires many thousands of calculations. The worst case is the one factor at a time (OFAT) variation, whereby all possible parameter combinations of the input variables are varied, one at a time, requiring an extreme number of calculations. Genetic algorithms or neural networks have been developed, which find an optimum solution with a lower amount of iterations and calculations [77]. The DOE approach reduces the necessary amount of machine-design calculations to a minimum, while handling the multi-parametric optimization.

The overall goal of DOE is to determine the cause and effect of parameters in a general system by providing a planned statistical methodology [96]. The number of calculations necessary are reduced mainly due to the fact that multiple parameters in the system are varied simultaneously, while still being able to determine the correct cause and effect relationship of each variable, to a certain extent. Thereby, the experiments as such are planned as full- or fractional factorial designs with two or more levels. Each level describes the amount of values used for each parameter. In a two level design only the minimum and maximum values (range) of the parameter is used, while in a three-level design an additional center point value between the minimum and maximum value is added [96]. A full factorial design enables an unambiguous prediction of cause and effect of each variable, consequently the amount of experiments necessary is large (e.g. 10 variables at

3 levels need $3^{10} = 59049$ experiments). To reduce the amount of experiments, a fractional factorial design is used, whereby aliasing occurs, which one has to be aware of. If for given input variables *a* to *e*, the combination of the variables *abcd* and *ae* cause the same effect, it is assumed, that the main contributor for this effect is *ae* and not the combination of the four variables *abcd*. If such an assumption is valid for a given system for 10 input variables, only 158 experiments are necessary.

For the DOE approach to work effectively it is imperative to minimize the side-effects by choosing input variables (design parameters), which are independent of each other (orthogonal to each other). Thus, choosing the appropriate input variables is important for this design process. This is especially true if the geometric design necessitates many variables as is the case when designing synchronous reluctance machines [97]. With synchronous reluctance machines there are about 37 input variables influencing the machine design. In such a case multiple DOE executions with various combinations of the input variables are executed. In contrast, for switched reluctance machines the number of geometric variables is considerably lower, making the choice of design parameters more simple. The reduced number of design variables, furthermore, allows the incorporation of control variables in the machine design process, which is the focus of the next section.

4.2.2 Design Approach

For the machine design process all variables are divided into either geometric, categorical or electrical variables. Geometric variables are, for example, the rotor radius r_1 or the stator tooth angle β_s shown in figure 4.18. The different machine configurations, depending on number of stator and rotor teeth, are categorical variables, while the number of windings N_w is an example for an electrical variable. The categorical variables are not varied in this thesis. Categorical variables are factors, which are fixed into discrete values, e.g. the material used for the machine is fixed and can not be a combination of different materials, as is the number of stator and rotor teeth, which should adhere to equation (2.2) and equation (2.3). The design process with DOE is divided into three steps as visualized in figure 4.19.

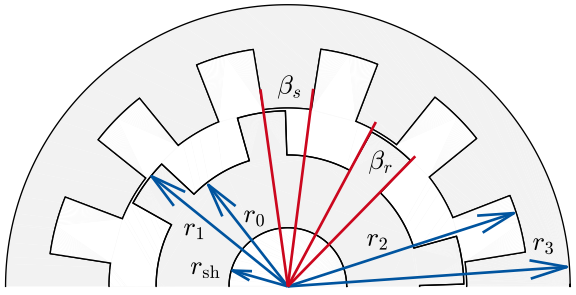

Figure 4.18: Geometric SRM parameters used for the machine design process

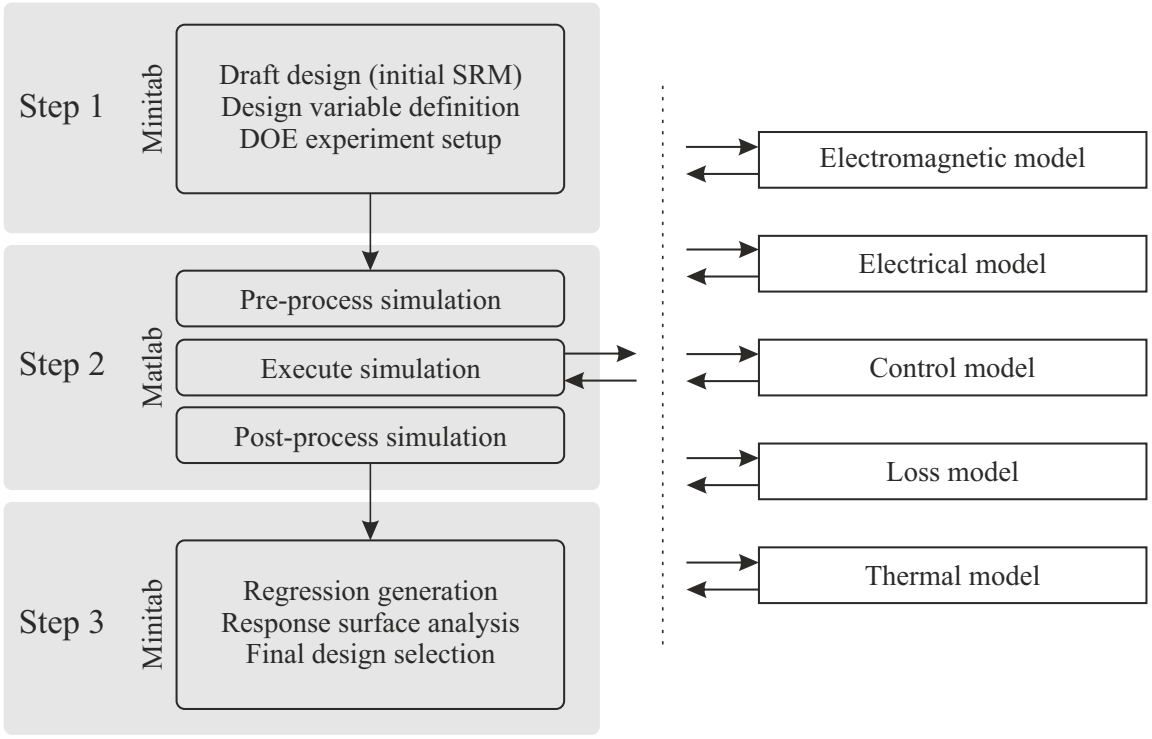

Figure 4.19: Overview of the design of experiments (DOE) design process with multiple simulation models

The three steps are discussed in the following in general, followed in section 4.2.3 by an exemplary execution of the design process for a 1 kW 12/8 SRM.

Step 1: Draft design and DOE setup

In the first step, a rough design (initial design) of the machine is taken to create a screening of all design variables. The main effect variables are identified and their individual effect on the overall result is determined. Once the main effect variables are established, these are formulated in a DOE experiment. Depending on the amount of variables to investigate simultaneously and which factorial design is chosen, the number of experiment executions necessary is determined. The experiment formulation is done in the software Minitab® [99], but can also be done in other software such as MATLAB. The result of *step 1* is a DOE-matrix containing all variable variations, which represent the experiments, or in this case, simulations calculated in *step 2*.

Step 2: Experiment / Simulation Execution

Step 2 consists of the execution of the experiments (or simulations) to determine the responses for the given parameter variations. The *pre-process simulation* prepares the simulation by taking the variables from the DOE-matrix from the previous step and applies it to the system simulation and machine model. Thereafter, the simulation is executed followed by the post-processing. The results are passed from MATLAB to Minitab® for the statistical analysis, i.e. *step 3*.

The various aspects of machine design (electromagnetic, electrical, control, loss and thermal) are accounted for by executing the DOE simulations with its respective model and evaluating each response during the regression analysis. Thus, different models and simulation software is used to cover all the different aspects. The *electromagnetic model* represents the most basic model necessary for the machine design process, as it contains the geometric cross-section of the machine and predicts the flux linkage distribution and torque production. In its simplest form, an analytical machine design software such as PC-SRD from SPEED is used. Thereby, the geometric and electrical main-effect variables (p_1 to p_{10}) from the DOE experiment are passed to PC-SRD. In PC-SRD the machine is simulated using hysteresis current control. Following the machine simulation, the output parameters necessary for the optimization and design boundary conditions are passed back to the DOE via a MATLAB-script.

PC-SRD not only incorporates the *electromagnetic model*, but also the *electrical model*, which is used to determine the number of windings N_{w}, the phase resistance R_{ph}, machine current i_{ph}, as well as the current density J_{RMS}. The active machine mass m_{active} consisting of the active rotor m_{rotor}, stator m_{stator} and copper coil mass m_{Cu} are also calculated for each machine.

To add the thermal limits to the design procedure a *loss model* and *thermal model* is required. The loss model is either taken from PC-SRD, or is implemented in the system simulation [86]. As a thermal model Motor-CAD is used [100]. The geometry and calculated losses from PC-SRD are linked to Motor-CAD. Motor-CAD executes its model and calculates the corresponding steady state hot-spot $T_{\mathrm{w,max}}$ and average winding temperatures $T_{\mathrm{w,avg}}$, which are handed back to PC-SRD. The updated temperature values are again used to execute the electromagnetic model in PC-SRD. This process is executed iteratively until a steady state operating point (e.g. no change in copper losses P_{Cu} or temperature $T_{\mathrm{w,max}}$ occur) is reached. The thermal model considers the application specific cooling and therefore, the losses which can be dissipated. The results (output variables) are handed to Minitab® for the statistical analysis.

The *control model* given in PC-SRD is limited to hysteresis current control. Therefore, designing a machine explicitly for other control types, for example DITC (section 2.3.2), requires a different modeling approach.

Figure 4.20 shows the proposed system simulation approach used for control types other than HCC. The *electromagnetic model* consists of a FEA model, which is generated via a MATLAB-script from the DOE-matrix. FEA generates the characteristic $T_{\mathrm{ph}}(i_{\mathrm{ph}},\theta_{\mathrm{el}})$- and $\psi_{\mathrm{ph}}(i_{\mathrm{ph}},\theta_{\mathrm{el}})$-LUTs. These tables then are used in a MATLAB/Simulink system simulation as introduced in section 2.3 (see figure 2.6 and figure 2.9). The system simulation consists of the SRM machine, represented as a phase-based LUT model (see section 3.2), an inverter and machine control. In this thesis PC-SRD is additionally used to determine the phase resistance R_{ph} and active machine mass (m_{active}). The loss model is implemented in the system simulation and iteratively executes the Motor-CAD thermal model to determine the stable operating condition.

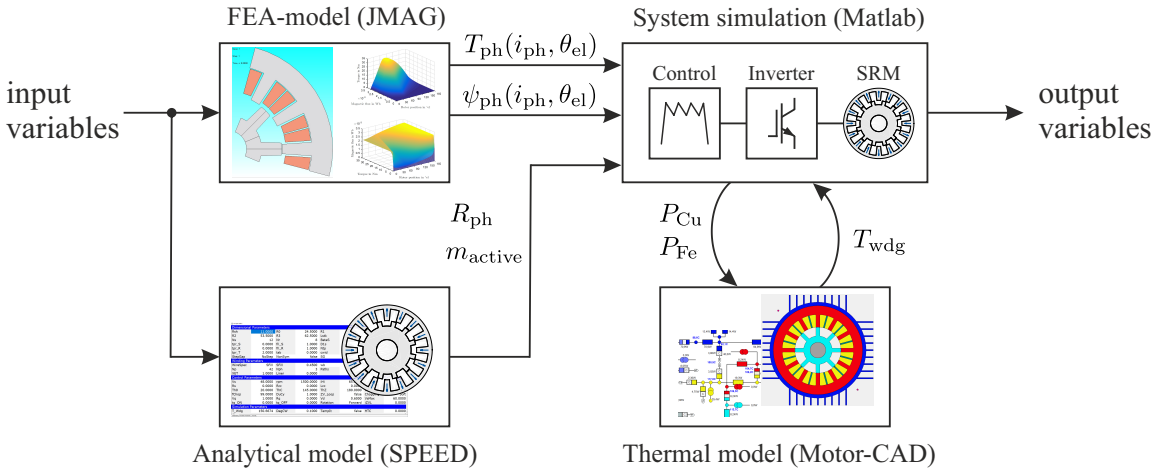

Figure 4.20: System simulation for the machine design process

Step 3: Statistical Analysis

In *step 3* all experiment results including the responses are gathered and analyzed. At first a regression equation is generated from the responses. The regression equation describes the predicted response (e.g. torque, torque ripple, efficiency, temperature, mass, etc.) in terms of the input variables (p_1 - p_{10}) as defined in 4.3. These equations are combined to a response surface method (RSM), which allows the machine designer to view the interactions and trade-offs between the design variables and all predicted responses of interest.

The residual of the regression equation describes the discrepancy between the predicted response by the equation and the actual response value from the experiment. A small residual increases the confidence with which the designer can predict and optimize the machine. A large residual usually indicates input variables, which are not independent of each other. In such a case the used input variables should be reconsidered.

The benefit of using DOE is in the possibility to change the optimization goals during the final design stage (step 3), without repeating the time-consuming experiments (simu-

lations). The RSM, therefore, enables the designer to understand how optimization goals interact with each other and how best to choose the input parameters to accomplish the desired overall goal.

4.2.3 Exemplary Machine Design: SRM-12/8

To illustrate the proposed design methodology, a three phase 12/8 1 kW SRM is used in this section. This SRM is similar to the final design of SRM-12/8.

At first, the generalized design parameter definitions and boundary conditions for SRM design are introduced. Thereafter, guidelines to create an initial machine design (first draft design) from the machine specifications and boundary conditions are presented. The DOE design process according to figure 4.19 is executed next. The execution is using the analytical SRM model (PC-SRD) with HCC control. The resulting machine designs for three differing optimization goals, maximum efficiency $\mathrm{SRM}_{\mathrm{eff}}$, minimum torque ripple $\mathrm{SRM}_{\mathrm{rpl}}$ and maximum torque per mass $\mathrm{SRM}_{\mathrm{mas}}$ are presented. In all simulations the SRM model is coupled with a thermal model (Motor-CAD) and iteratively executed to adapt the winding temperatures T_{wdg} and phase resistance R_{ph} respectively as displayed in figure 4.20.

4.2.3.1 Design Parameter Definition & Boundary Conditions

In the presented three-level DOE design process with center point, 10 independent design variables (p_1 - p_{10}) are varied simultaneously resulting in 158 experiments that need to be executed. The specifications for the machine design, given by the application, are summarized in table 4.1. The goal is to design a three-phase machine with an output power $P_{\mathrm{design}} = 1\,\mathrm{kW}$, at a speed of $n_{\mathrm{design}} = 1500\,\mathrm{rpm}$ supplied by a $v_{\mathrm{design}} = 48\,\mathrm{V}$ inverter. A machine with 12 stator and 8 rotor teeth is designed. The machine configuration is either defined by the application or determined by a pre-design process as described in [101].

Additionally to the design parameters and machine specifications, a number of boundary conditions are defined. Table 4.2 contains the geometric-, electrical- and application parameters fixed during the DOE process. The shaft radius r_{sh} and outer stator radius r_3 are usually defined by the application. The minimum air-gap length δ_{ag} and maximum copper slot-fill factor S_{fill} is defined by the motor manufacturer and the type of production techniques used. The slot-fill factor S_{fill} is defined by the type of coil winding used, i.e. needle winding, bobbins or pressed coils [102]. As a general slot-fill factor S_{fill} for SRMs in industry a value between 30 % and 55 % is found [94]. The manufacturer used by the author defined a maximum slot-fill factor of 45 %. The slot-fill factor in this thesis is defined as the coil copper area divided by the entire slot area including all isolation and

Table 4.1: Machine design specifications

	Description	Values
P_{design}	Power rating	1 kW
n_{design}	Speed rating	1500 rpm
T_{design}	Torque rating	6.36 Nm
v_{design}	Voltage rating	48 V
N_{ph}	Phase number	3
	Steel material	M330-35A

spacers. For the design, an isolation material for temperature class F is chosen. According to EN60034-1 this allows a hot-spot temperature of 155 °C and a maximum temperature rise of ΔT_{max} of 105 °C assuming an ambient temperature of $T_{\text{amb}} = 40$ °C. The maximum winding design temperature results in $T_{\text{w,max}} = 145$ °C.

Table 4.2: Geometric-, electrical- and application parameters fixed during DOE as boundary conditions

		Description	Values
r_{sh}	b_1	Rotor-shaft radius	11 mm
r_3	b_2	Outer stator radius	62.5 mm
δ_{ag}	b_3	Air-gap length	0.35 mm
S_{fill}	b_4	Slot-fill factor	$\leqslant 45\,\%$
$T_{\text{w,max}}$	b_5	Max. winding temp.	$\leqslant 145$ °C
T_{amb}	b_6	Ambient temp.	40 °C

From parameter screenings and design literature [94, 95, 103] the main effect contribution geometric design parameters (p_1 - p_6), electrical and control parameters (p_7 - p_{10}) varied during the DOE process are determined and displayed in table 4.3. The table contains the range (minimum and maximum values) used. These ranges are defined around an initial machine design SRM_{ini}, which is introduced in the following section.

4.2.3.2 Initial SRM Design

The initial design relies on generic assumptions and experiences, which have proven successful in the past by a number of machine designers [56, 95, 97, 102, 104, 105]. What initial machine design is chosen does not influence the DOE design process, however, the following guidelines result in a good starting point for the design methodology.

All geometric parameters varied are shown in the SRM cross section in figure 4.18. From

Table 4.3: Geometric- and electrical parameters varied in DOE with the initial SRM_{ini} machine design parameters

		Description	unit	DOE	SRM_{ini}
r_0	p_1	Rotor-yoke radius	mm	$20-29$	28.4
r_1	p_2	Air-gap radius	mm	$32-43$	37.5
r_2	p_3	Stator-yoke radius	mm	$50-57$	55.0
l_{stk}	p_4	Stack length	mm	$60-90$	76.0
β_r	p_5	Rotor-tooth arc	°	$14-18$	16
β_s	p_6	Stator-tooth arc	°	$13-17$	15
N_w	p_7	No. of turns		$30-55$	40
θ_{on}	p_8	Turn-on angle	°	$-10-50$	10
θ_{off}	p_9	Turn-off angle	°	$120-170$	145
i_{pk}	p_{10}	Peak current	A	$40-90$	70

the stator tooth number N_s, the stator-tooth arc β_s is determined as in equation (4.2). The factor $k_{arc,s}$ is usually between 0.85 and 1, depending on the optimization criteria, i.e. either if machine efficiency or power density is more important [102, 104]. For the initial design $k_{arc,s} = 1$ is chosen, because for the initial machine no optimization preference is required.

$$\beta_s = \frac{360^\circ}{2 \cdot N_s} \cdot k_{arc,s} = \frac{360^\circ}{2 \cdot 12} \cdot 1 = 15^\circ \tag{4.2}$$

In most applications the rotor-tooth arc β_r is equal or larger than the stator-tooth arc β_s. A rotor tooth adjustment factor $k_{arc,r}$ shown in equation (4.3) is added to the calculation of β_r as shown in equation (4.4). Increasing β_r reduces an overly saturated rotor tooth and thus losses, while also allowing more time for the current to demagnetize in the aligned position before producing negative torque [56, 95]. For the initial design $k_{arc,r} = 1$ would suffice, even though $k_{arc,r} = 1.07$ is chosen in the example so that $\beta_r = 16^\circ$.

$$1 < k_{arc,r} < 1.1 \tag{4.3}$$

$$\beta_r = \beta_s \cdot k_{arc,r} = 15^\circ \cdot 1.07 = 16^\circ \tag{4.4}$$

In [95] an air-gap radius r_1 between 40 % and 70 % of the outer stator radius r_3 is suggested. In equation (4.5) a value of $r_1/r_3 = 60\,\%$ is selected for the initial design. The range of r_1 for the DOE process shown in table 4.3 equates to 50 % and 70 % of r_3. The maximum air-gap radius r_1 is limited by the slot area necessary for the windings N_w and resulting maximum current density J_{RMS}^{max}, which in turn determines the thermal loading (maximum

winding temperature $T_{\mathrm{w,max}}$) of the machine. Machines with a lower electrical loading (lower current densities allowed) will generally have a smaller ratio between r_1/r_3.

$$r_1 = 60\,\% \cdot r_3 = 37.5\,\mathrm{mm} \tag{4.5}$$

In machines with long flux path coil configurations the magnetic flux ϕ through a stator tooth divides into the stator yoke to the left and right of said tooth. To reduce the influence of saturation the stator-yoke width $w_{\mathrm{s,yoke}}$ is overdimensioned in relation to half the stator-tooth width $w_{\mathrm{s,tooth}}$ by the factor $k_{\mathrm{w,sy}} = w_{\mathrm{s,yoke}}/w_{\mathrm{s,tooth}}$ as shown in equation (4.6) [95, 104]. Increasing the value of $k_{\mathrm{w,sy}}$ beyond 50 % is done when dominant yoke saturation due to multi-phase excitation in high phase number machines is expected, or to influence the mechanical stability and thus, the acoustic behavior (vibrational noise) of the machine by intentionally increasing the yoke thickness [40, 89, 105, 106]. For the initial design $k_{\mathrm{w,sy}} = 50\,\%$ is chosen resulting in a stator-yoke radius r_2 according to equation (4.7). Lower values of $k_{\mathrm{w,sy}}$ are used when torque density is of highest priority.

$$20\,\% < k_{\mathrm{w,sy}} < 50\,\% \tag{4.6}$$

$$r_2 = r_3 - \left(\sin(\frac{\beta_{\mathrm{s}}}{2}) \cdot (r_1 + \delta_{\mathrm{ag}}) \cdot (1 + k_{\mathrm{w,sy}})\right) = 55.0\,\mathrm{mm} \tag{4.7}$$

The rotor-yoke radius r_0 is calculated from the rotor-tooth height $h_{\mathrm{tooth,r}}$. To minimize stray flux between the stator teeth and rotor yoke, a minimum height for the rotor teeth is determined. The maximum distance between the stator- and rotor tooth tips $d_{\mathrm{gap,rs}}$ at the unaligned rotor position is defined in equation (4.8). The rotor-tooth height $h_{\mathrm{tooth,r}}$ should be a factor larger than the distance $d_{\mathrm{gap,rs}}$ to reduce stray flux between the stator and rotor yoke. The relationship $h_{\mathrm{tooth,r}}/d_{\mathrm{gap,rs}}$ is defined and investigated in [106, 107]. Radun and Anwar et.al. determine that a rotor-tooth height $h_{\mathrm{tooth,r}}$ of at least 1.5, or more conservative 2 to 2.5 times the length of $d_{\mathrm{gap,rs}}$ as in equation (4.9) is necessary. At such heights the unaligned inductance does not increase any more due to stray flux, and therefore, torque production in the machine is not compromised.

$$d_{\mathrm{gap,rs}} = \frac{2\pi \cdot r_1}{360^\circ} \cdot \left[\left(\frac{360^\circ}{2 \cdot N_{\mathrm{r}}} - \frac{\beta_{\mathrm{r}}}{2}\right) - \left(1 + \frac{\delta_{\mathrm{ag}}}{r_1}\right) \cdot \frac{\beta_{\mathrm{s}}}{2}\right] = 4.53\,\mathrm{mm} \tag{4.8}$$

$$1.5 < \frac{h_{\mathrm{tooth,r}}}{d_{\mathrm{gap,rs}}} < 2.5 \tag{4.9}$$

With equation (4.8) and the factor from equation (4.9) of $h_{\mathrm{tooth,r}}/d_{\mathrm{gap,rs}} = 2$, the rotor-yoke

radius r_0 for the initial design is calculated in equation (4.10).

$$r_0 = r_1 - h_{\text{tooth,r}} = 28.4\,\text{mm} \tag{4.10}$$

The machine stack length l_{stk} is either estimated from the rotor volume consisting of the rotor area $A_{\text{ag,rotor}}$ (equation (4.11)) and stack length l_{stk}, and application torque T_{design} if a fitting thrust factor σ for the used cooling and machine size is known as in equation (4.12).

$$A_{\text{ag,rotor}} = \pi \cdot r_1^2 = 0.0044\,\text{m}^2 \tag{4.11}$$

$$l_{\text{stk}} = \frac{T_{\text{design}}}{\sigma \cdot A_{\text{ag,rotor}}} \tag{4.12}$$

Without a thrust factor σ the machine length l_{stk}, as well as the magneto motive force Θ_{MMF} necessary for the machine to produce roughly the desired torque has to be determined from a first machine simulation. As a starting point for the turn-on θ_{on} and turn-off angle θ_{off} the values 10° and 145° are selected respectively, which are commonly used switching angles for switched operation using HCC. The Θ_{MMF} is divided into number of windings N_{w} and a peak current i_{pk} (maximum current given by inverter rating to be used) used by the control. In the example $l_{\text{stk}} = 76.0\,\text{mm}$, $N_{\text{w}} = 40$ and $i_{\text{pk}} = 70\,\text{A}$. These starting values should roughly produce the required torque at the given voltage v_{design} and speed n_{design}. The final desired torque and control values (θ_{on}, θ_{off}, i_{pk}) will be selected once the DOE is completed and the regression equations are evaluated.

The cross section of the initial machine design SRM_{ini} is shown in figure 4.21a.

4.2.3.3 Machine Design with Hysteresis Current Control

In this design execution a machine model and hysteresis current control from PC-SRD is used. The machine is designed with a self-ventilated cooling, which is considered in the Motor-CAD model. Three design optimization criteria, *maximum efficiency* SRM_{eff}, *minimized torque ripple* SRM_{rpl} and *maximum torque per mass* SRM_{mas} are pursued. The main benefit of the DOE approach is that the shift between the different design optimizations is possible after the time consuming experiments (simulations) are done. Therefore, the optimization in regard to the different trade-offs is possible during the final analysis (step 3).

The ranges of all ten design variables p_1 - p_{10} varied simultaneously in DOE are given in table 4.3. All DOE responses and machine results for the different optimization criteria, SRM_{eff}, SRM_{rpl} and SRM_{mas} are summarized in table 4.4. The corresponding machine cross sections are shown in figure 4.21. To maximize the efficiency, the losses have to be

Table 4.4: SRM design results and DOE responses for various optimization criteria (SRM_{eff}, SRM_{rpl} and SRM_{mas})

		Description	unit	SRM_{ini}	SRM_{eff}	SRM_{rpl}	SRM_{mas}
r_0	p_1	Rotor-yoke radius	mm	28.4	25.0	21.0	20.5
r_1	p_2	Air-gap radius	mm	37.5	33.8	32.0	43
r_2	p_3	Stator-yoke radius	mm	55.0	55.9	57.0	56
l_{stk}	p_4	Stack length	mm	76.0	75.0	75.0	74.0
β_r	p_5	Rotor-tooth arc	°	16	16.9	17	16.5
β_s	p_6	Stator-tooth arc	°	15	16	16	14
N_w	p_7	No. of turns		40	55	44	39
θ_{on}	p_8	Turn-on angle	°	10	14	6	30
θ_{off}	p_9	Turn.off angle	°	145	120	170	120
i_{pk}	p_{10}	Peak current	A	70	66	71	80
η_{eff}		Efficiency	%	79.1	**83.1**	76.7	77.9
T_{rpl}		Torque ripple	%	101	146	**45**	182
$T/_{wt}$		Torque per mass	$Nm/_{kg}$	1.25	1.28	1.27	**1.33**
T_{nom}		Torque	Nm	6.87	6.86	6.66	6.38
m_{active}		Active total mass	kg	5.49	5.36	5.23	4.8
m_{Fe}		Iron mass	kg	4.45	3.94	3.59	3.88
m_{Cu}		Copper coil mass	kg	1.04	1.42	1.64	0.92
J_{RMS}		Current density	kg	8.2	6.1	6.3	8.2
$T_{w,max}$		Max. winding temp.	°C	145.8	116.3	144.4	145.4
$T_{w,avg}$		Avg. winding temp.	°C	137.2	112.5	141.0	136.6

minimized for the given power rating of 1 kW. In the low speed SRM, copper loss P_{Cu} is dominating, therefore, the copper cross sectional area is maximized by increasing the slot area by maximizing the stator-yoke radius r_2, while keeping the stator teeth relatively wide at $\beta_s = 16°$ for torque production. Reducing the current density J_{RMS} from 8.2 A/mm² in the initial design SRM_{ini} to 6.1 A/mm² results in the highest efficiency and corresponding in the lowest overall operating temperature at $T_{w,max} = 116.3\,°C$.

From the maximum winding temperatures $T_{w,max}$ of the other machine designs (SRM_{ini}, SRM_{rpl}, SRM_{mas}) it can be concluded that the chosen power (1 kW) and given machine volume is limited by the cooling. The machines can not be designed completely freely, but the copper losses in all the designs have to be reduced to fit the winding temperature boundary condition of 145 °C. In figure 4.22 the torque and current waveforms from PC-SRD simulations for the machines SRM_{eff}, SRM_{rpl} and SRM_{mas} are presented. The control for efficiency optimization results in a single pulse current trajectory, producing the most

torque for the lowest RMS current. The single pulse results from the maximum possible windings ($N_\mathrm{w} = 55$) in the DOE.

The torque ripple optimized SRM has a similar cross section compared to $\mathrm{SRM}_\mathrm{eff}$. For low torque ripple in a three phase machine a certain phase overlap is necessary, possible by wide stator ($\beta_\mathrm{s} = 16°$) and rotor teeth ($\beta_\mathrm{r} = 17°$). Furthermore, in contrast to $\mathrm{SRM}_\mathrm{eff}$, the low current density and therefore, efficiency is traded for a current waveform (i.e. turn-on angle θ_on, turn-off angle θ_off, peak current i_pk), which produces a constant output torque. The current waveform $i_\mathrm{ph,rpl}$ in figure 4.22b is such, that the phase overlap produces a constant torque with only 45 % torque ripple, visible for T_rpl in figure 4.22a.

Optimizing a SRM for minimum mass, results in the smallest stator ($\beta_\mathrm{s} = 14°$) and rotor teeth ($\beta_\mathrm{r} = 16.5°$) possible in the DOE experiment. For the given machine the teeth would ideally be even smaller, but are limited by the range chosen for the DOE setup. In such a case a second DOE run should be done, adjusting the boundaries of the main effect variables. For a mass optimized machine smaller teeth arcs between 12° and 14° should be used. However, if only such small teeth would have been varied, no SRM with constant torque would have been in the solution. This shows, that depending on the design criteria

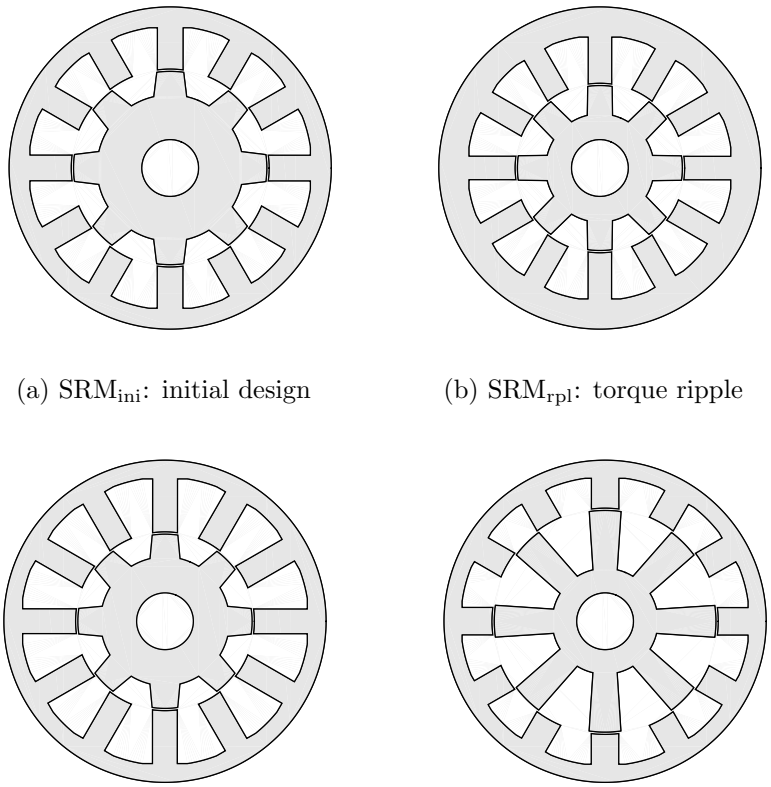

(a) $\mathrm{SRM}_\mathrm{ini}$: initial design

(b) $\mathrm{SRM}_\mathrm{rpl}$: torque ripple

(c) $\mathrm{SRM}_\mathrm{eff}$: efficiency

(d) $\mathrm{SRM}_\mathrm{mas}$: torque per mass

Figure 4.21: Cross sections depending on different optimization criteria

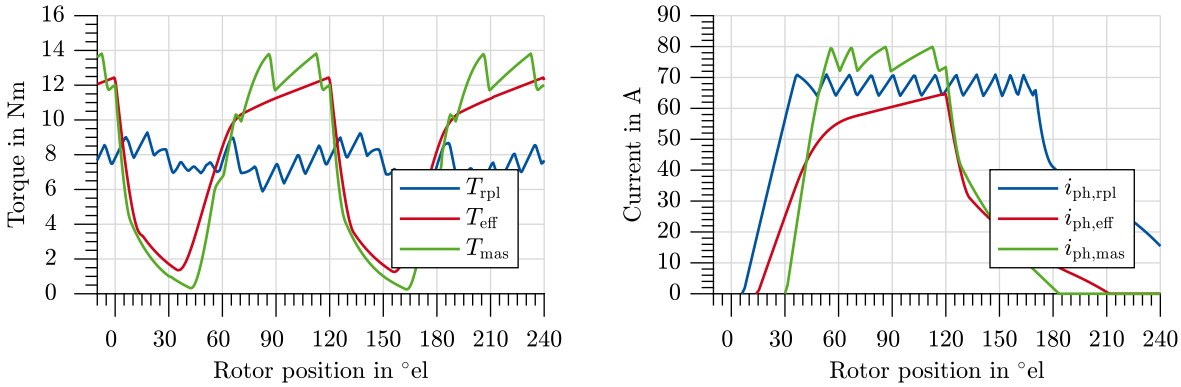

(a) Torque waveforms

(b) Current waveforms

Figure 4.22: Torque and current trajectories for various optimization criteria simulated in PC-SRD

a second DOE execution, extending the variable range used in a first DOE execution, can be necessary.

DOE presents an iterative approach to find the target solution, however, the convergence to the best result is very efficient and thus, fast. In the example of the 12/8 machine shown, the optimization criteria are only applied once the DOE experiment is done and the regression equations have been determined. The impact, changes in the optimization criteria have, can directly be linked to changes in the geometry, electrical or control setup.

An additional benefit in the proposed machine design methodology is that the optimal control parameters for hysteresis current control (HCC) are determined along with the geometric and electrical parameters. The waveforms of torque and current shown in figure 4.22 represent the optimal control parameters for each machine $\mathrm{SRM}_{\mathrm{rpl}}$, $\mathrm{SRM}_{\mathrm{eff}}$ and $\mathrm{SRM}_{\mathrm{mas}}$. The parameters resulting in these waveforms are displayed in table 4.4 The different winding number N_{w} and turn-on θ_{on}, turn-off angle θ_{off} and reference peak current i_{pk} depending on the optimization is clearly visible.

From the torque waveforms in figure 4.22a it is visible that not all machine designs are capable of producing a constant torque with low torque ripple. Due to their limited phase overlap not all three phase machine designs are capable of producing low torque ripple operation independent of whether HCC or DITC is used. In three phase machines the phase overlap has to be large enough by means of geometric design [108]. In this example only $\mathrm{SRM}_{\mathrm{eff}}$ can effectively be operated with DITC resulting in an even lower torque ripple compared to the HCC results shown in figure 4.22a. In higher phase number machines ($N_{\mathrm{ph}} \geqslant 4$) a minimum phase overlap is inherently present making them intrinsically able to produce torque with low ripple when using DITC.

4.2.4 Conclusions

The DOE approach enables a streamlined design process incorporating the control. The exemplary design clearly shows how the different contradicting optimization criteria result in different machine cross sections (figure 4.21) and torque trajectories (figure 4.22). With only one DOE execution with 158 experiments, the interactions between the design variables are visible and made understandable for the design engineer.

The time-saving design process with the introduced system simulation in figure 4.20 combining an electromagnetic FEA machine model, temperature model in Motor-CAD and an arbitrary control (HCC, DITC or fault tolerant strategies) in MATLAB, allows a holistic design approach for future drive system (machine and control) developments.

4.3 Excursion: PWM-DITC Considering Mutual Coupling

The different influences and effects mutual coupling, due to coil orientation of the individual phases have on each other, has been shown in section 3.4. In this short excursion a method for incorporating the coupling effect in DITC is presented and simulation results for alternating and non-alternating coil arrangement for SRM-16/12 are discussed.

Control Approach

The main difference to conventional DITC is that the interaction between the two active phases is considered during torque estimation, torque sharing algorithm and flux linkage allocation. Figure 4.23 shows the schematic overview of a LUT-based control approach, which considers phase coupling.

The flux linkage estimation (minimum and maximum flux linkage possible in the next switching period) is determined for each phase individually from the applied duty cycle d_n, phase voltage v_{ph} and measured phase current i_{ph}. The torque is estimated by using the lookup table $T(\psi_1,\psi_2,\theta_{\mathrm{el}})$. The machine characteristics and influence due to coil arrangement is incorporated within this one LUT, as it is dependent on the flux linkage of both active phases and represents one coil arrangement. In case of even phase machines, where both alternating and non-alternating phase neighbors are present, two $T(\psi_1,\psi_2,\theta_{\mathrm{el}})$ tables are necessary. One for each coil arrangement. Furthermore, as three input variables ψ_1, ψ_2 and θ_{el} are required, implementing this LUT in hardware becomes computationally expensive. However, as the back calculation from torque reference to flux linkage reference is done with torque samples, as introduced in section 4.1.2, only the torque lookup table is necessary for the entire control algorithm. The arbitrary number of torque states used during the lookup and allocation process is marked by the index k, i.e. T_k, $\psi_{1,k}$, and $\psi_{2,k}$.

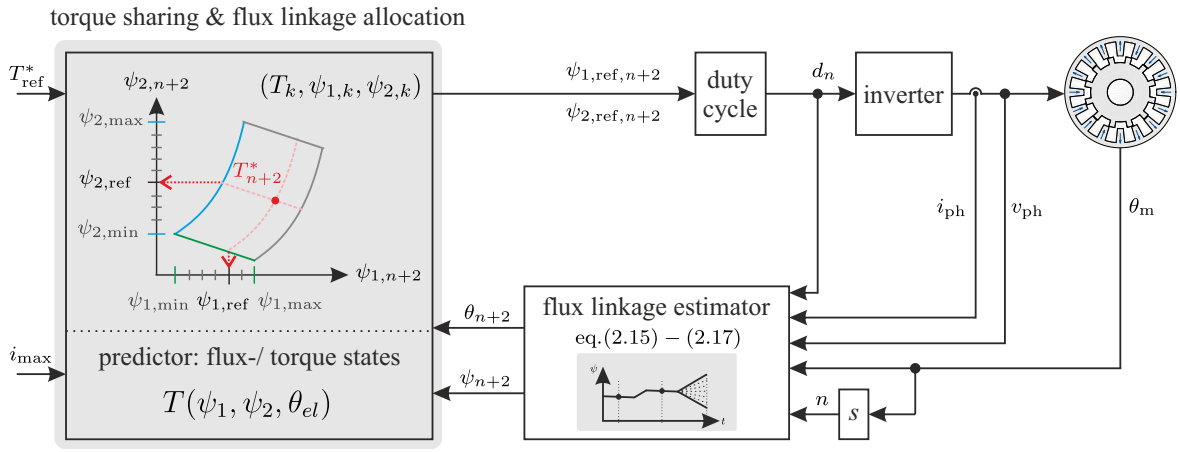

Figure 4.23: Schematic overview of predictive PWM based DITC control structure considering mutual phase coupling [83]

The torque sharing algorithm usually is done by a phase priority stack [49]. This is changed to a two dimensional nearest fit problem [13]. As depicted in figure 4.23 the possible torque values T_k, due to the flux linkage range of incoming phase 1 (ψ_1) and outgoing phase 2 (ψ_2) for the next switching period, spans a two dimensional matrix (T_k,$\psi_{1,k}$,$\psi_{2,k}$). According to the reference torque T^*_{ref} the nearest torque value from T_k is selected. Similar to the priority stack, the incoming phase (phase 1) has priority to ensure adequate magnetization of the phase. This leads to an additional control condition that the torque value from T_k is selected, where flux linkage of phase 1 ψ_1 is maximized. The reference flux linkage for both active phases is calculated from the tuples T_k,$\psi_{1,k}$,$\psi_{2,k}$.

Simulative Results

PWM-DITC with mutual coupling is implemented in MATLAB Simulink. The machine model used is presented in section 3.4 and results thereof are denoted in the simulation graphs by *Simulink*, while the reference values from the control are denoted by *Control ref.* The MATLAB results are compared to the results from a coupled FEA model presented in section 3.5. The FEA results are denoted as *FEA SRM model*.

The simulation results are performed for SRM-16/12 at an operation of 5 Nm and 400 rpm with an alternating coil arrangement (see figure 3.7a) and non-alternating coil arrangement (see figure 3.7b). As SRM-16/12 is a four phase machine there are always both types of phase commutations (parallel and anti-parallel) present, independent of the coil arrangement chosen.

The first results discussed are for the non-alternating coil arrangement in figure 4.24 when no phase coupling is considered in the control and in figure 4.25 when phase coupling is considered. Without phase coupling the control is implemented as presented in

section 2.3.2, where all phases are considered individually. The torque waveforms in figure 4.24a show that the controlled torque is constant. However, the output torque from the LUT-based coupled SRM model (Simulink SRM model) and the coupled FEA torque (FEA SRM model) is not as flat, the influences of the parallel and anti-parallel phase commutation are visible. The harmonic torque components are displayed in figure 4.24b, the corresponding current and flux linkage waveforms for each phase are shown in figure 4.24c and figure 4.24d respectively.

The torque results demonstrate that even though the absolute values of phase coupling are very small ($< 6\,\%$), the different coupling effects present can clearly be identified in the high harmonic content visible in figure 4.24b. In SRM-16/12 only the 16^{th} harmonic is expected due to the 16 stator teeth, which also is present when coupling is considered (see figure 4.25b). The high 4^{th} harmonic, representing the high singular peak in figure 4.24a at 5 ms, is due to anti-parallel coil coupling of phase 1 and phase 2. During the anti-parallel coupling, the flux linkage of the two phases act additive, increasing the overall output torque. In contrast, the subsequent next three phase commutations ($2 \rightarrow 3$, $3 \rightarrow 4$, $4 \rightarrow 1$) are coupled parallel as the flux linkage is orientated in the same direction, resulting in subtractive coupling and, thus, reducing the output torque. The parallel coupling results in the 12^{th} harmonic, visible in the fast fourier transform (FFT) of the torque (figure 4.24b). Per mechanical revolution thus 4 high instantaneous peaks occur due to anti-parallel coupling and 12 low dips due to anti-parallel coupling. In between these dips there are smaller peaks which cause the visible 8^{th} harmonic.

The torque waveforms when the DITC algorithm considers phase coupling are shown in figure 4.25a. All three torque waveforms are similar and virtually independent of phase coupling, which is reflected in the low harmonic content in figure 4.25b. Both results show that the LUT-based modeling approach matches very well with the coupled FEA results. This is especially visible from the matching coupled flux linkage trajectories in figure 4.25d. In figure 4.25d, negative values for phase flux linkage show that not only the self-flux linkage of the corresponding phase induces flux into the phase, but also the mutual flux of neighboring phases. The negative value for flux linkage resemble coupled flux linkage induced into the opposite direction, i.e. parallel connection. Only the flux linkage of phase 1 during $6.5\,\text{ms} < t < 9\,\text{ms}$ shows a positive flux linkage value during phase coupling with phase 2. All other phases show a small negative flux linkage value due to parallel phase coupling.

The results for SRM-16/12 with alternating coil arrangement are shown in figure 4.26 when control does not consider phase coupling and in figure 4.27 when coupling is considered. In contrast to the previous torque waveform figure 4.26a shows the torque ripple with three anti-parallel and one parallel phase coupling torque peak.

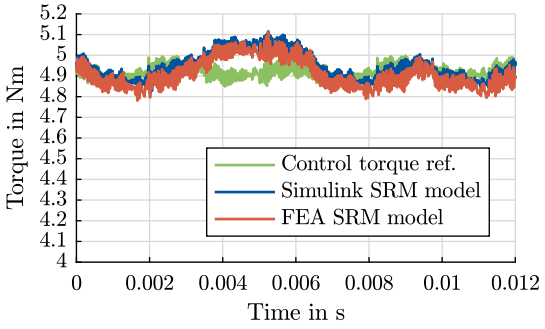

(a) Total torque

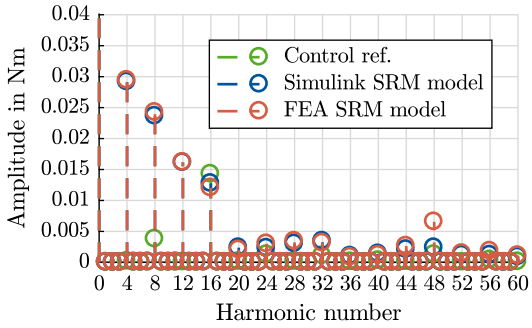

(b) FFT of output torque

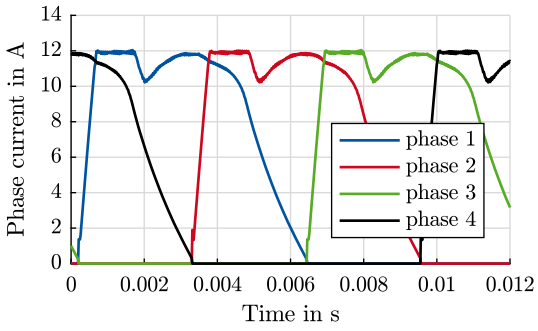

(c) Phase current

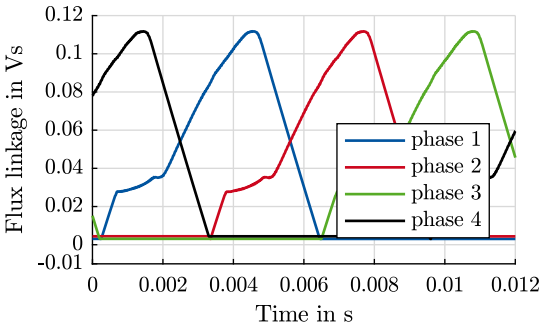

(d) Flux linkage

Figure 4.24: SRM-16/12: Simulation results for non-alternating excitation without considering mutual coupling in the control [83]

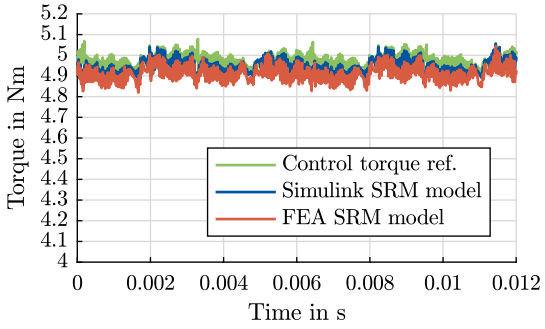

(a) Total torque

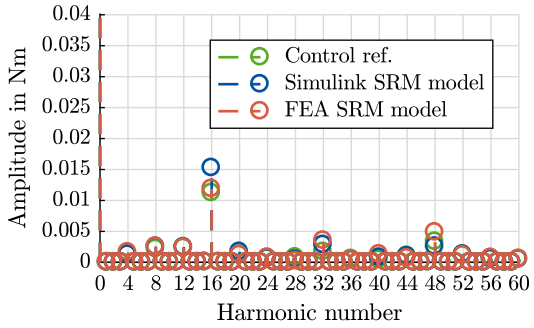

(b) FFT of output torque

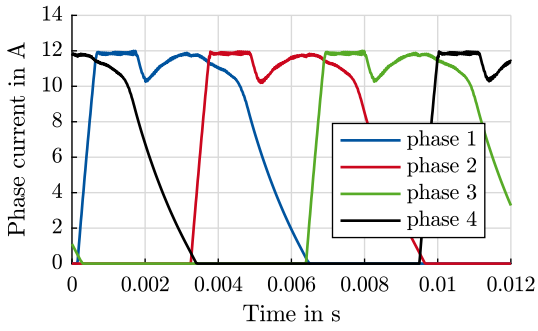

(c) Phase current

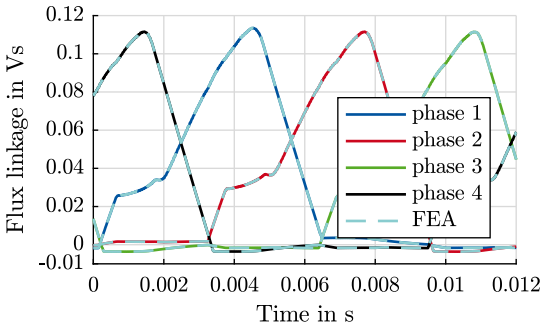

(d) Flux linkage

Figure 4.25: SRM-16/12: Simulation results for non-alternating excitation considering mutual coupling in the control [83]

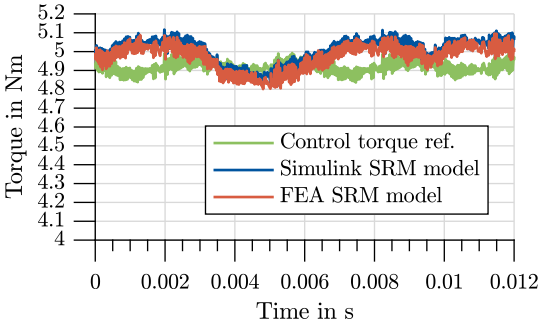

(a) Total torque

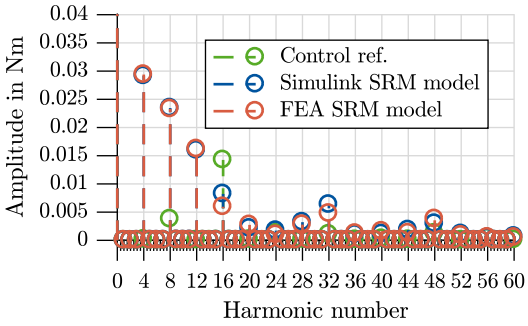

(b) FFT of output torque

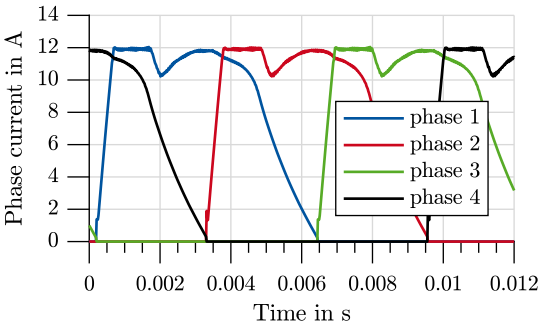

(c) Phase current

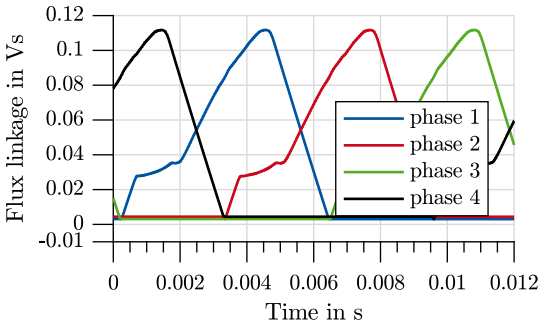

(d) Flux linkage

Figure 4.26: SRM-16/12: Simulation results for alternating excitation without considering mutual coupling in the control

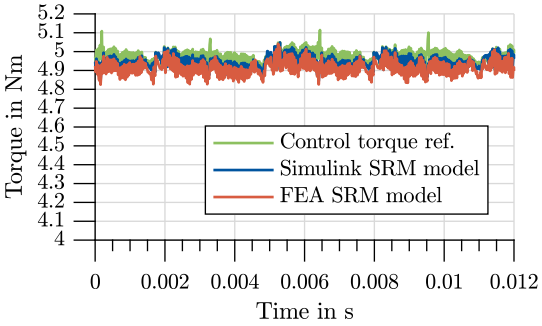

(a) Total torque

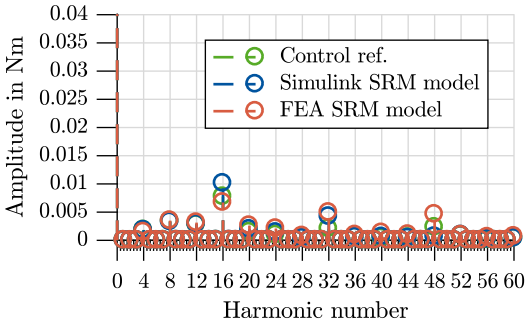

(b) FFT of output torque

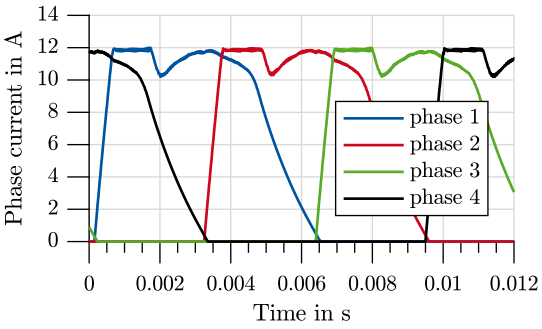

(c) Phase current

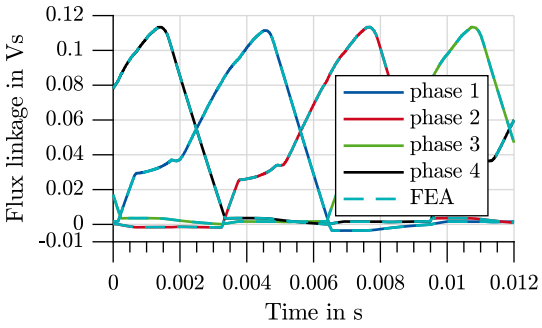

(d) Flux linkage

Figure 4.27: SRM-16/12: Simulation results for alternating excitation considering mutual coupling in the control

Conclusions

In the simulated SRM-16/12 an additional torque ripple due to mutual coupling of 6 % is observed, which is comparable to a discussion presented in [109], where a torque ripple of 5 % is accounted for by mutual coupling.

In SRMs with an odd number of phases and alternating coil arrangement only the spatial harmonics of the stator teeth are present. This is due to the fact that the harmonics due to coupling co-inside with the phase commutation harmonics. A control considering mutual coupling would, however, reduce the absolute value of the stator tooth harmonic. When using a non-alternating coil arrangement, additional lower harmonics are introduced as again both parallel and anti-parallel neighboring phase commutations are present, which cause different torque coupling.

5 Control of Distributed Inverters - Fault Tolerant Control

In this chapter, radial force minimization controls (RFMCs) in conjunction with direct instantaneous torque control (DITC) are proposed. The main goal remains minimizing torque ripple during fault, while also minimizing the radial unbalanced magnetic pull (UMP).

At first only DITC is used in fault-free and single pole fault operation. An *elementary fault control* is introduced, whereby, the stator pole opposite the fault pole is switched off to avoid unbalanced magnetic pull. The resulting limits are investigated, followed by a proposal of the RFMC control strategy. A simplified radial force minimization control for single pole fault (S-RFMC) is proposed, which is implemented on the FPGA of the used rapid prototyping hardware. Especially, the thermal ramifications of the fault tolerant control strategies in respect to different SRM configurations are investigated.

5.1 Unbalanced Magnetic Pull During Single Pole Fault

The *torque sharing algorithm* (see figure 4.4) is principally responsible for a smooth torque output of the SRM. The algorithm controls the torque ripple and the average output torque. The reference torque T^*_{ref} is divided amongst all active phases. In case of a distributed inverter the torque is, furthermore, distributed amongst all active pole modules of one phase. During fault-free operation the torque is distributed equally resulting in a symmetrical flux distribution. The symmetrical flux causes equal symmetric radial pole forces in opposing directions, resulting in a balanced condition, as displayed in figure 5.1a for phase 1 of SRM-16/12.

Distributed inverters cause each stator tooth to be electrically independent from each other even in case of a fault. A fault in a pole inverter module or stator tooth coil does not cause the complete failure of the machine's phase, but only one inverter module, i.e. stator tooth, is rendered non-functional. The remaining poles in the faulty phase are still operational and can be used to produce torque.

In figure 5.1b pole 1.1 is faulty, resulting in three remaining active poles (1.5, 1.9 and 1.13). The opposite poles 1.5 and 1.13 create a balanced condition in the horizontal axis,

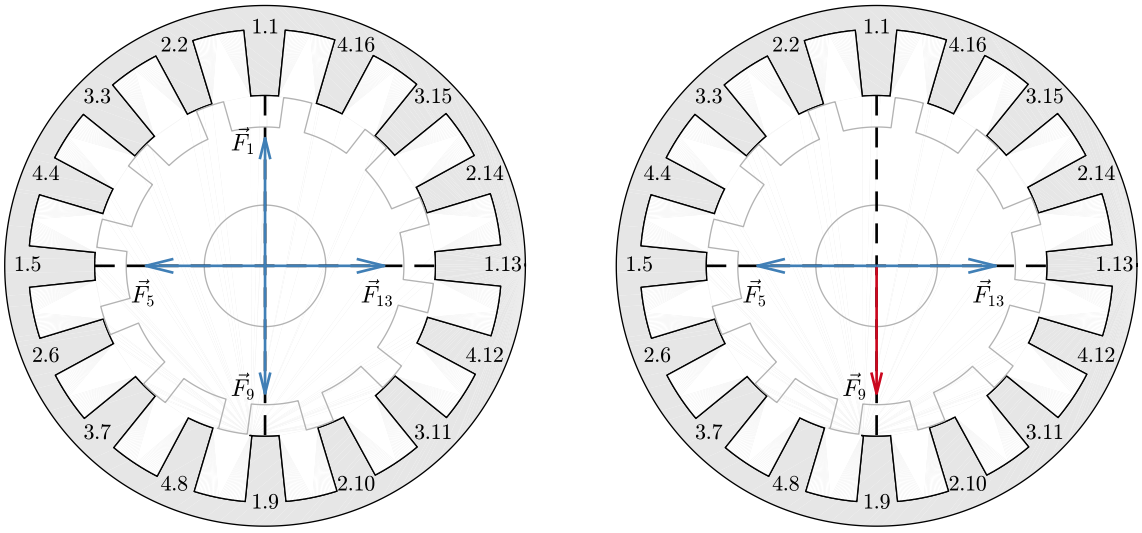

(a) Fault free: balanced pole force condition

(b) Fault pole 1.1: UMP caused by pole 1.9

Figure 5.1: Unbalanced magnetic pull (UMP) due to fault in pole 1.1 and resulting force caused by critical pole 1.9 (F_9)

however, pole 1.9 causes an unbalanced radial force F_9. This force is called critical pole force, as it causes an unbalanced magnetic pull (UMP) on the bearing during operation.

In figure 5.2 a simulation result for SRM-16/12 is shown at the operating point 5 Nm and 400 rpm. The first half of the result shows fault-free DITC operation, while the second half shows the operation during a single pole fault of pole 1.1. If the fault is not detected by the control a torque dip of 1.25 Nm in the overall torque $T_{\text{sum}}^{\text{no}}$ becomes visible, as phase 1 is only producing 75 % of the reference torque.

If the pole fault is detected by the control, DITC can react to the torque dip by distributing the reference torque T_{ref}^{*} amongst all three remaining healthy poles, as long as the power limit of the machine and the pole inverters are not reached. From figure 5.2b it is visible that the increased current in the healthy poles, required to compensate for the missing torque, increases the UMP from 350 N to 430 N. The per pole RMS current thereby, changes from 1.98 A to 2.19 A.

Requirements for Fault Tolerant Switched Reluctance Drives

For a switched reluctance drive to be operable during single pole fault, the drive system has to fulfill a few requirements. The first is that the machine used has at least two pole pairs. This allows control flexibility compensating the UMP during fault. Furthermore, the machine requires a similar phase overlap as found in DITC. In DITC the phase overlap

is necessary for a smooth and continuous torque production during phase commutation. Similar, in the following sections it will be shown that for fault control, a certain phase overlap is necessary for radial force compensation.

For the control to be able to react to a fault, the fault has to be detected by appropriate sensing and isolated from the functioning drive system as mentioned in section 2.2.3. Furthermore, in the following sections it will become evident, that the fault tolerant control strategy requires voltage reserve. This again is similar to the requirements of DITC to ensure flexibility controlling the current trajectory.

In the following sections different fault tolerant control (FTC) algorithms are proposed with the task to keep the output torque stable, while reducing the amount of UMP on the bearings.

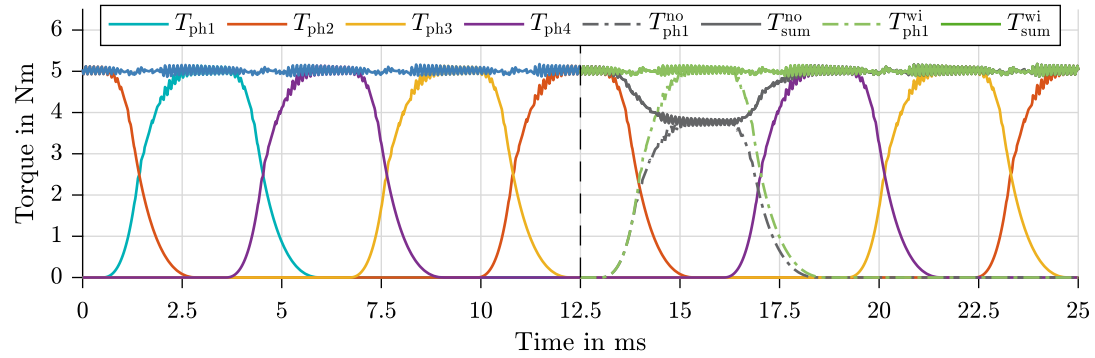

(a) Total torque and per phase torque

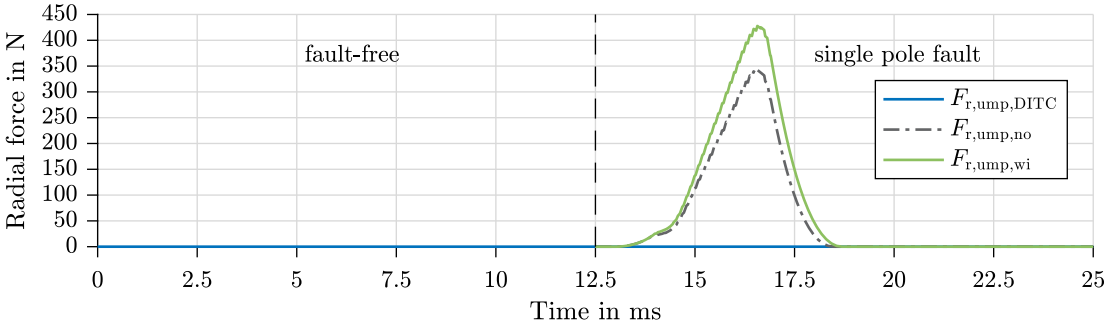

(b) Net radial force (UMP)

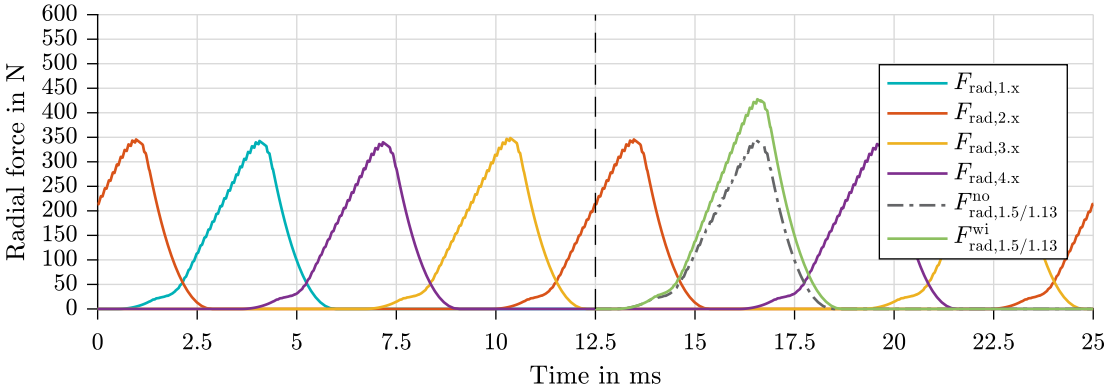

(c) Radial force per pole

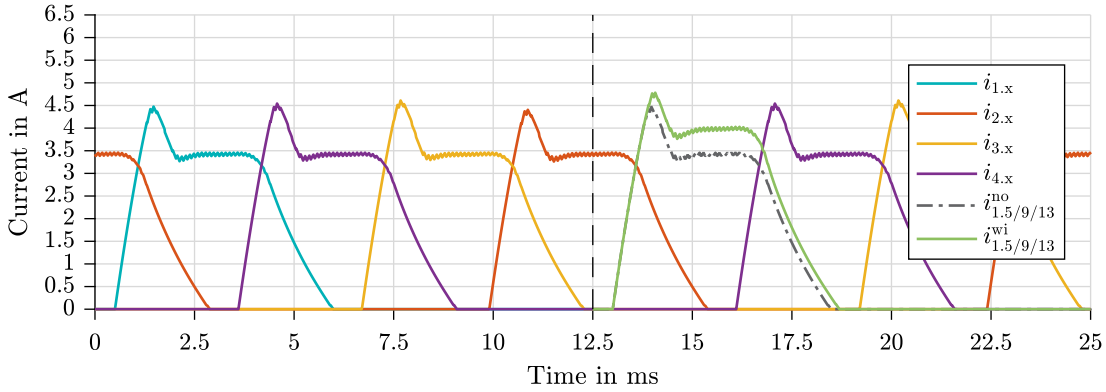

(d) Current per pole

Figure 5.2: SRM-16/12: Simulation result of UMP switching from fault-free to single pole fault during PWM-DITC operation at 5 Nm and 400 rpm with (T^{wi}_{sum}) and without (T^{no}_{sum}) fault detection in the control

5.2 Elementary Fault Control - Critical Pole Turn off

In machines with more than two pole pairs an elementary fault control (EFC) can be implemented. Thereby, during single pole fault, the critical pole producing the UMP is switched off, leaving the remaining poles of that phase to produce the reference torque. Once the pole fault is detected, the *torque sharing algorithm* distributes the torque amongst the remaining poles. This creates a symmetrical excitation and equal radial forces of all opposite poles. This elementary control method is very effective in reducing UMP [32], however, with the limitation that the healthy poles of only the faulty phase compensate the missing torque by increasing their current loading.

5.2.1 DITC Approach: From Healthy Phase to Fault

During fault-free operation all poles of a phase are excited symmetrically resulting in an even flux distribution, named *4polesA* (4A), as shown for SRM-16/12 in figure 5.3a. Always two opposite poles have the same coil orientation causing four flux loops in a SRM with two pole pairs. During a single pole fault, as previously introduced, an asymmetric current excitation and flux distribution occurs in the machine resulting in UMP. The simplest method to avoid UMP is to switch off the pole producing the UMP, i.e. the pole opposite to the faulty pole. Switching off the critical pole minimizes the UMP, but also creates stray flux through the faulty and switched off poles as visible in figure 5.3b. This two pole excitation, named *2polesA* (2A), is not common as both remaining coils produce a flux in the same direction, which then is forced through the inactive poles. In contrast, figure 5.3c shows the flux distribution of a common two pole excitation (*2polesB*, 2B), where both poles produce flux in opposite directions, in respect to rotor and stator, resulting in only two flux loops. However, this coil orientation is only possible if one of

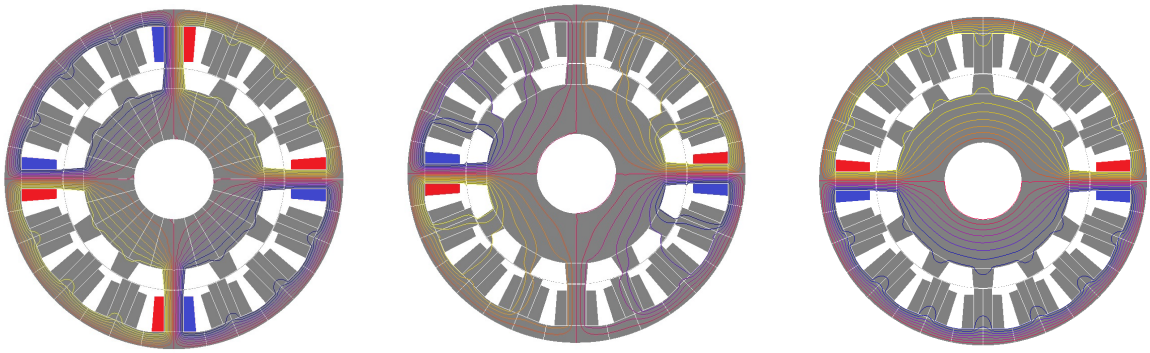

(a) Fault-free: 4polesA (b) EFC: 2polesA (c) 2polesB

Figure 5.3: SRM-16/12: Magnetic flux distribution from different coil excitation during fault-free (a) and fault (b) & (c) condition

the pole inverters can operate its current in the opposite direction, i.e. if the pole inverter were a full-bridge inverter and could produce positive and negative current.

The stray flux, which arises in 2polesA when the critical pole is turned off, results in a change of the torque characteristic of the machine [20]. In figure 5.4 the measured static torque profile for SRM-16/12 with different coil excitation conditions is shown. Thereby, the torque per pole and current per pole values are used to make all configurations comparable. It is evident that the fault-free condition 4polesA and the common two pole excitation 2polesB are very similar in their per tooth torque capability. The torque produced by the 2polesA configuration is considerably lower, especially at rotor position θ_{el} values larger than 60°.

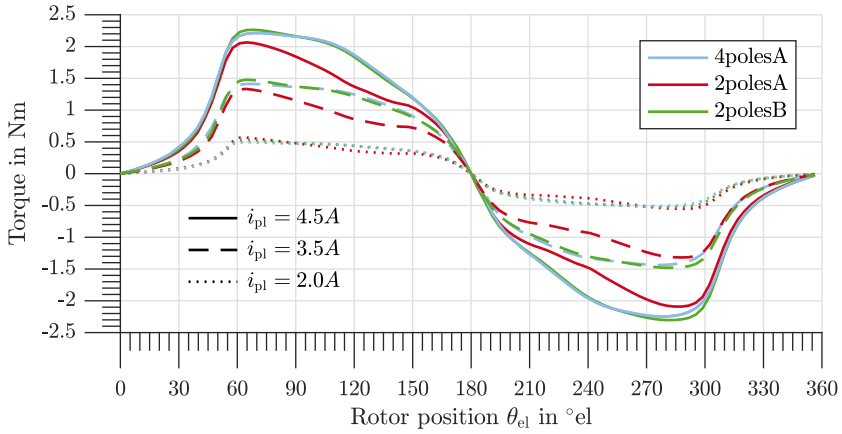

Figure 5.4: SRM-16/12: Pole torque measurements of the different coil excitation possibilities during fault-free and fault (EFC) conditions

Therefore, using the fault-free DITC $T_{\mathrm{ph}}(\psi_{\mathrm{ph}},\theta_{\mathrm{el}})$-LUT during EFC may not be sufficient to control a smooth torque. For EFC to have the same instantaneous torque output as fault-free DITC, a second $T_{\mathrm{ph}}(\psi_{\mathrm{ph}},\theta_{\mathrm{el}})$-LUT containing values for the 2polesA excitation is necessary.

5.2.2 Simulation and Thermal Implications

In figure 5.5 the simulation result for SRM-16/12 at 5 Nm and 400 rpm during single pole fault and EFC is shown. The superscripts 4A and 2A, in the figures, represent the use of a $T_{\mathrm{ph}}(\psi_{\mathrm{ph}},\theta_{\mathrm{el}})$-LUT, either of the normal 4polesA from DITC or a 2polesA-LUT in the EFC control.

The results clearly show the effectiveness of EFC in reducing the UMP (figure 5.5b). The torque waveform in figure 5.5a shows a dip from 5 Nm to 4.5 Nm for $T_{\mathrm{sum}}^{4\mathrm{A}}$, when the 4polesA LUT is used. This dip is caused by the change in torque characteristics mentioned previously due to the flux distribution in the SRM. The torque dip is compensated if EFC

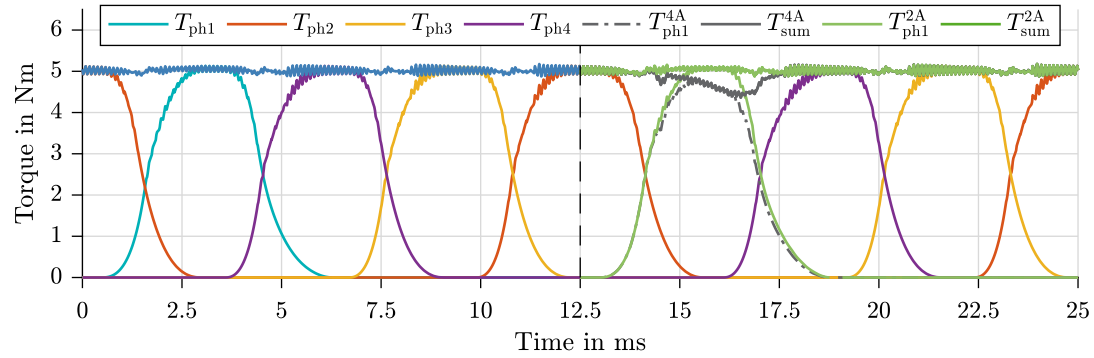

(a) Total torque and per phase torque

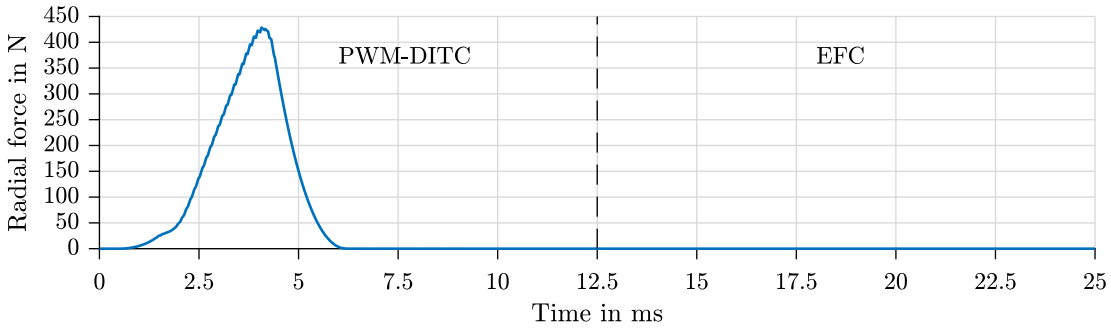

(b) Net radial force (UMP)

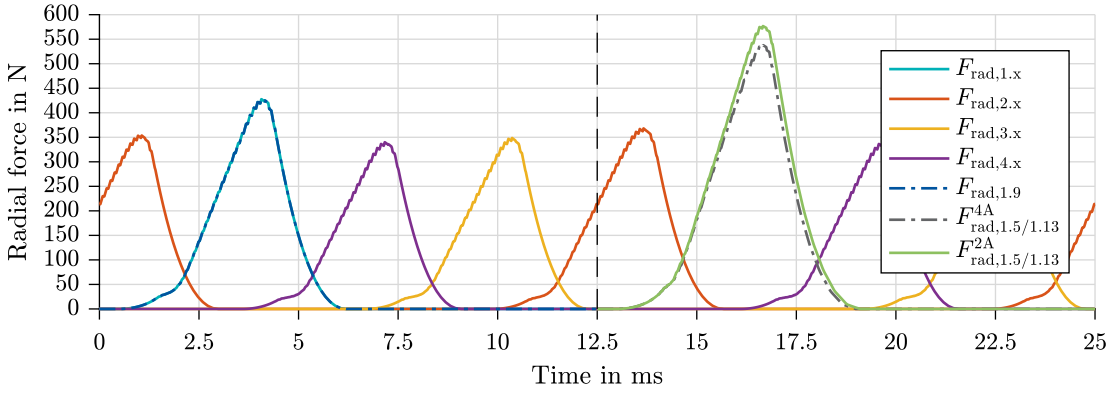

(c) Radial force per pole

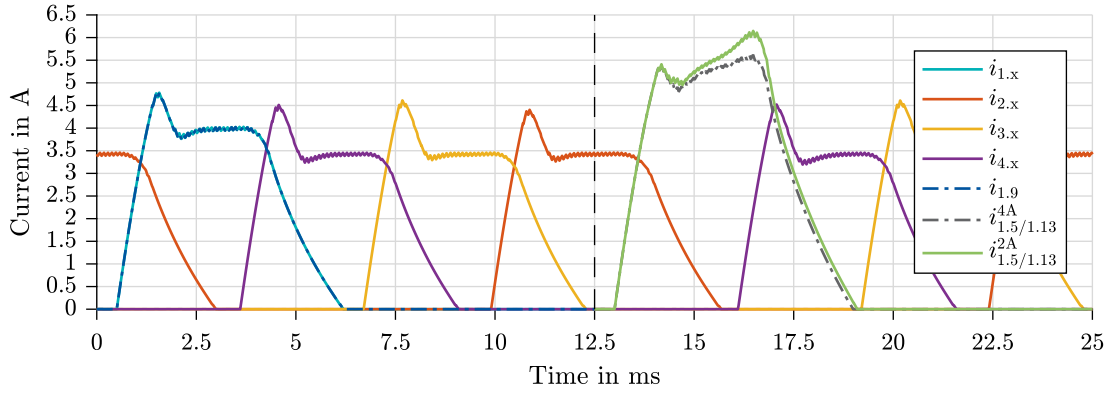

(d) Current per pole

Figure 5.5: SRM-16/12: Simulation results during single pole fault switching to EFC operation at 5 Nm and 400 rpm with 4polesA and 2polesA control models

uses the $T_{\mathrm{ph}}(\psi_{\mathrm{ph}},\theta_{\mathrm{el}})$ table for the 2polesA excitation and thereby, considering the change of flux distribution in the machine.

The increase in pole current of the remaining healthy poles 1.5 and 1.13 in the faulty phase (phase 1) is visible in figure 5.5d. Using the 4polesA table the RMS pole current increases from $i_{1,\mathrm{x}} = 2.19\,\mathrm{A}$ to $i^{4\mathrm{A}}_{1.5/1.13} = 2.84\,\mathrm{A}$, while with the correct 2polesA tables the current increases to $i^{2\mathrm{A}}_{1.5/1.13} = 2.98\,\mathrm{A}$. The healthy pole current of the faulty phase therefore, increases by 36 % resulting in an 85 % increase of the copper losses due to the change in current trajectory.

Table 5.1: Change in per pole RMS current and ohmic DC-losses when switching from DITC to EFC operating at 5 Nm and 400 rpm

Control method	Poles	$F_{\mathrm{r,ump}}$	$F_{\mathrm{r},i}$	ΔT_{pole}	i_{RMS}	Δi_{RMS}	ΔP_{Cu}
DITC no fault	4/4	$\sim 0\,\mathrm{N}$	340 N	100 %	1.98 A	100.0 %	100.0 %
DITC with fault	3/4	430 N	430 N	133 %	2.19 A	110.6 %	122.3 %
EFC 4A	2/4	$\sim 0\,\mathrm{N}$	540 N	200 %	2.84 A	143.4 %	205.7 %
EFC 2A	2/4	$\sim 0\,\mathrm{N}$	575 N	200 %	2.98 A	150.5 %	226.5 %

Table 5.1 displays the change in current and radial pole force $F_{\mathrm{r},i}$ during a single pole fault and when EFC is used. As the active poles decrease from four to only two in EFC the RMS current necessary increases to 150.5 % from the fault-free DITC operation. The corresponding copper loss increases to 226.5 %, which corresponds to the required increase in per pole torque of 200 %. The copper losses increase slightly more than is expected from the per pole torque production when using EFC. Therefore, considering the healthy state thermal loading of the machine, the RMS current and therefore, also the torque production per pole has to be limited to not only 50 %, but to 44 %. EFC is a viable option to reduce the UMP when operating the machine in partial load. To increase the torque operation area during fault, all three healthy poles of the faulty phase have to be used. In the next section a fault control strategy is introduced, which uses all healthy poles to maximize the output torque during fault condition.

5.3 Radial Force Minimization with Least Square

The challenge of UMP during fault operation in electrical machines can be formulated as a vector sum problem of all forces acting on the rotor. Thereby, the sum of radial forces, i.e. net radial force should be minimized, while the sum of tangential forces should add up to the reference torque necessary for the drive's operating point. This minimization problem and its effect on radial and tangential forces for different machine configurations and their thermal behavior is discussed in this section.

5.3.1 Theory and Control Scheme

The formulation of the vector sum problem is shown in equation (5.1) comprising of the linear equations to be solved using a least square algorithm [110]. Thereby, C ($[3 \times N_\mathrm{s}]$) represents the input matrix consisting of the estimated radial and tangential forces, d is the target vector, x is the solution vector. The lower and upper boundary conditions for the solution x are depicted by lb and ub, respectively. Thus, the matrix size and, therefore, the computational complexity depends on the SRM's number of stator teeth N_s.

$$\min_x \|Cx - d\|_2 \text{ for } lb \leq x \leq ub \tag{5.1}$$

The radial forces $F_{\mathrm{rad},i}$ of each stator tooth i are necessary by the control as in equation (5.5). The forces are determined from the estimated flux linkage ψ_{n+1} and rotor position θ_el by using the $F_\mathrm{rad}(\psi,\theta_\mathrm{el})$-LUT as shown in the control scheme in figure 5.10. The radial tooth forces are transformed from polar coordinates into a stator fixed cartesian coordinate system with equations (5.2) - (5.4).

$$F^\mathrm{X}_{\mathrm{rad},i,n+1} = F_{\mathrm{rad},i,n+1} \cdot \cos\varphi_i \tag{5.2}$$

$$F^\mathrm{Y}_{\mathrm{rad},i,n+1} = F_{\mathrm{rad},i,n+1} \cdot \sin\varphi_i \tag{5.3}$$

$$\varphi_i = (i-1)\frac{2\pi}{N_\mathrm{s}} \text{ for } i \in [1,\, N_\mathrm{s}] \tag{5.4}$$

In C the first two rows comprise of the radial tooth forces at time $t = n + 1$ separated in their x and y component $F^\mathrm{X}_{\mathrm{rad},i}$ and $F^\mathrm{Y}_{\mathrm{rad},i}$ respectively. The last row consists of the tangential forces produced by each pole. The tangential force too is obtained from the estimated flux linkage and rotor position and $F_\mathrm{tan}(\psi,\theta_\mathrm{el})$-LUT (or $T_\mathrm{ph}(\psi_\mathrm{ph},\theta_\mathrm{el})$-LUT), as also necessary for PWM-DITC.

The vector d ($[3 \times 1]$), shown in equation (5.6), defines the optimization target. The first two rows represent the net radial force in x and y direction respectively. The radial forces should be minimized, therefore, zero is chosen. The third row represents the tangential force reference $F_\mathrm{tan,ref}$ to be set. The tangential reference force is calculated from torque reference T^*_ref and air-gap radius r_ag as in equation (5.7).

$$C = \begin{pmatrix} F^{\mathrm{X}}_{\mathrm{rad},1,n+1} & F^{\mathrm{X}}_{\mathrm{rad},2,n+1} & \cdots & F^{\mathrm{X}}_{\mathrm{rad},\mathrm{N_s},n+1} \\ F^{\mathrm{Y}}_{\mathrm{rad},1,n+1} & F^{\mathrm{Y}}_{\mathrm{rad},2,n+1} & \cdots & F^{\mathrm{Y}}_{\mathrm{rad},\mathrm{N_s},n+1} \\ F_{\mathrm{tan},1,n+1} & F_{\mathrm{tan},2,n+1} & \cdots & F_{\mathrm{tan},\mathrm{N_s},n+1} \end{pmatrix} \tag{5.5}$$

$$d = \begin{pmatrix} 0 \\ 0 \\ F_{\mathrm{tan,ref}} \end{pmatrix} \tag{5.6}$$

$$F^{*}_{\mathrm{tan,ref}} = \frac{T^{*}_{\mathrm{ref}}}{r_{\mathrm{ag}}} \tag{5.7}$$

The algorithm generates a best fit vector x (5.8), which minimizes the sum of radial forces shown in equation (5.9). Furthermore, the x-vector solution tries to produce the desired reference torque as stated in equation (5.10).

$$x = \begin{pmatrix} x_1 \\ x_2 \\ \vdots \\ x_{\mathrm{N_s}} \end{pmatrix} \tag{5.8}$$

$$\sum_{i=1}^{N_{\mathrm{s}}} x_i F^{\mathrm{X}}_{\mathrm{rad},i,n+1} = 0 \quad \text{and} \quad \sum_{i=1}^{N_{\mathrm{s}}} x_i F^{\mathrm{Y}}_{\mathrm{rad},i,n+1} = 0 \tag{5.9}$$

$$\sum_{i=1}^{N_{\mathrm{s}}} x_i F_{\mathrm{tan},i,n+1} = F^{*}_{\mathrm{tan,ref}} \tag{5.10}$$

Similar to PWM-DITC where torque can only change at a certain rate during one switching period when minimum and maximum duty cycle is applied (see section 2.3.2), the radial tooth force too, can only change at a given rate. The least square algorithm adheres to this limited rate change by defining boundary conditions when finding the solution x. The boundaries are defined by the ratio of minimum and maximum radial force, which can be reached at $t = n + 2$ to the value of currently estimated radial force at $t = n + 1$ as in equation (5.11).

$$lb = \frac{F^{\min}_{\mathrm{rad},i,n+2}}{F_{\mathrm{rad},i,n+1}} \quad \text{and} \quad ub = \frac{F^{\max}_{\mathrm{rad},i,n+2}}{F_{\mathrm{rad},i,n+1}} \tag{5.11}$$

The matrix C consists of both radial and tangential forces. Therefore, the boundary conditions also have to be applicable to the tangential forces to be effective in the algorithm.

Boundary Condition 1: Linearization of Radial and Tangential Force

In the following the validity of the boundary conditions for both radial and tangential forces are presented. As both radial and tangential force characteristics are usually symmetrical around $\theta_{\mathrm{el}} = 180°$, the following results are limited to the rotor positions between $\theta_{\mathrm{el}} \in [0°, 180°]$. The boundary conditions are calculated for each sampling period during which the rotor position θ_{el} remains constant. Therefore, a linearization of the radial and tangential force along the flux linkage axis for an equal and constant rotor position is investigated. In figure 5.6 the change in radial and tangential force with respect to flux linkage at a constant rotor position $\theta_{\mathrm{el}} = 72°$ is displayed. The non-linear relationship of both forces is clearly visible. However, the calculation of boundary conditions is confined to a limited flux linkage range depending on the volt-second area, which can be applied during one switching period, i.e. the switching frequency the drive is operated at. In the shown case, SRM-16/12 is operated at $f_{\mathrm{PWM}} = 10\,\mathrm{kHz}$ and a dc-link voltage of $v_{\mathrm{dc}} = 60\,\mathrm{V}$ results in a maximum flux linkage change $\Delta\psi = 0.006\,\mathrm{Vs}$.

$$\begin{aligned} v_{\mathrm{dc}} &= 60\,\mathrm{V} \\ T_s &= 0.1\,\mathrm{ms} \\ \Delta \cdot \psi = v_{\mathrm{dc}} \cdot T_s &= 0.006\,\mathrm{Vs} \end{aligned}$$

As an example, an arbitrary flux linkage $\psi_{\mathrm{n+1}} = 0.3\,\mathrm{Vs}$ is chosen and displayed as a close-up in figure 5.6 (right). For this operating point the boundary values are given in equation (5.12) with a calculated error between the radial and tangential force linearization of $\epsilon_{\mathrm{ub}} = 1.34\,\%$.

$$\begin{aligned} ub_{\mathrm{tan}} &= \frac{F^{\mathrm{max}}_{\mathrm{tan},n+2}}{F_{\mathrm{tan},n+1}} = \frac{49.2\,\mathrm{N}}{47.1\,\mathrm{N}} = 1.044 \\ ub_{\mathrm{rad}} &= \frac{F^{\mathrm{max}}_{\mathrm{rad},n+2}}{F_{\mathrm{rad},n+1}} = \frac{163.2\,\mathrm{N}}{158.4\,\mathrm{N}} = 1.030 \qquad (5.12) \\ \epsilon_{\mathrm{ub}} &= 1 - \frac{ub_{\mathrm{rad}}}{ub_{\mathrm{tan}}} = 1.34\,\% \qquad (5.13) \end{aligned}$$

The error ϵ_{ub} is calculated for all four SRMs and the results are presented in figure 5.7.

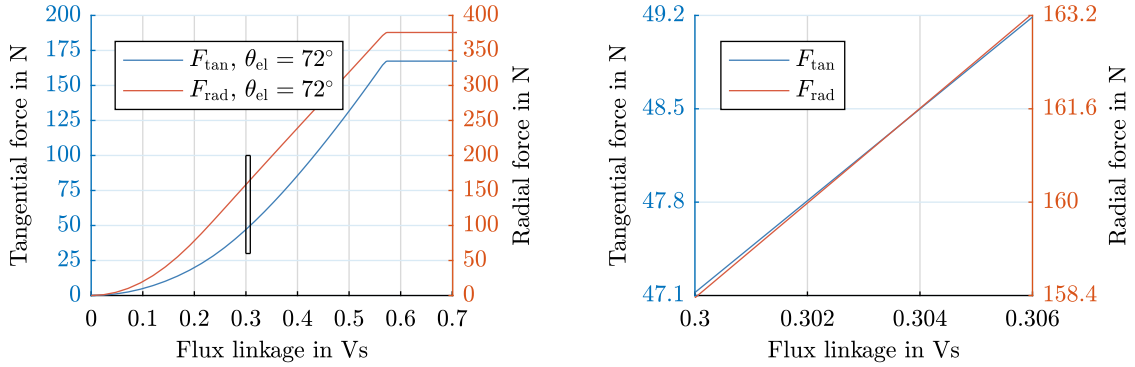

Figure 5.6: Linearization of $F_{rad}(\psi,\theta_{el})$ and $F_{\tan}(\psi,\theta_{el})$ characteristics of SRM-16/12 at $\theta_{el} = 72°$, shown over the entire flux linkage range (left) and zoomed in at $\psi = 0.3\,\mathrm{Vs}$ (right)

The relatively high error visible for SRM-18/12 suggests that this drive is not as suitable to operate with radial force minimization control (RFMC) at $f_{PWM} = 20\,\mathrm{kHz}$. In figure 4.1 the torque ripple simulation results for fault-free PWM-DITC already show that only at $f_{PWM} = 40\,\mathrm{kHz}$ the torque ripple reduces to below 10 %. Therefore, if operation with RFMC is desired, SRM-18/12 has to be operated at higher switching frequencies as is visible in figure 5.8b. This figure displays the frequency dependency of the maximum error ϵ_{ub}. The results for the other three machines are presented in figure 5.8a.

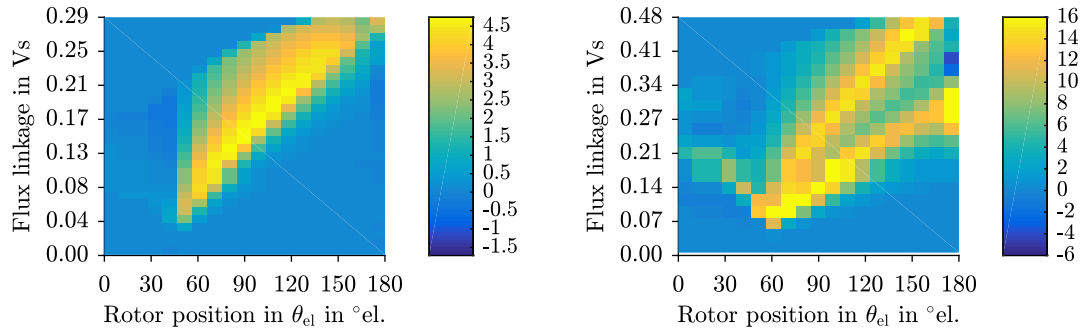

(a) SRM-12/8: $f_{PWM} = 10\,\mathrm{kHz}$

(b) SRM-18/12: $f_{PWM} = 20\,\mathrm{kHz}$

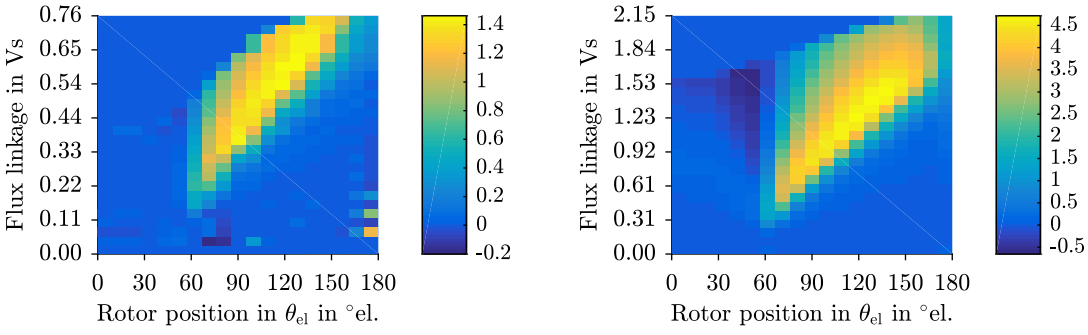

(c) SRM-16/12: $f_{PWM} = 10\,\mathrm{kHz}$

(d) SRM-20/16: $f_{PWM} = 10\,\mathrm{kHz}$

Figure 5.7: Boundary error ϵ_{ub} from the ratio of ${}^{ub_{rad}}/_{ub_{\tan}}$ in percent

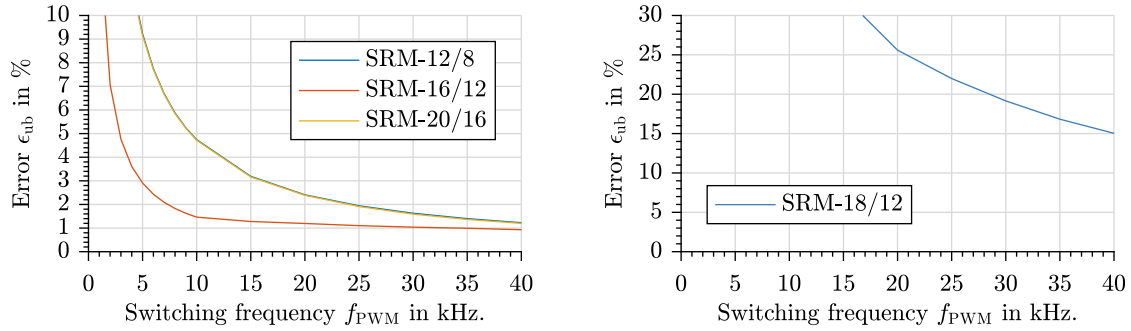

(a) SRM-12/8, SRM-16/12, SRM-20/16 (b) SRM-18/12

Figure 5.8: Boundary error ϵ_{ub} in percent versus switching frequency

A generalization of the defined upper and lower boundaries as in equation (5.11) is valid for the radial and tangential forces. As long as the flux linkage stays within the given boundaries $\psi \in [\psi_{n+2}^{min}, \psi_{n+2}^{max}]$, a linear relative relation can be assumed and thus, be formulated as a similarity statement as in equation (5.14).

$$\left.\frac{\Delta F_{rad}}{F_{rad}}\right|_{\Delta\psi,\ \theta_{el}=const.} \approx \left.\frac{\Delta F_{tan}}{F_{tan}}\right|_{\Delta\psi,\ \theta_{el}=const.} \implies \begin{array}{l} F_{rad} = m_1\psi \\ F_{tan} = m_2\psi \end{array} \text{ for } \psi \in [\psi_{n+2}^{min}, \psi_{n+2}^{max}] \tag{5.14}$$

Limits of Linearization: Masking at $\theta_{el} = 180°$

Near the aligned rotor position $\theta_{el} = 180°$, the introduced boundary condition stated in equation (5.14) is not sufficient anymore. Near the aligned rotor position the values for torque (tangential force F_{tan}) are near zero, while the radial force values are at their maximum. The near zero value causes an extreme of the ratio, which is not usable. Therefore, the ratio between radial force and torque necessary for S-RFMC is limited to values lower than 180° by adding a masking. At rotor positions between $\theta_{el} \in [178°, 182°]$ the ratio values from $\theta_{el} = 178°$ is used.

Boundary Condition 2: Limiting Maximum Pole Current

In regular PWM-DITC the inverter peak current and thus, the maximum possible flux linkage and torque for the next period is limited by i_{inv}^{max} as displayed in figure 5.10. The control algorithm predicts machine torque values, while remaining within the physical temperature boundary of the inverter. The machine temperature itself usually is not directly limited by the peak current i_{inv}^{max}, but rather by the losses caused during operation.

At lower speeds, where PWM-DITC and RFMC are active, the RMS current density $J_{\mathrm{RMS}}^{\mathrm{max}}$ over time predominantly determines the machine's temperature and limits machine operation.

Maximum current density $J_{\mathrm{RMS}}^{\mathrm{max}}$ is determined by the cooling and winding diameter used, and the current waveform (losses) during operation. Therefore, the machine design and intended control strategy determine the maximum operating temperature and maximum RMS current rating of a machine. For fault control this is especially visible for the machines, which have been designed with HCC in mind. The current trajectory of HCC and RFMC differ considerably, resulting in a higher current density during fault control. However, the current trajectory of PWM-DITC and RFMC differ only marginally, resulting in a similar thermal loading of the machine. To keep the thermal loading on a machine within its bounds, the RMS current density during fault control should be similar to the current density the machine was designed for.

In RFMC, the maximum allowed pole current $i_{\mathrm{RFMC}}^{\mathrm{max}}$ changes how the forces are distributed amongst all poles and, therefore, also each current trajectory as is shown for the faulty phase (phase 1) of SRM-16/12 in figure 5.9. It is visible in figure 5.9a that the control maximizes current of the two opposite healthy poles 1.5 and 1.13 of the faulty phase to the given current limit $i_{\mathrm{pl}}^{\mathrm{max}}$. This produces the maximum torque while not creating additional unbalanced radial forces. The corresponding current change in pole 1.9, which predominantly creates the unbalanced critical force is shown in figure 5.9b.

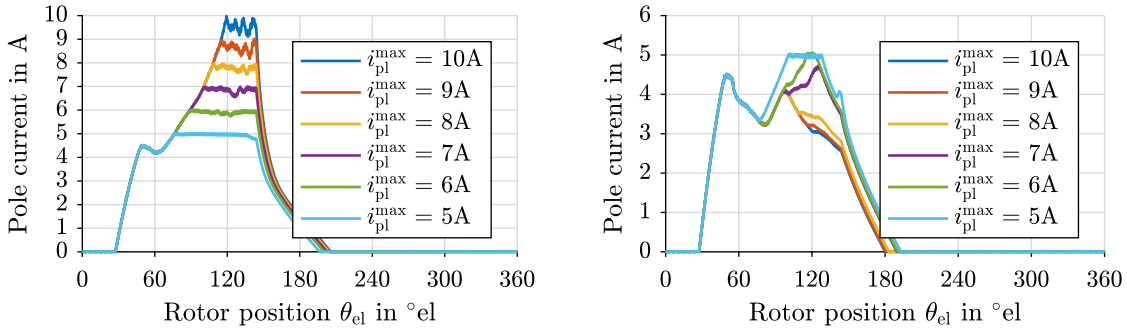

(a) Current trajectories of pole 1.5 and 1.13

(b) Current trajectory of pole 1.9

Figure 5.9: SRM-16/12: Current trajectories for different pole current limits $i_{\mathrm{RFMC}}^{\mathrm{max}}$ operating at 7 Nm and 400 rpm

As the pole current limit $i_{\mathrm{RFMC}}^{\mathrm{max}}$ is decreased from 10 A to 5 A so does the current peak in the healthy poles 1.5 and 1.13, which in turn reduces the RMS current density J_{RMS} of these poles. At 5 A the current trajectory again is similar to the current trajectory seen when operating SRM-16/12 in DITC control (see figure 2.10a). Therefore, the thermal stress of the healthy poles during the fault tolerant control is reduced by limiting the peak current.

In contrast to poles 1.5 and 1.13 the peak current value of pole 1.9 changes in the opposite

direction for rotor positions $\theta_{\mathrm{el}} > 100°$. The decrease of current limit reduces the amount of torque to be produced by poles 1.5 and 1.13, which has to be compensated by the critical pole 1.9, until at $i^{\max}_{\mathrm{RFMC}} = 5\,\mathrm{A}$ the critical pole too reaches its pole current limit. As an initial peak current limit $i^{\max}_{\mathrm{RFMC}}$, a peak current limit similar to $i^{\max}_{\mathrm{inv}}$ found in PWM-DITC should be used. For nominal DITC operation at $T = 9.5\,\mathrm{Nm}$ and $n = 400\,\mathrm{rpm}$ of SRM-16/12, a peak current $i^{\max}_{\mathrm{inv}} = 5\,\mathrm{A}$ is required, while for RFMC $i^{\max}_{\mathrm{RFMC}} = 5.2\,\mathrm{A}$ is necessary. A further benefit of the current limit, while using the least squares algorithm, is a more symmetrical current density distribution across the three healthy poles of phase 1 as is discussed in detail in section 5.3.3.

Combining DITC and RFMC

The schematic overview of the control used for fault tolerant control (FTC) based on least squares is displayed in figure 5.10. A combination of common PWM-DITC and the radial force control RFMC is suggested. Thereby, when a fault occurs the control switches to RFMC at $\theta^{\mathrm{RFMC}}_{\mathrm{on}}$ during the faulty phase conduction. Once the faulty phase has passed, at $\theta^{\mathrm{RFMC}}_{\mathrm{off}}$, the control switches back to direct instantaneous torque control.

As the control is implemented as a PWM-based control, the structure for torque and radial force control is similar. The estimated flux linkage ψ_{n+2} and rotor position θ_{n+2} is

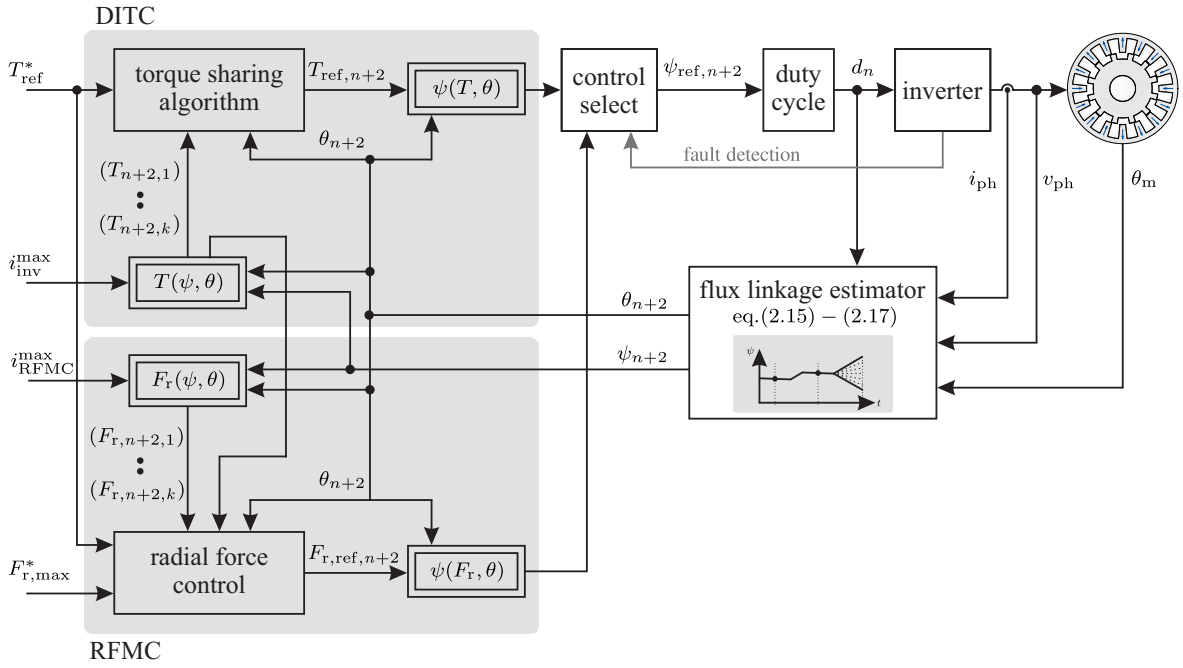

Figure 5.10: Schematic overview of fault tolerant control structure combining direct instantaneous torque control (DITC) and radial force minimization control (RFMC)

used in the $F_{\mathrm{rad}}(\psi,\theta_{\mathrm{el}})$-LUT, representing the radial force characteristics of the machine, to determine the present unbalanced pole force during fault condition. Following the radial force control algorithm the force reference for each pole $F_{\mathrm{r,ref},n+2}$ is passed to the flux linkage allocation block. This is either implemented as a $\psi(F_{\mathrm{r}},\theta_{\mathrm{el}})$-LUT or analogous to the previously presented samples-based flux linkage allocation, before calculating each pole's duty cycle for the distributed inverter.

5.3.2 Simulative Investigation

The predominant goal of RFMC is to reduce the UMP during a single pole fault. Therefore, in the following simulation results the first half shows the machine control with only PWM-DITC, while in the second half the control uses a combination of PWM-DITC and RFMC.

In figure 5.11 the simulation result for SRM-16/12 operating at 5 Nm and 400 rpm is shown. The torque can be produced continuously for both control types, however, the net radial force in figure 5.11b shows the difference in UMP. The critical pole F_9 produces around 500 N radial pole force, which has to be compensated. RFMC reduces this force to about 45 N. The force compensation is achieved by individual control of the poles as seen for the forces in figure 5.11c and pole currents in figure 5.11d. RFMC causes the poles of the preceding phase (phase 2) to be excited asymmetrically. Especially, poles 2.2 and 2.14 are excited strongly compared to poles 2.6 and 2.10.

The least square optimization causes opposite poles 1.5 and 1.13 of phase 1 to be excited symmetrically and more strongly compared to pole 1.9, thus producing the majority of torque. During RFMC the radial force F_9 is reduced from 500 N during PWM-DITC to around 320 N resulting in the maximum of critical force, which is compensated by the preceding phase (phase 2). The force compensation furthermore, causes the preceding phase to be excited longer compared to common PWM-DITC ($\theta_{\mathrm{el}} > 180°$) resulting in negative torque between $15.6\,\mathrm{ms} < t < 18.7\,\mathrm{ms}$. The negative torque in figure 5.11a is in turn compensated by the faulty phase (phase 1) and by the phase following the faulty phase (phase 4). This results in a higher overlap of the current waveforms and an increase in thermal strain also for the following phase. The ramifications regarding the thermal strain on the machine is presented in section 5.3.3. In figure 5.11b two remaining peaks can be observed in the UMP. The first net radial force peak is limited by the turn-on angle $\theta_{\mathrm{on}}^{\mathrm{RFMC}}$, where the control changes from PWM-DITC to RFMC ($t = 14.6\,\mathrm{ms}$). At this point the control reduces the UMP to zero. As is explained in more detail in the next section, to minimize the thermal loading on the machine during RFMC the control switches back to PWM-DITC as soon as possible. Once the radial forces are not directly controlled anymore ($t = 17.1\,\mathrm{ms}$) a residual force peak occurs. This is due to the pole currents of the preceding phase (2.2 and 2.14) and pole 1.9 being demagnetized, causing the pole forces not to be identical anymore and thus, resulting in a small force misalignment and UMP.

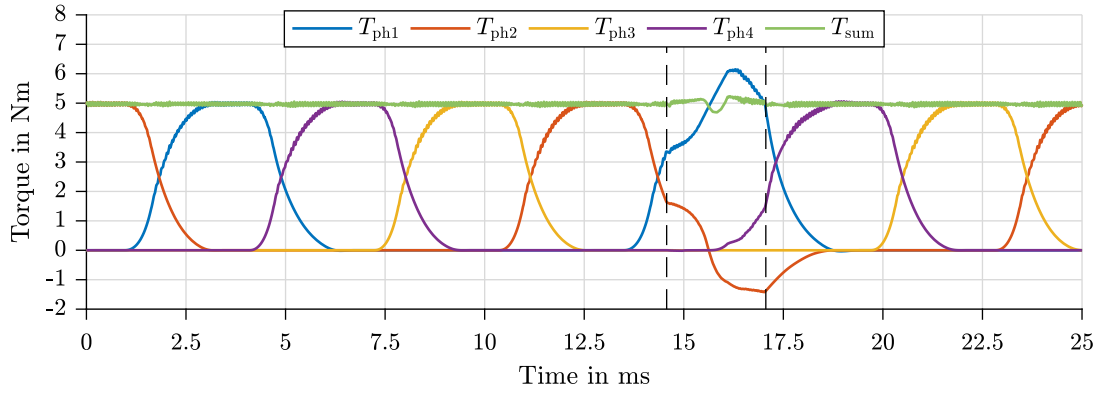

(a) Total torque and per phase torque

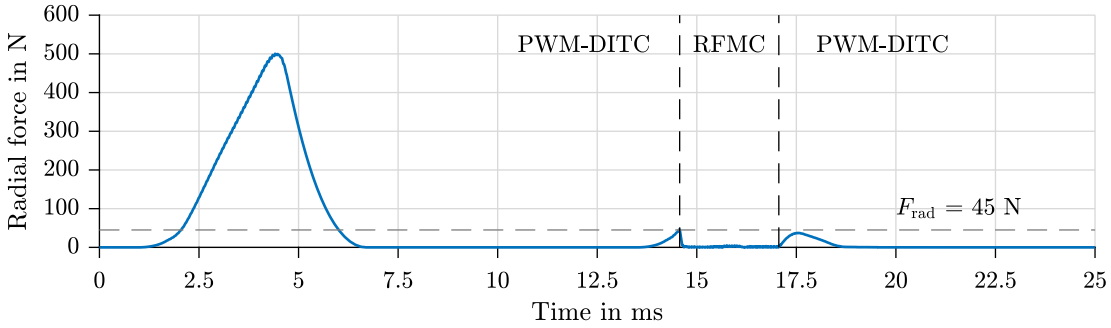

(b) Net radial force (UMP)

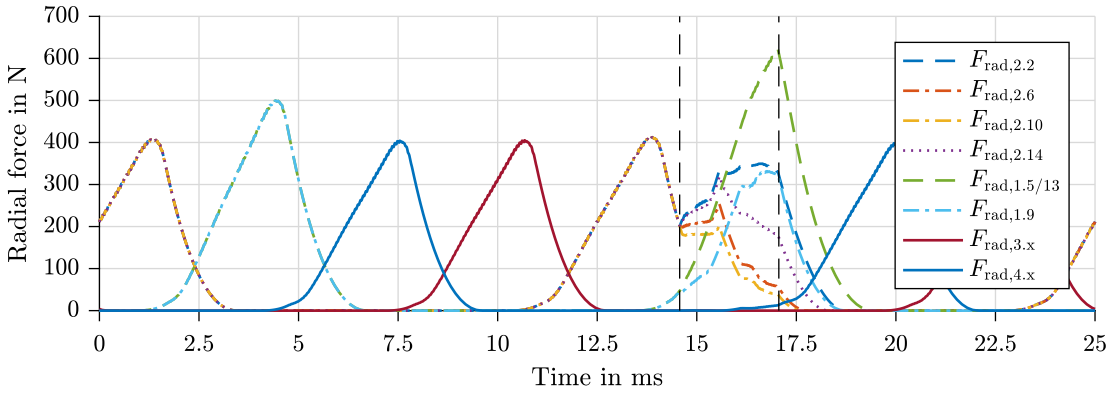

(c) Radial force per pole

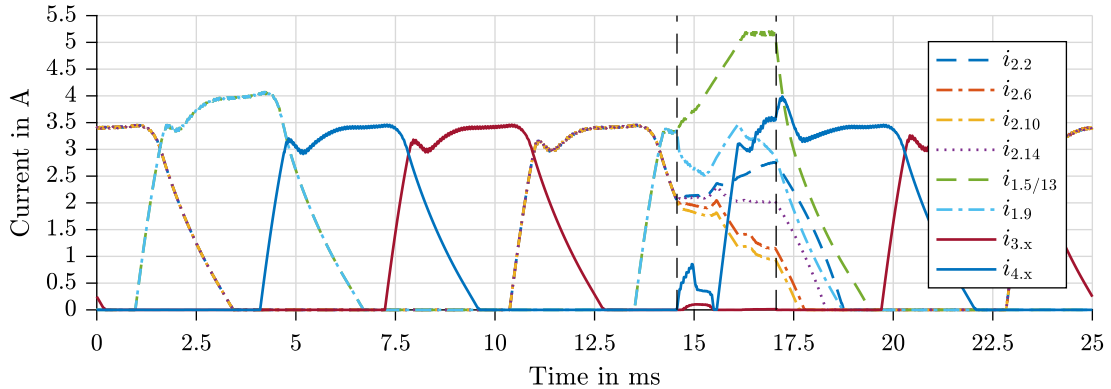

(d) Current per pole

Figure 5.11: SRM-16/12: Simulation results with single pole fault during PWM-DITC and RFMC operation at 5 Nm and 400 rpm

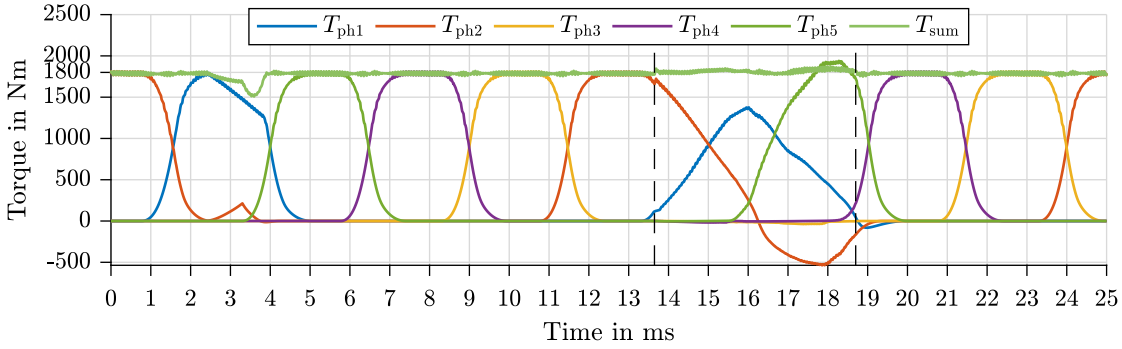

(a) Total torque and per phase torque

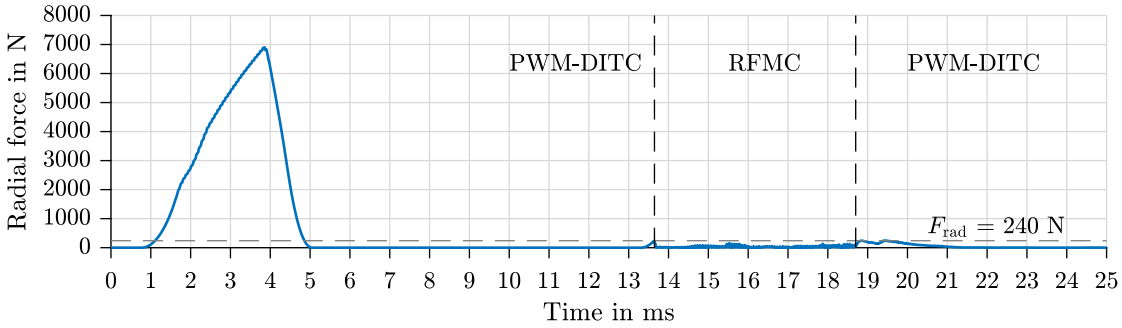

(b) Net radial force (UMP)

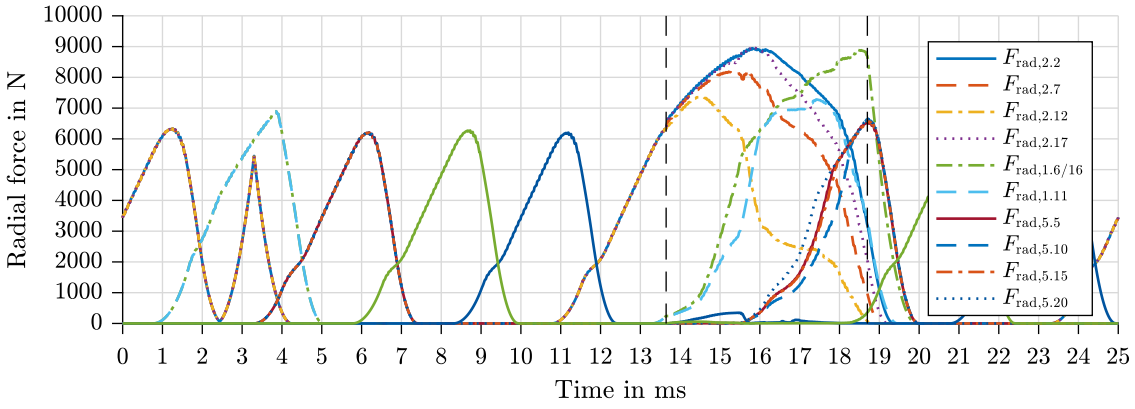

(c) Radial force per pole

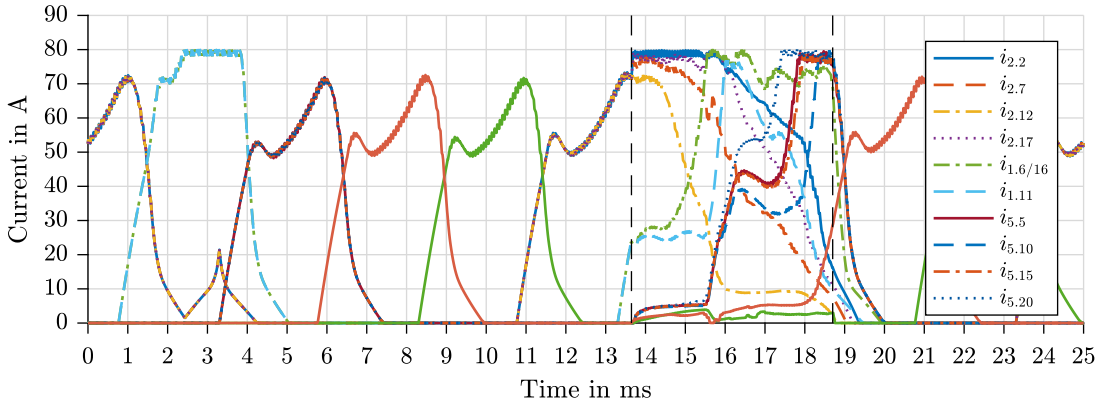

(d) Current per pole

Figure 5.12: SRM-20/16: Simulation results with single pole fault during PWM-DITC and RFMC operation at 1800 Nm and 300 rpm

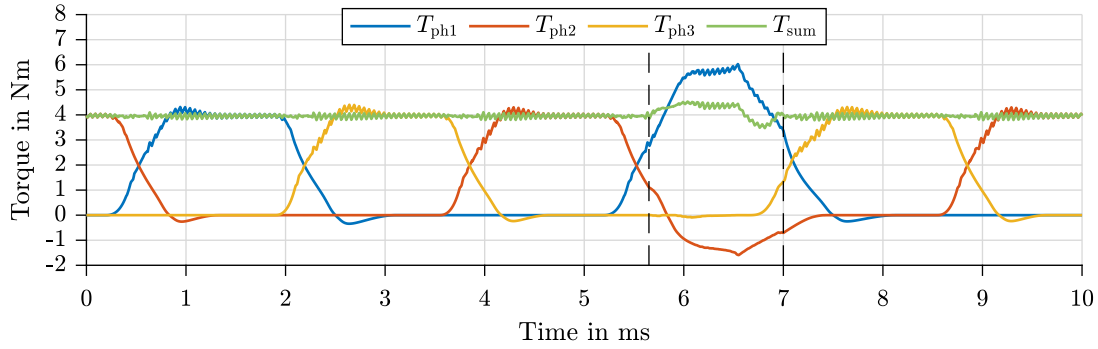

(a) Total torque and per phase torque

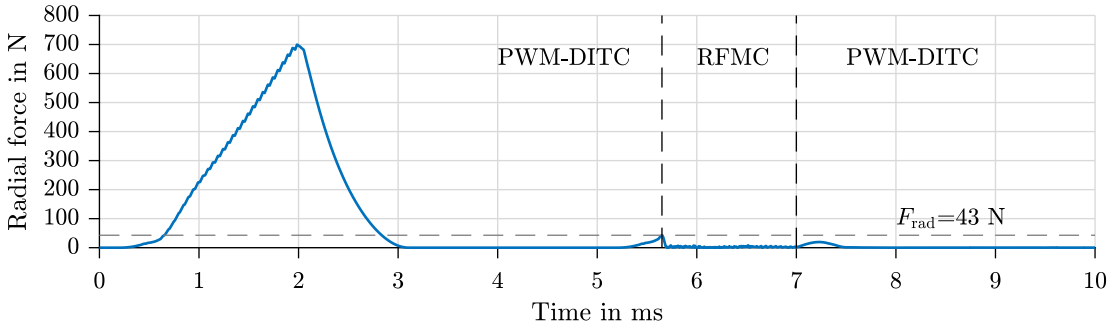

(b) Net radial force (UMP)

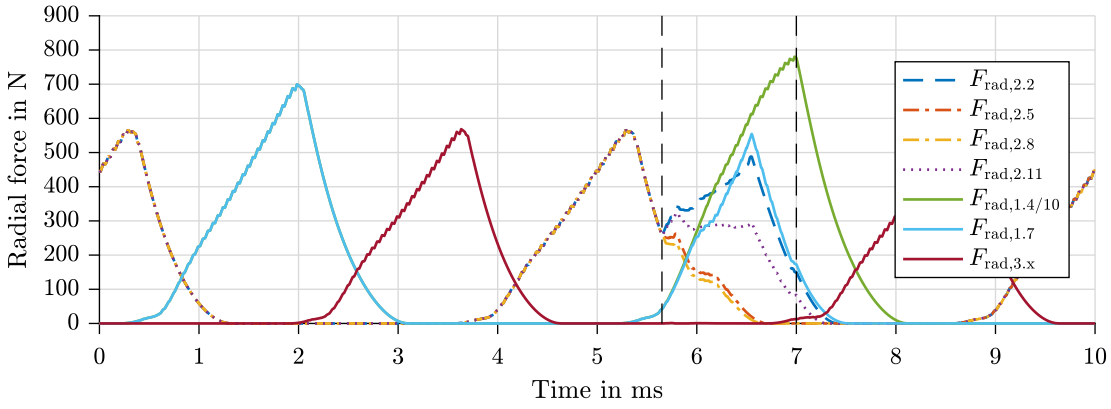

(c) Radial force per pole

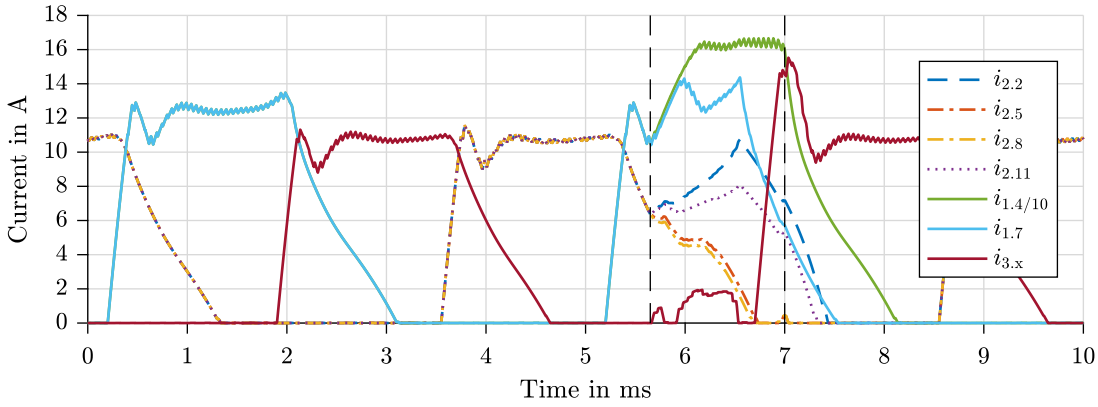

(d) Current per pole

Figure 5.13: SRM-12/8: Simulation results with single pole fault during PWM-DITC and RFMC operation at 4 Nm and 1500 rpm

In figure 5.12 a simulation result of SRM-20/16 operating at 1800 Nm and 300 rpm, and in figure 5.13 a result for SRM-12/8 operating at 4 Nm and 1500 rpm is shown.

For SRM-20/16 it is noticeable that in single pole fault PWM-DITC is not able to produce the nominal torque with the inverter pole current limit of $i_{\mathrm{inv}}^{\mathrm{max}} = 80\,\mathrm{A}$ and its remaining three healthy poles. During RFMC nominal torque can be produced while reducing the UMP from 7000 N to around 240 N (figure 5.12b). The healthy poles of the faulty phase (poles 1.6, 1.11 and 1.16) are nearly completely excited to the given inverter current limit of 80 A the entire conduction period (figure 5.12d). Even though phase 1 is maximally excited, the phase torque T_{ph1} produced is much lower compared to the other phases. The missing torque causes a torque dip during PWM-DITC operation, but can be compensated during RFMC. As SRM-20/16 is a five phase machine a large phase overlap is present. The benefit of such an overlap is clearly visible in figure 5.12a where the following phase (phase 5) can completely compensate the missing torque of the faulty phase (phase 1) and the negative torque being produced by the preceding phase (phase 2). In the five phase machine the unbalanced radial force is compensated by the preceding (phase 2) and the following phase (phase 5). However, it is noticeable that, as with the other two SRMs, the majority of UMP is compensated by the preceding phase (phase 2).

The least squares algorithm causes a late magnetization of the healthy poles of phase 1 in SRM-20/16 resulting in a low torque production of phase 1 and therefore, causing a long conduction period and high current density for the poles of the preceding phase (phase 2). The least squares does not naturally prioritize the healthy poles of the faulty phase. In the later introduced simplified radial force minimization control (section 5.4) the prioritization, as in DITC with multi-phase torque sharing, is used resulting in the use of all healthy poles of the faulty phase to produce torque. This reduces the additional thermal stress on the preceding phase, which can be extensive as seen for SRM-20/16.

In contrast SRM-12/8 has three phases, which results in only a small overlap between phases. The negative torque caused by phase 2, therefore, has to solely be compensated by the faulty phase (phase 1). In contrast to the four phase SRM-16/12 and five phase SRM-20/16, the following phase (phase 3) in three phase machines is not able to compensate the faulty phase's missing torque production. This is a considerable drawback to the fault tolerant capability of three phase machines resulting in only a small partial load region where UMP can be compensated while producing a constant torque. In three phase machines during single pole fault a torque dip is present already at an early stage due to the limited phase overlap. In case of SRM-12/8 the torque dip is already present at 4 Nm (61 % of nominal torque T_{nom}).

The results of the different machine configurations show that RFMC with least square optimization is capable of considerably reducing the UMP largely independent of the machine configuration.

5.3.3 Operating Limits and Thermal Influence

The operating range during fault is limited in each machine by the maximum possible radial force compensation, while still being able to produce torque. As has been stated in the previous section, the preceding phase (phase 2) compensates the radial force, i.e. reduces the UMP. At higher torque levels (SRM-16/12: $T^*_{\mathrm{ref}} > 6.5\,\mathrm{Nm}$), the preceding phase (phase 2) has to compensate higher radial forces and, therefore, is still active at rotor position values $\theta_{\mathrm{el}} > 180°$ resulting in negative torque (figure 5.11a). This negative torque has to be compensated by the faulty phase. Thus, there is a limit up to what value the radial force and torque can be controlled without introducing a torque dip.

For SRM-16/12 simulation results of various reference torque values and speeds are shown in figure 5.14. For 5 Nm and 6.5 Nm no relevant torque dip can be seen, independently from the operation speed. However, at higher reference torque values ($T^*_{\mathrm{ref}} = 8\,\mathrm{Nm}$ and

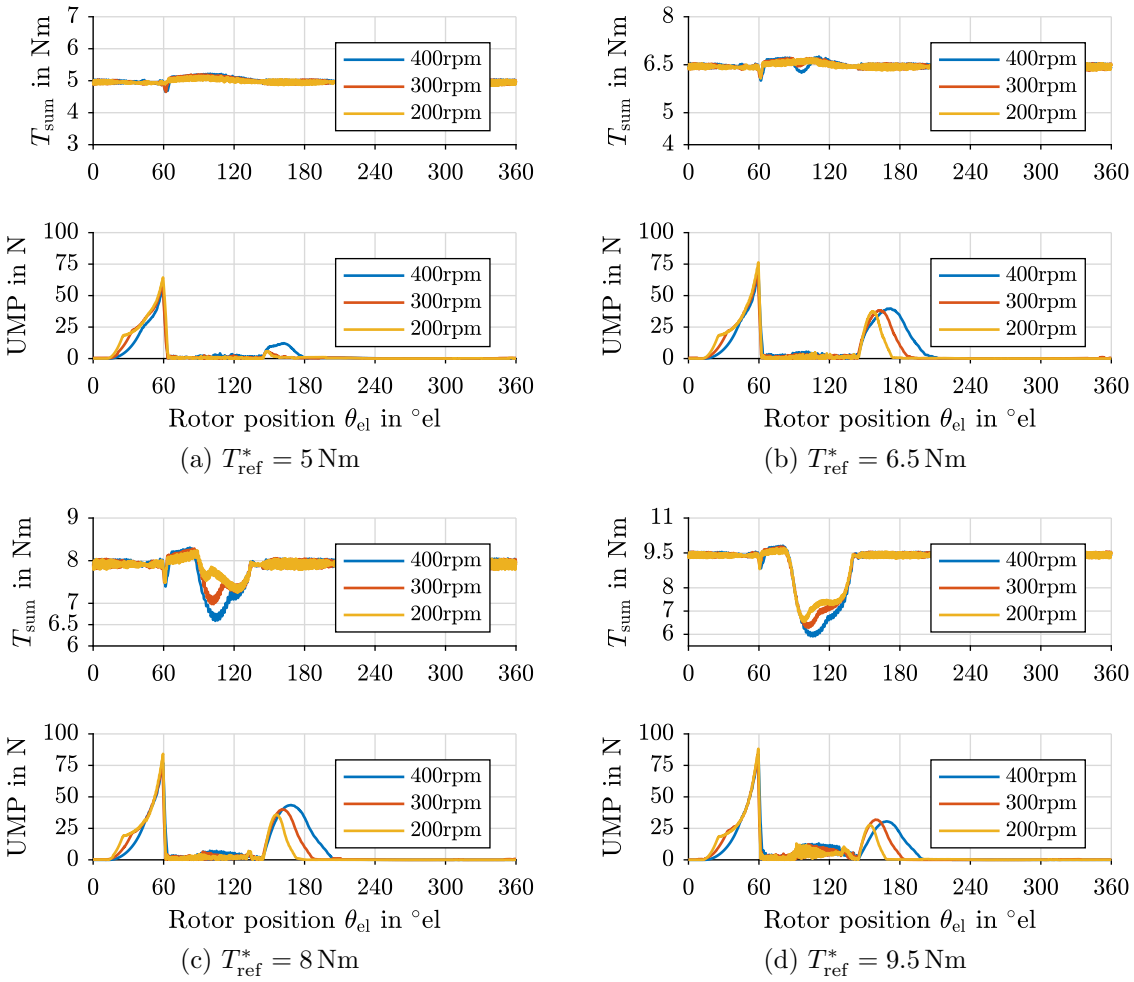

Figure 5.14: SRM-16/12: Simulation results of the torque dip and UMP occurring during RFMC at various operating points

$T^*_{\text{ref}} = 9.5\,\text{Nm}$), a torque dip appears, which increases in amplitude along with the reference torque value. Furthermore, an influence of speed starts to be clearly visible. At higher speeds larger torque dips are present, while generally also the UMP increases. At higher speeds, the current causing the negative torque and, thus, the torque dip is only demagnetized at a slower rate. This slower rate is caused from an increase in back-EMF, which increases the time of the negative torque production, and results in a larger torque dip. Similar, the smaller current gradient when RFMC switches back to PWM-DITC causes a longer period of misalignment between the radial forces ($F_{1.5/13}$, $F_{1.9}$, $F_{2.2}$ and $F_{2.14}$) resulting in a longer and higher UMP.

In figure 5.15 the average torque and torque dip in percent versus the per unit torque are displayed. Thus, during single pole fault the average torque of SRM-16/12 at 400 rpm decreases to around 95.5 % of the nominal torque (9.07 Nm), while the instantaneous torque dip increases to around 30 % − 37 % of nominal torque. These results represent a theoretical achievable operating region without considering the actual thermal loading on the machine. The achievable average torque of a three phase machine will be lower than the presented result due to lower phase overlap and therefore, a lower rate of torque compensation from the faulty phase, while for a five phase machine with its phase overlap there will be no dip at all, as is seen for SRM-20/16 using RFMC in figure 5.12.

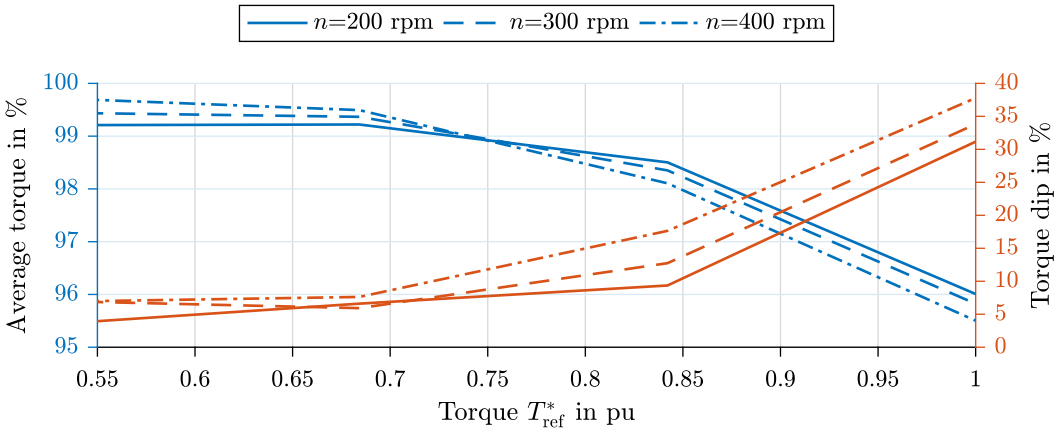

Figure 5.15: SRM-16/12: Average torque reduction and increase in torque dip versus increasing reference torque while using RFMC

As the previous section has shown, RFMC causes higher current peaks and prolonged conduction periods for the preceding, faulty and following phases. Consequently, higher RMS current densities and, thus, operating temperatures are observed.

A machine's thermal operating limit is defined by its design, i.e. through the choice of insulation material (thermal classification) and the amount of losses, which can be dissipated by the cooling method used. The temperature rise is directly proportional to the losses occurring during operation. Copper (ohmic) losses can directly be linked to the RMS current density in the windings, while the iron losses are dependent on the actual current trajectory. The main loss component influenced by RFMC compared to

PWM-DITC are the copper loss components. Thus, the thermal limit of the algorithm is defined by using the RMS current density. Similar to PWM-DITC, RFMC is used at low operational speeds, which reduces the influence iron loss compared to copper loss has on the machine temperature.

In figure 5.16 the pole current density distribution of SRM-16/12 at nominal operation and RFMC (9.5 Nm, 400 rpm) is displayed. In a four phase machine, phase 3 does not take part in force compensation of phase 1, resulting in the DITC current trajectory and, thus, design current density $J_{\mathrm{RMS}}^{\mathrm{max}} = 6.5\,\mathrm{A/mm^2}$. During fault-free DITC all poles of all four phases would have the same current density $J_{\mathrm{RMS}}^{\mathrm{max}} = 6.5\,\mathrm{A/mm^2}$ as phase 3 in figure 5.16. The increase in current density of the individual poles due to radial force compensation is clearly visible. Especially, for the preceding phase (phase 2) pole 2.2 and 2.14 the current density increases from $6.5\,\mathrm{A/mm^2}$ to $9.28\,\mathrm{A/mm^2}$ and $8.51\,\mathrm{A/mm^2}$ respectively. The remaining two poles of phase 2 increase to around $7.5\,\mathrm{A/mm^2}$. This increase results from the prolonged conduction period of the preceding phase into the phase 1 conduction region to compensate the UMP. The standard RFMC algorithm thus, considerably increases the thermal loading, especially causing a hot-spot winding temperature in pole 2.2.

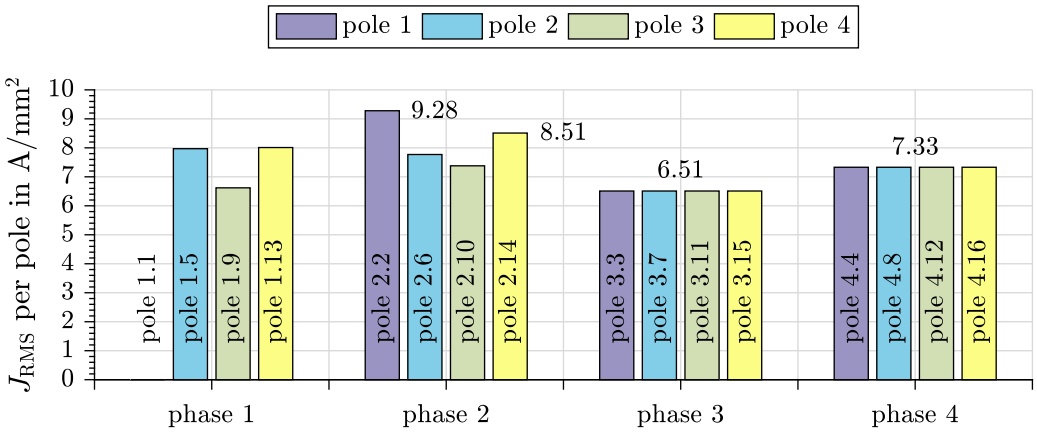

Figure 5.16: SRM-16/12: Pole RMS current densities during RFMC operating at 9.5 Nm and 400 rpm (all values shown in table 5.2)

The thermal loading of the machine can be reduced by redistributing the pole current density more equally by optimizing the angles, when the control switches between PWM-DITC and RFMC.

In figure 5.17 net radial force is shown for different torque and speed values within the DITC operation region. The higher the allowed UMP, the later the control can switch from torque control (DITC) to radial force control (RFMC). It is recognizable that the turn-on angle $\theta_{\mathrm{on}}^{\mathrm{RFMC}}$ is largely independent of the operating point for this machine. Generally, the highest flux linkage value, which results from the highest regarded reference torque (9.5 Nm) causes the largest radial force at the earliest rotor position. Therefore, $\theta_{\mathrm{on}}^{\mathrm{RFMC}}$ is defined by the maximal acceptable net radial force $F_{\mathrm{r,max}}$, which can directly be determined from the SRM's radial force characteristic $F_{\mathrm{rad}}(\psi,\theta_{\mathrm{el}})$ and the magnetization

of the critical pole. In figure 5.17 an exemplary acceptable net radial force of 100 N is taken, which results in a turn-on angle $\theta_{\text{on}}^{\text{RFMC}}$ of 62° for SRM-16/12.

The turn-off angle $\theta_{\text{off}}^{\text{RFMC}}$ when to switch back to PWM-DITC, is not only dependent on the faulty phase magnetization, but on the interaction of all active poles during UMP compensation. SRM-16/12 is simulated for various operating points and the resulting UMP is shown in figure 5.18. Thereby, the minimum turn-off angle $\theta_{\text{off}}^{\text{RFMC}}$ is again defined by the net radial force of 100 N. From the results it is determined that the highest torque value at the lowest operational speed determines the highest turn-off angle valid for all operation points and the given $F_{\text{r,max}}$ limit of 100 N. Therefore, $\theta_{\text{off}}^{\text{RFMC}} = 139.4°$ is chosen for the thermal investigation as it is valid for all DITC operation speed and torque values.

In figure 5.19 the RMS pole current densities of SRM-16/12 determined for $\theta_{\text{on}}^{\text{RFMC}}$ between

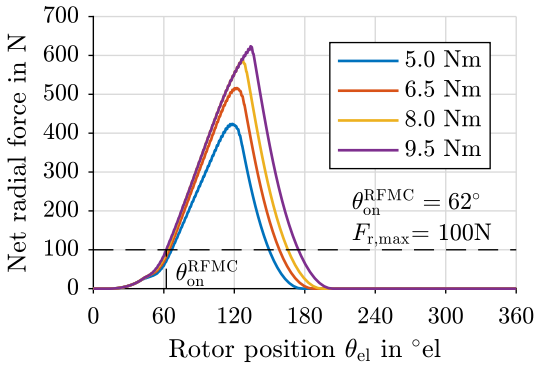

(a) Net radial force for different reference torque values at 400 rpm

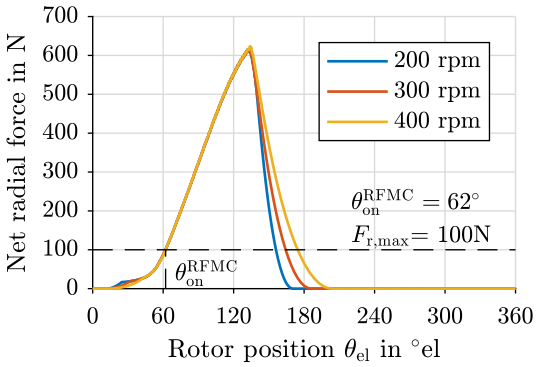

(b) Net radial force for different operating speeds at $T_{\text{ref}}^{*} = 9.5$ Nm

Figure 5.17: SRM-16/12: Net radial force (UMP) at different torque and speed values

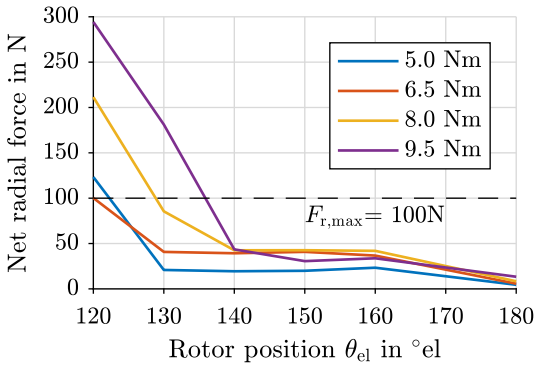

(a) Net radial force for different reference torque values at 400 rpm

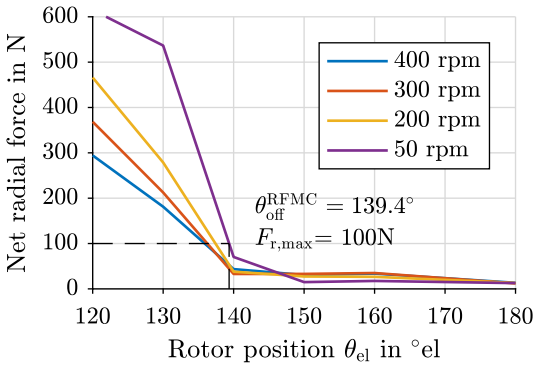

(b) Net radial force for different operating speeds at $T_{\text{ref}}^{*} = 9.5$ Nm

Figure 5.18: SRM-16/12: Net radial force peak (UMP) for different torque and speed values

[40°,62°] and $\theta_{\text{off}}^{\text{RFMC}}$ between [139.4°,180°] are shown. The minimum values are shown in red. In figure 5.19a the values for poles 1.5 and 1.13 and in figure 5.19b the values for the critical pole 1.9 are shown. The pole values for the preceding phase (phase 2) are displayed in figure 5.19c, figure 5.19d, figure 5.19e and figure 5.19f, while for the following phase (phase 4) are given in figure 5.19g. As the stationary operating temperature is minimized also during fault condition, the average RMS current density of all poles are given in figure 5.19h. From the results it can be seen that the current density decreases for all the poles when the turn-off angle $\theta_{\text{off}}^{\text{RFMC}}$ is its minimum value. Using a lower turn-off angle $\theta_{\text{off}}^{\text{RFMC}}$ means that the control switches back to PWM-DITC earlier. This substantiates that reverting to DITC, when force compensation is not required, results in a more thermally viable and balanced current profile. Using a higher turn-on value $\theta_{\text{on}}^{\text{RFMC}}$ reduces the conduction period of the preceding phase (phase 2) and therefore, a reduction in RMS current density is observed. For the preceding phase the turn-on angle $\theta_{\text{on}}^{\text{RFMC}}$ has a considerably higher effect than the turn-off angle $\theta_{\text{off}}^{\text{RFMC}}$. The overall minimum current density is observed at the maximum turn-on and minimum turn-off angle.

In case of the following phase (phase 4), shown in figure 5.19g, the main parameter responsible for reducing the RMS current density is the turn-off angle $\theta_{\text{off}}^{\text{RFMC}}$. Varying the turn-on angle only shows an insignificant change in the current density. The poles of the following phase (phase 4) are excited once the preceding phase (phase 2) produces negative torque and therefore, are independent of the turn-on angle $\theta_{\text{on}}^{\text{RFMC}}$. However, the point at which the preceding phase (phase 2) reduces its negative torque and therefore, the point at which the negative torque compensation by the following phase (phase 4) decreases, is determined by the turn-off angle $\theta_{\text{on}}^{\text{RFMC}}$. Consequently, the lowest RMS current density of the following phase (phase 4) is observed at the smallest turn-off angle $\theta_{\text{off}}^{\text{RFMC}}$.

For SRM-16/12 the optimum combination of turn-on and turn-off angle for the nominal operating point is $\theta_{\text{on}}^{\text{RFMC}} = 62°$ and $\theta_{\text{off}}^{\text{RFMC}} = 139.4°$. It should be noted that the lowest pole current densities of the preceding phase (figure 5.19c to figure 5.19f) correspond to the lowest average current density in figure 5.19h. The result demonstrates that the optimal combination of turn-on and turn-off angle is strongly influenced by the preceding phase (phase 2). This is attributed to the fact that the preceding phase experiences the longest period of conduction amongst all phases. Therefore, the pole current densities are higher compared to all other poles, visible in figure 5.16. The overall minimum current density is thus, directly linked to the minimum of the poles of the preceding phase (phase 2). The change in RMS current density for all poles of SRM-16/12 due to turn-on $\theta_{\text{on}}^{\text{RFMC}}$ and turn-off $\theta_{\text{off}}^{\text{RFMC}}$ angle optimization is shown in table 5.2. An operating point of $T_{\text{ref}}^{*} = 9.5\,\text{Nm}$ ($\overline{T}_{\text{avg}} = 9.07\,\text{Nm}$) and $n = 400\,\text{rpm}$ is simulated. Without angle optimization the poles 2.2 and 2.14 have considerably higher values compared to the other poles. It can clearly be observed that with an optimum combination of angles, the current density of poles belonging to phase 2 and 4 are reduced. In case of the faulty phase (phase 1) the load is shared more uniformly amongst the three healthy poles and thus, the current density of the critical pole 1.9 increases, while those of poles 1.5 and 1.13 decreases. Phase 3 is independent of RFMC resulting in no change of the current density values.

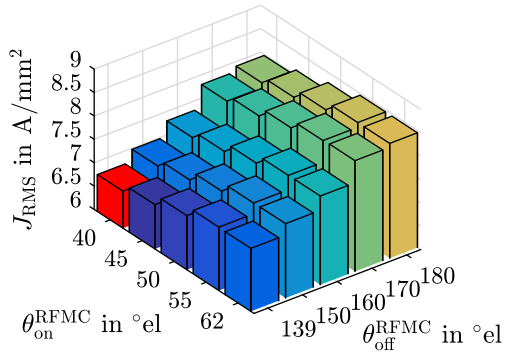

(a) Pole 1.5 and 1.13

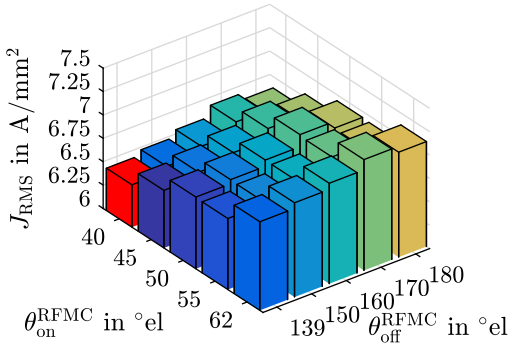

(b) Pole 1.9

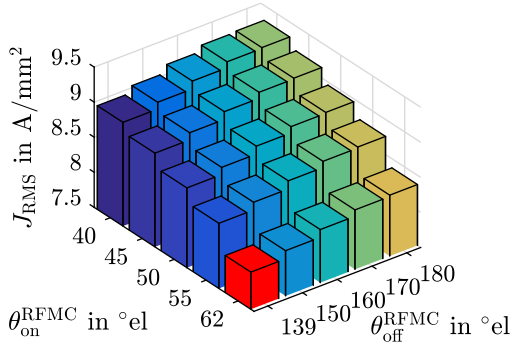

(c) Pole 2.2

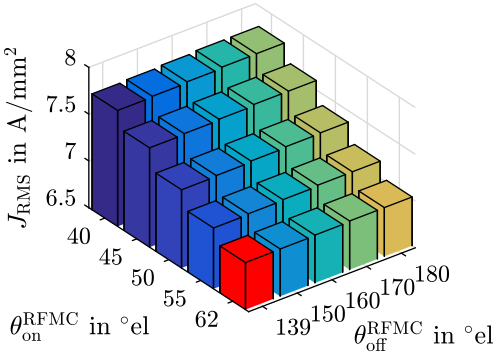

(d) Pole 2.6

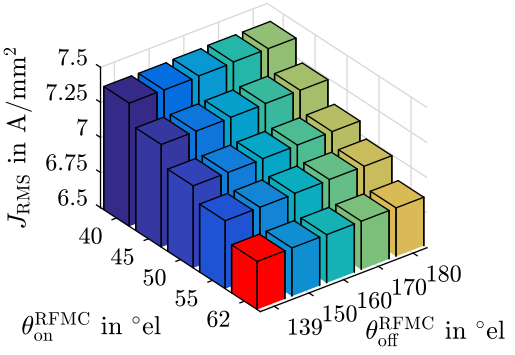

(e) Pole 2.10

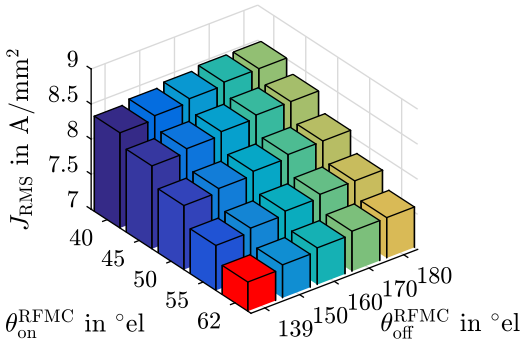

(f) Pole 2.14

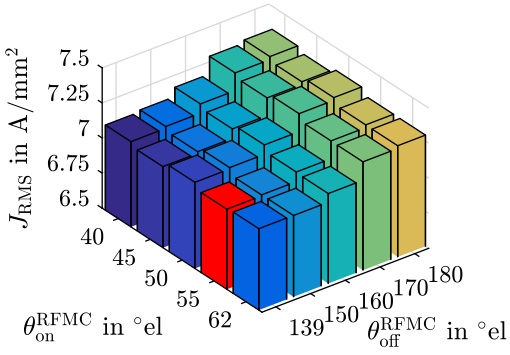

(g) Pole 4.x

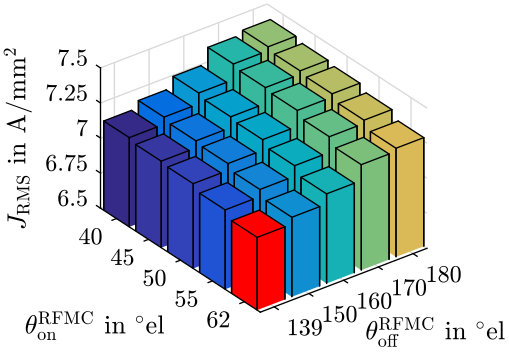

(h) Average J_{RMS} of all poles

Figure 5.19: SRM-16/12: RMS current density for various turn-on $\theta_{\mathrm{on}}^{\mathrm{RFMC}}$ and turn-off $\theta_{\mathrm{off}}^{\mathrm{RFMC}}$ angles operating with RFMC at 9.5 Nm and 400 rpm

Even though the current densities can be reduced, the absolute tolerable values have to be defined for a given application. What maximum hot-spot temperatures and what average machine temperature are allowable are highly dependent on where the motor is operated. For RFMC operation the maximum average temperature of each pole is of interest, so as to define the maximum current density during fault operation. Increasing the allowed temperature and thus, current density shortens the overall lifetime of the winding insulation in correlation to the Arrhenius equation, i.e. an increase of 10 °C halves the lifetime [111]. The absolute temperature and resulting pole current density determines the overall operating range of the fault tolerant control.

From thermal measurements and simulations in Motor-CAD presented in section A.1, a current density of 7.3 A/mm^2 results in a hot spot temperature $T_{\mathrm{wdg}} = 155\,°\mathrm{C}$, which SRM-16/12 can operate at continously. Therefore, at a current density lower to 7.3 A/mm^2 the machine is able to operate continuously even during single pole fault. Considering the machine's thermals $\overline{T}_{\mathrm{avg}} = 9.07\,\mathrm{Nm}$ can not be produced continuously with RFMC as the optimized pole current density of 2.2 is 8.0 A/mm^2. In table 5.3 the current density distribution of all poles, with a maximum of $J_{\mathrm{RMS}}^{\mathrm{max}} = 7.3\,\mathrm{A/mm^2}$, is displayed. Thus, SRM-16/12 can continuously operate at $\overline{T}_{\mathrm{avg}} = 6.15\,\mathrm{Nm}$ with EFC and $\overline{T}_{\mathrm{avg}} = 7.58\,\mathrm{Nm}$ with RFMC, while having a single pole fault. The thermally limiting pole for RFMC is pole 2.2 from the preceding phase, which has to be reduced from a current density value of 8.00 A/mm^2 to 7.3 A/mm^2. Using RFMC increases the possible operating torque by 23 % compared to EFC operation. The fault operation operating range without torque loss of SRM-16/12 can only be increased by allowing a higher machine temperature during fault operation.

Switching between the two control algorithms is either done at fixed angles defined for each machine at the highest operating torque and at low speed, or is dynamically changed

Table 5.2: SRM-16/12: RMS pole current density J_{RMS} in A/mm^2 operating at RFMC

Pole no.	Not optimized	Optimized
1.5	7.97	7.35
1.9	6.62	6.94
1.13	8.01	7.25
2.2	**9.28**	**8.00**
2.6	7.77	7.00
2.10	7.38	6.84
2.14	**8.51**	7.41
3.x	6.51	6.51
4.x	7.33	7.08
Avg. J_{RMS}	7.40	7.02
Avg. torque	9.07 Nm	9.07 Nm

Table 5.3: SRM-16/12: J_{RMS} in A/mm^2 with $J_{\mathrm{RMS}}^{\mathrm{max}} = 7.3\,\mathrm{A/mm^2}$ operating at RFMC and EFC

Pole no.	RFMC (opt.)	EFC
1.5	**7.21**	**7.30**
1.9	6.72	0
1.13	7.05	**7.30**
2.2	**7.30**	5.44
2.6	6.12	5.44
2.10	6.02	5.44
2.14	6.55	5.44
3.x	5.85	5.29
4.x	6.44	5.23
Avg. J_{RMS}	6.41	5.61
Avg. torque	7.58 Nm	6.15 Nm

depending on the operating point. Calculating the UMP online and adjusting the turn-on $\theta_{\text{on}}^{\text{RFMC}}$ and turn-off $\theta_{\text{off}}^{\text{RFMC}}$ angles dynamically further reduces the machine's thermal stress as for each operating point the minimal conduction period is determined. The UMP is already calculated in the FPGA for the radial force compensation algorithm and, therefore, can also be used to tune the turn-on $\theta_{\text{on}}^{\text{RFMC}}$ and turn-off $\theta_{\text{off}}^{\text{RFMC}}$ angle during operation.

Similar to the RFMC thermal influence investigation for SRM-16/12, the turn-on $\theta_{\text{on}}^{\text{RFMC}}$ and turn-off $\theta_{\text{off}}^{\text{RFMC}}$ angles are investigated for SRM-12/8 and SRM-20/16. For conciseness only the averaged RMS current density graphs are shown in figure 5.20. In table 5.4 and table 5.5 the respective RMS current density values for the nominal operating point of each machine is displayed. The tables show the change in current density J_{RMS} when optimizing the turn-on $\theta_{\text{on}}^{\text{RFMC}}$ and turn-off $\theta_{\text{off}}^{\text{RFMC}}$ angle.

For the three phase machine SRM-12/8 the selected angles are $\theta_{\text{on}}^{\text{RFMC}} = [30°, 52°]$ and $\theta_{\text{off}}^{\text{RFMC}} = [150°, 180°]$, resulting from an exemplary maximum UMP of 100 N. Increasing the allowed net radial force reduces the range when operating with RFMC and increases the DITC operation. As already seen with SRM-16/12 the optimized angles to be used are the largest possible turn-on angle $\theta_{\text{on}}^{\text{RFMC}}$ and smallest turn-off angle $\theta_{\text{off}}^{\text{RFMC}}$. By using these angles the average current density is reduced from 7.49 A/mm^2 to 7.15 A/mm^2. Changing the turn-off angle $\theta_{\text{off}}^{\text{RFMC}}$ effectively changes the current density for three and four phase SRMs. In these machines the second residual force peak, which is directly dependent on the turn-off angle results from a minor misalignment of the radial forces of the still active preceding phase and the faulty phase. As visible in figure 5.11 and figure 5.13 for SRM-16/12 and SRM-12/8 respectively, the radial forces of the following phase (phase 4 for SRM-16/12 and phase 3 for SRM-12/8) only marginally overlap with the forces of the faulty phase. Therefore, the residual force peak is largely independent of the radial forces of the following phase.

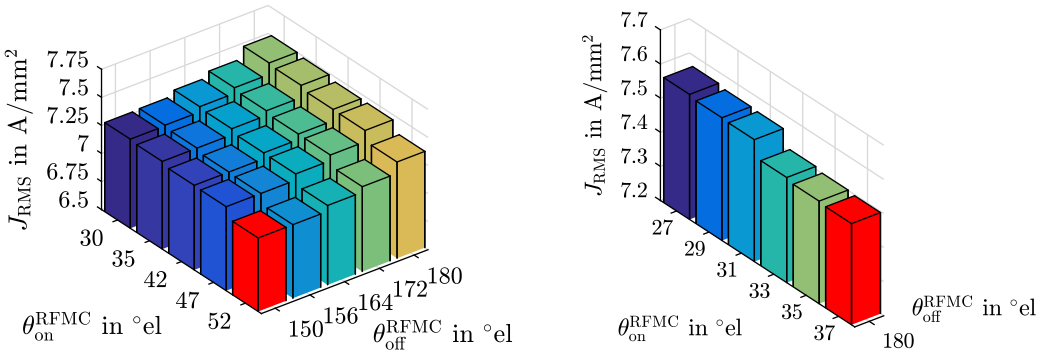

(a) SRM-12/8: Average J_{RMS} of all poles

(b) SRM-20/16: Average J_{RMS} of all poles

Figure 5.20: Average RMS pole current densities of SRM-12/8 and SRM-20/16 for various turn-on $\theta_{\text{on}}^{\text{RFMC}}$ and turn-off $\theta_{\text{off}}^{\text{RFMC}}$ angles

Table 5.4: SRM-12/8: RMS pole current density J_{RMS} in A/mm^2 operating with RFMC at 5.9 Nm and 1500 rpm

Pole no.	Not optimized	Optimized
1.4	**7.94**	**7.53**
1.7	5.97	6.37
1.10	**7.98**	**7.54**
2.2	**8.48**	**7.69**
2.5	7.39	6.82
2.8	7.28	6.77
2.11	**8.02**	**7.31**
3.x	7.5	5.15
Avg. J_{RMS}	7.49	7.15

Table 5.5: SRM-20/16: RMS pole current density J_{RMS} in A/mm^2 operating with RFMC at 1800 Nm and 300 rpm

Pole no.	Not optimized	Optimized
1.6	9.18	9.18
1.11	6.55	6.55
1.16	9.22	9.22
2.2	**11.20**	**11.20**
2.7	9.65	9.07
2.12	8.05	7.47
2.17	**10.54**	**10.54**
3.x	6.46	6.46
4.x	6.56	6.56
5.5	6.78	6.78
5.10	5.72	5.70
5.15	6.85	6.61
5.20	7.79	7.46
Avg. J_{RMS}	7.56	7.47

However, in five phase SRMs this changes due to the higher phase number and thus, larger phase overlap. The benefit of the increased overlap is a better force compensation as already seen in figure 5.12, where RFMC can compensate for a single pole fault up to SRM-20/16 designed nominal operating point of 1800 Nm and 300 rpm. The high phase overlap allows the following phase (phase 5) to compensate the negative torque produced by the preceding phase (phase 2) as seen in figure 5.12a. However, this also causes the second radial force peak to be dependent on the preceding phase (phase 2) and the following phase (phase 5). Simulation results of SRM-20/16 showing the residual radial force peak for different speed and torque values are presented in figure 5.21. It is visible that the net radial force value does not reduce consequently with increasing turn-off $\theta_{\mathrm{off}}^{\mathrm{RFMC}}$ angle as is the case for the three and four phase machine (SRM-16/12: see figure 5.18). For SRM-20/16 it is not possible to optimize the current density by reducing the turn-off angle $\theta_{\mathrm{off}}^{\mathrm{RFMC}}$ without creating a large residual radial force peak. Furthermore, the residual force peak increases when decreasing the torque reference. The individual radial forces for two operating points $T_{\mathrm{ref}}^{*} = 900\,\mathrm{Nm}$ and $T_{\mathrm{ref}}^{*} = 1800\,\mathrm{Nm}$ are presented in figure 5.22. The small residual force peak visible in figure 5.22b is caused by a slight misalignment of the forces $F_{5.5}$, $F_{5.10}$, $F_{5.15}$ and $F_{5.20}$ from the following phase (phase 5) when the control switches from RFMC to PWM-DITC. In contrast for lower torque values the radial forces are not aligned when the control switches back to PWM-DITC as exemplary presented for 900 Nm in figure 5.22a. The radial forces of phase 5 are not equal (aligned) at $\theta_{\mathrm{off}}^{\mathrm{RFMC}}$, especially between the opposing radial forces $F_{5.10}$ and $F_{5.20}$ there is a large difference, resulting in a UMP of $F_{\mathrm{r,ump}} > 800\,\mathrm{N}$.

As this residual force peak is not directly controlled anymore when switching to PWM-

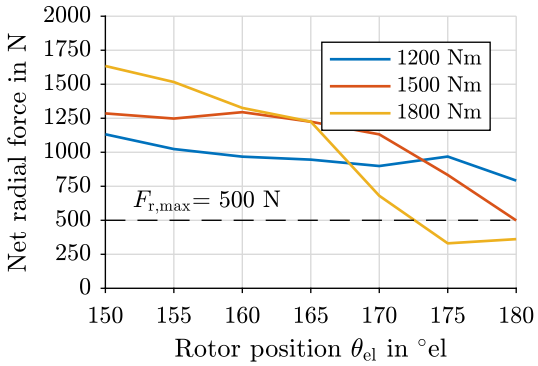

(a) Force peak for different reference torque values at 300 rpm

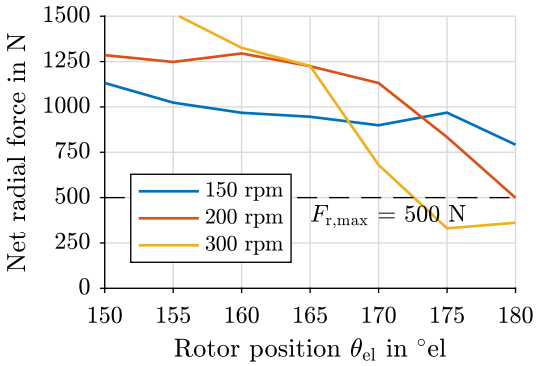

(b) Force peak for different operating speeds at T^*_{ref} = 1800 Nm

Figure 5.21: SRM-20/16: Residual radial force peak (UMP) for different torque and speed values versus rotor position, which are largely independent of the turn-off angle θ^{RFMC}_{off} for five phase machines

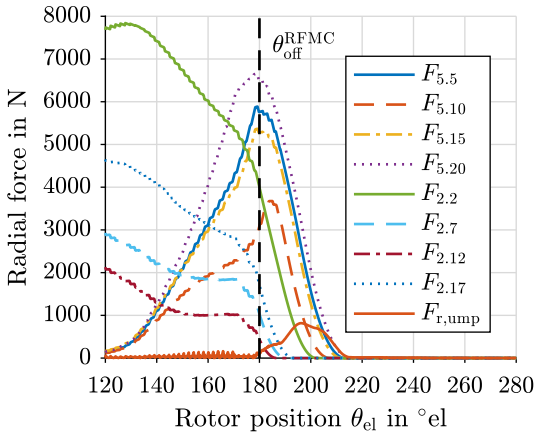

(a) T^*_{ref} = 900 Nm and n = 300 rpm

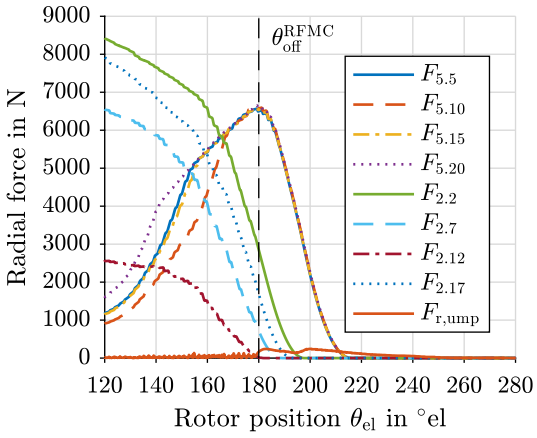

(b) T^*_{ref} = 1800 Nm and n = 300 rpm

Figure 5.22: SRM-20/16: Simulation result of the residual radial force peak at different torque values showing difference in UMP because of non-aligned radial pole forces when switching back to PWM-DITC at θ^{RFMC}_{off}

DITC, no turn-off angle $\theta_{\text{off}}^{\text{RFMC}}$ can be used. For five phase SRMs, RFMC has to be used for the entire period of the faulty phase to ensure a controlled and defined UMP. Therefore, the current density and thermal loading during fault tolerant control is determined by the control algorithm RFMC and is not influenced by the turn-off angle, as is possible with three and four phase machines. The turn-on angle $\theta_{\text{on}}^{\text{RFMC}}$ always has the same effect independent of the phase number and thus, can also be used for the five phase machine.

As an example for the nominal operating point 1800 Nm and 300 rpm, the turn-on angle $\theta_{\text{on}}^{\text{RFMC}}$ is varied between $[27°, 37°]$ and turn-off angle $\theta_{\text{off}}^{\text{RFMC}}$ is fixed to 180°. The minimal change in current density due to the turn-on angle is visible in figure 5.20b and table 5.5. Five phase machines are well suited for fault tolerant control, however, there exists an extensive thermal loading of individual poles during the fault control. The operational limit of SRM-20/16 during single pole fault is directly coupled to the allowed thermal limits and respective maximum current density per pole $J_{\text{RMS}}^{\text{max}}$.

In figure 5.23 simulation results of the maximum RMS pole current density in SRM-20/16 for different torque values at $n = 300$ rpm are presented. The two different control types EFC and RFMC are used. It is visible that up to 1245 Nm and a current density of $J_{\text{RMS}} = 9.6\,\text{A/mm}^2$ EFC is the more effective fault tolerant control strategy concerning the thermal loading of a single pole. Up to this operating point, dividing the missing torque amongst the two remaining healthy poles, is more effective than increasing the conduction period of the preceding phase (phase 5) to compensate for the critical pole, as is done in RFMC. However, at torque values higher than 1245 Nm it is more effective to compensate the UMP and distribute the missing torque amongst all poles and thus, use the proposed RFMC control algorithm. Therefore, if during a single pole fault a short-time current density $J_{\text{RMS}}^{\text{max}} \approx 11.2\,\text{A/mm}^2$ is allowed in the application, SRM-20/16 can be operated in its entire operating range also with a fault. Otherwise, the operating region has to be reduced according to the allowable fault-case current density.

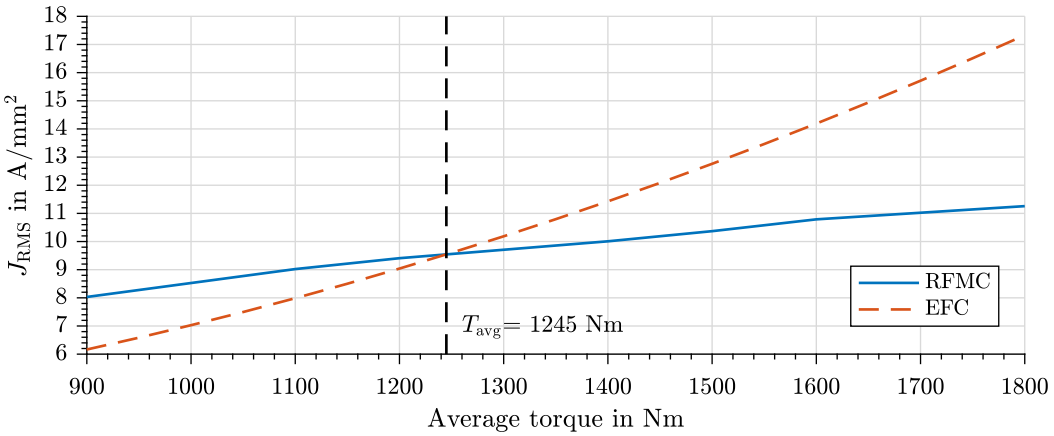

Figure 5.23: SRM-20/16: Comparison of J_{RMS} during RFMC and EFC operation at various torque values and $n = 300$ rpm

5.4 Simplified Radial Force Minimization for Single Pole Fault

The generalized radial force minimization control from the previous section revolves around solving the linear least square equation (5.1). This main algorithm is based on an iterative solution, which leads to multiple matrix multiplications with a high computational burden [112]. Therefore, solving this problem on a FPGA becomes computationally intensive, requiring a different, simplified approach to the algorithm.

The discussion in the previous section has shown that irrespective of the machine configuration only the preceding and following phase in regard to the faulty phase are necessary to compensate the radial and tangential forces during a single pole fault. Therefore, the control algorithm for implementation on a FPGA can be reduced in complexity. This section proposes a simplified radial force minimization control (S-RFMC) explicitly for single pole fault followed by a comparison of this algorithm with the general RFMC algorithm. Experimental test bench results using S-RFMC are presented in chapter 6.

5.4.1 Approach and FPGA Implementation

During single pole fault the radial force compensation produced by RFMC is shown for SRM-16/12 in figure 5.24. It is visible that the compensation forces are predominantly active during the period $40° < \theta_{\mathrm{el}}^{\mathrm{ph1}} < 150°$. The two main forces responsible for compensation of UMP are $F_{\mathrm{rad},2}$ and $F_{\mathrm{rad},14}$ corresponding to the poles 2.2 and 2.14 respectively. This selective excitation is due to the spatial distribution of the poles in the machine in relation to the faulty pole 1.9.

Figure 5.25 shows the spatial pole distribution due to the geometry and configuration of SRM-16/12. During a fault of pole 1.1 the critical pole force to be compensated is $F_{\mathrm{rad},9}$

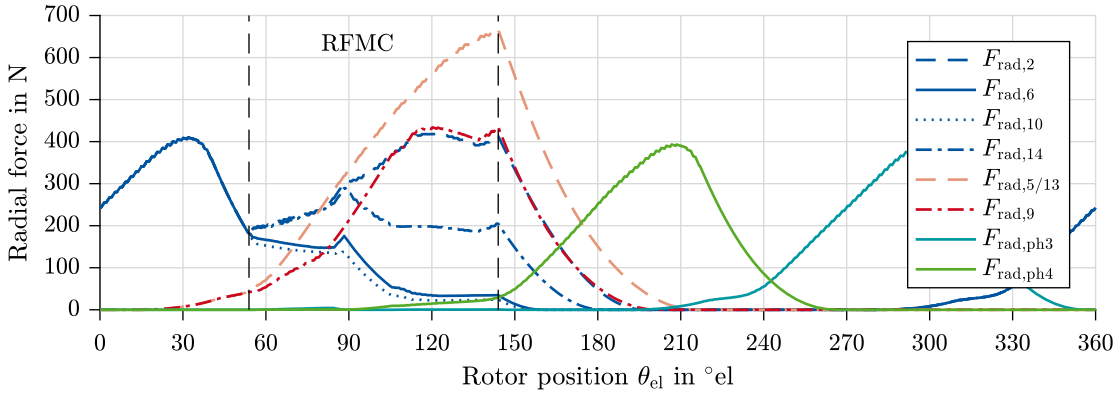

Figure 5.24: SRM-16/12: Radial forces produced by poles during RFMC

of pole 1.9. The force directions of the preceding phase (phase 2) clearly shows that $F_{\mathrm{rad},9}$ is mainly compensated by $F_{\mathrm{rad},2}$ and $F_{\mathrm{rad},14}$. The two remaining pole forces from the preceding phase $F_{\mathrm{rad},6}$ and $F_{\mathrm{rad},10}$ are orientated in the same direction as the critical force $F_{\mathrm{rad},9}$ increasing the UMP. Therefore, the magnetization of these two poles are reduced to a minimum.

To neutralize the critical pole force $F_{\mathrm{rad},9}$ both equations (5.15) and (5.16), describing the geometric spatial force distribution, have to be satisfied. These equations are used to define the simplified version of the least square radial force compensation algorithm. The radial force prediction for S-RFMC is done, as previously in RFMC, with the help of the $F_{\mathrm{rad}}(\psi,\theta_{\mathrm{el}})$-LUT.

$$F_{\mathrm{rad},2} = F_{\mathrm{rad},9}\cos\varphi + F_{\mathrm{rad},10} \tag{5.15}$$

$$F_{\mathrm{rad},14} = F_{\mathrm{rad},9}\sin\varphi + F_{\mathrm{rad},6} \tag{5.16}$$

$$\varphi = \frac{2\pi}{N_{\mathrm{s}}} \tag{5.17}$$

From the general equations (5.15) and (5.16) more specific equations (5.18) and (5.19) corresponding to the PWM control structure are formulated. Thereby, the goal is to formulate the reference values for $F_{\mathrm{rad},2}$ and $F_{\mathrm{rad},14}$. The forces $F_{\mathrm{rad},6}$ and $F_{\mathrm{rad},10}$ are kept

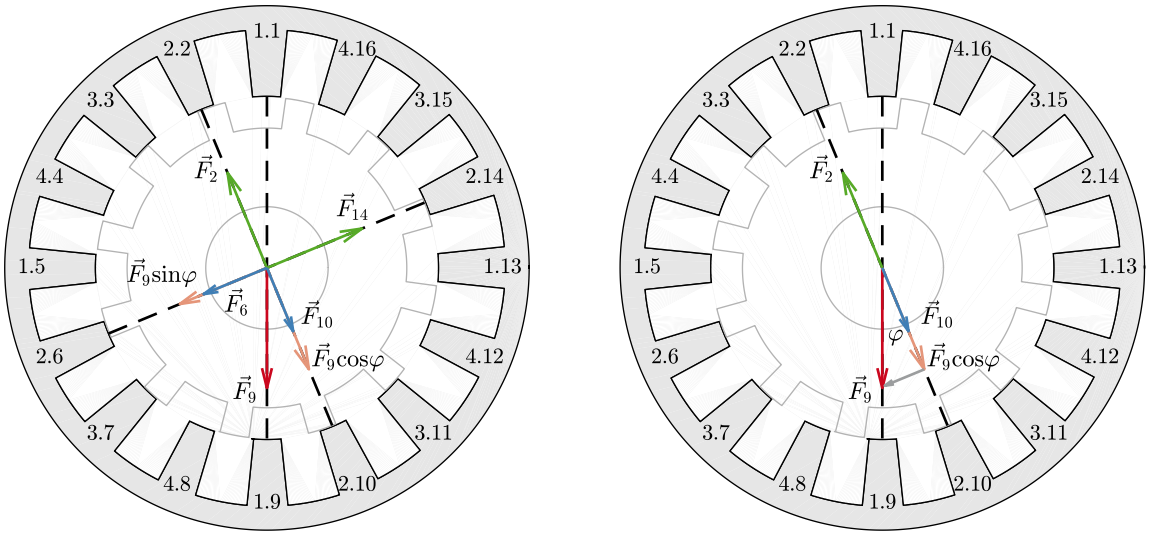

(a) Sine and cosine component of critical pole F_9

(b) Force compensation of cosine component of critical pole F_9

Figure 5.25: SRM-16/12: Radial force produced by critical pole (1.9) in red and compensation poles of the preceding phase 2 (counter clockwise rotor rotation), the green arrows show the main compensating forces of poles 2.2 and 2.14, the orange arrows are sine- & cosine components of the critical force F_9

at a minimum value irrespective of the value of the critical pole $F_{\mathrm{rad},9}$. Similar to RFMC the minimum and maximum values of $F_{\mathrm{rad},2}$ and $F_{\mathrm{rad},14}$ for the next period are limited by the boundary condition of a duty cycle d_n between -1 and 1.

$$F_{\mathrm{rad},2,n+2} = F_{\mathrm{rad},9,n+1}\cos\varphi + F^{\min}_{\mathrm{rad},10,n+2} \quad \text{for } F_{\mathrm{rad},2,n+2} \in [F^{\min}_{\mathrm{rad},2,n+2},\, F^{\max}_{\mathrm{rad},2,n+2}] \tag{5.18}$$

$$F_{\mathrm{rad},14,n+2} = F_{\mathrm{rad},9,n+1}\sin\varphi + F^{\min}_{\mathrm{rad},6,n+2} \quad \text{for } F_{\mathrm{rad},14,n+2} \in [F^{\min}_{\mathrm{rad},14,n+2},\, F^{\max}_{\mathrm{rad},14,n+2}] \tag{5.19}$$

To fulfill these two equations three possible cases for each equation are possible in the control. For equation (5.18) the following cases are possible:

Case 1: $F_{\mathrm{rad},9,n+1}\cos\varphi > F^{\max}_{\mathrm{rad},2,n+2} - F^{\min}_{\mathrm{rad},10,n+2}$

For the first case the unbalanced magnetic pull $F_{\mathrm{rad},9,n+1}\cos\varphi$ along the axis of $F_{\mathrm{rad},2}$ is larger than the maximum value of the compensation force. Thus, the control can not excite pole 2.2 enough to compensate the entire unbalanced force. Therefore, the control sets the maximum duty cycle for pole 2.2 by setting the reference force value $F_{\mathrm{rad},2,\mathrm{ref}}$ to the maximum radial force $F^{\max}_{\mathrm{rad},2,n+2}$ as given in equation (5.20). The force $F_{\mathrm{rad},10,\mathrm{ref}}$ in the opposite direction is set to its minimum as in equation (5.21).

$$F_{\mathrm{rad},2,\mathrm{ref}} = F^{\max}_{\mathrm{rad},2,n+2} \implies T_{2,\mathrm{ref}} = T^{\max}_{2,n+2} \tag{5.20}$$

$$F_{\mathrm{rad},10,\mathrm{ref}} = F^{\min}_{\mathrm{rad},10,n+2} \implies T_{10,\mathrm{ref}} = T^{\min}_{10,n+2} \tag{5.21}$$

The minimum and maximum radial force values are realized by applying the minimum and maximum duty cycle. Consequently, the reference torque values are analogous the minimum and maximum torque values.

Case 2: $F^{\max}_{\mathrm{rad},2,n+2} - F^{\min}_{\mathrm{rad},10,n+2} > F_{\mathrm{rad},9,n+1}\cos\varphi > F^{\min}_{\mathrm{rad},2,n+2} - F^{\min}_{\mathrm{rad},10,n+2}$

The second case resembles the situation, where the critical pole force is between the minimum and maximum of the compensation force. Therefore, the unbalanced magnetic pull can be compensated by the compensation force $F_{\mathrm{rad},2}$ and is determined by equation (5.22) and equation (5.23).

$$F_{\mathrm{rad},2,\mathrm{ref}} = F^{\min}_{\mathrm{rad},2,n+2} + \Delta F_2 \text{ with } \Delta F_2 = F_{\mathrm{rad},9,n+1}\cos\varphi - (F^{\min}_{\mathrm{rad},2,n+2} - F^{\min}_{\mathrm{rad},10,n+2}) \tag{5.22}$$

$$F_{\mathrm{rad},10,\mathrm{ref}} = F^{\min}_{\mathrm{rad},10,n+2} \tag{5.23}$$

In section 5.3.1 (see equation (5.14)) it is shown that even though the radial force and torque in SRMs are non-linear, a linearization between both components can be used within a switching period. The reference radial force is used to calculate the reference torque by using the scaling factor k_i as defined in equation (5.24), whereby r_{ag} is the air-gap radius.

$$k_i = \frac{F^{\max}_{\mathrm{tan},i,n+2} - F^{\min}_{\mathrm{tan},i,n+2}}{F^{\max}_{\mathrm{rad},i,n+2} - F^{\min}_{\mathrm{rad},i,n+2}} \cdot r_{\mathrm{ag}} \qquad \text{for } i \in [1,\, N_{\mathrm{s}}] \tag{5.24}$$

Thus, the change in radial force ΔF_i and the scaling factor k_i is used to calculate the change in torque (equation (5.25)) resulting in the reference torque $T_{2,\mathrm{ref}}$ definition as in equation (5.26).

$$\Delta T_i = \Delta F_i \cdot k_i \tag{5.25}$$

$$T_{2,\mathrm{ref}} = T^{\min}_{2,n+2} + (\Delta F_2 \cdot k_2) \tag{5.26}$$

For stator pole 10 the reference torque remains at its minimum:

$$T_{10,\mathrm{ref}} = T^{\min}_{10,n+2} \tag{5.27}$$

Case 3: $F_{\mathrm{rad},9,n+1} \cos\varphi < F^{\min}_{\mathrm{rad},2,n+2} - F^{\min}_{\mathrm{rad},10,n+2}$

In the last case, the critical pole force is smaller than the minimum value of the compensation force. Therefore, the minimum value of compensation force is set as reference $F_{\mathrm{rad},2,\mathrm{ref}}$ and the minimum value is set for pole force $F_{\mathrm{rad},10,\mathrm{ref}}$ as in equation (5.28) and equation (5.29) respectively.

$$F_{\mathrm{rad},2,\mathrm{ref}} = F^{\min}_{\mathrm{rad},2,n+2} \implies T_{2,\mathrm{ref}} = T^{\min}_{2,n+2} \tag{5.28}$$

$$F_{\mathrm{rad},10,\mathrm{ref}} = F^{\min}_{\mathrm{rad},10,n+2} \implies T_{10,\mathrm{ref}} = T^{\min}_{10,n+2} \tag{5.29}$$

Analogue to the presented three cases for the cosine force component $F_{\mathrm{rad},9,n+1} \cos\varphi$ another three cases for the sine component $F_{\mathrm{rad},9,n+1} \sin\varphi$ are defined:

Case 4: $F_{\mathrm{rad},9,n+1} \sin\varphi > F^{\max}_{\mathrm{rad},14,n+2} - F^{\min}_{\mathrm{rad},6,n+2}$

$$T_{14,\mathrm{ref}} = T^{\max}_{14,n+2} \tag{5.30}$$

$$T_{6,\mathrm{ref}} = T^{\min}_{6,n+2} \tag{5.31}$$

Case 5: $F^{\max}_{\mathrm{rad},14,n+2} - F^{\min}_{\mathrm{rad},6,n+2} > F_{\mathrm{rad},9,n+1}\sin\varphi > F^{\min}_{\mathrm{rad},14,n+2} - F^{\min}_{\mathrm{rad},6,n+2}$

$$F_{\mathrm{rad},14,\mathrm{ref}} = F^{\min}_{\mathrm{rad},14,n+2} + \Delta F_{14} \text{ with } \Delta F_{14} = F_{\mathrm{rad},9,n+1}\sin\varphi - (F^{\min}_{\mathrm{rad},14,n+2} - F^{\min}_{\mathrm{rad},6,n+2}) \tag{5.32}$$

$$T_{14,\mathrm{ref}} = T^{\min}_{14,n+2} + (\Delta F_{14} \cdot k_{14}) \tag{5.33}$$

$$F_{\mathrm{rad},6,\mathrm{ref}} = F^{\min}_{\mathrm{rad},6,n+2} \implies T_{6,\mathrm{ref}} = T^{\min}_{6,n+2} \tag{5.34}$$

Case 6: $F_{\mathrm{rad},9,n+1}\sin\varphi < F^{\min}_{\mathrm{rad},14,n+2} - F^{\min}_{\mathrm{rad},6,n+2}$

$$T_{14,\mathrm{ref}} = T^{\min}_{14,n+2} \tag{5.35}$$

$$T_{6,\mathrm{ref}} = T^{\min}_{6,n+2} \tag{5.36}$$

For S-RFMC a modified version of the torque sharing algorithm is implemented. During DITC the torque sharing is done as described in section 2.3.2 and the minimum produced torque of all phases is subtracted from the reference torque T^*_{ref}, according to their priority, to determine the remaining torque T_{rem}, which has to be produced. During the time S-RFMC is active the preceding phase (phase 2) is excluded from the torque sharing process, as the reference values for this phase are determined according to the fault compensation in equation (5.18) and equation (5.19). The torque set by these reference values are subtracted from T^*_{ref} to calculate the remaining torque T_{rem} according to equation (5.37), which has to be produced by the remaining healthy phases.

$$T_{\mathrm{rem}} = \begin{cases} T^*_{\mathrm{ref}} - \sum_{i\neq 2,6,10,14}^{N_\mathrm{s}} T^{\min}_{i,n+2} - \sum_{j=2,6,10,14} T_{j,\mathrm{ref}} & \text{for} \quad \theta^{\mathrm{ph1}}_{\mathrm{el}} \in [\theta^{\mathrm{S-RFMC}}_{\mathrm{on}},\, \theta^{\mathrm{S-RFMC}}_{\mathrm{off}}] \\ T^*_{\mathrm{ref}} - \sum_{i=1}^{N_\mathrm{s}} T^{\min}_{i,n+2} & \text{for} \quad \theta^{\mathrm{ph1}}_{\mathrm{el}} \notin [\theta^{\mathrm{S-RFMC}}_{\mathrm{on}},\, \theta^{\mathrm{S-RFMC}}_{\mathrm{off}}] \end{cases} \tag{5.37}$$

Similar to RFMC there exists an optimal turn-on and turn-off angle for the fault compensation control in regard to RMS current minimization while still reducing the UMP. As

the operation and, therefore, the current trajectories of S-RFMC and RFMC are similar, the influence of the operation angles and thus also the thermal ramifications are the same. Therefore, the same turn-on ($\theta_{\mathrm{on}}^{\mathrm{S-RFMC}} = 62°$) and turn-off ($\theta_{\mathrm{off}}^{\mathrm{S-RFMC}} = 139.4°$) angles are taken for the nominal operating point of SRM-16/12 as defined in section 5.3.3.

As with PWM-DITC the remaining torque is distributed amongst the other phases not taking part in the fault compensation. In the pole-based control the torque of a healthy phase is evenly distributed amongst all the poles of that phase. From the reference torque values the corresponding flux linkage references and duty cycles are determined.

The schematic overview of the implemented S-RFMC is shown in figure 5.26. It is visible that, in contrast to RFMC, the torque and radial force prediction is done in parallel, while the torque sharing algorithm is executed after the radial force control, i.e. S-RFMC is done. In RFMC the algorithm for torque control during healthy operation and the fault tolerant radial force control are executed independently of each other. In RFMC the control switches between either DITC or RFMC, while in S-RFMC a cascaded combination of the radial force control and DITC is used.

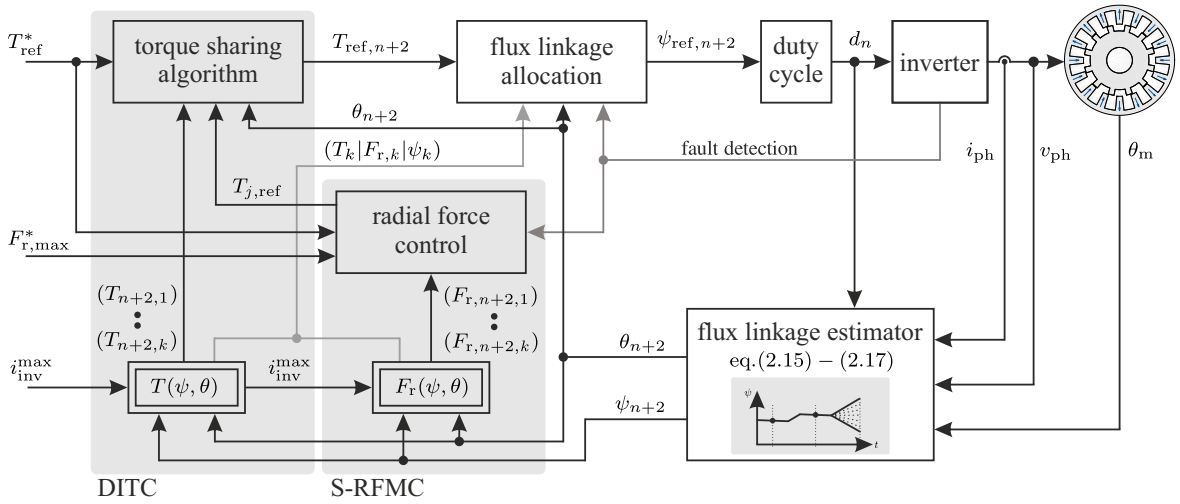

Figure 5.26: Schematic overview of fault tolerant control structure combining direct instantaneous torque control (DITC) and implemented simplified radial force minimization control (S-RFMC)

5.4.2 Comparison of S-RFMC to RFMC with Least Square

In figure 5.27 a simulation result of SRM-16/12 during single pole fault with S-RFMC operating at 5 Nm and 400 rpm is presented. The first half of the simulation result shows the operation with only PWM-DITC and a resulting UMP of 420 N. The second half of the simulation shows the reduction of the UMP to 78 N with the use of S-RFMC. In figure 5.27a the negative torque produced by the preceding phase (phase 2) due to its

increased conduction period is visible. The negative torque is compensated by the faulty phase (phase 1) and partially by the following phase (phase 4). In figure 5.27b the first force peak reduces as soon as the FTC switches to S-RFMC. When S-RFMC is switched on, the pole currents of the preceding phase diverge from their DITC trajectory visible in figure 5.27d. Pole currents $i_{2.2}$ and $i_{2.14}$ increase at time $t = 14.8\,\text{ms}$ to produce the corresponding compensating pole forces $F_{\text{rad},2.2}$ and $F_{\text{rad},2.14}$ shown in figure 5.27c. The critical force to be compensated is $F_{\text{rad},1.9}$. The remaining pole currents of the preceding phase 2.6 and 2.10 continue to be demagnetized as they are minimized by the S-RFMC algorithm. Furthermore, the main compensation force opposing $F_{\text{rad},1.9}$ is $F_{\text{rad},2.2}$, while $F_{\text{rad},2.14}$ is used to balance the forces spatially.

In figure 5.28 simulation results for RFMC and S-RFMC are presented, allowing a closer comparison of the two fault control methods. In contrast to the previous simulation results (figure 5.27), this result for S-RFMC is generated from the control code implemented on the FPGA and simulated as software in the loop (SIL) in Simulink.

The main difference between RFMC and S-RFMC is how strongly the critical pole 1.9 is used during the single pole fault. In RFMC the UMP is reduced by decreasing the excitation of pole 1.9, and therefore, $F_{\text{RFMC},1.9}$. The critical pole force $F_{\text{RFMC},1.9}$ stays below 150 N, compared to $F_{\text{SRFMC},1.9}$, which reaches nearly 450 N. Therefore, to compensate the UMP, the pole forces $F_{\text{RFMC},2.2}$ and $F_{\text{RFMC},2.14}$ are excited considerably lower compared to those of S-RFMC. Furthermore, RFMC uses all poles of the preceding phase, i.e. also pole 2.6 and pole 2.10 to compensate the single pole fault, while S-RFMC only uses the two main contributor forces $F_{\text{rad,SRFMC},2.2}$ and $F_{\text{rad,SRMFC},2.14}$.

Compared to RFMC, the net radial force curve of S-RFMC in figure 5.28b maintains a higher absolute value during the period in which force compensation is active. The two peaks seen in the UMP are generally similar for both methods. The first peak is due to the single pole fault and only reduces once the fault compensation algorithm is turned on at $\theta_{\text{on}}^{\text{S-RFMC}} = 60°$. This peak is the same for both fault tolerant methods. The second hump is the residual, uncontrolled peak when the fault control switches back to PWM-DITC. Once the radial force is not actively compensated anymore, the asymmetric pole excitation returns to a symmetric pole excitation. During this period a misalignment in pole current trajectory causes pole forces, which result in a net radial force. As already discussed in section 5.3.3 for RFMC, the residual force peak can be reduced for both control methods by moving the turn-off angle $\theta_{\text{off}}^{\text{S-RFMC}}$ to higher values.

In figure 5.28c a small difference between the two control methods is visible in the torque waveform. In RFMC the primary controlled variable is the radial force, while the torque is only secondary. From the UMP and torque graphs it can be seen that the controlled UMP is completely flat, while the torque curve does not match the reference torque of 5 Nm exactly. In S-RFMC the controlled variable is the torque, while the secondary variable is the radial force. From the torque graph, a flat torque curve is visible, while the UMP of S-RFMC is not exactly zero, but a value varying below 50 N.

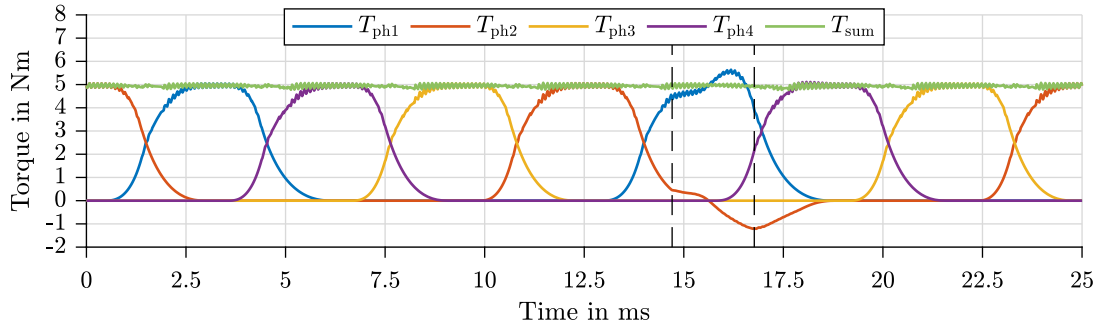

(a) Total torque and per phase torque

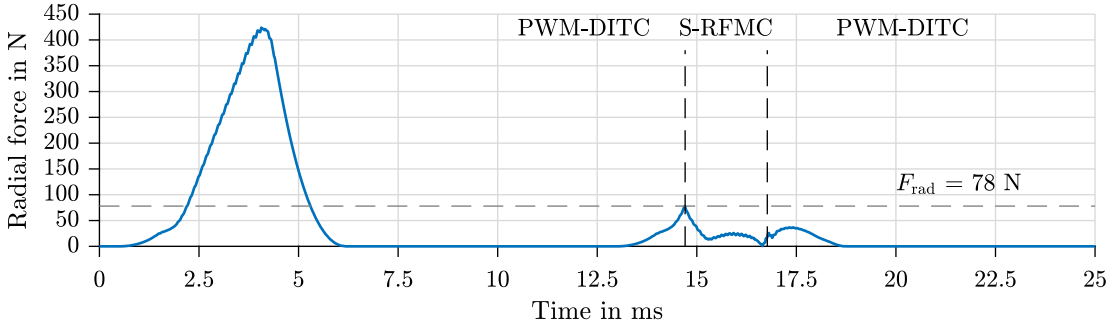

(b) Net radial force (UMP)

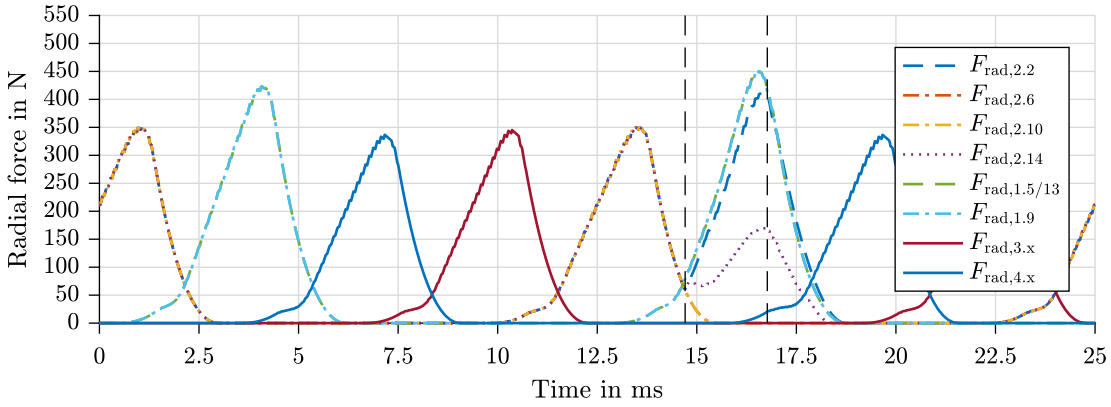

(c) Radial force per pole

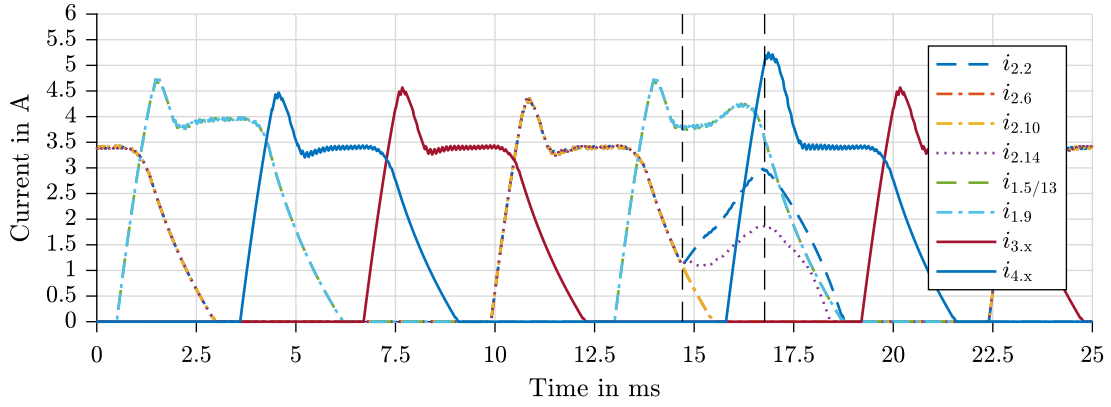

(d) Current per pole

Figure 5.27: SRM-16/12: Simulation results in Simulink with single pole fault during S-RFMC operation at 5 Nm and 400 rpm

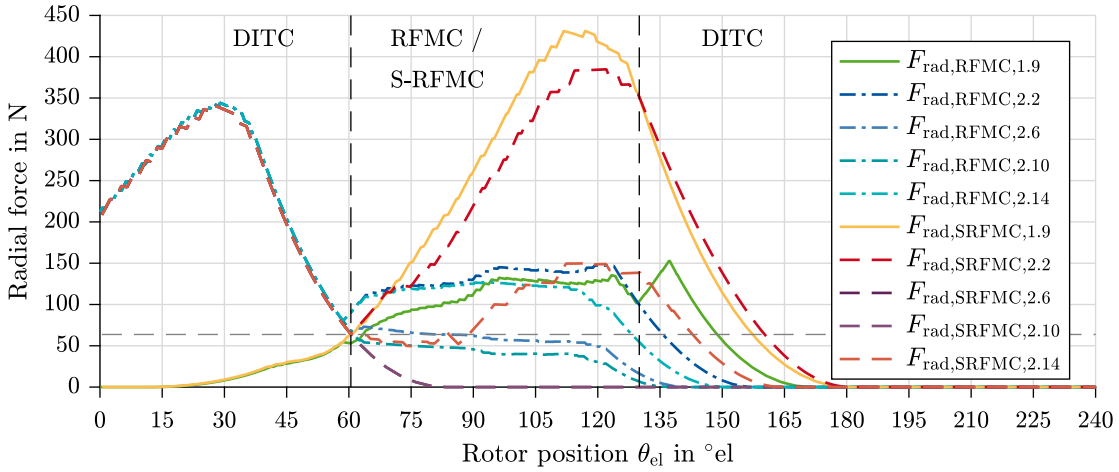

(a) Radial forces of preceding (compensation) phase

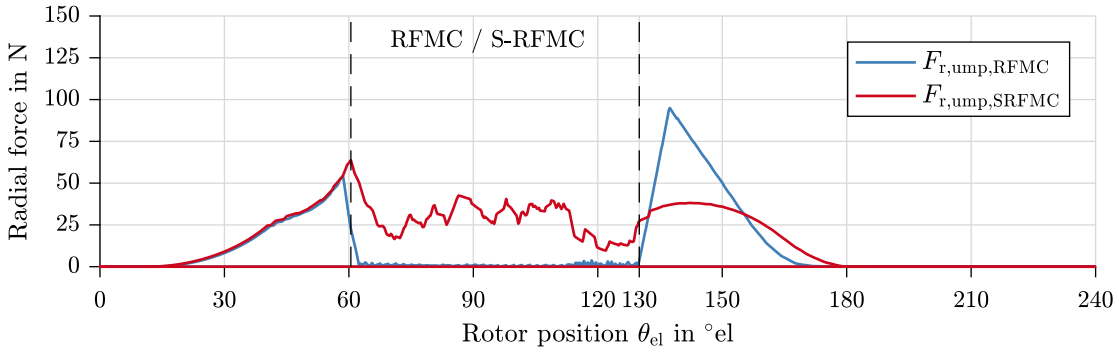

(b) Net radial force (UMP)

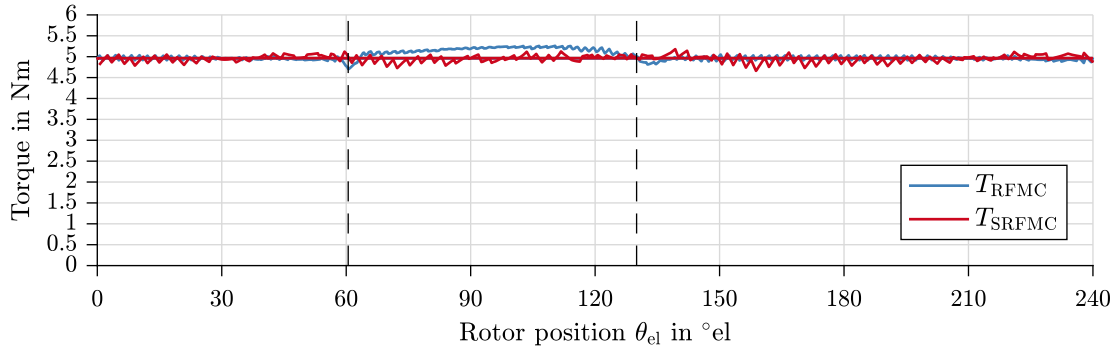

(c) Total torque

Figure 5.28: SRM-16/12: Simulation comparison of RFMC and S-RFMC (FPGA SIL implementation) at 5 Nm and 400 rpm with turn-on θ_{on}^{S-RFMC} and turn-off θ_{off}^{S-RFMC} angles of 60° and 130° respectively

5.5 Conclusions

In chapter 5 two fault tolerant control strategies, EFC and RFMC, for single pole faults in SRMs with distributed inverters are proposed. Both control methods are suitable for SRMs with at least two pole pairs ($p \geqslant 2$) and a sufficient phase overlap ($N_{\mathrm{ph}} \geqslant 3$). In machines with only one pole pair EFC is not possible, while RFMC and S-RFMC is restricted to only the main compensation force opposite the critical pole. The second compensation force ($F_{\mathrm{rad},2.14}$ in SRM-16/12) used to spatially balance the pole forces is not present in one pole pair machines, limiting the UMP reduction.

The control methods RFMC and S-RFMC are based on the phase overlap, resulting in the ability to compensate UMP with the preceding phase. For three phase machines a phase overlap, as is found in SRMs designed for DITC operation with low torque ripple, is required for an effective radial force control.

A distributed inverter, where each stator pole has its own power module is necessary to have individual flux control in each pole. Additionally, machine, inverter and control require fault detection capabilities to identify the faulty phase. For RFMC/S-RFMC operation a voltage reserve for the current control, similar to DITC, is necessary.

The investigations in this chapter have shown, that to use EFC effectively and continue smooth torque operation during fault, a second $T_{\mathrm{ph}}(\psi_{\mathrm{ph}},\theta_{\mathrm{el}})$-LUT should be implemented for the control. This LUT represents the flux linkage distribution when two opposite poles are active and the flux linkage is in the same direction, causing excessive coupling flux in the machine.

The algorithms RFMC and S-RFMC are capable of reducing the UMP, while maintaining a smooth torque output. To determine the operating area of the control during fault, the thermal limits for machine and inverters have to be defined according to the application at hand. Once the temperature limits and thus, RMS current and current densities for fault tolerant operation are defined, the torque and speed limits can be determined. It has been shown that four and five phase machines are best capable to operate at single pole fault. For five phase machines the thermal stress increases considerably higher (SRM-20/16: from $7.0\,\mathrm{A/mm^2}$ to $11.2\,\mathrm{A/mm^2}$) compared to the four phase machine (SRM-16/12: from $6.5\,\mathrm{A/mm^2}$ to $8.0\,\mathrm{A/mm^2}$). However, the torque producing capability of the five phase machine is considerably better compared to the four phase machine and allows for a higher torque limit. Therefore, to effectively use a five phase machine during single pole fault, a higher RMS current density (not so much current peak) is required, as the conduction period of the preceding phase, in respect to the fault, is extended considerably. This extension is lower in three and four phase machines, reducing the additional thermal stress during fault control. Therefore, in applications with high reliability requirements the machine and inverter limits have to be defined for the single pole fault operation range.

6 Experimental Results and Analysis: SRM-16/12

This chapter presents the test bench and measurement results of the proposed control strategies. The effects of machine asymmetries and coupling between the poles when using DITC and S-RFMC during fault-free and single pole fault operation are investigated.

6.1 Experimental Hardware Setup

The experimental investigations in this thesis are performed on the laboratory test bench shown in figure 6.1 consisting of SRM-16/12, a 10 Nm torque sensor and a 750 W induction machine as the load machine. The SRM stator poles can be connected individually depending on the winding configuration to be investigated. The test bench is either operated phase based, where all four poles of a phase are connected in parallel and four inverter modules are used to run the machine (see section 4), or the test bench is operated with a distributed inverter. Thereby, each pole can be connected to its own inverter module.

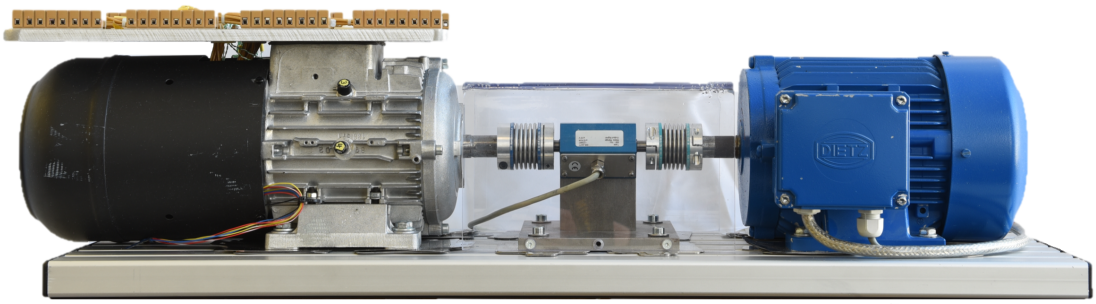

Figure 6.1: Test bench with SRM-16/12 (left) and induction machine as load (right)

The test bench inverters are controlled by a dSPACE MicroLabBox rapid prototyping hardware as shown in the test bench overview in figure 6.2. The load machine's control is implemented on the DSP, while the SRM's control algorithm is implemented on the FPGA. The software ControlDesk by dSPACE, running on an external computer, is used as the user interface to the test bench [113].

The SRM inverter modules used are based on an integrated full-bridge modular inverter using DirectFETs for synchronous machines [25]. In this thesis, however, the inverter modules are operated as asymmetric half bridges because bi-directional currents are not necessary for SRM operation. The current i_{SRM} of each inverter module is measured with 50 A CMS3050 Sensitec current sensors. Furthermore, the dc-link voltage v_{dc} and mechanical rotor position θ_{m} is measured.

The measurements taken are captured with 100 MHz MSO3014A and DSO3014A oscilloscopes from Keysight Technologies. The current is measured with 30 A/100 MHz (N2783B) current probes from Keysight Technologies. The voltage signals are measured with 70 V/100 MHz Testec differential probes. For the mechanical rotor position θ_{m} the resolver TS2224N-184E102 by Tamagawa with a 12 bit resolution connected to SRM-16/12 is used.

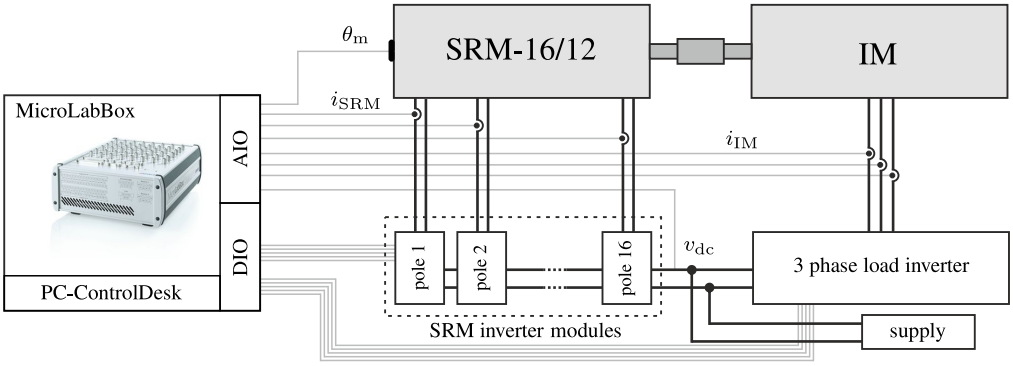

Figure 6.2: Overview of test bench layout

All measurements are done with a clockwise rotor movement resulting in a reverse phase sequence 2→1→4→3. Phase 1 will always represent the phase with a fault, therefore, phase 2 will always be the preceding phase and phase 4 is called the following phase. The naming convention for the coil arrangement is a four digit code, with either a 1 or 0 representing the flux direction. The first three digits represent the preceding, faulty and following phases. The faulty phase is underlined and the fourth digit is the remaining phase (phase 3). The digit code (11-1) represents a blockwise coil connection, where all first poles ($p_{1.1}$, $p_{2.2}$, $p_{3.3}$ and $p_{4.4}$) of each phase have the same orientation.

In section 6.4 single pole fault compensation is investigated. The developed control algorithm controls each pole of the preceding phase (phase 2), while the pole flux linkage of the remaining phases are controlled symmetrically amongst a phase, allowing for a simplified test bench setup. All four poles of phase 2 are connected to individual inverter modules, while all poles of phase one, three and four are each connected in parallel to an inverter module. Thus, instead of 16 inverter modules, 7 modules are used. For the presentation of the results all pole currents are measured with current probes and shown in the respective figures.

6.2 Direct Instantaneous Torque Control - Fault Free

The first experimental result of SRM-16/12 with PWM-DITC in fault-free operation at $T = 5\,\mathrm{Nm}$ and $n = 400\,\mathrm{rpm}$ is shown in figure 6.3. In figure 6.3a the measured torque T_{sensor} from the torque transducer is shown. In figure 6.3b the radial pole forces $F_{\mathrm{rad,x}}$ and resulting synthesized unbalanced magnetic pull (UMP) $F_{\mathrm{r,ump}}$ are displayed. Figure 6.3c and figure 6.3d present the pole current trajectories of phase 2 and the phase current trajectories of all phases respectively.

In an ideal symmetrical machine the UMP during DITC operation would be zero. However, from figure 6.3b a non-zero net radial force (UMP) is visible. Similarly, the pole currents of phase 2 in figure 6.3c should be equally divided amongst each other. This implies that SRM-16/12 has physical manufacturing asymmetries.

6.2.1 Influence of Manufacturing Asymmetries

The manufacturing tolerances, especially in regard to rotor eccentricity affects the presented results. In figure 6.4a the pole voltages of phase 2 for one electrical period is displayed for SRM-16/12 during fault-free operation using DITC control.

Each stator pole is excited by its own distributed inverter. The corresponding pole current waveforms are shown in figure 6.4b. Even though all four pole voltage signals match each other very well, the individual pole currents are not symmetrical. A difference of $0.5\,\mathrm{A}$ at an average current of $3.5\,\mathrm{A}$ is present. These different current waveforms suggest an asymmetric pole inductance due to a rotor eccentricity present in SRM-16/12. These asymmetric pole current values are used to synthesize the radial pole forces, which then cause a peak UMP force of $F_{\mathrm{r,ump}} = 125\,\mathrm{N}$ as visible in figure 6.4c.

As DITC controls the flux linkage, the pole currents react according to their pole inductances. Therefore, a large pole inductance causes a smaller current, which is possible if the air-gap length is smaller compared to its neighboring stator pole of the same phase. Thus, to correctly synthesize the radial pole forces all individual pole inductances for SRM-16/12 have to be determined in a separate measurement.

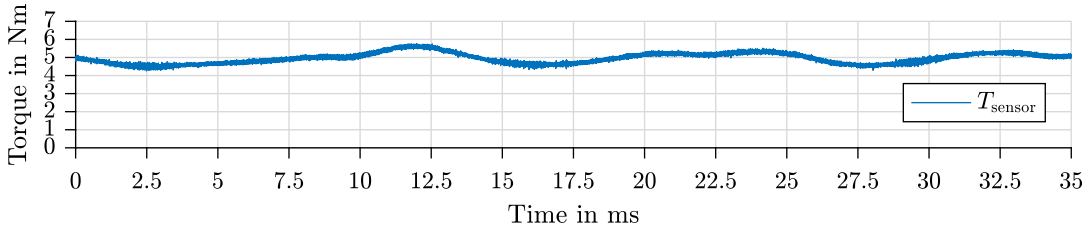

(a) Total torque

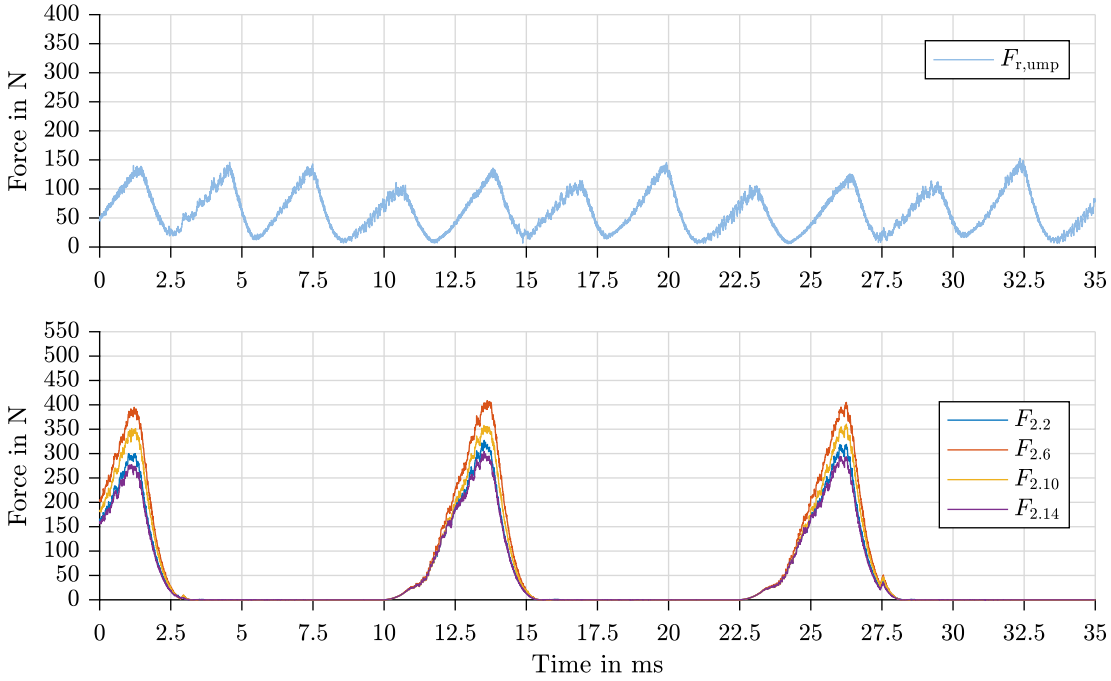

(b) Net radial force (UMP) and radial pole forces

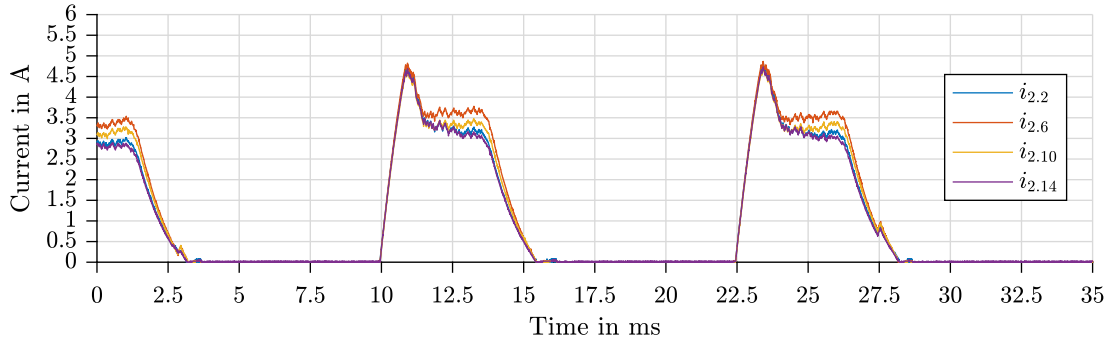

(c) Current per pole of phase 2

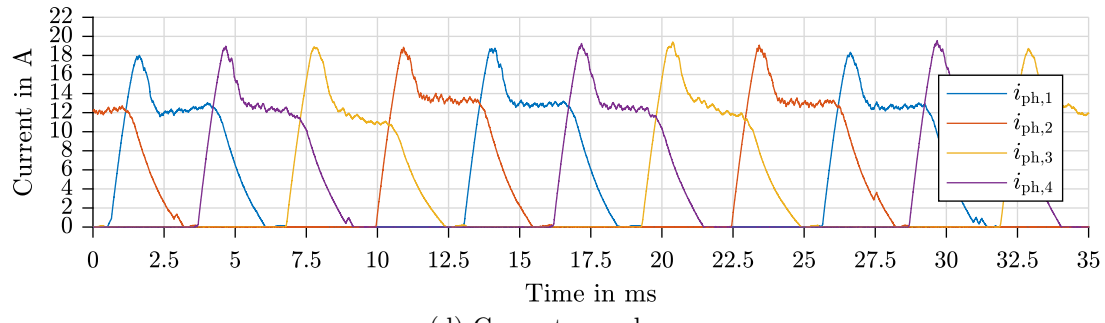

(d) Current per phase

Figure 6.3: SRM-16/12: Measurement results of DITC during fault-free operation at 5 Nm and 400 rpm

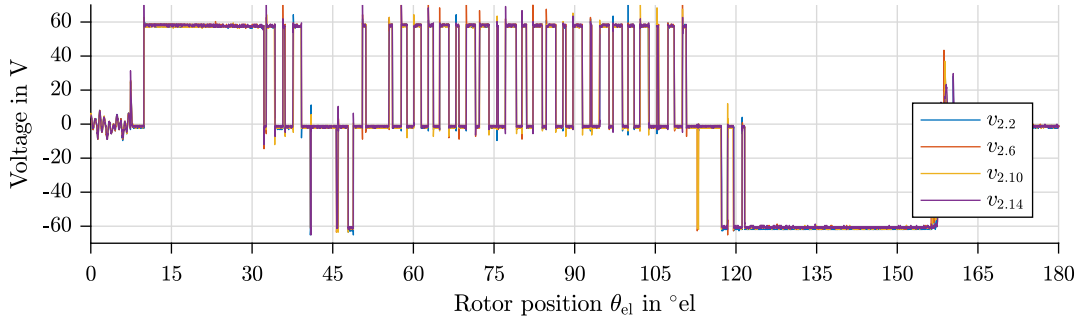

(a) Pole voltage measurement of phase 2

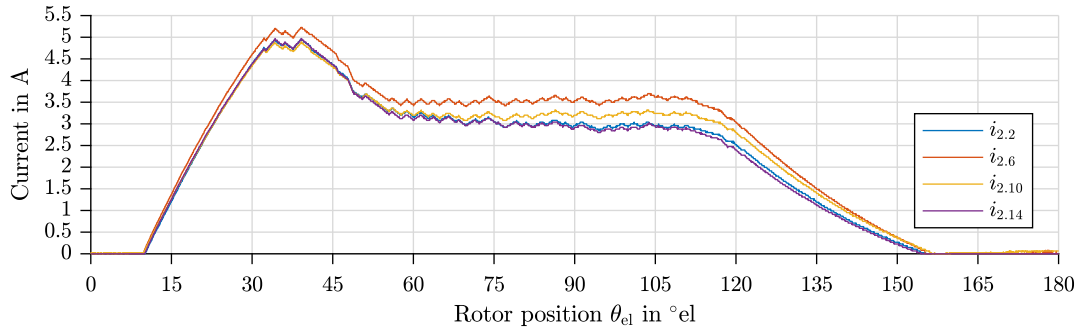

(b) Asymmetric pole currents of phase 2

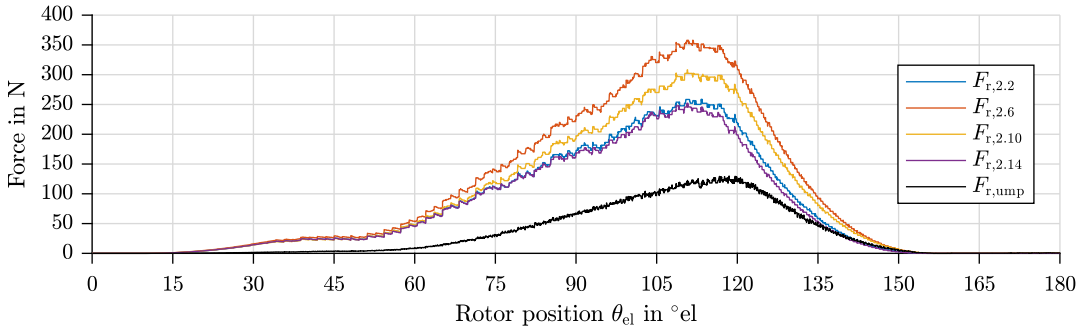

(c) Radial pole forces and resulting UMP of phase 2

Figure 6.4: SRM-16/12: Manufacturing asymmetries visible in the pole currents of phase 2 during fault-free DITC operation ($T = 5\,\mathrm{Nm}$ and $n = 350\,\mathrm{rpm}$)

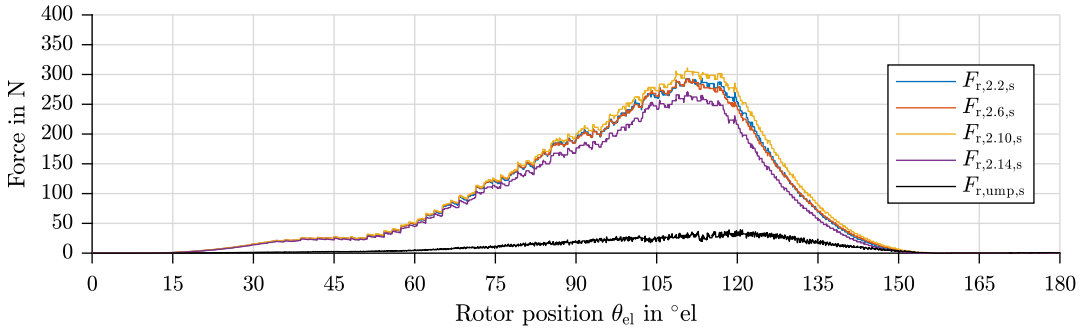

Figure 6.5: SRM-16/12: Corrected radial pole forces according to inductance pole asymmetries operating at fault-free DITC ($T = 5\,\mathrm{Nm}$ and $n = 350\,\mathrm{rpm}$)

The pole inductances for all phases are determined by applying a constant duty cycle $d_\mathrm{n} = 0.51$ and measuring the triangular current response as shown for four periods in figure 6.6a. From the current gradient and the applied voltage, the pole inductances are calculated as shown in figure 6.6c to figure 6.6f [47]. A clear difference in inductance between $L_{2.6}$ and its opposite pole $L_{2.14}$ of phase 2 is visible (figure 6.6d), which implies a difference in air-gap length. As the measured current waveforms in figure 6.6a are independent of the rotor position (rotor teeth position) the main asymmetric effect is caused by a static rotor eccentricity. A dynamic eccentricity would cause the pole currents to be different for each electrical period and repeat itself with the mechanical frequency. For SRM-16/12 the change in current values is nearly independent of the rotor position.

The pole inductances are summed up for the phase inductances, which are shown in figure 6.6b. Even though the individual pole inductances are very different, the phase inductances are very similar for three of the four phases. Rotor eccentricities of up to 10 % are common due to manufacturing tolerances as has been found in literature [36, 114]. The phase inductance of phase 3 is considerably higher than the other phases suggesting an additional manufacturing error. The pole inductances of phase 3 (figure 6.6e) implies that the manufacturer has accidentally added more windings to this phase, especially visible for pole 3.7.

Parallel connected coils of a phase in electrical machines cause an inherent current and therefore, force balancing [82, 115]. This is also true for SRMs using a distributed inverter. The distributed inverters act as flux linkage sources and not current sources. The radial force is dependent on the flux linkage in each pole, i.e. current multiplied with the inductance. Therefore, to synthesize the correct radial pole forces the asymmetric inductance distribution has to be taken into account. Using the asymmetric pole inductances and asymmetric pole currents to calculate the radial forces, the synthesized UMP force reduces to only 32 N as shown in figure 6.5. A further benefit of distributed inverters are that all poles of a phase are not directly connected in parallel, but are only connected via the dc-link. In case of a severe asymmetry or pole fault no circulating currents can be introduced between the poles of a phase, which is possible in normal parallel connected phases with phase-based inverters.

In chapter 6 all measurement radial forces $F_{\mathrm{rad},x,\mathrm{s}}$ with a subscript s have been synthesized with the asymmetric pole inductances. In the appendix section A.2.1 measurement supplements are added, where the radial forces with and without asymmetric pole inductance synthesis are displayed for all measurements presented in this chapter.

In figure 6.7 the synthesized measurement results for SRM-16/12 with DITC during fault-free operation considering the previously investigated pole inductance asymmetry is shown. As for the fault tolerant control to be discussed in the next sections the main contributing phases are the faulty phase (phase 1) and the preceding phase (phase 2). Therefore, the pole current and pole force values of these two phases are only shown in figure 6.7c and figure 6.7b. The estimated radial unbalanced magnetic pull, as displayed

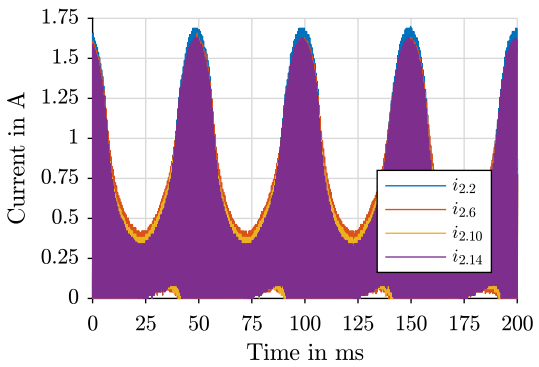

(a) Phase 2: Pole current waveforms with $d_n = 0.51$, $f_{PWM} = 2\,kHz$ and $100\,rpm$

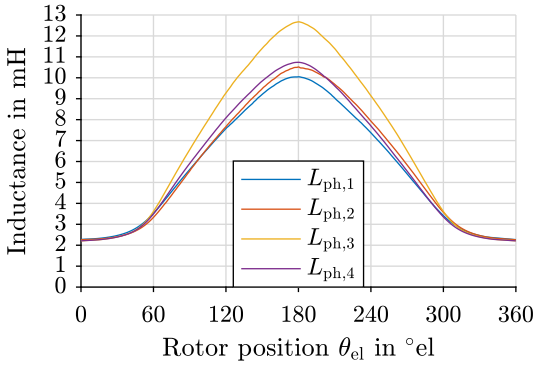

(b) Measured and smoothed average phase inductance profile

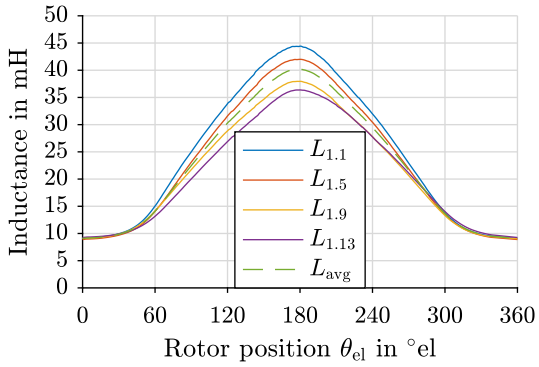

(c) Phase 1: Measured and smoothed per pole inductance profile

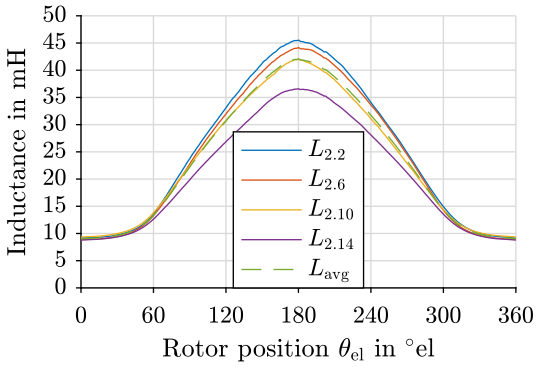

(d) Phase 2: Measured and smoothed per pole inductance profile

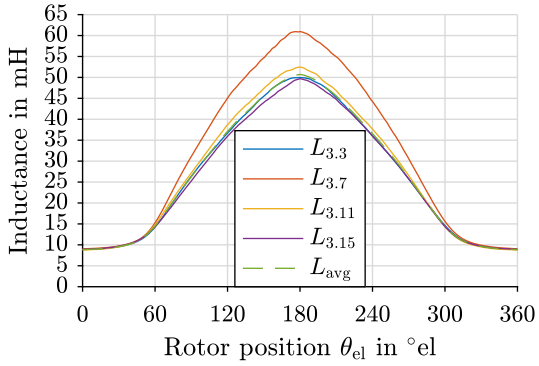

(e) Phase 3: Measured and smoothed per pole inductance profile

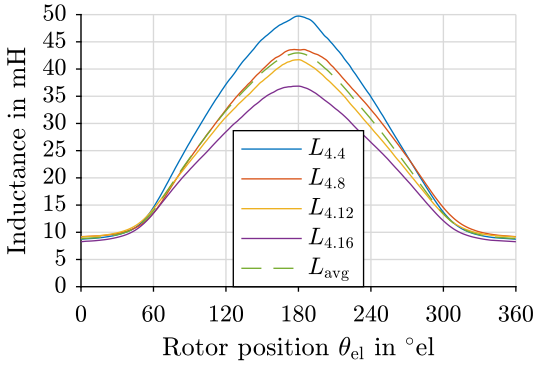

(f) Phase 4: Measured and smoothed per pole inductance profile

Figure 6.6: SRM-16/12: Asymmetric phase and pole inductances of all phases from current measurement at $n = 100\,rpm$, $d_n = 0.51$ and $f_{PWM} = 2\,kHz$

in figure 6.7b during fault-free operation, is below 50 N.

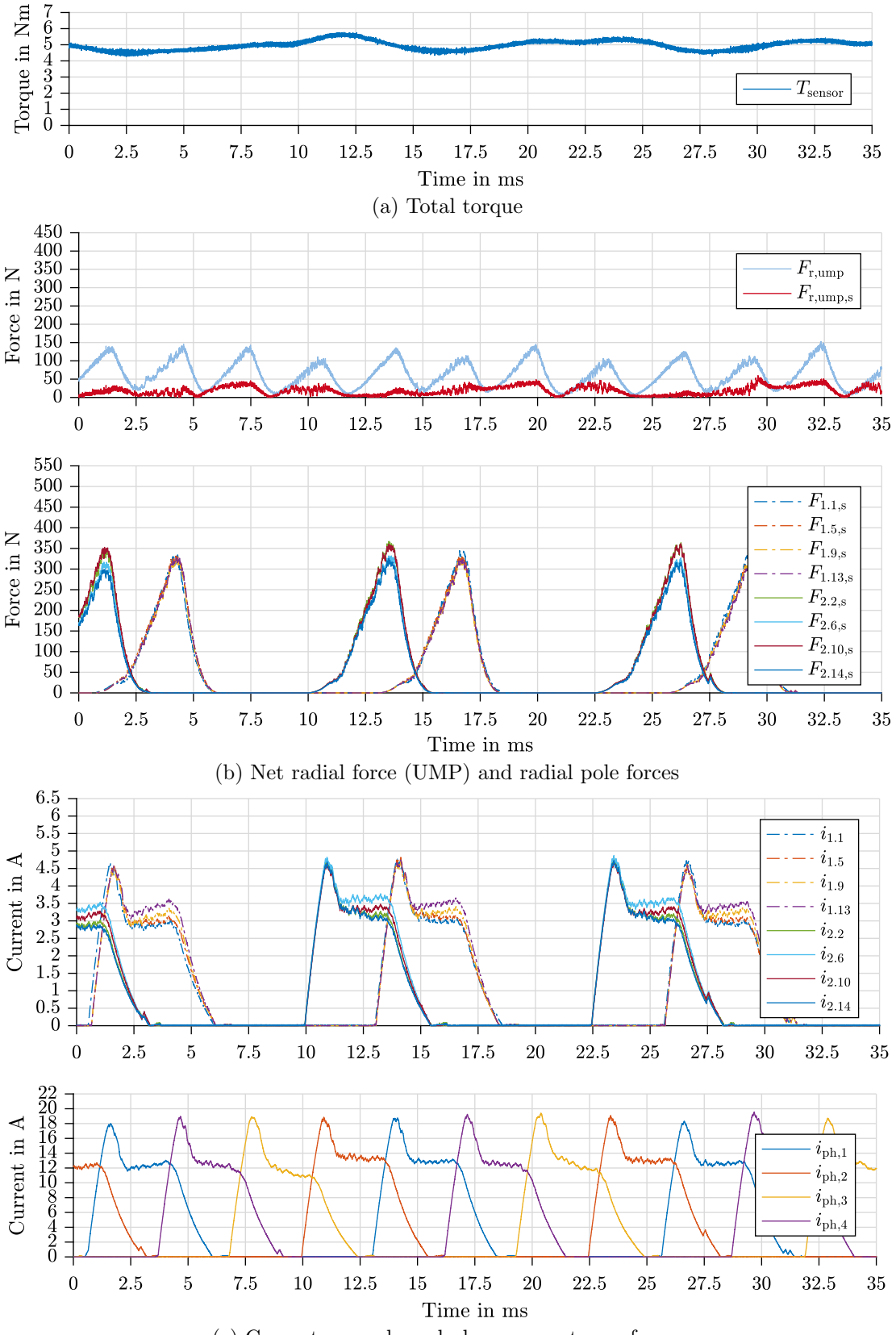

(a) Total torque

(b) Net radial force (UMP) and radial pole forces

(c) Current per pole and phase current waveforms

Figure 6.7: SRM-16/12: Measurement results of DITC during fault-free operation at 5 Nm and 400 rpm (waveforms corrected with asymmetric pole inductances)

6.3 Direct Instantaneous Torque Control - Single Pole Fault

In this section measurement results operating with PWM-DITC control during single pole fault are presented. The differences between a control algorithm with and without fault detection are presented. Furthermore, a measurement operating at the introduced EFC control is presented.

6.3.1 DITC With and Without Fault Detection

Figure 6.8 and figure 6.9 show two results where SRM-16/12 is operated with DITC during a single pole fault. In the first measurement no fault detection is implemented, therefore, the control does not react to the pole fault. This results in a reduced torque production of the faulty phase (phase 1) as the reference torque is divided amongst four poles of a phase, but only three poles are active to produce the torque. The failure of pole 1.1 causes an unbalanced radial force of 250 N visible in figure 6.8b.

By implementing fault detection methods [32] the DITC torque sharing algorithm reacts to the fault and, therefore, increases the torque each of the remaining healthy poles have to produce as shown in the measurement in figure 6.9. In contrast to the previous experiment the phase current value of phase 1 is more similar to the other phases especially in the single conduction period. In single conduction the current changes from 10 A to slightly above 12 A. The increased height of the pole currents are also clearly visible in figure 6.9c.

The overall torque in figure 6.9a compared to figure 6.8a is more constant as all phases produce the required torque. The increased torque production of pole 1.9 causes an increase of the unbalanced radial force by 48 %, which results in an absolute peak value of 370 N visible in figure 6.9b. This resembles the radial force to be balanced by the implemented fault tolerant control algorithms.

The faulty pole and the resulting unbalanced distribution of magnetic flux in the machine causes visible coupling in figure 6.9c between the faulty phase (phase 1) and its preceding phase (phase 2) compared to figure 6.7c ($13.4\,\text{ms} < t < 15.2\,\text{ms}$). As soon as the faulty phase conducts current the poles $p_{2.6}$ and $p_{2.14}$ are coupled in a subtractive way. In the shown experiment the coupling effect is not considered in the FPGA control, which results in the pole current $i_{2.6}$ and $i_{2.14}$ to decrease compared to $i_{2.2}$ and $i_{2.10}$. The coupling effect is symmetrical around the faulty pole, therefore the opposite poles of the preceding phase (phase 2) are coupled nearly equally. The other two poles $p_{2.2}$ and $p_{2.14}$ are coupled additively resulting in a slightly higher pole current. The symmetrical coupling of opposite poles is visible in the radial pole forces $F_{2.2,\text{s}}$ and $F_{2.10,\text{s}}$, which are considerably larger than

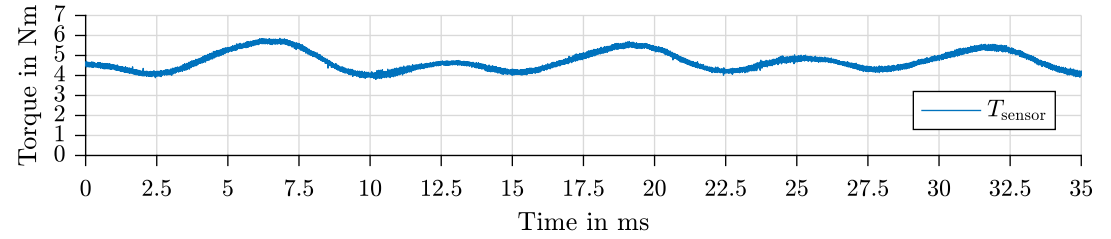

(a) Total torque

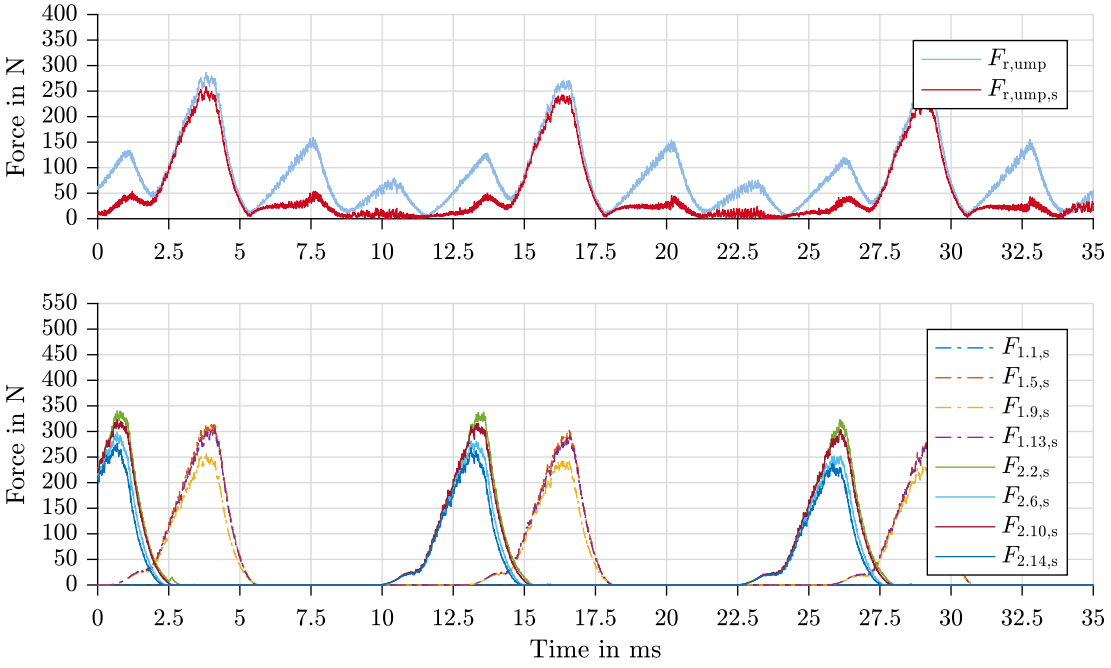

(b) Net radial force (UMP) and radial pole forces

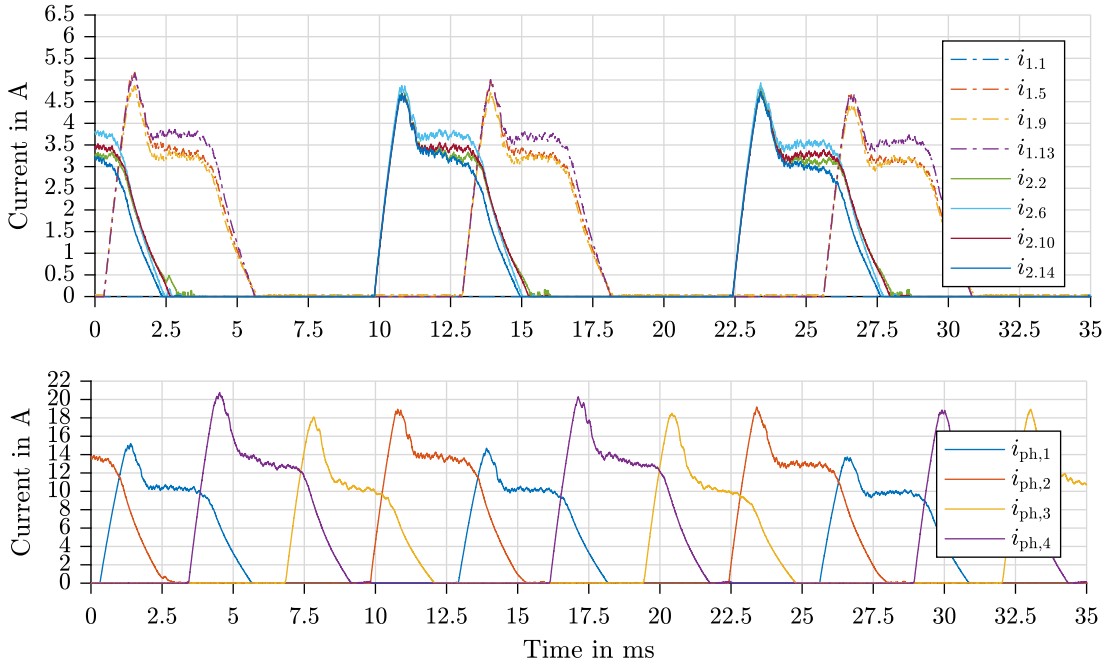

(c) Current per pole and phase current waveforms

Figure 6.8: SRM-16/12: Measurement results of DITC during fault operation without fault detection at 5 Nm and 400 rpm (1̲10-1)

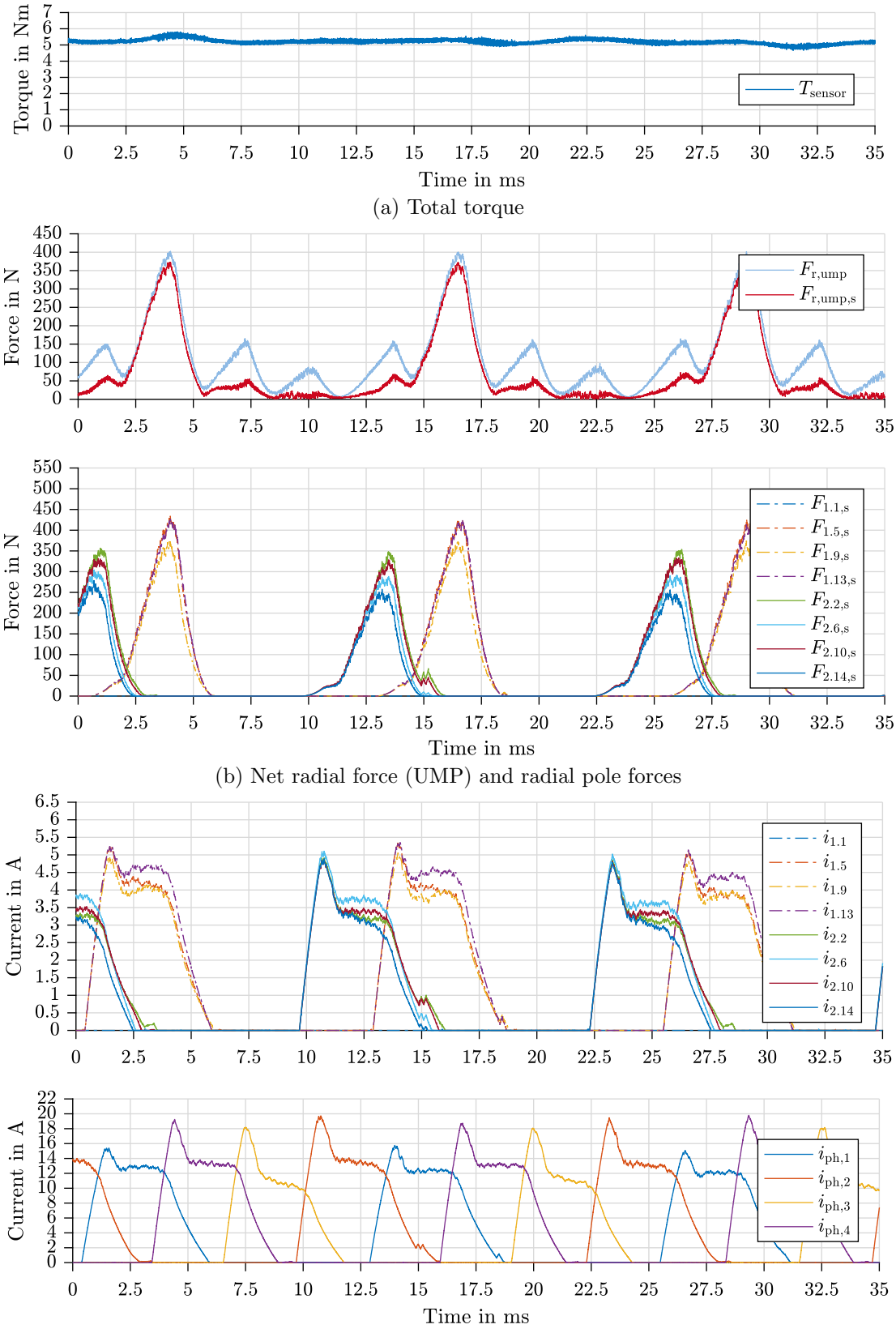

(a) Total torque

(b) Net radial force (UMP) and radial pole forces

(c) Current per pole and phase current waveforms phase

Figure 6.9: SRM-16/12: Measurement results of DITC during fault operation with fault detection at 5 Nm and 400 rpm (1$\underline{1}$0-1)

the forces $F_{2.6,\mathrm{s}}$ and $F_{2.14,\mathrm{s}}$. As the opposite forces are nearly equal to each other there exists only a small UMP of 50 N from the preceding phase (phase 2). Considering the preceding phase (phase 2) is actually operated at normal DITC, the current and force trajectories of all poles should be equal. This change in radial forces does not influence the unbalanced magnetic pull, but will excite additional vibrational modes, i.e. Mode 2 [32].

6.3.2 Elementary Fault Control - Critical Pole Turn off

The first method to reduce the UMP during single pole fault is the *elementary fault control* (EFC), whereby the critical pole $p_{1.9}$ opposite the fault pole $p_{1.1}$ is turned off [32]. The torque sharing algorithm distributes the reference torque amongst the remaining two poles of the faulty phase without producing an unbalanced magnetic pull, as is introduced simulatively in section 5.2. The measurement result for EFC at $T^*_{\mathrm{ref}} = 5\,\mathrm{Nm}$ and $n = 400\,\mathrm{rpm}$ is presented in figure 6.10.

In figure 6.10c the pole current values are displayed. Of the faulty phase (phase 1) only poles $p_{1.5}$ and $p_{1.13}$ are active. The phase 1 pole currents of 5.5 A to 6 A, necessary for torque production, are very similar to the simulated currents shown in figure 5.5d. One difference in the current waveforms for the preceding phase (phase 2) is visible. In the measurements the pole currents split into two currents which reduce strongly, while the remaining two currents increase to create a small peak. This prolonged current waveform with the peak is also visible in the phase current between $13\,\mathrm{ms} < t < 17.3\,\mathrm{ms}$. These current waveforms are explainable by a considerable increase in mutual coupling amongst the poles. This pole coupling is caused by the flux direction of the active poles, $p_{1.5}$ and $p_{1.13}$, causing an excessive flux in the machine, which increases the current in poles $p_{2.2}$ and $p_{2.10}$. As the opposite poles experience the same coupling, symmetrical around the faulty pole $p_{1.1}$, a balanced radial force distribution exists, causing a UMP well below 50 N.

The EFC control uses the 4polesA LUT, i.e. the same LUT as in fault-free operation, which results in an uneven torque waveform. The measurement with EFC control is only done with the 4polesA LUT and no additional coupling compensation. To decrease the torque ripple an additional 2polesA LUT as described in section 5.2 would have to be used. Furthermore, the pole coupling effects need to be incorporated as introduced in the next section for S-RFMC.

Nonetheless, the UMP is minimized as visible in figure 6.10b. The remaining net radial force $F_{\mathrm{r,ump,s}}$ reduces from 370 N to below 50 N. EFC is an effective method for SRM partial load operation. Once the thermal limit of the remaining two poles of the faulty phase ($p_{1.5}$ and $p_{1.13}$) is reached due to the increased current loading, S-RFMC is required to increase the torque production by better distributing the ohmic losses amongst more poles.

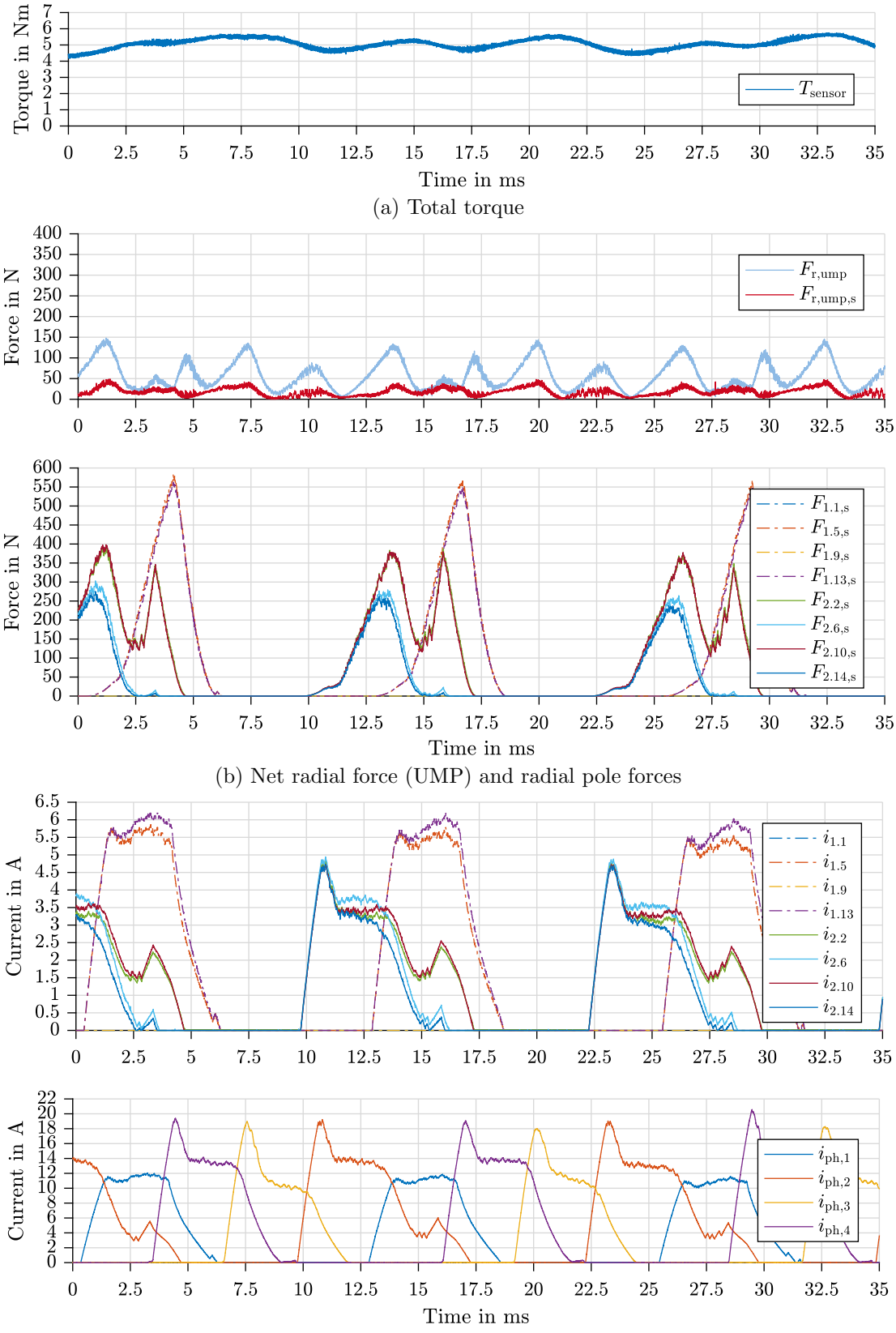

(a) Total torque

(b) Net radial force (UMP) and radial pole forces

(c) Current per pole and phase current waveforms

Figure 6.10: SRM-16/12: Measurement results of DITC-EFC (with 4polesA-LUT) during fault operation with critical pole turn-off at 5 Nm and 400 rpm (1$\underline{1}$0-1)

6.4 Simplified Radial Force Minimization Control - Single Pole Fault

This section presents test bench results for the proposed simplified radial force minimization control (S-RFMC), which has been introduced in section 5.4. Four different coil arrangements in SRM-16/12 in regard to the faulty phase (phase 1) are presented and the coupling between the poles is investigated.

6.4.1 Compensating for Coil Orientation and Mutual Coupling

As introduced in section 3.4, there exists additive and subtractive mutual coupling in SRMs. During fault operation the effect of coupling increases due to the asymmetric flux distribution in the machine. Especially the neighboring coils to the faulty pole are affected by the coil orientation. In S-RFMC the critical radial force $F_{1.9}$ is mainly compensated by the force $F_{2.2}$ of the preceding phase (phase 2). The goal of the control algorithm remains to match the vector sum of forces $F_{2.2}$ and $F_{2.14}$ to $F_{1.9}$.

If no coupling between the poles is considered, the estimated flux linkage and estimated radial forces are incorrect. As poles 2.2 and 2.14 are the main contributors for UMP compensation, the coupling influence on these two poles is considered. The additive and subtractive effects between phases as introduced in section 3.4 holds for pole 2.14, however, for pole 2.2 the opposite is true, because of its faulty neighboring pole 1.1. For pole 2.2 a non-alternating neighboring coil orientation, as displayed in figure 6.11, results in an additive coupling instead of the expected subtractive coupling. From figure 6.11 it is visible that even though both poles 2.2 and 2.14 are part of the same phase and have the same coil orientation in respect to their neighboring poles, the coupling influence from the faulty phase (phase 1) are opposite. The following discussion is based on pole 2.2, but can be applied analogously to pole 2.14.

In a non-alternating phase orientation (i.e. 1$\underline{1}$x or 0$\underline{0}$x) pole 2.2 experiences an additive coupling effect from the flux linkage of phase 1 poles, while pole 2.14 experiences subtractive coupling as visualized in figure 6.11. This causes the flux linkage $\psi_{2.2}$ and radial force $F_{2.2}$ to be higher than desired by the control if coupling is not considered, as the excitation of the faulty phase (phase 1) influences the preceding phase (phase 2). Analogously, the force of pole 2.14, $F_{2.14}$, will be lower than expected. This results in a high UMP as $F_{2.2}$ over compensates the critical force $F_{1.9}$ and thus, creates a new resulting net radial force. The synthesized UMP $F_{\mathrm{r,ump,s}}$ increases during compensation as seen in figure 6.12a. The individual radial forces are displayed in figure 6.12c. The overcompensation of $F_{1.9}$ in figure 6.12c results from a too high magnetization from the control, i.e. pole current $i_{2.2}$ is too high, while force $F_{2.14}$ is nearly zero. The control reduces the magnetization and pole current $i_{2.14}$, shown in figure 6.12e, as the flux linkage in $p_{2.14}$ is overestimated by

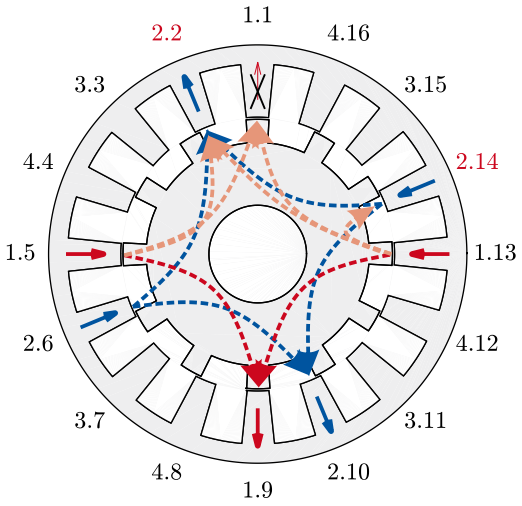

Figure 6.11: SRM-16/12: Cross section with non-alternating coil arrangement showing flux directions of phase 1 and phase 2 during single pole fault of $p_{1.1}$ indicating magnetic flux distribution of phase 1 (red) and phase 2 (blue) with pole coupling of phase 1 onto poles $p_{2.2}$ (additive) and $p_{2.14}$ (subtractive)

the control when coupling is not considered.

For S-RFMC to work correctly, it is unavoidable to incorporate pole coupling into the force control. In figure 6.12b the resulting UMP and in figure 6.12d the radial forces are shown when mutual coupling is considered. The radial force $F_{2.2}$ matches the critical force $F_{1.9}$. The currents $i_{2.2}$ and $i_{2.14}$ are controlled according to the influence experienced from the faulty phase (phase 1). Investigations have shown that the influence of the following phase (phase 4) can be neglected for this machine even though it is active during the radial force minimization section. The main contributor by far is the faulty phase (phase 1) with its asymmetric flux distribution.

The primary possibility to consider mutual coupling is by using a LUT, which contains the coupling factors between the contributing poles. In figure 6.13 the flux linkage $\psi_{2.2}$ of pole 2.2 versus rotor position of phase 1 $\theta_{\mathrm{el,ph1}}$ resulting from a FEA simulation is shown. $\psi_{2.2,\mathrm{self}}$ represents the self-flux linkage of phase 2 when no coupling is considered and only pole 2.2 is magnetized at $i_{2.2} = 2.8\,\mathrm{A}$. The equivalent self-flux linkage of phase 1, for pole 1.9 is $\psi_{1.9,\mathrm{self}}$ with an applied pole current of 5.1 A. The flux linkage of pole 2.2 when considering the coupling influence of phase 1 is shown by the trajectory of $\psi_{2.2}$. From the difference between $\psi_{2.2}$ and $\psi_{2.2,\mathrm{self}}$ the additive influence, between the rotor positions 45° and 210°, is clearly visible. Thus, to correctly estimate flux linkage $\psi_{2.2}$ the coupling of phase 1 is necessary.

As introduced in the SRM model considering phase coupling in figure 3.10, the non-linear flux linkage components can generally be formulated as in equation (6.1). Thereby, a general coupling factor $k_{12}(i_1,i_2,\theta_{\mathrm{el}})$ is introduced in equation (6.2), which couples the

self-flux linkage values $\psi_{11}(i_1)$ and $\psi_{22}(i_2)$. The factor $k_{12}(i_1,i_2,\theta_{el})$ is extracted from FEA and either stored as a LUT or formulated as an equation.

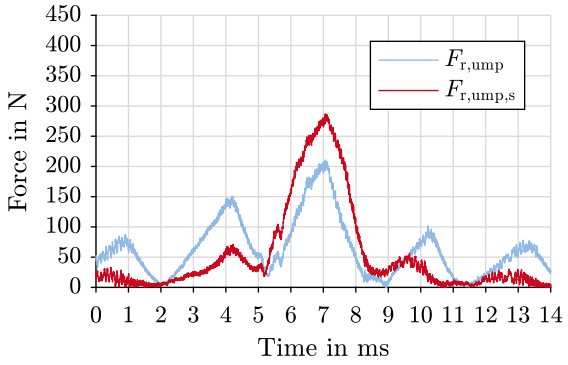

(a) Net radial force (UMP) without considering coupling

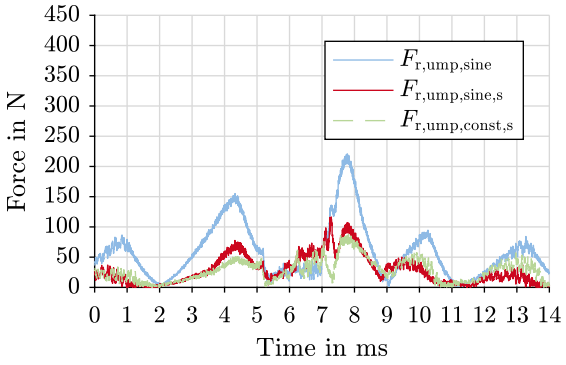

(b) Net radial force (UMP) considering mutual pole coupling

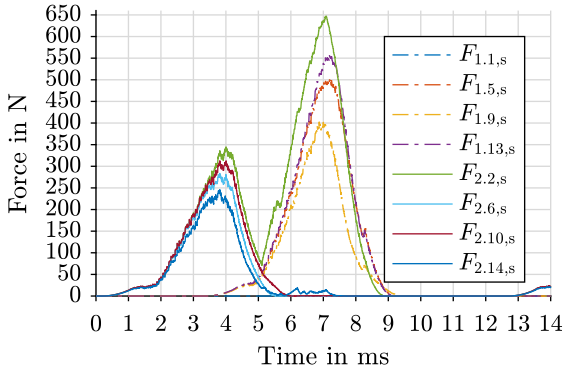

(c) Radial pole forces without considering coupling

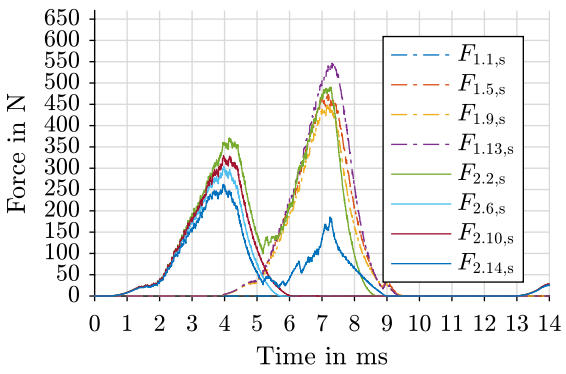

(d) Radial pole forces considering mutual pole coupling with sine-LUT

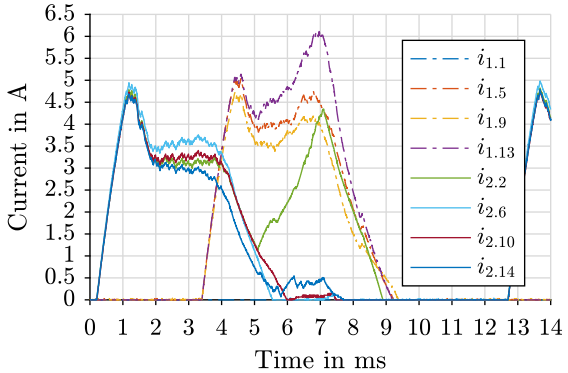

(e) Pole currents for phase 1 and 2 without considering coupling

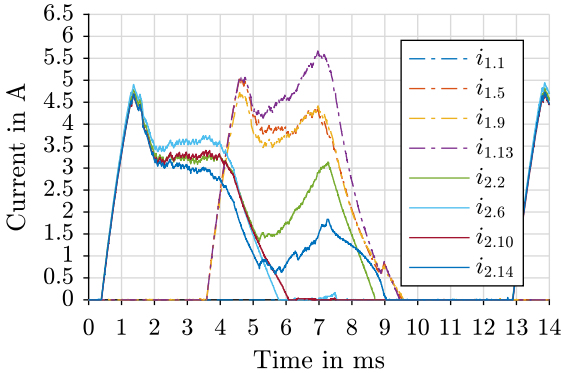

(f) Pole currents for phase 1 and 2 considering mutual pole coupling with sine-LUT

Figure 6.12: SRM-16/12: Measurement comparison with and without considering pole coupling between phase 1 and phase 2 for non-alternating coil arrangement, $k_{mc,2.2}$ and $k_{mc,2.14}$ either as sine-LUT or constant

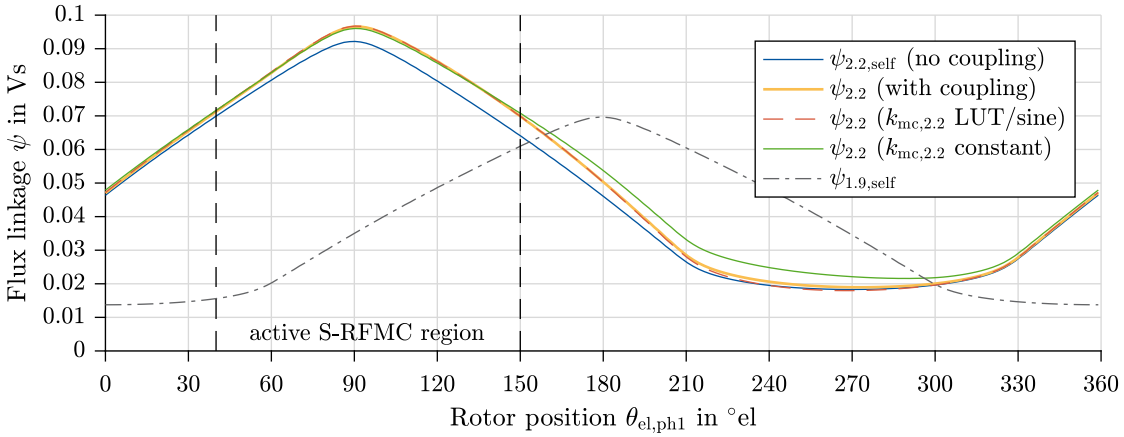

Figure 6.13: Simulation of flux linkage $\psi_{2.2}$ in pole 2.2 considering only self inductance and mutual coupling for non-alternating coil orientation at $i_{2.2} = 2.8\,\mathrm{A}$ and $i_{1.9} = 5.1\,\mathrm{A}$, also shown are two compensation approaches with $k_{\mathrm{mc,2.2}}$ resembled by a constant ($k_{\mathrm{mc,2.2}} = 0.11$) and by a sine-LUT ($k_{\mathrm{mc,2.2}} = 0.07 \cdot \sin(\theta_{\mathrm{el}}) + 0.06$)

$$\psi_1(i_1,i_2) = \psi_{11}(i_1) + \psi_{12}(i_1,i_2) \tag{6.1}$$

$$\psi_1(i_1,i_2) = \psi_{11}(i_1) + k_{12}(i_1,i_2,\theta_{\mathrm{el}}) \cdot \psi_{22}(i_2) \tag{6.2}$$

$$\psi_{2.2}(i_{2.2},i_{1.9}) = \psi_{2.2,\mathrm{self}}(i_{2.2}) + k_{\mathrm{mc,2.2}}(i_{2.2},i_{1.9},\theta_{\mathrm{el}}) \cdot \psi_{1.9,\mathrm{self}}(i_{1.9}) \tag{6.3}$$

$$\psi_{2.14}(i_{2.14},i_{1.9}) = \psi_{2.14,\mathrm{self}}(i_{2.14}) + k_{\mathrm{mc,2.14}}(i_{2.14},i_{1.9},\theta_{\mathrm{el}}) \cdot \psi_{1.9,\mathrm{self}}(i_{1.9}) \tag{6.4}$$

For SRM-16/12 the coupling factors are defined as $k_{\mathrm{mc,2.2}}(i_{2.2},i_{1.9},\theta_{\mathrm{el}})$ for pole 2.2 and $k_{\mathrm{mc,2.14}}(i_{2.14},i_{1.9},\theta_{\mathrm{el}})$ for pole 2.14. The respective formulations for a single pole fault of pole 1.1 are displayed in equation (6.3) and equation (6.4). In figure 6.13 FEA results show that a sinusoidal ($k_{\mathrm{mc,2.2}} = a \cdot \sin(\theta_{\mathrm{el}}) + b$) and constant ($k_{\mathrm{mc,2.2}} = c$) approximation of $k_{\mathrm{mc,2.2}}$ fits the coupled value of $\psi_{2.2}$. For the sinusoidal equation $a = 0.07$ and $b = 0.06$ is chosen, while for the constant approximation $c = 0.11$.

Applying the constant factor results in an accurate flux linkage to the coupled flux linkage in the region $0° < \theta_{\mathrm{el,ph1}} < 140°$. The compensation region of S-RFMC is operating point dependent, however, less than $\theta_{\mathrm{el,ph1}} < 150°$. Thus, if calculation resources are limited, using a constant factor to fit the coupling can be considered.

The coupling factors $k_{\mathrm{mc,2.2}}$ and $k_{\mathrm{mc,2.14}}$ are defined from FEA results shown in figure 6.14 for various pole current values, $0\,\mathrm{A} < i_{2.2}/i_{2.14} < 3.4\,\mathrm{A}$ and $1.7\,\mathrm{A} < i_{1.9} < 5.1\,\mathrm{A}$. For pole current values $i_{2.2}/i_{2.14} < 3\,\mathrm{A}$ the coupling factors are close to a sinusoidal trajectory and quite independent of phase 1 ($i_{1.9}$) current. The previously presented sine- and constant

factor $k_{\mathrm{mc},2.2}$ is a fit from the graph figure 6.14a with respect to the self-flux linkage $\psi_{1.9,\mathrm{self}}$ and $\psi_{2.2,\mathrm{self}}$ according to equation (6.3).

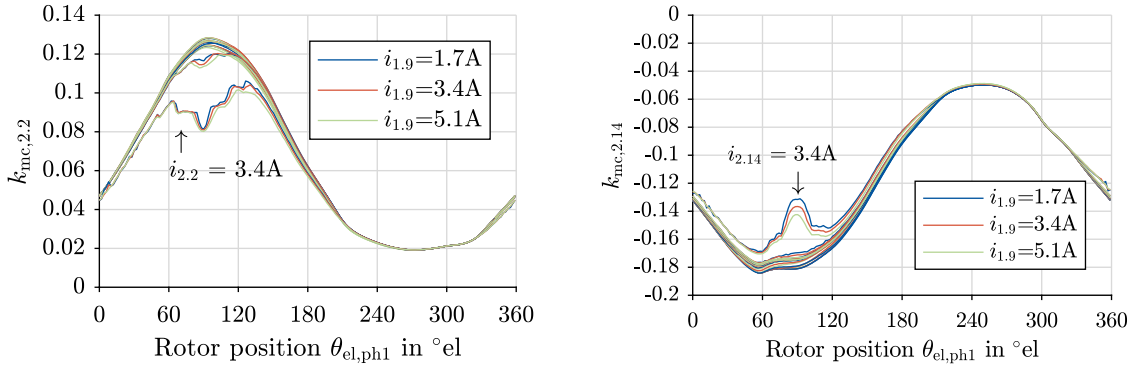

(a) $k_{\mathrm{mc},2.2}$: influence of phase 1 on pole 2.2

(b) $k_{\mathrm{mc},2.14}$: influence of phase 1 on pole 2.14

Figure 6.14: Simulation results for various current values ($0\,\mathrm{A} < i_{2.2}/i_{2.14} < 3.4\,\mathrm{A}$ and $1.7\,\mathrm{A} < i_{1.9} < 5.1\,\mathrm{A}$) showing the influence phase 1 ($i_{1.9}$) current has on the mutual coupling factor $k_{\mathrm{mc},2.2}$ and $k_{\mathrm{mc},2.14}$ for non-alternating coil orientation

In figure 6.12b the resulting UMP values are shown when using the sine and constant $k_{\mathrm{mc},2.2}$ factor. The radial forces in figure 6.12d and pole currents in figure 6.12f are corresponding to the sine-LUT factor.

For S-RFMC to work effectively, the coupling of the faulty phase (phase 1) onto the compensating poles ($p_{2.2}$ and $p_{2.14}$) has to be compensated for by adding the coupling effect in the flux linkage estimation. The rotor position and pole current $i_{\mathrm{pl},2.2}$ determine the value of the coupling factors $k_{\mathrm{mc},2.2}$ and $k_{\mathrm{mc},2.14}$. Therefore, the factors can readily be stored in a LUT. Furthermore, as the primary contributor for the coupling factors is the rotor position, the LUT can be reduced to a position dependent equation.

For SRM-16/12 both approaches, *sine* and *constant* term are valid and fit the reality well for pole current values of $i_{\mathrm{pl},2.2} < 3\,\mathrm{A}$. At the nominal operating point of $T_{\mathrm{nom}} = 9.5\,\mathrm{Nm}$ a pole current of $i_{\mathrm{pl},2.2} < 4.5\,\mathrm{A}$ is required to compensate the critical pole. The higher current values, $3\,\mathrm{A} < i_{2.2}/i_{2.14} < 4.5\,\mathrm{A}$, reduce the coupling factor for SRM-16/12 (see figure 6.14). For an effective fault control at nominal operation the influence of the pole currents $i_{2.2}/i_{2.14}$ should be incorporated into the coupling factors. If a one dimensional sine-LUT, which is only dependent on the rotor position is sufficient, or if the influence of the pole current $i_{2.2}/i_{2.14}$ has to be incorporated by adding a second dimension to the coupling LUT has to be determined individually for each machine considered for S-RFMC operation.

6.4.2 S-RFMC Measurement Result Comparison

To verify the proposed simplified radial force minimization control (S-RFMC) it is implemented on the FPGA of the rapid prototyping hardware (dSPACE MicroLabBox) and run on the test bench presented in section 6.1.

A single pole fault in SRM-16/12 operating with PWM-DITC and fault detection at 5 Nm and 400 rpm results in a UMP of 370 N as shown in figure 6.9. This UMP is the reference value, which has to be reduced by the implemented fault tolerant algorithm. In figure 6.15 to figure 6.19 measurements of SRM-16/12 with non-alternating (phase sequence 2$\underline{1}$4-3: 0$\underline{0}$0-1, 0$\underline{0}$0-0, 1$\underline{1}$0-1) and alternating (0$\underline{1}$0-1, 0$\underline{1}$1-1) coil orientations between the faulty phase (phase 1) and the preceding phase (phase 2) are presented. The region during which S-RFMC is active, e.g. $14.64\,\text{ms} < t < 16.75\,\text{ms}$, is indicated in the graphs in figure 6.15 by dashed lines. The remaining time SRM-16/12 is operated with PWM-DITC.

The characteristic UMP shape, already seen in the simulations for RFMC (see figure 5.11) and S-RFMC (see figure 5.27), can also be seen in these measurements. There are always two humps during the uncontrolled radial force sections just before and after S-RFMC is active. The first hump is controlled by the S-RFMC turn-on angle $\theta_{\text{on}}^{\text{S-RFMC}}$. To reduce this hump further, S-RFMC would have to be turned on earlier. To reduce the second UMP hump the S-RFMC turn-off angle $\theta_{\text{off}}^{\text{S-RFMC}}$ would have to be increased, so that the active radial force control is active for a longer period, as discussed in section 5.3.3. In all measurements, when using S-RFMC, a considerable reduction of UMP from 370 N to below 120 N is observed. During the region, where S-RFMC actively controls the radial pole forces, the UMP is well below 100 N, usually around 50 N confirming the controls effectiveness during single pole fault.

The active asymmetric force control is visible in figure 6.15b with the corresponding pole current waveforms in figure 6.15c. Especially the pole currents show a deviation to the fault-free DITC waveform. The currents $i_{2.2}$ and $i_{2.14}$ stop demagnetizing and start increasing again as soon as the control switches to S-RFMC. The critical force ($F_{1.9}$) is mainly compensated by pole 2.2 ($F_{2.2}$), while force $F_{2.14}$ only adds a spatial offset to exactly balance $F_{1.9}$ due to the geometrical arrangement of each pole. The necessary compensation pole currents, $i_{2.2}$ and $i_{2.14}$, are clearly visible as two peaks in the current waveform in figure 6.15c.

Once the control switches back to PWM-DITC at $\theta_{\text{off}}^{\text{RFMC}}$ the *phase priority stack* of DITC is active again (section 2.3.2). At this time the following phase (phase 3) has highest priority, i.e. is the torque producing phase. Therefore, all other phases, preceding phase (phase 2) with pole currents $i_{2.2}$ and $i_{2.14}$ and faulty phase (phase 1) with pole currents $i_{1.5}$, $i_{1.9}$ and $i_{1.13}$, are demagnetized as long as the reference torque can still be produced. If at $\theta_{\text{off}}^{\text{RFMC}}$ negative torque is being produced by the preceding phase (phase 2) it is compensated for by the following phase (phase 3).

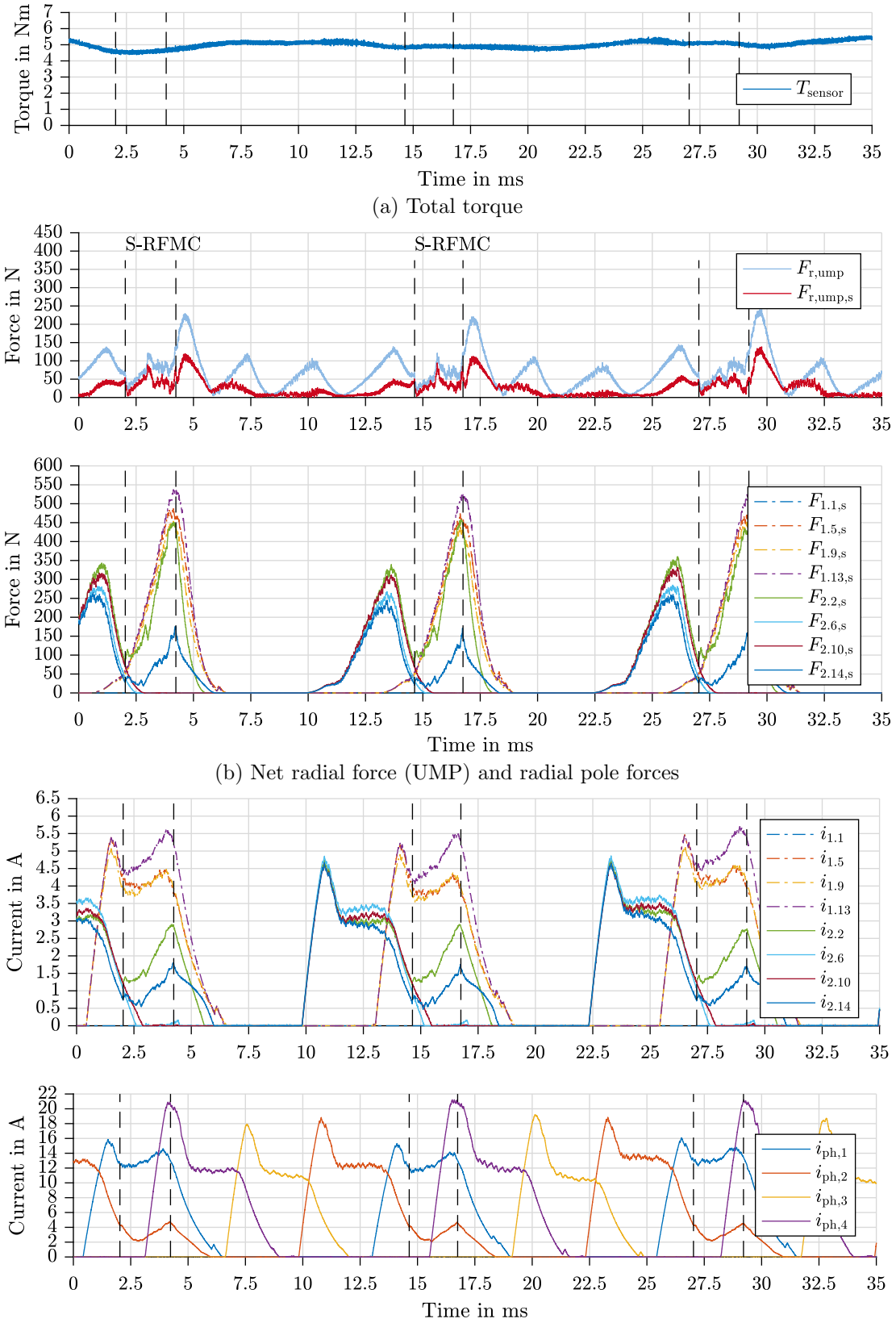

(a) Total torque

(b) Net radial force (UMP) and radial pole forces

(c) Current per pole and phase current waveforms

Figure 6.15: SRM-16/12 (000-1): Measurement results of S-RFMC during fault operation at 5 Nm and 400 rpm considering mutual coupling with a LUT representing the sine-term factor for $k_{\text{mc},2.2}$ and $k_{\text{mc},2.14}$

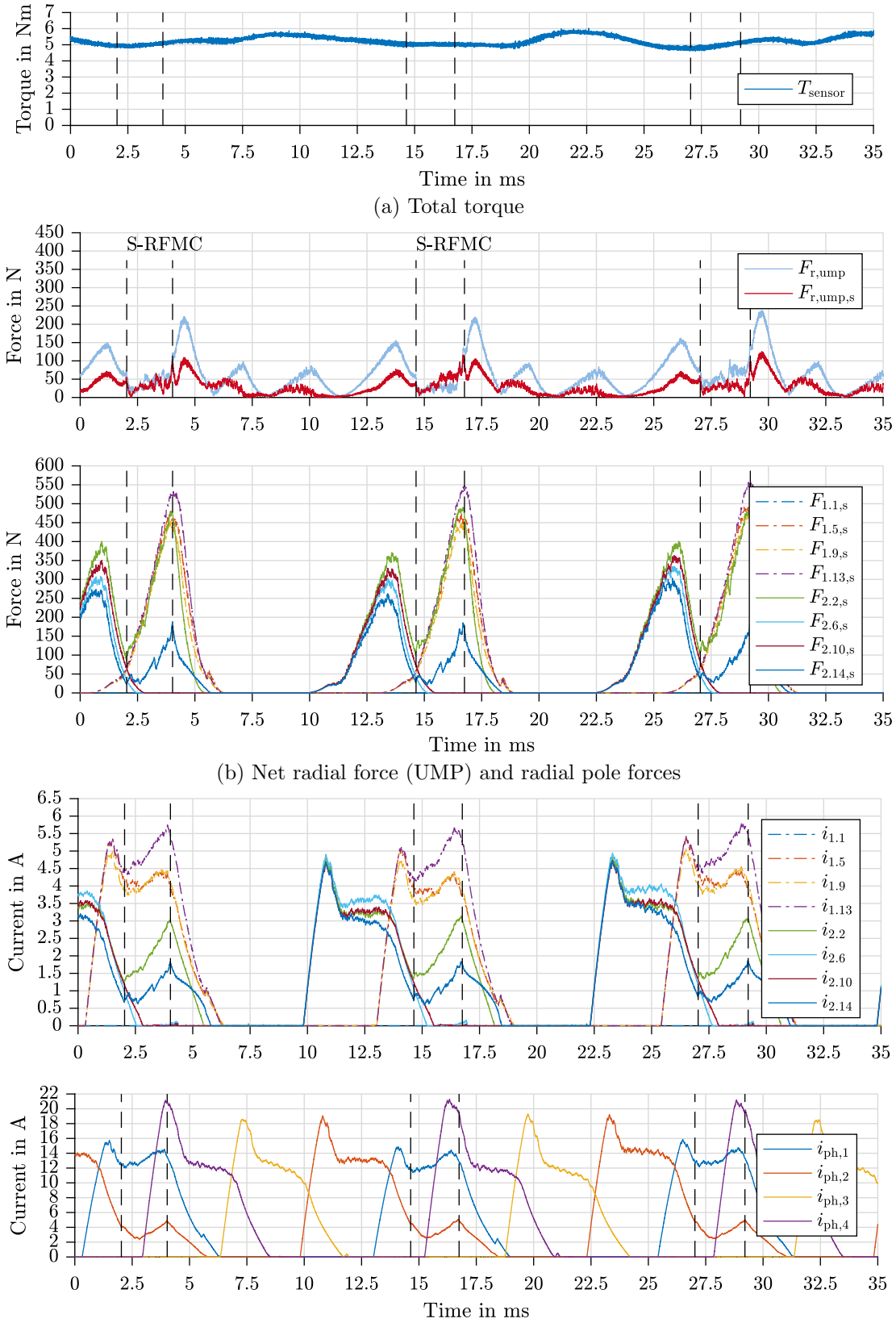

(a) Total torque

(b) Net radial force (UMP) and radial pole forces

(c) Current per pole and phase current waveforms

Figure 6.16: SRM-16/12 (00̲0-0): Measurement results of S-RFMC during fault operation at 5 Nm and 400 rpm considering mutual coupling with a LUT representing the sine-term factor for $k_{\text{mc,2.2}}$ and $k_{\text{mc,2.14}}$

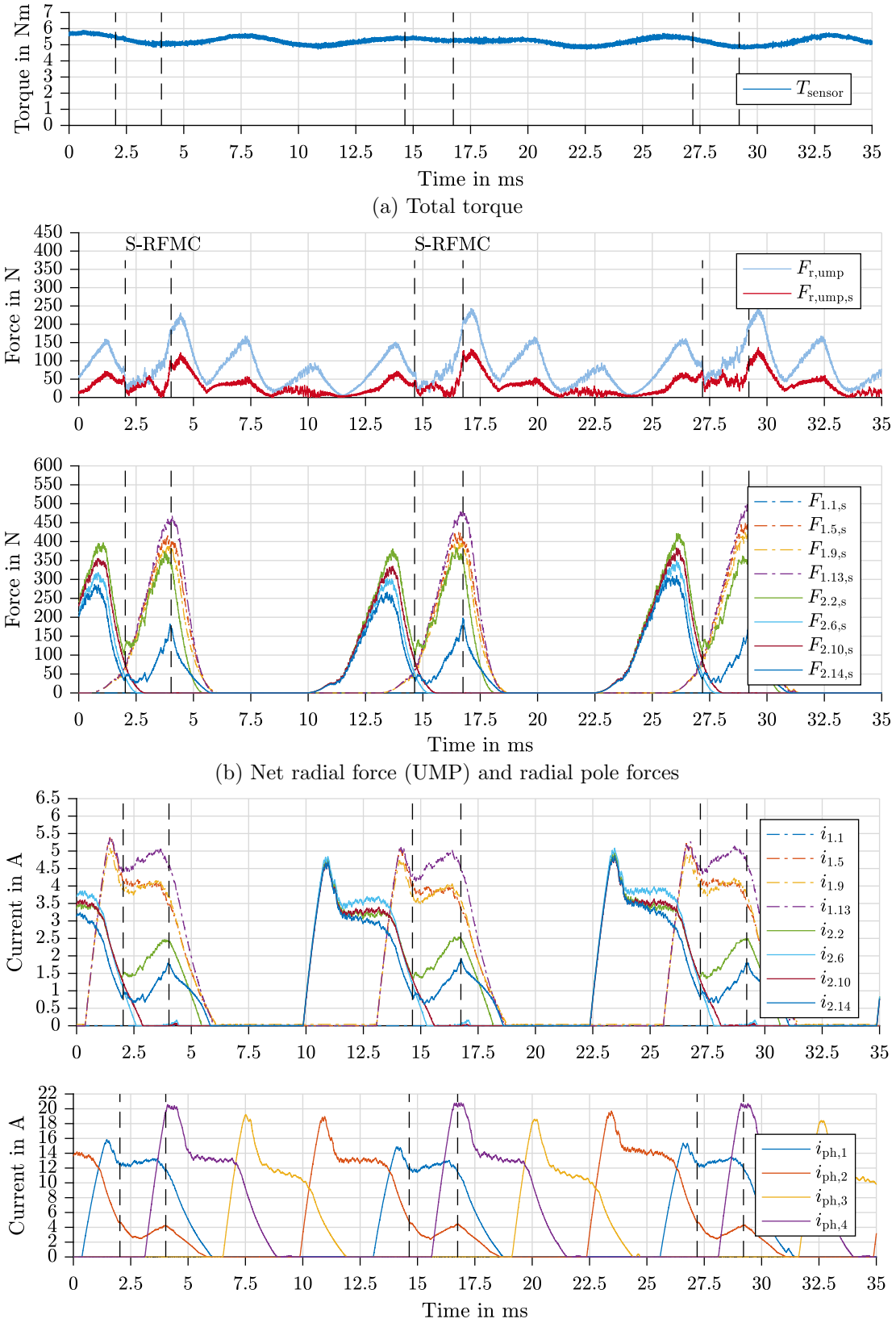

(a) Total torque

(b) Net radial force (UMP) and radial pole forces

(c) Current per pole and phase current waveforms

Figure 6.17: SRM-16/12 1$\underline{1}$0-1: Measurement results of S-RFMC during fault operation at 5 Nm and 400 rpm considering mutual coupling with a LUT representing the sine-term factor for $k_{\text{mc,2.2}}$ and $k_{\text{mc,2.14}}$

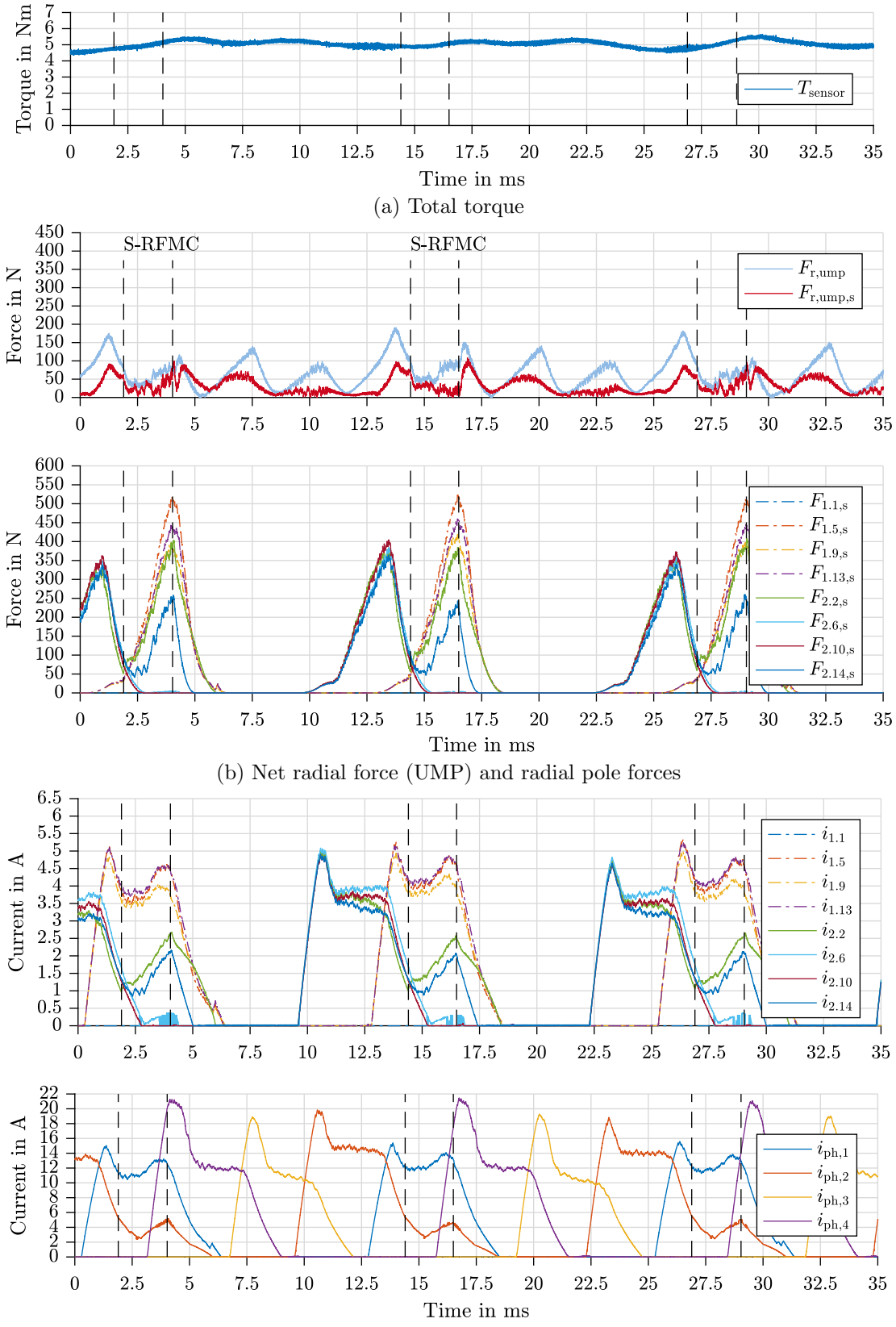

(a) Total torque

(b) Net radial force (UMP) and radial pole forces

(c) Current per pole and phase current waveforms

Figure 6.18: SRM-16/12 0$\underline{1}$0-1: Measurement results of S-RFMC during fault operation at 5 Nm and 400 rpm considering mutual coupling with $k_{\text{mc,2.2}} = -0.02$ and $k_{\text{mc,2.14}} = -0.06$

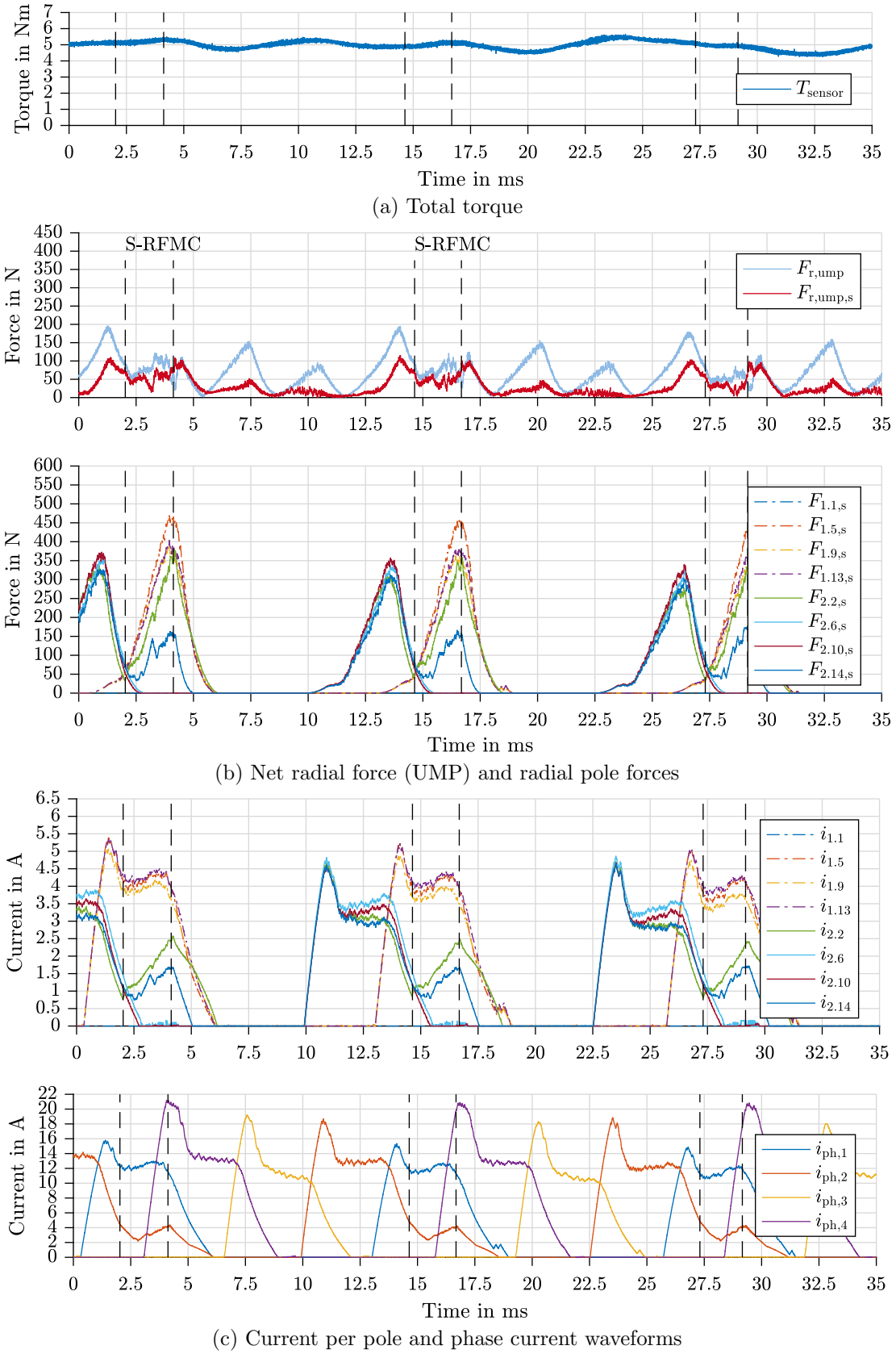

(a) Total torque

(b) Net radial force (UMP) and radial pole forces

(c) Current per pole and phase current waveforms

Figure 6.19: SRM-16/12 011-1: Measurement results of S-RFMC during fault operation at 5 Nm and 400 rpm considering mutual coupling with $k_{\text{mc,2.2}} = -0.02$ and $k_{\text{mc,2.14}} = -0.06$

The torque from the torque transducer shown in figure 6.15a is relatively flat, however, as already seen in the DITC measurements is not that representative, due to the small size of the used machine. In future, the proposed algorithm should be used on machines with higher torque rating to better determine, how accurate the torque can be controlled during the short time, where S-RFMC is active. However, as the radial force compensation works with independent current control and considering mutual coupling, it is expected that accurate torque control is also realizable.

Changing the coil orientations in the measurements changes the pole coupling during single pole fault. From the measurements presented it is visible that S-RFMC works for all variations. From the results displayed in figure 6.15 and figure 6.16, representing the coil orientation 0$\underline{0}$0-1 and 0$\underline{0}$0-0, no difference is observable regarding the fault tolerant control. This is expected, because phase 3 is not active during S-RFMC and, therefore, is not part of the fault control and its orientation does not matter. Only a difference in torque is observable, though this may be because of the small torque value measured. Furthermore, phase 3 of SRM-16/12 has an unwanted winding asymmetry (see section 6.2.1 and figure 6.6e), which is visible in the measurements as a sagging current waveform of phase 3 and can cause the visible torque ripple. Additional results regarding the direction of phase 3 are presented in the appendix in section A.2.2.

A visible difference in the results is due to the coil arrangement of the faulty (phase 1) and preceding phase (phase 2). The change in pole coupling between phase 1 and 2 caused from the non-alternating and alternating coil coupling, results in a changed pole current waveform of the faulty (phase 1) and preceding phase (phase 2). The results presented in figure 6.17 and figure 6.18 with coil orientation 1$\underline{1}$0-1 and 0$\underline{1}$0-1 respectively are compared. In the alternating coil arrangement the pole current waveforms of the faulty phase (phase 1) are much more close to each other, while in the non-alternating arrangement pole current $i_{1.13}$ is usually $1-1.5$ A higher than the other currents of the same phase $i_{1.5}$ and $i_{1.9}$. For the preceding phase (phase 2) the change in coupling influence is visible during the demagnetization of the pole $p_{2.2}$ and $p_{2.14}$. In the non-alternating arrangement (figure 6.17c) the demagnetization gradient of current $i_{2.2}$ is steeper than of $i_{2.14}$, which is attributed to a subtractive coupling from phase 1 onto pole $p_{2.2}$, while pole $p_{2.14}$ experiences an additive coupling resulting in a prolonged current slope even though both poles are demagnetized with the same negative dc-link voltage. The opposite effect is visible when the coil arrangement is alternating as in figure 6.18c. In this case, pole 2.2 experiences an additive coupling causing the current slope of $i_{2.2}$ to be less steep compared to the current $i_{2.14}$ of pole 2.14.

During the active region of S-RFMC the non-alternating and alternating pole coupling is correctly considered resulting in compensation radial forces $F_{2.2}$ and $F_{2.14}$ to match the critical unbalanced force $F_{1.9}$ independent of the coil orientation. Investigations on coil orientation have shown that for S-RFMC to work correctly, the fault tolerant control not only has to detect and identify the faulty pole, but also requires to know the coil orientation of the preceding phase in respect to the faulty phase.

6.5 Conclusions

The experimental results in this chapter show that the fault tolerant strategies EFC and S-RFMC proposed in this thesis can effectively be incorporated into direct instantaneous torque control (DITC). The test bench measurements of SRM-16/12 show that a considerable reduction in UMP can be achieved. The UMP is reduced from over 370 N to below 50 N during the active radial pole force control. The remaining UMP peaks have to be controlled by adjusting the turn-on $\theta_{\mathrm{on}}^{\mathrm{RFMC}}$ and turn-off $\theta_{\mathrm{off}}^{\mathrm{RFMC}}$ angles as described in section 5.3.3, depending on the requirements of the application.

The pole coupling caused by the asymmetric flux distribution during single pole fault can effectively be incorporated into the control by either using a constant or sine-LUT coupling factor. Once the pole coupling is incorporated, the radial force compensation is a viable solution for UMP minimization, and therefore, enabling the SRM with its distributed inverter as a fault tolerant drivetrain.

To minimize torque ripple during single pole fault while using EFC, a second $T_{\mathrm{ph}}(\psi_{\mathrm{ph}},\theta_{\mathrm{el}})$-LUT, representing the *2polesA* machine characteristic, has to be implemented in the control. Furthermore, the existing pole coupling should be incorporated as has been done for S-RFMC.

To demonstrate all benefits regarding radial force compensation and torque ripple minimization, a larger SRM with a higher torque rating should be used.

7 Summary and Outlook

This chapter summarizes all key findings and provides an outlook on future topics related to the research presented in this thesis.

7.1 Final Conclusions

This thesis contributes to the understanding of fault tolerant drive systems by proposing hands-on control schemes, simulation results, experimental results and design limits. Specifically the following topics were addressed:

DITC Complexity Reduction for Fault-Free Operation

In chapter 4 it has been shown that besides a $T_{\mathrm{ph}}(\psi_{\mathrm{ph}},\theta_{\mathrm{el}})$-LUT no additional machine LUT is required for pulse width modulation direct instantaneous torque control (PWM-DITC). During each switching period, lookups are executed to determine multiple corresponding flux linkage and torque samples. These flux linkage and torque samples are used for the flux linkage allocation, after the reference torque has been established, without using the previously necessary $\psi_{\mathrm{ph}}(T_{\mathrm{ph}},\theta_{\mathrm{el}})$-LUT. To enable the effective execution of this approach parallel processing hardware, such as an FPGA, which is able to perform at least five lookup cycles per switching period, is required (section 4.1.2.2).

A benefit of fault-free PWM-DITC with only one LUT is the possibility to add online machine model tuning algorithms. Previously, multiple LUTs had to be updated if a direct instantaneous torque control tuning was considered. Now, online control model tuning algorithms can be implemented with greater flexibility as only the torque characteristic $T_{\mathrm{ph}}(\psi_{\mathrm{ph}},\theta_{\mathrm{el}})$ used in the control has to be adapted to the real machine connected to the inverter.

In respect to fault tolerant SRM operation the additional memory saved, by implementing only one LUT, can be used to add a radial pole force table, which is necessary for fault tolerant control (FTC) strategies as proposed in this thesis. The amount of hardware memory would not change, but instead of storing $\psi_{\mathrm{ph}}(T_{\mathrm{ph}},\theta_{\mathrm{el}})$, a $F_{\mathrm{rad}}(\psi,\theta_{\mathrm{el}})$-LUT is added as proposed in section 5.3. Furthermore, the required LUTs for considering pole coupling

can also be incorporated, thus enabling a radial force minimization control implementation for fault tolerant SRM operation (section 6.4).

Effective Machine Design Methodology using DOE

For DITC and fault tolerant control strategies to work effectively the SRM machine design has to incorporate the machine, inverter and control. The machine and inverter require a voltage reserve and geometric phase overlap to freely set the required pole currents and control the tangential and radial pole forces to minimize torque ripple during phase commutation, as well as UMP during fault condition. Therefore, an effective machine design methodology incorporating the control algorithm during the design process is presented.

The major benefit of the proposed *Design of Experiments* (DOE) design process is not only the reduced design time because of reduced number of calculations required (158 executions instead of 59049 for 10 independent variables), but the understanding gained of how the design variables interact amongst each other (section 4.2). Creating a regression equation and applying the response surface method (RSM) enables the engineer a comprehensive understanding of the trade-offs from contradicting optimization criteria (efficiency, torque ripple, torque per weight, etc.) found in machine design, while immensely simplifying the overall process.

Distributed Inverter as the Enabler for Future Fault Tolerant SRMs

The most probable electrical fault in drive systems is an open-circuit fault of one stator pole. Thus, for a drive to be fault tolerant, a single pole fault ride through is required independent of which pole fails. The solution is a distributed inverter, where each stator pole is connected to its own inverter module (section 2.2.2). Such an approach allows fault detection with the appropriate sensing, hardware isolation of the fault by switching off the respective pole, and continuing machine operation by using the remaining healthy poles. By adding a redundant power supply, short-circuit faults in the dc-link (capacitor) can also be bypassed. Therefore, by incorporating a distributed inverter and appropriate fault control strategies, all electrical faults in the drive (machine and inverter) can be handled (section 2.2.3).

Furthermore, a distributed inverter enables the control to observe machine asymmetries by calculating the pole inductances from pole current measurements. The correct pole inductances can be used to correct the calculated radial forces and, therefore, effectively control the respective poles (section 6.2.1).

SRM Configurations for Fault Tolerant Operation

SRMs with at least two pole pairs ($p \geqslant 2$) and three phases ($N_{\mathrm{ph}} \geqslant 3$) are required for the proposed EFC and S-RFMC fault tolerant control schemes. The higher the number of phases and pole pairs in the SRM, the larger its theoretical operation region during a single pole fault.

In section 5.3.3 it is shown that, without regarding the thermal limits, the five phase SRM (SRM-20/16) with its high phase overlap can actively minimize the UMP up to its nominal torque. In three and four phase machines the maximum operating torque during fault is limited by an occurring torque dip. The operating torque of SRM-12/8 is reduced to 93 % and SRM-16/12 to 96 % of their respective nominal torque.

The theoretical operation region is limited by the thermal loading of the pole inverter and machine poles. The increase in RMS current density is caused by the required prolonged conduction period of the UMP compensating poles. The higher the number of phases, the larger the relative increase of conduction period compared to the fault-free conduction period.

An application specific trade-off between the theoretical operating range, i.e. torque production capability and thermal loading has to be found. If the application allows torque dips resulting in an increase in torque ripple during fault operation, then three and four phase machines can be used. In terms of thermal loading the four phase SRM is the better choice. If, however, the same minimum torque ripple as in fault-free DITC is required during fault, a five (or higher) phase machine should be used.

SRM Operation During Single Pole Fault

Two fault tolerant control strategies, *elementary fault control* (EFC) and *radial force minimization control* (RFMC & S-RFMC) are proposed to continue SRM operation during a single pole fault. EFC is a very effective method for SRM operation during partial load, while avoiding unbalanced magnetic pull (UMP). As EFC switches off the critical pole, which produces the UMP, and only uses the remaining poles of the faulty phase, the operation area is limited by the thermal loading of those remaining inverter and machine poles. Once the thermal limit is reached, S-RFMC has to be used for continued operation at higher torque levels.

S-RFMC utilizes all healthy poles of the faulty phase to produce torque, allowing for a better current distribution amongst the faulty phase. The UMP is compensated by the phase preceding the faulty phase. This operation prolongs and, therefore, increases the RMS current density of the compensating poles of the preceding phase. The thermal limit of S-RFMC is determined by the thermal limit of these compensating poles.

S-RFMC is effective in reducing the unbalanced radial pole force in SRM-16/12 by 86.5 % from 370 N to under 50 N, while maintaining constant torque control during fault operation in system simulations (section 5.4.2) and test-bench measurements (section 6.4.2). The FPGA implementation and experimental results of S-RFMC demonstrate its viability, including the online pole coupling during single pole fault.

7.2 Future Work

The complexity reduction of PWM-DITC by only using one $T_{\mathrm{ph}}(\psi_{\mathrm{ph}},\theta_{\mathrm{el}})$-LUT offers the possibility to add adaptive model tuning algorithms for fault-free SRM operation. In future the control can adapt the machine parameters stored in the $T_{\mathrm{ph}}(\psi_{\mathrm{ph}},\theta_{\mathrm{el}})$-LUT, which may change over time, either due to surrounding conditions or material aging in the machine.

The experimental results of EFC and S-RFMC have shown that UMP compensation is possible while operating at constant torque. However, to validate the constant torque waveform a SRM with a higher torque capability or better torque sensor is necessary. Furthermore, by measuring the surface vibration the change in vibrational modes can be identified during fault operation [32]. From surface vibration measurements or with rotor shaft force sensors better estimations on the effectiveness of torque control and radial force control are possible. During the change from DITC with fault detection to S-RFMC, a clear change in audible noise is perceived on the test bench, which could not be measured practically on the small test bench. For effective vibration measurements a larger SRM is necessary, where the expected frequency spectrum from the machine is not within the eigenfrequencies of the mechanical setup, as is the case with the SRM-16/12 setup.

The asymmetric pole inductances determined offline in separate measurements for SRM-16/12 can be implemented into an adaptive per pole based online model tuning to reduce the control sensitivity of S-RFMC on machine asymmetries.

A generalized version of RFMC could be implemented, however, as the simulation results have shown, additional boundary conditions regarding pole priority are necessary to optimize pole magnetization. Furthermore, the challenge of solving the linear matrix equation online has to be overcome.

A Appendix

A.1 SRM-16/12: Thermal Model

The thermal limits of SRM-16/12 are determined by temperature measurements conducted on the test bench, which are shown in figure A.1a and figure A.1b. From these measurements the maximum loss dissipation possible is determined resulting in the maximum current density $J_{\mathrm{RMS}}^{\mathrm{max}}$ for the machine. To determine the temperature distribution and hot-spot temperature within the machine a Motor-CAD model is built up and fitted to the measurements.

Two heat-up measurements are conducted. During the first measurement, shown in figure A.1a, only natural convection is used to determine the temperature and thermal resistances between the copper windings $T_{\mathrm{w,avg}}$, the housing surface T_{surf} and the ambient temperature T_{amb}. Thereby, the windings are heated with P_{Cu}=163 W by exciting the phases with a constant dc-current. The resulting Motor-CAD model fit and FEA solution of the slot to determine the hot-spot temperature $T_{\mathrm{w,max}}$ is displayed in figure A.1c and figure A.1e respectively.

During the second measurement a fan cooling is added, as is normally the case during operation. In the second measurement an overall power of 266 W can be dissipated from the machine. The warm-up curve is shown in figure A.1b, while the corresponding simulation results from Motor-CAD are shown in figure A.1d and figure A.1f. Once the Motor-CAD model is adjusted a good consistency between measurement and simulation is observed. As no rotor temperatures could be measured on the test bench, the thermal resistances for the rotor and calculated rotor temperatures in Motor-CAD have to be regarded with caution. Especially rotor temperatures are usually limited by the bearing temperature, which in standard applications should be less than 100 °C.

The maximum current density of SRM-16/12 is determined as $J_{\mathrm{RMS}}^{\mathrm{max}} = 7.3\,\mathrm{A/mm^2}$ for a maximum winding temperature of $T_{\mathrm{w,max}} = 155\,^{\circ}\mathrm{C}$. This current density is used as the limit for continuous operation of SRM-16/12 during fault condition.

For the machine design process of a three phase 12/8 SRM in section 4.2.3, a thermal model with similar cooling and heat dissipation is used.

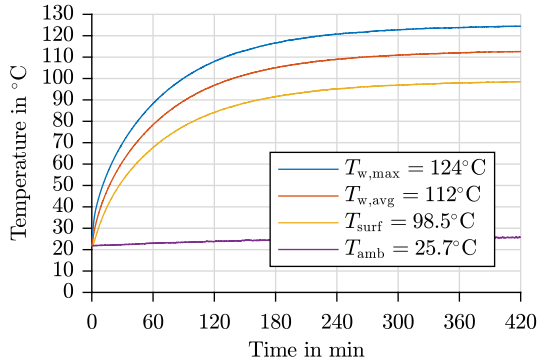

(a) Measurement: $P_{Cu} = 163\,W$, natural convection

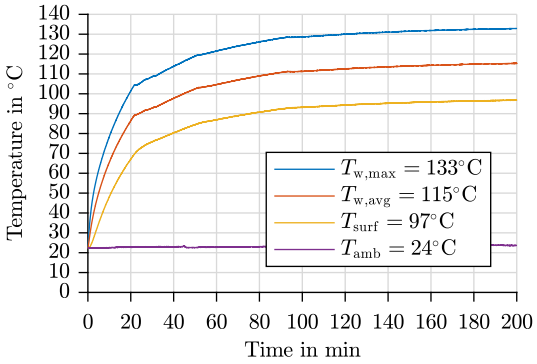

(b) Measurement: $P_{Cu} = 266\,W$, fan cooling

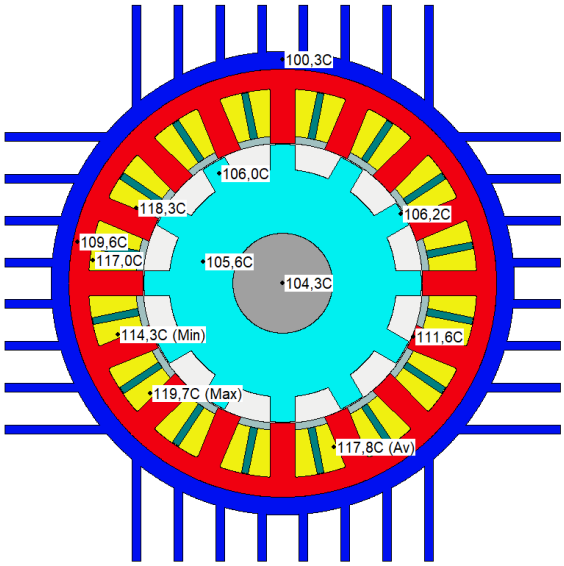

(c) Motor-CAD: model fit, natural convection

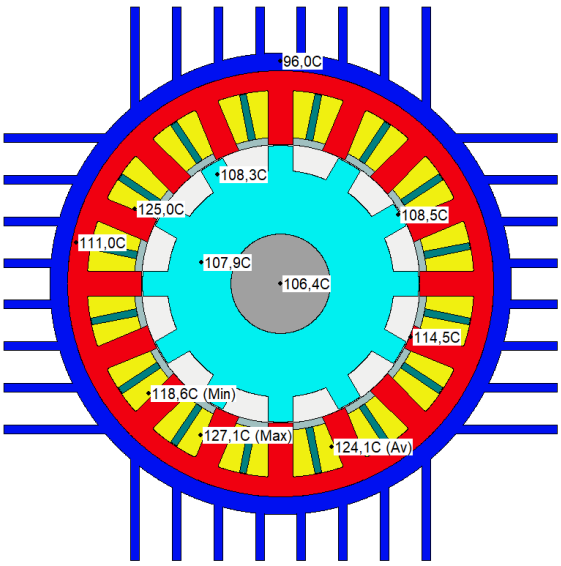

(d) Motor-CAD: model fit, fan cooling

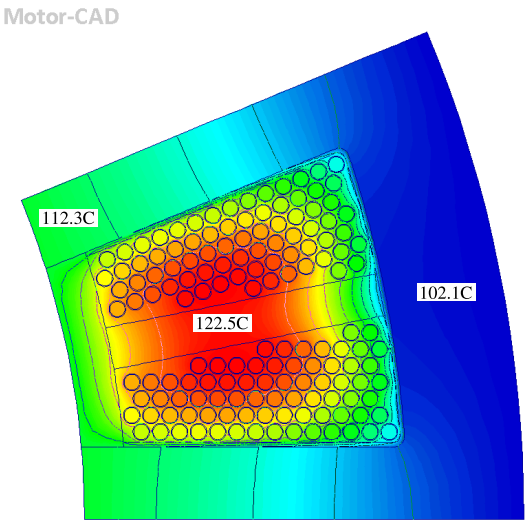

(e) Motor-CAD: FEA slot solution, natural convection

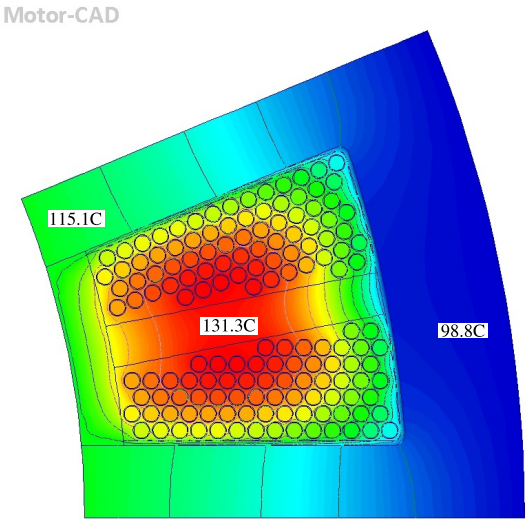

(f) Motor-CAD: FEA slot solution, fan cooling

Figure A.1: SRM-16/12: Thermal model fit from test bench heat-up measurement

A.2 Measurement Supplements

This section contains additional measurements of SRM-16/12 complementing the results from chapter 6.

A.2.1 Asymmetric Inductance Synthesis

The results in this section correspond to those presented in chapter 6, however, for the purpose of completeness all pole currents measured are presented here. Therefore, all the pole current waveforms $i_{\mathrm{x.x}}$ of each phase and the corresponding radial forces are displayed. Both the non-synthesized $F_{\mathrm{r,x.x}}$ and correctly synthesized radial forces $F_{\mathrm{r,x.x,s}}$, taking the asymmetric pole inductances into account are shown. From the radial forces the respective unbalanced magnetic pull $F_{\mathrm{r,ump}}$ and $F_{\mathrm{r,ump,s}}$ for each individual phase is determined.

DITC fault-free operation

In figure A.2 and figure A.3 results for DITC at fault-free operation are displayed. The UMP $F_{\mathrm{r,ump,s}}$ show only small unbalanced forces once correctly synthesized as is expected during symmetric excitation.

DITC with Single Pole Fault and Fault Detection

Figure A.4 and figure A.5 show the results when SRM-16/12 is operated at DITC with single pole detection of the faulty pole $p_{1,1}$. The control reacts by increasing the torque production of the faulty phase to compensate for the missing torque. The single pole fault is clearly visible from the high UMP of phase 1 in figure A.4b.

DITC and EFC with Fault

SRM-16/12 operation at elementary fault control, turning off the critical pole $p_{1.9}$ during single pole fault is shown in figure A.6 and figure A.7. In all phases the UMP reduces as expected to values well below 50 N.

S-RFMC with coil arrangements: 0$\underline{0}$0-1, 0$\underline{0}$0-0, 1$\underline{1}$0-1, 0$\underline{1}$0-1, 0$\underline{1}$1-1

The results from figure A.8 to figure A.13 show the non-alternating coil arrangements between the preceding phase 2 and faulty phase 1: 1, 0$\underline{0}$0-1, 0$\underline{0}$0-0, 1$\underline{1}$0-1. The results for alternating coil arrangements 0$\underline{1}$0-1 and 0$\underline{1}$1-1 are displayed in figure A.14 to figure A.17.

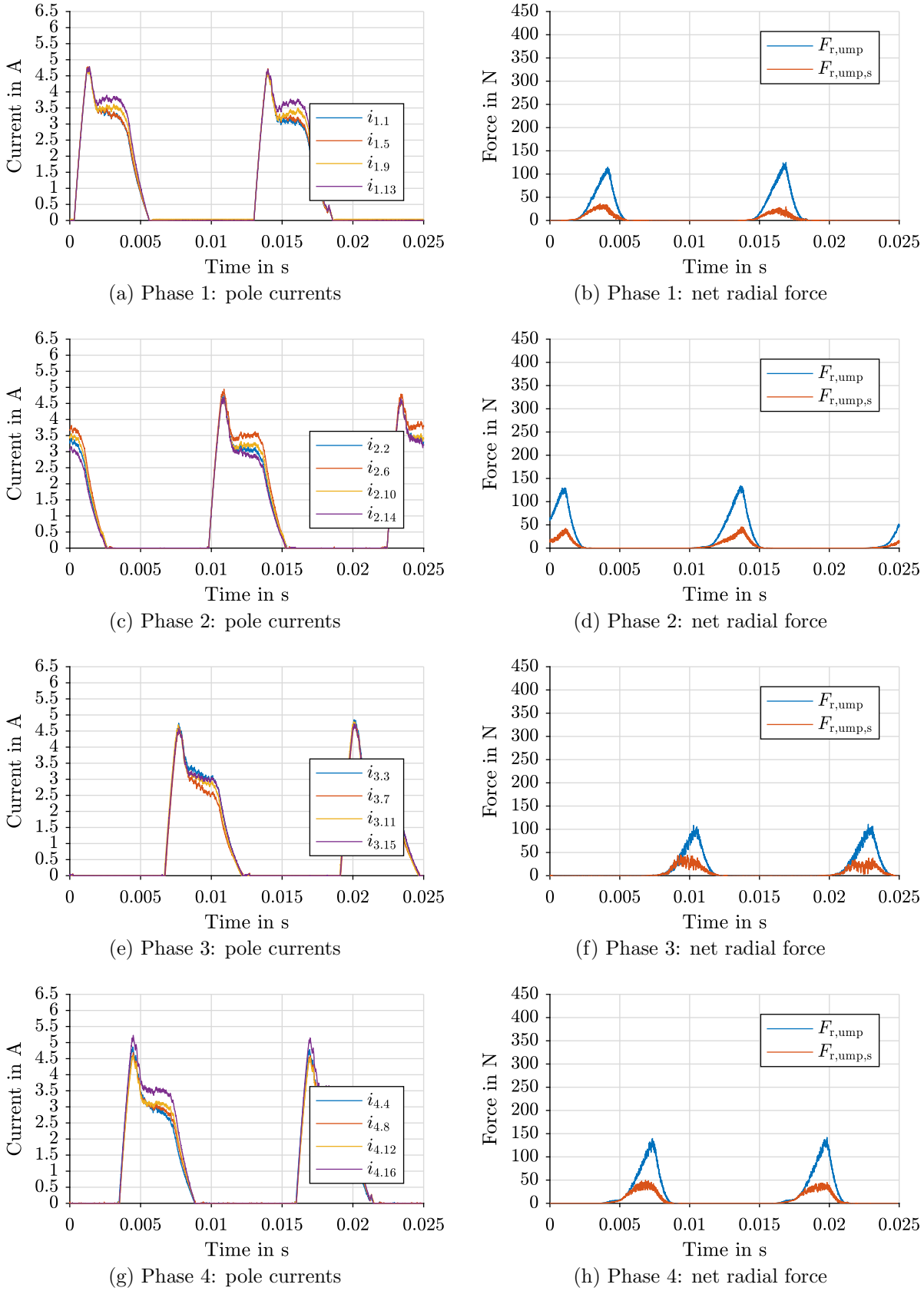

(a) Phase 1: pole currents

(b) Phase 1: net radial force

(c) Phase 2: pole currents

(d) Phase 2: net radial force

(e) Phase 3: pole currents

(f) Phase 3: net radial force

(g) Phase 4: pole currents

(h) Phase 4: net radial force

Figure A.2: SRM-16/12: Measurement results of pole currents and UMP with and without asymmetric inductance synthesis of fault-free DITC operation at $T = 5\,\mathrm{Nm}$ and $n = 400\,\mathrm{rpm}$

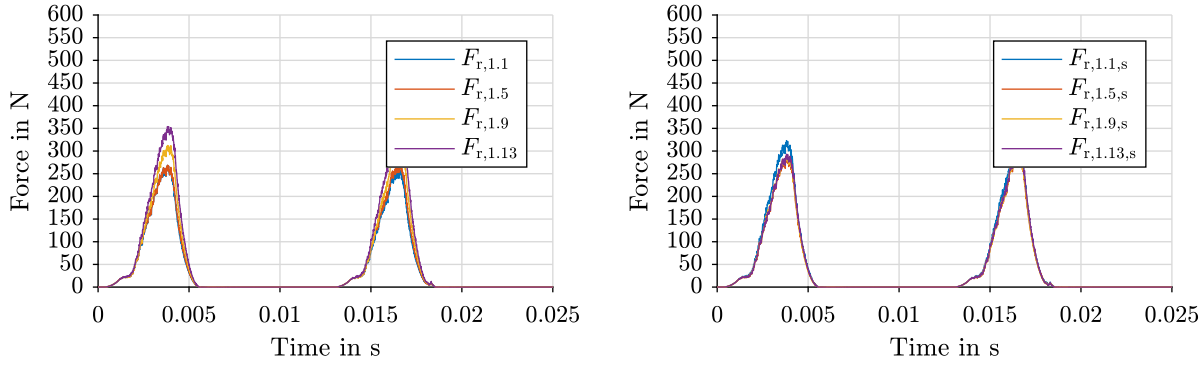

(a) Phase 1: no synthesis

(b) Phase 1: with synthesis

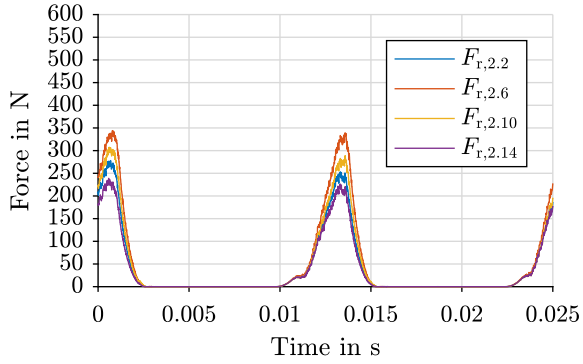

(c) Phase 2: no synthesis

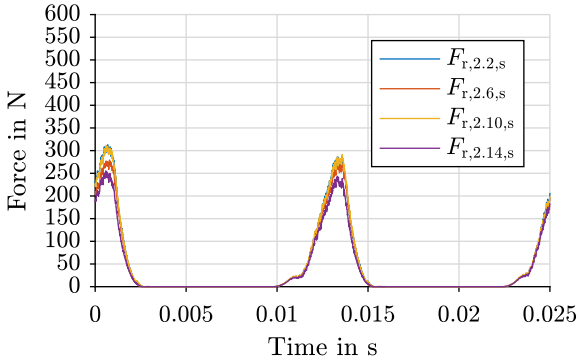

(d) Phase 2: with synthesis

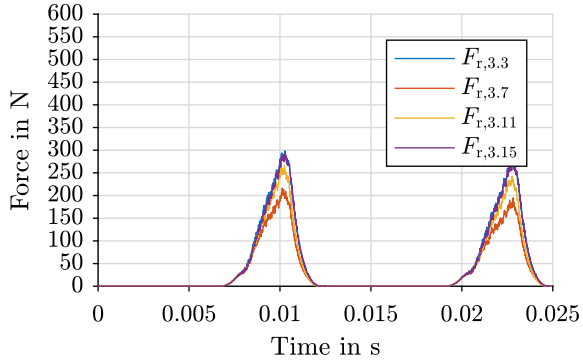

(e) Phase 3: no synthesis

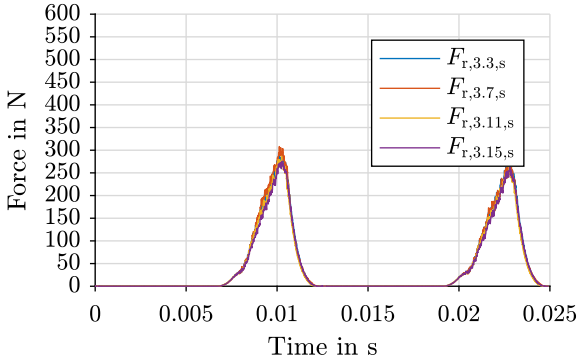

(f) Phase 3: with synthesis

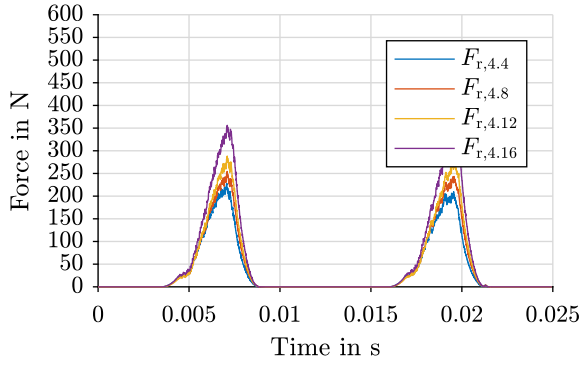

(g) Phase 4: no synthesis

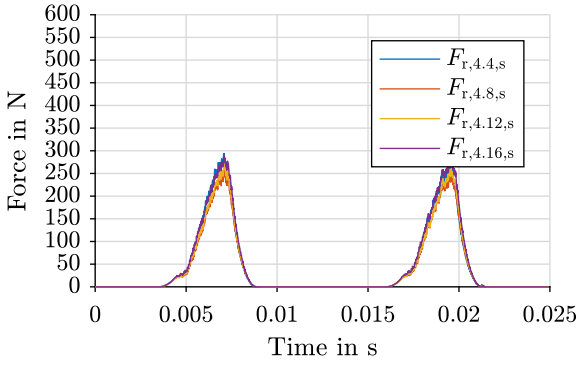

(h) Phase 4: with synthesis

Figure A.3: SRM-16/12: Measurement results of radial pole forces with and without asymmetric inductance synthesis of fault-free DITC operation at $T = 5\,\mathrm{Nm}$ and $n = 400\,\mathrm{rpm}$

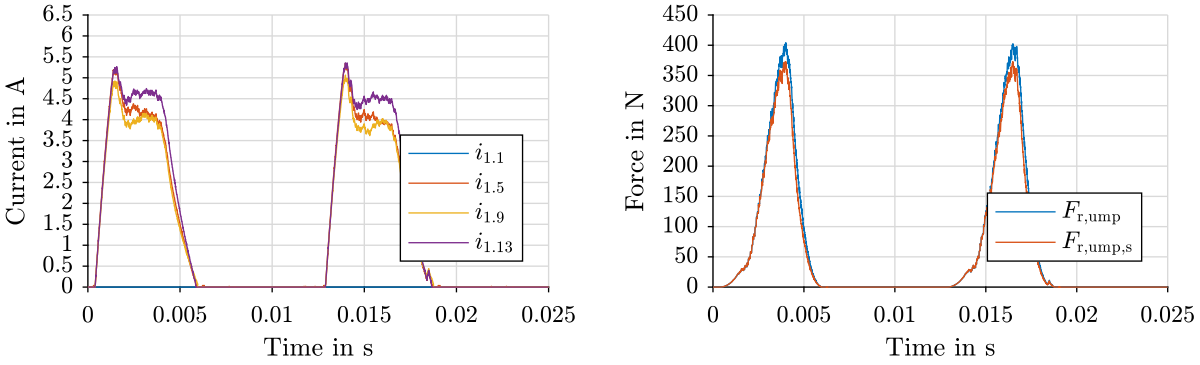

(a) Phase 1: pole currents

(b) Phase 1: net radial force

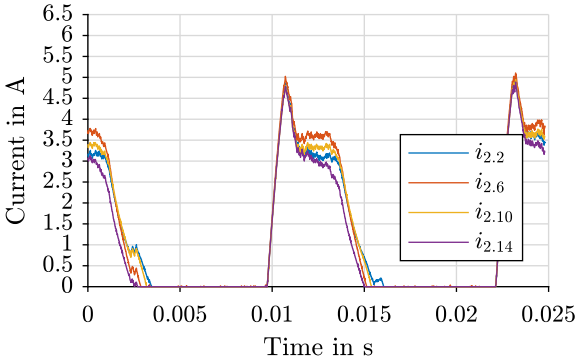

(c) Phase 2: pole currents

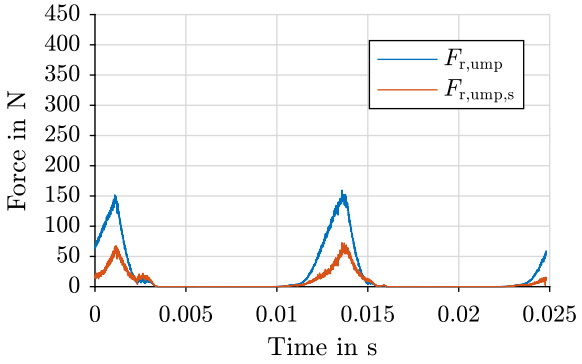

(d) Phase 2: net radial force

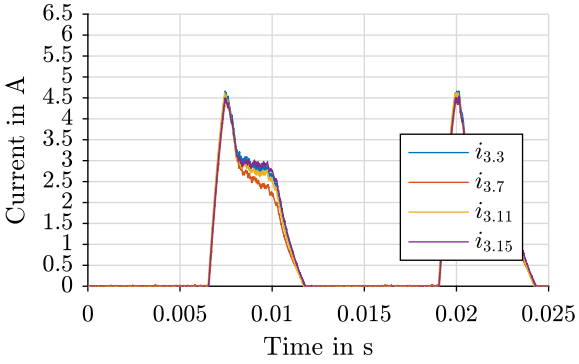

(e) Phase 3: pole currents

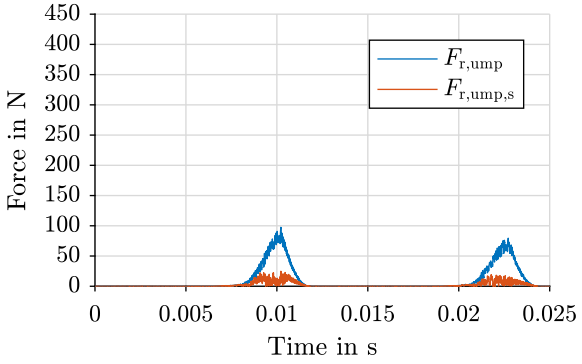

(f) Phase 3: net radial force

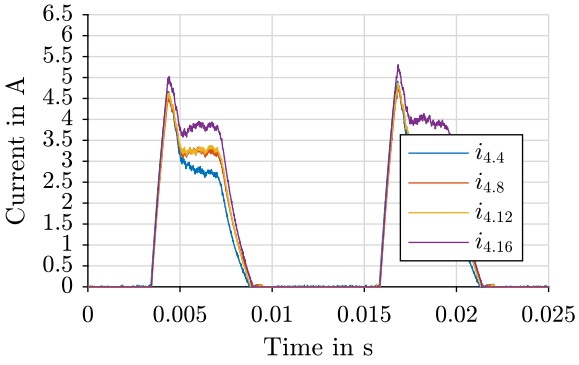

(g) Phase 4: pole currents

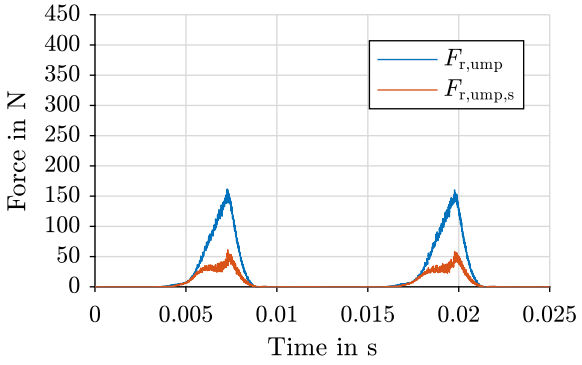

(h) Phase 4: net radial force

Figure A.4: SRM-16/12: Measurement results with and without asymmetric inductance synthesis of DITC with single pole fault and fault detection at $T = 5\,\mathrm{Nm}$ and $n = 400\,\mathrm{rpm}$

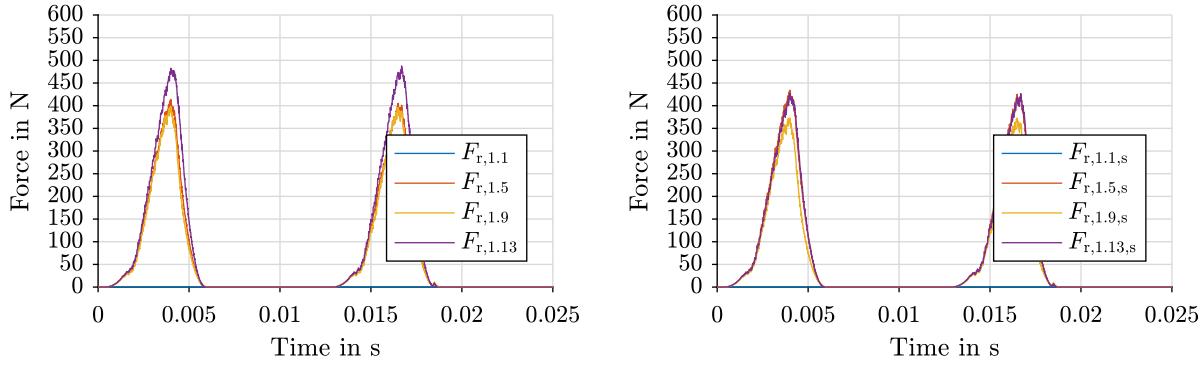

(a) Phase 1: no synthesis

(b) Phase 1: with synthesis

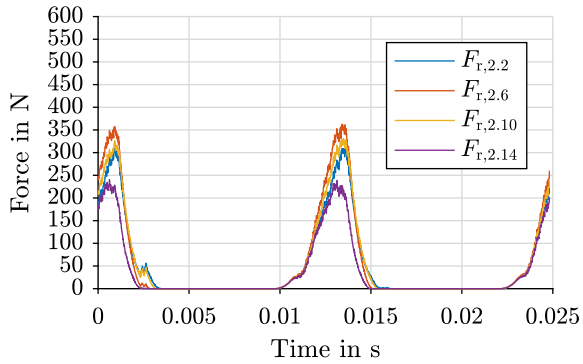

(c) Phase 2: no synthesis

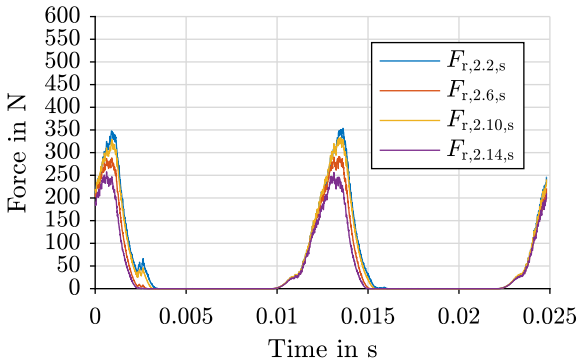

(d) Phase 2: with synthesis

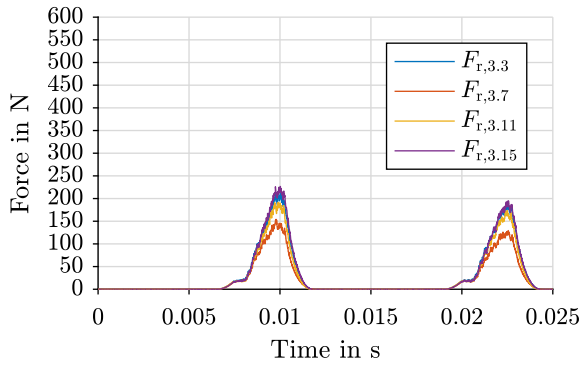

(e) Phase 3: no synthesis

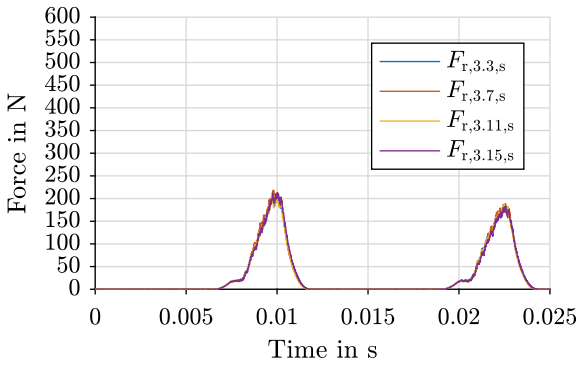

(f) Phase 3: with synthesis

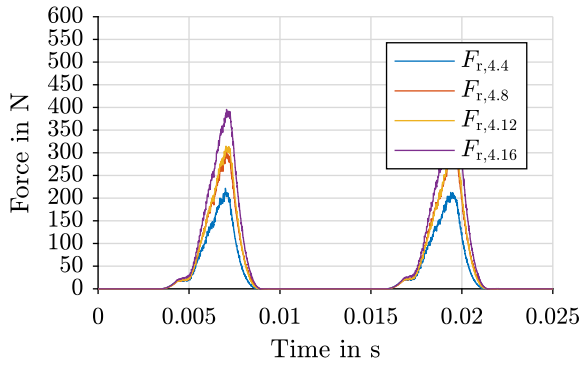

(g) Phase 4: no synthesis

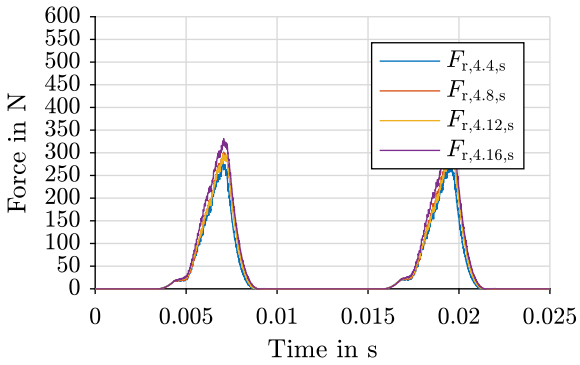

(h) Phase 4: with synthesis

Figure A.5: SRM-16/12: Measurement results of radial pole forces with and without asymmetric inductance synthesis of DITC with single pole fault and fault detection at $T = 5\,\mathrm{Nm}$ and $n = 400\,\mathrm{rpm}$

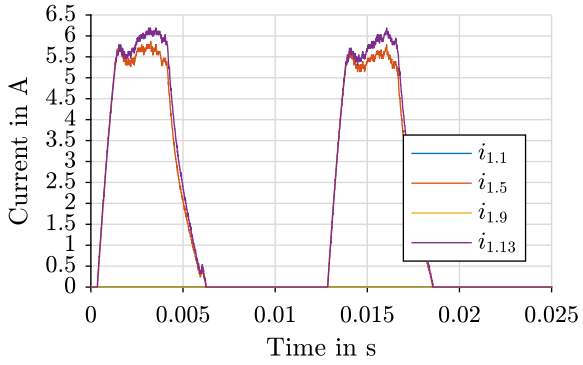

(a) Phase 1: pole currents

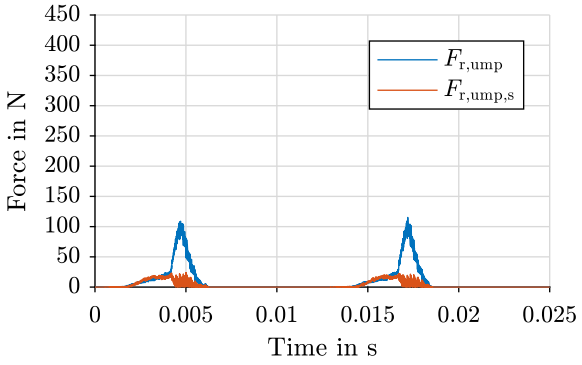

(b) Phase 1: net radial force

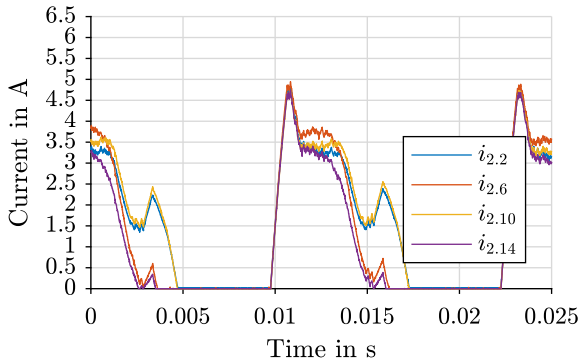

(c) Phase 2: pole currents

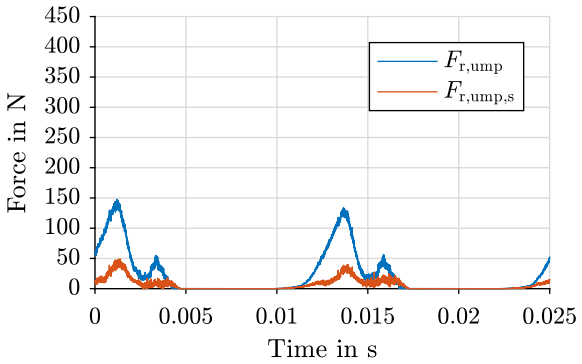

(d) Phase 2: net radial force

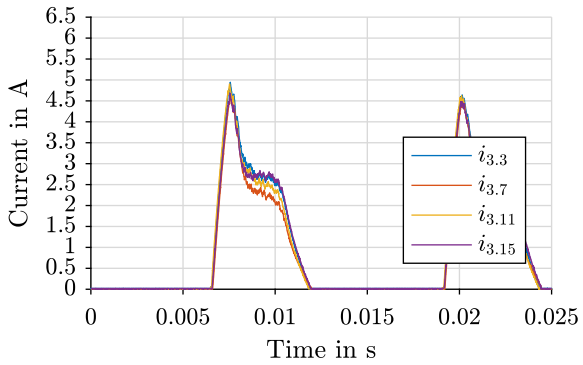

(e) Phase 3: pole currents

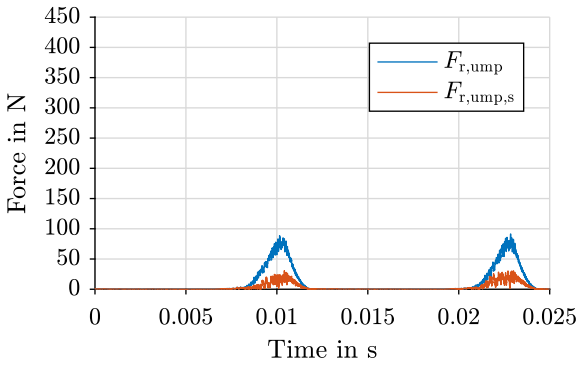

(f) Phase 3: net radial force

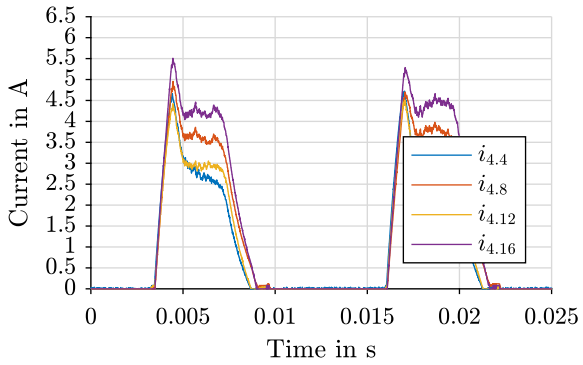

(g) Phase 4: pole currents

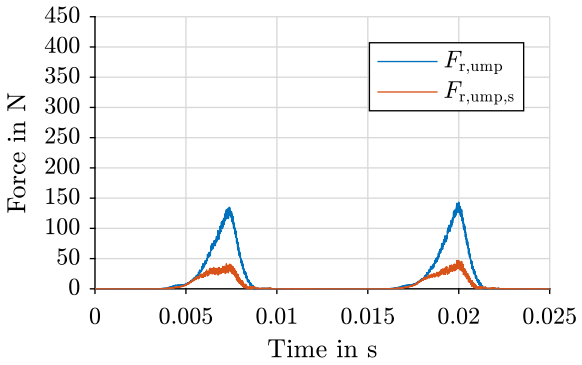

(h) Phase 4: net radial force

Figure A.6: SRM-16/12: Measurement results of pole currents and UMP with and without asymmetric inductance synthesis of DITC with EFC at $T = 5\,\mathrm{Nm}$ and $n = 400\,\mathrm{rpm}$

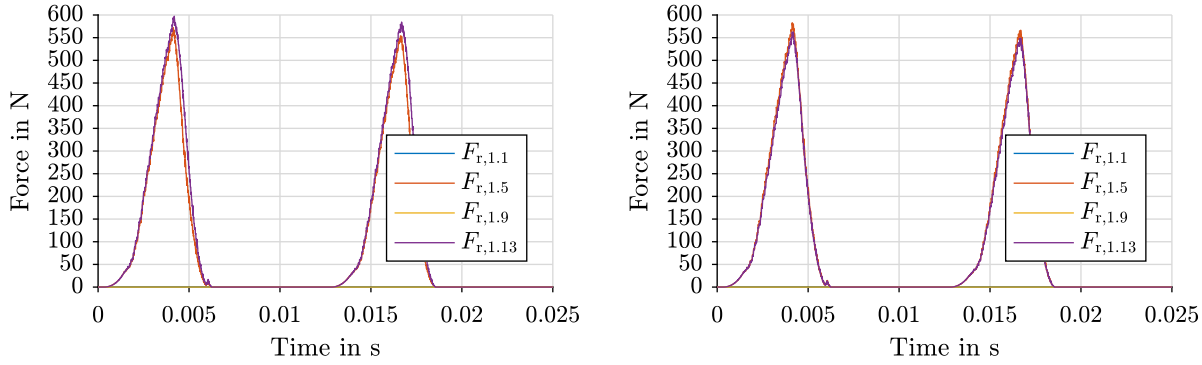

(a) Phase 1: no synthesis

(b) Phase 1: with synthesis

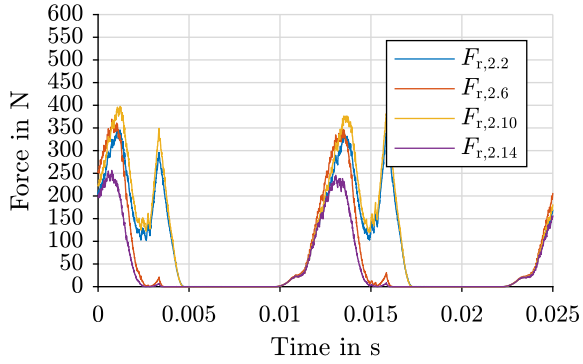

(c) Phase 2: no synthesis

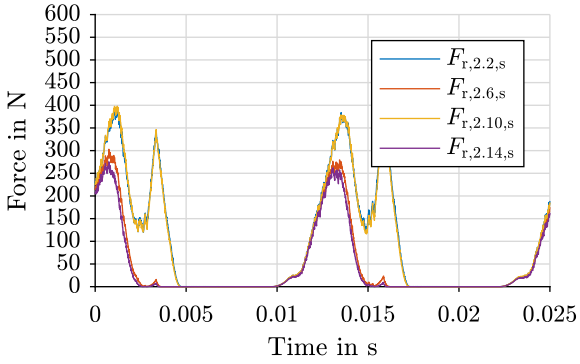

(d) Phase 2: with synthesis

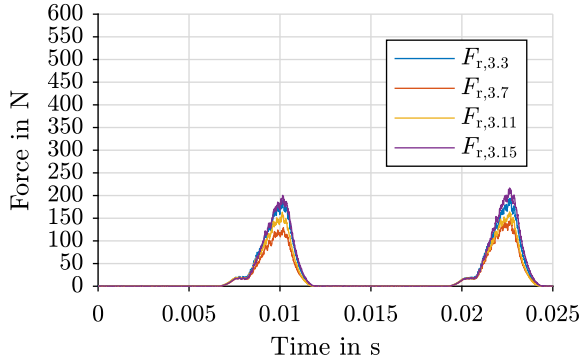

(e) Phase 3: no synthesis

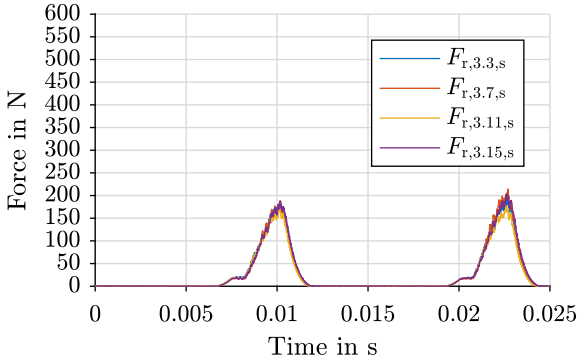

(f) Phase 3: with synthesis

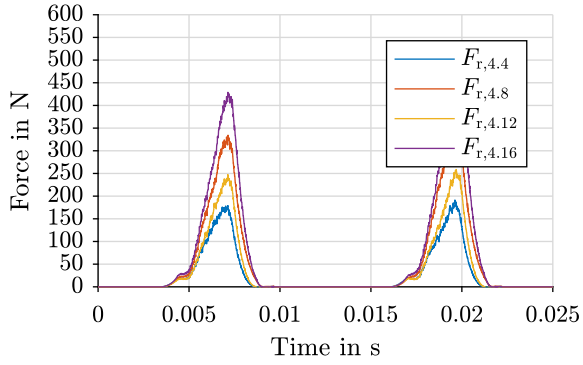

(g) Phase 4: no synthesis

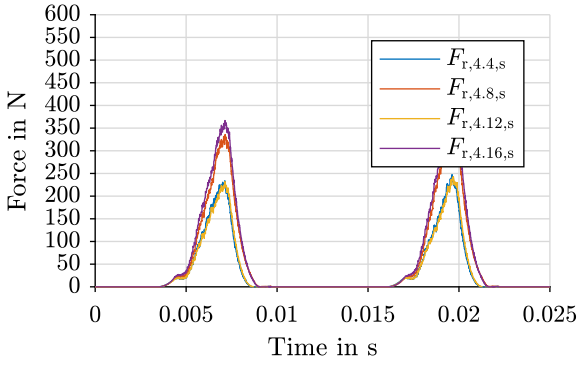

(h) Phase 4: with synthesis

Figure A.7: SRM-16/12: Measurement results of radial pole forces with and without asymmetric inductance synthesis of DITC with EFC at $T = 5\,\mathrm{Nm}$ and $n = 400\,\mathrm{rpm}$

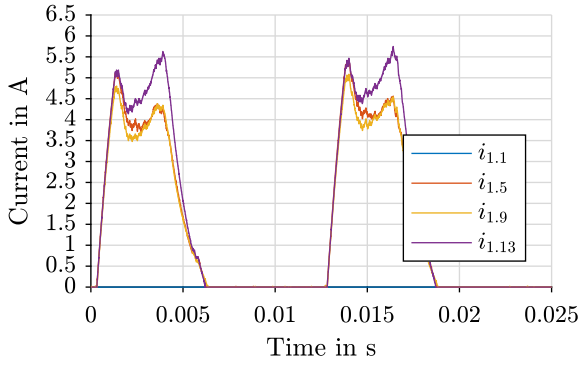

(a) Phase 1: pole currents

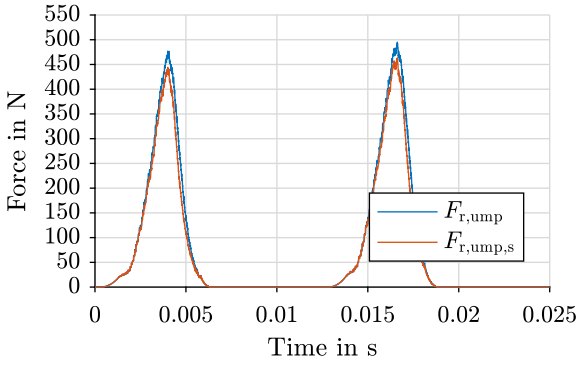

(b) Phase 1: net radial force

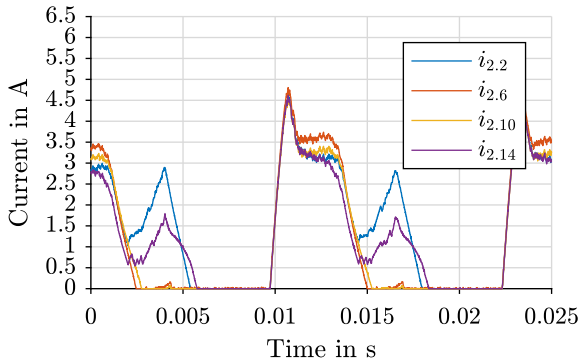

(c) Phase 2: pole currents

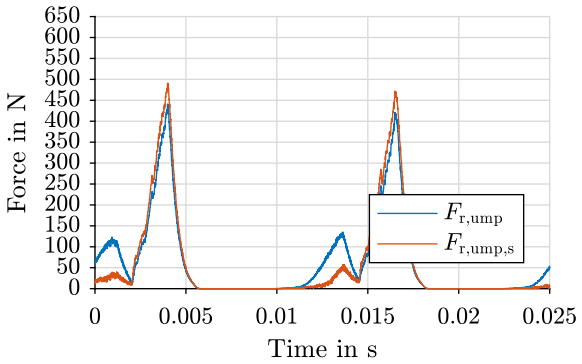

(d) Phase 2: net radial force

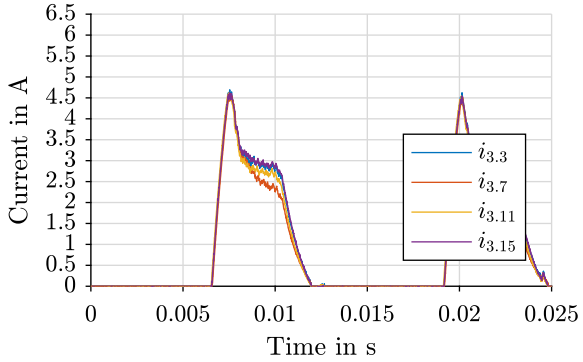

(e) Phase 3:pole currents

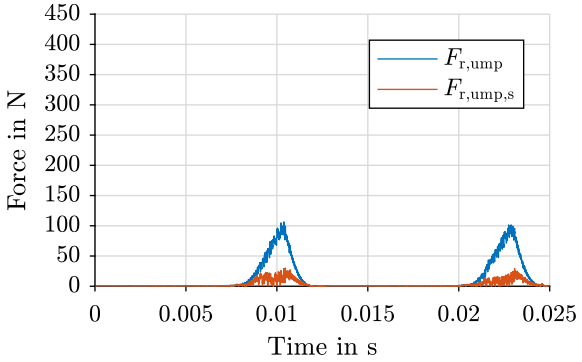

(f) Phase 3: net radial force

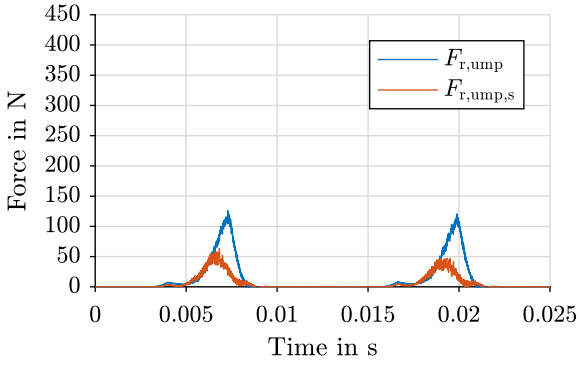

(g) Phase 4: pole currents

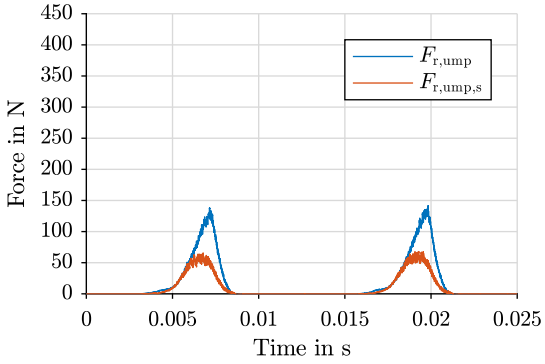

(h) Phase 4: net radial force

Figure A.8: SRM-16/12: Measurement results of pole currents and UMP with and without asymmetric inductance synthesis of DITC with S-RFMC at $T = 5\,\mathrm{Nm}$ and $n = 400\,\mathrm{rpm}$ (0̲0-1)

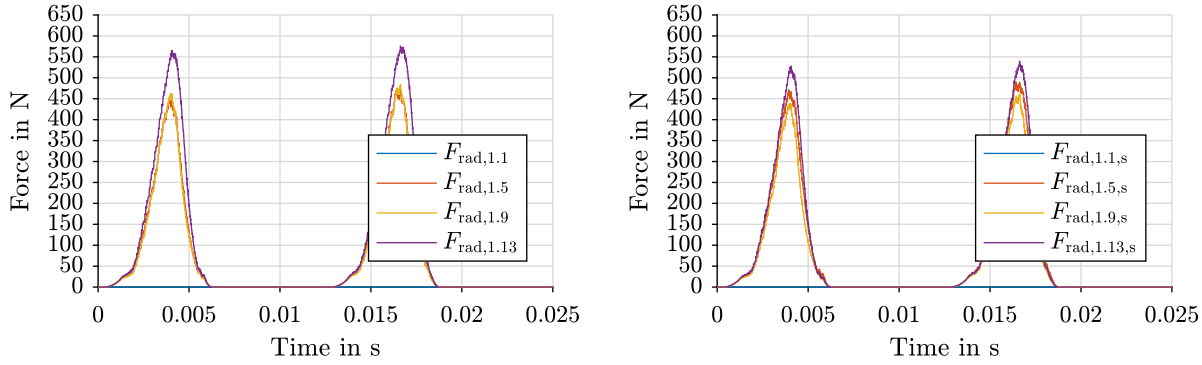

(a) Phase 1: no synthesis

(b) Phase 1: with synthesis

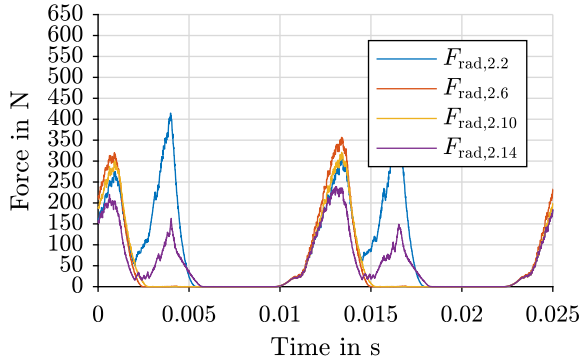

(c) Phase 2: no synthesis

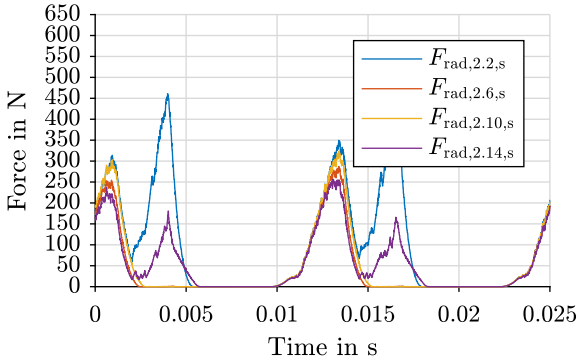

(d) Phase 2: with synthesis

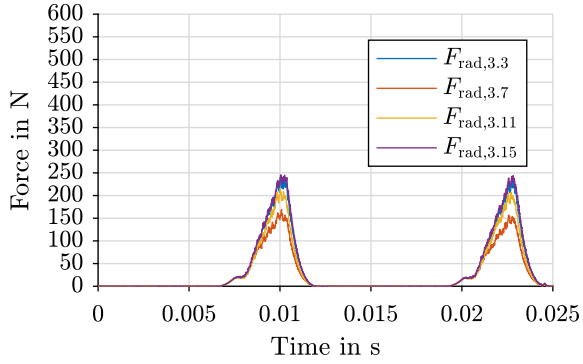

(e) Phase 3: no synthesis

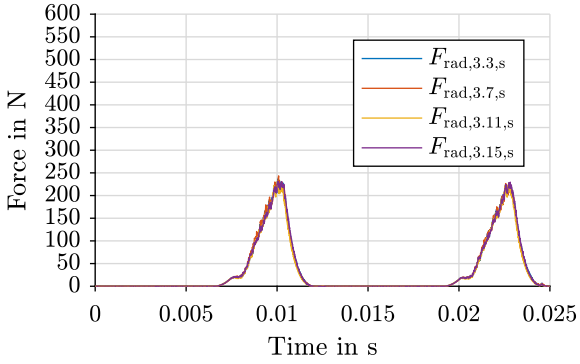

(f) Phase 3: with synthesis

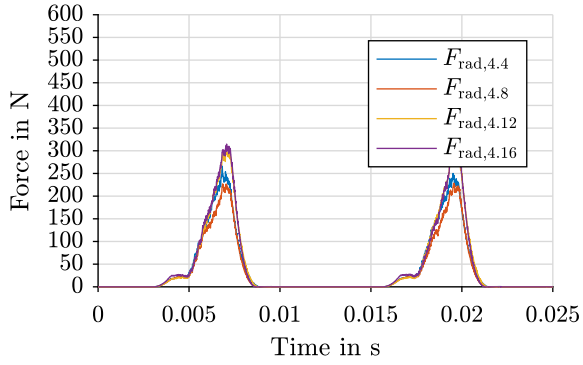

(g) Phase 4: no synthesis

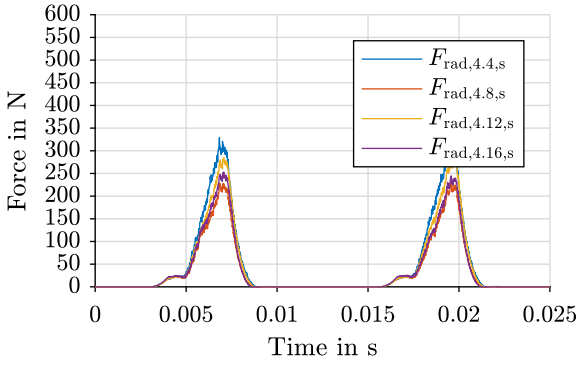

(h) Phase 4: with synthesis

Figure A.9: SRM-16/12: Measurement results of radial pole forces with and without asymmetric inductance synthesis of DITC with S-RFMC at $T = 5\,\mathrm{Nm}$ and $n = 400\,\mathrm{rpm}$ (0$\underline{0}$0-1)

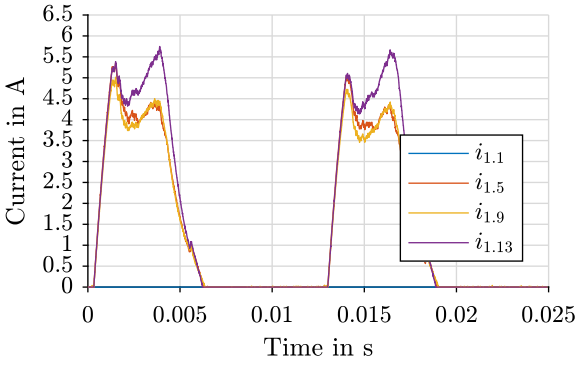

(a) Phase 1: pole currents

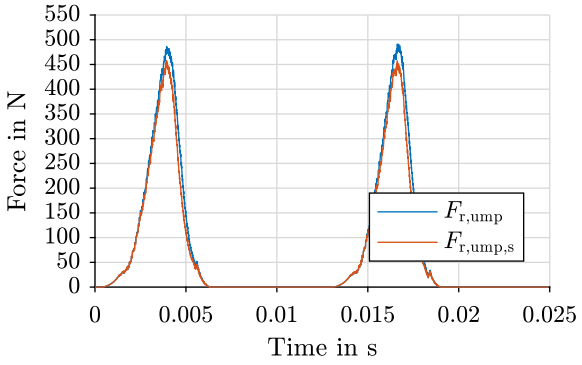

(b) Phase 1: net radial force

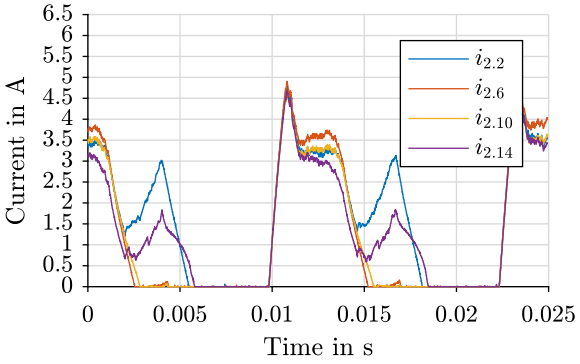

(c) Phase 2: pole currents

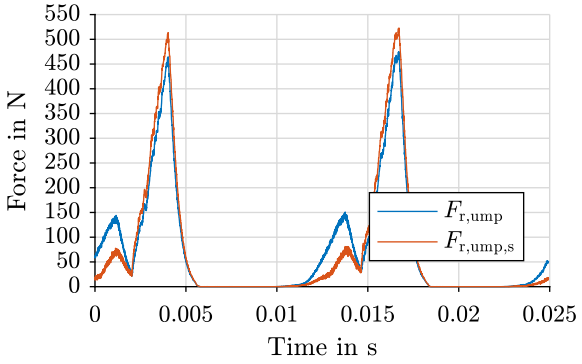

(d) Phase 2: net radial force

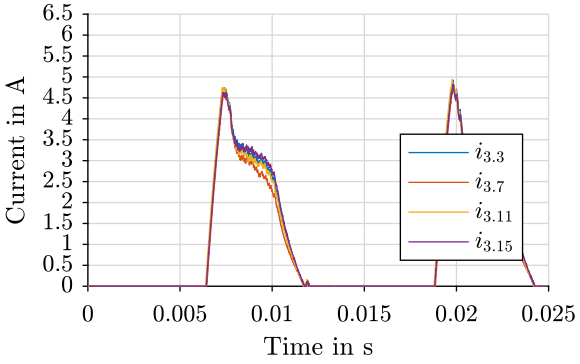

(e) Phase 3: pole currents

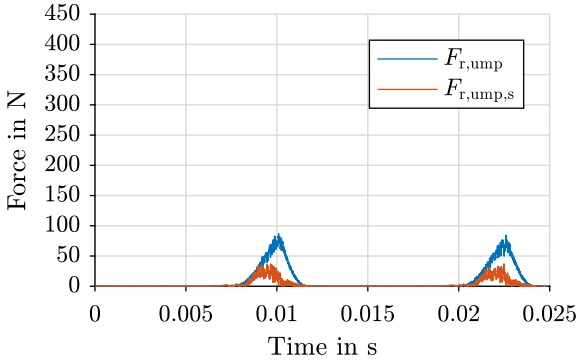

(f) Phase 3: net radial force

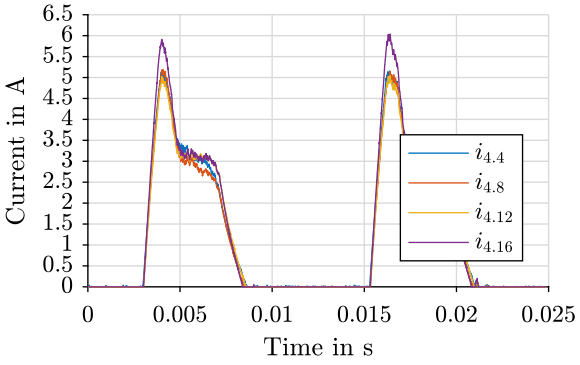

(g) Phase 4: pole currents

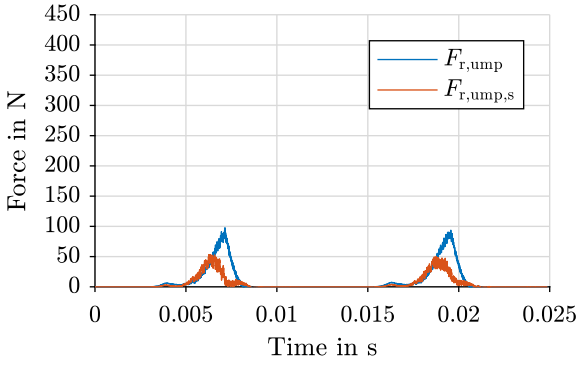

(h) Phase 4: net radial force

Figure A.10: SRM-16/12: Measurement results of pole currents and UMP with and without asymmetric inductance synthesis of DITC with S-RFMC at $T = 5\,\mathrm{Nm}$ and $n = 400\,\mathrm{rpm}$ (0$\underline{0}$0-0)

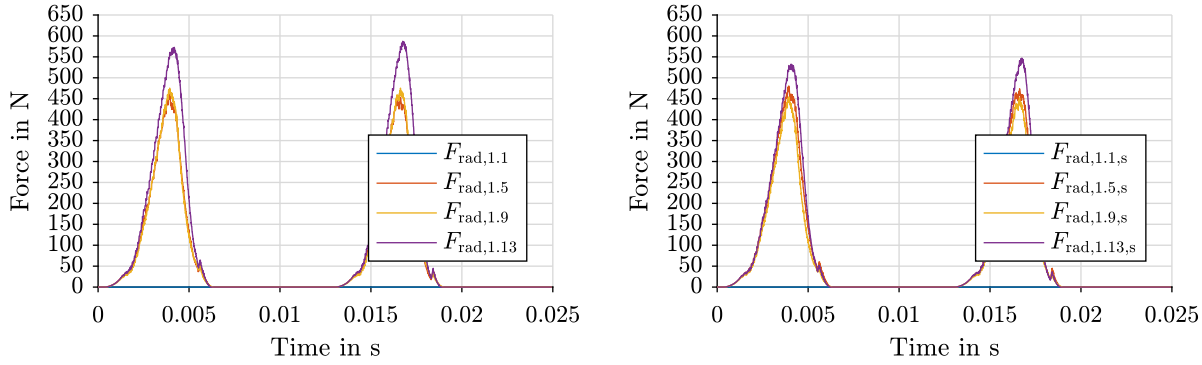

(a) Phase 1: no synthesis

(b) Phase 1: with synthesis

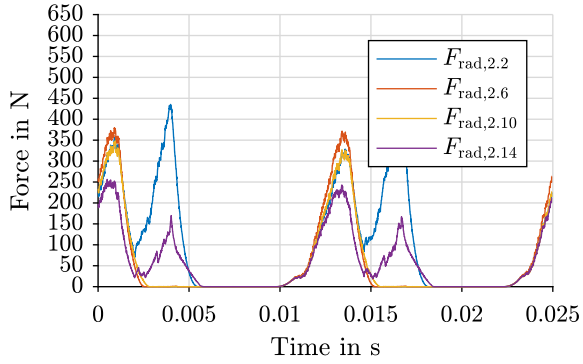

(c) Phase 2: no synthesis

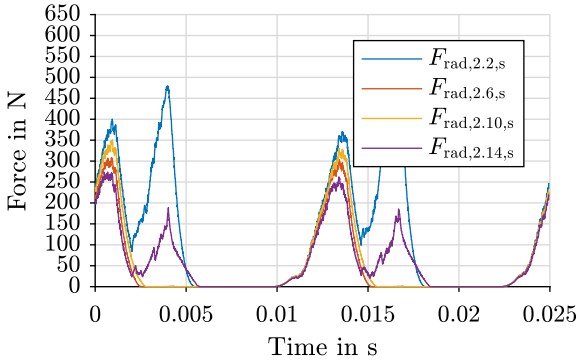

(d) Phase 2: with synthesis

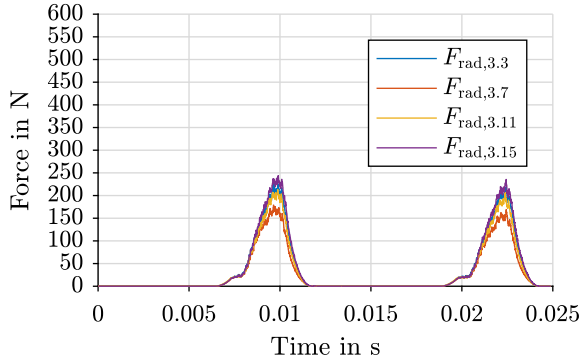

(e) Phase 3: no synthesis

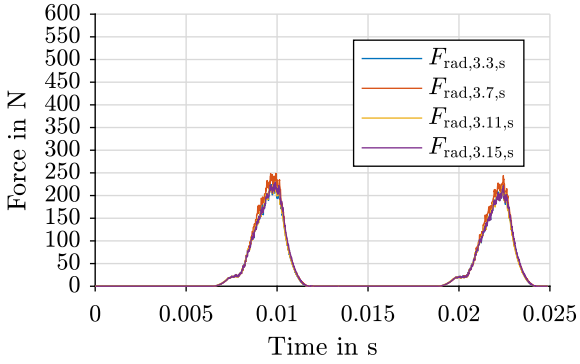

(f) Phase 3: with synthesis

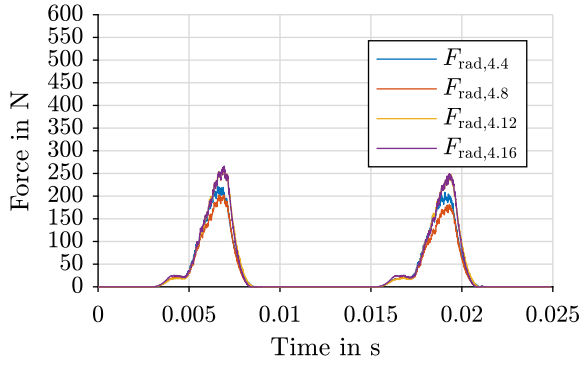

(g) Phase 4: no synthesis

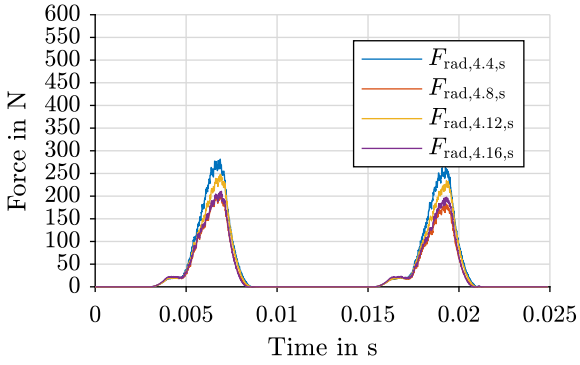

(h) Phase 4: with synthesis

Figure A.11: SRM-16/12: Measurement results of radial pole forces with and without asymmetric inductance synthesis of DITC with S-RFMC at $T = 5\,\mathrm{Nm}$ and $n = 400\,\mathrm{rpm}$ (0$\underline{0}$0-0)

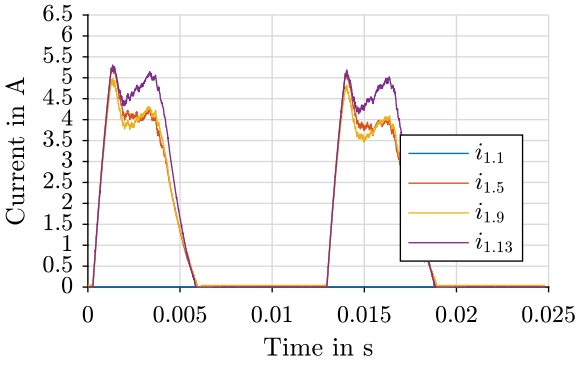

(a) Phase 1: pole currents

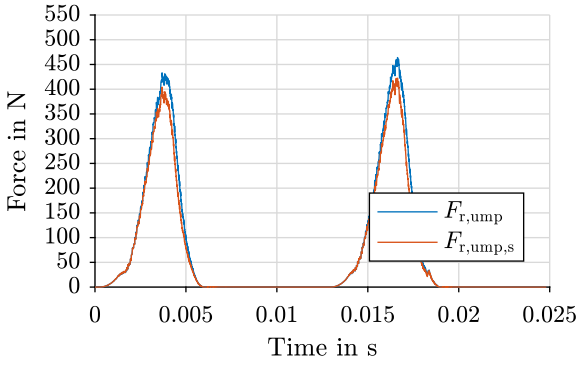

(b) Phase 1: net radial force

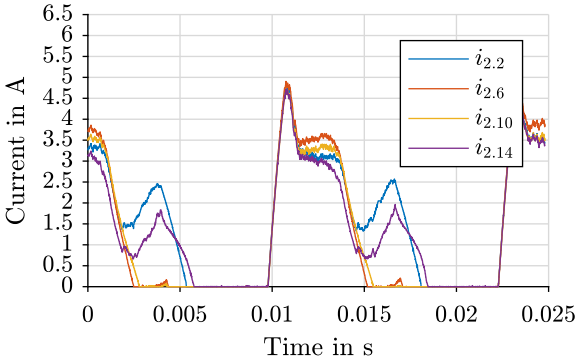

(c) Phase 2: pole currents

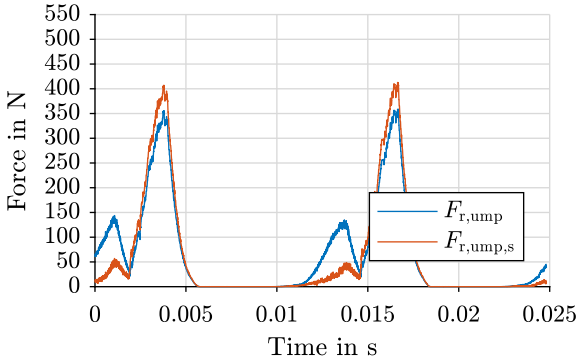

(d) Phase 2: net radial force

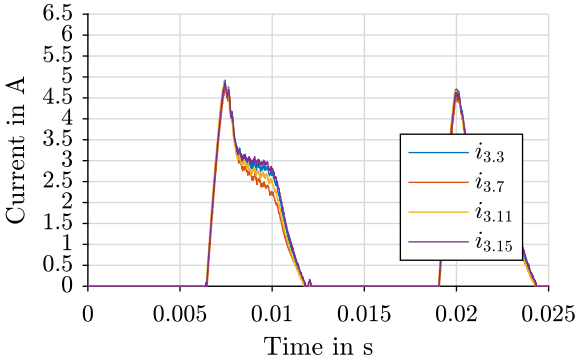

(e) Phase 3: pole currents

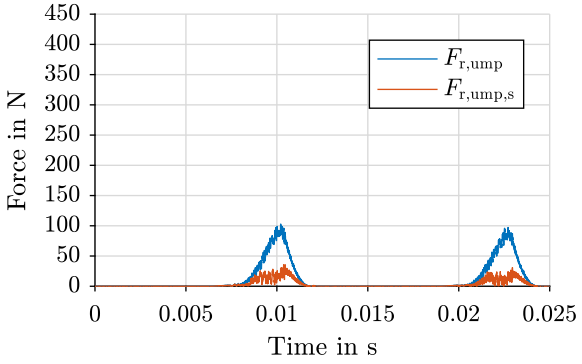

(f) Phase 3: net radial force

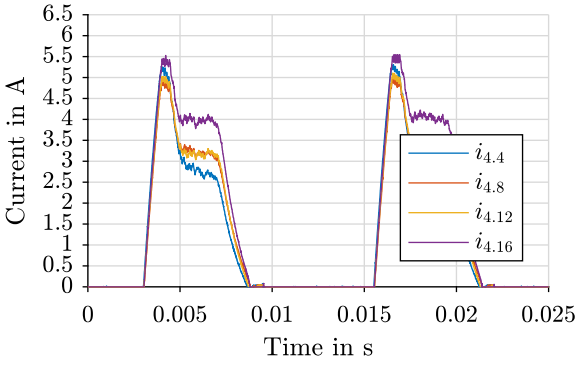

(g) Phase 4: pole currents

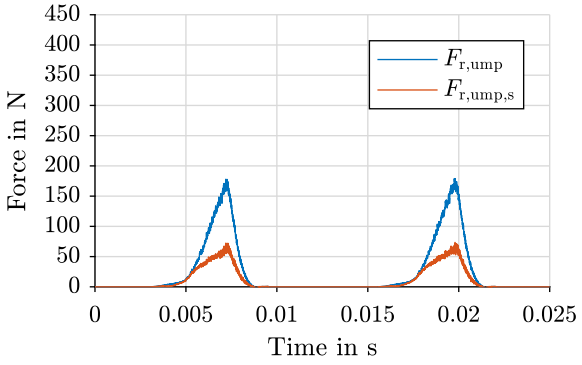

(h) Phase 4: net radial force

Figure A.12: SRM-16/12: Measurement results of pole currents and UMP with and without asymmetric inductance synthesis of DITC with S-RFMC at $T = 5\,\mathrm{Nm}$ and $n = 400\,\mathrm{rpm}$ (1$\underline{1}$0-1)

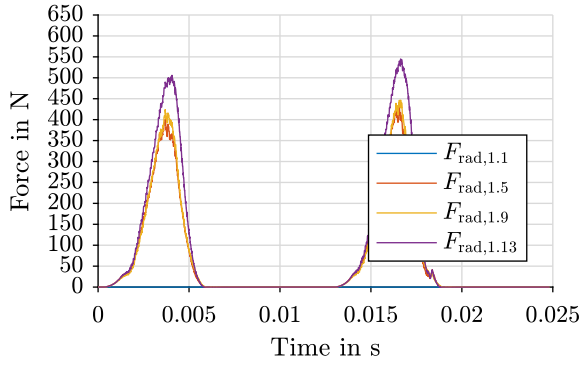

(a) Phase 1: no synthesis

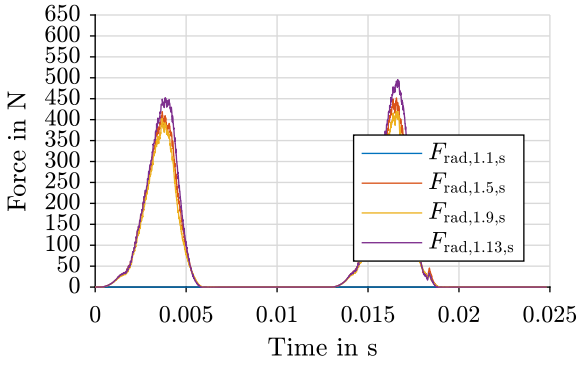

(b) Phase 1: with synthesis

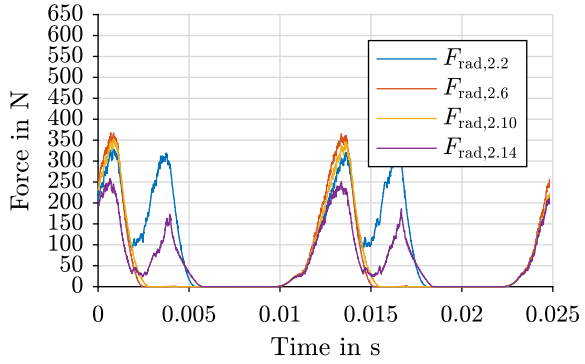

(c) Phase 2: no synthesis

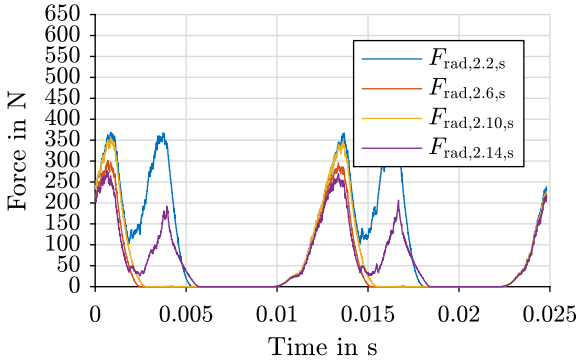

(d) Phase 2: with synthesis

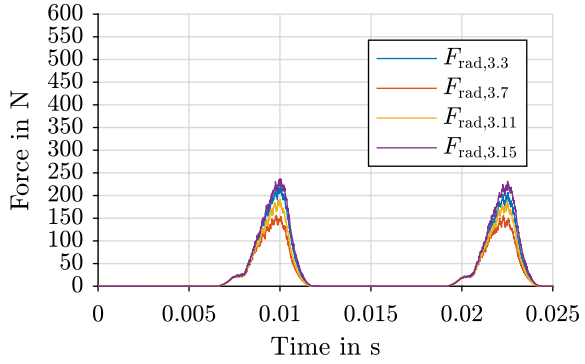

(e) Phase 3: no synthesis

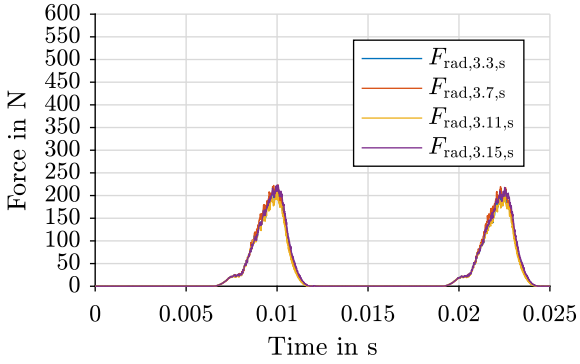

(f) Phase 3: with synthesis

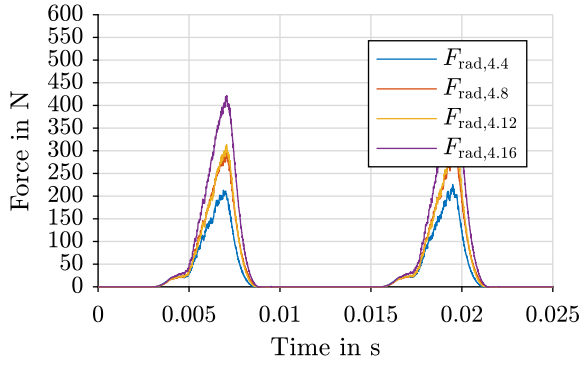

(g) Phase 4: no synthesis

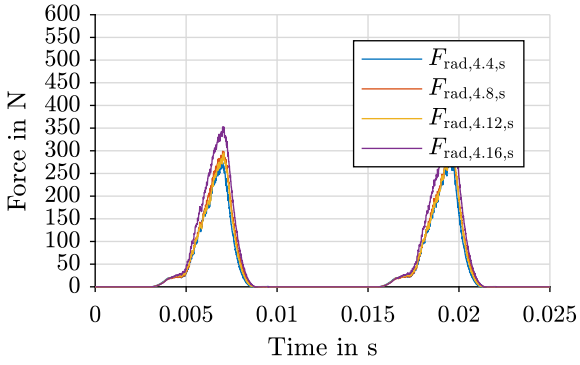

(h) Phase 4: with synthesis

Figure A.13: SRM-16/12: Measurement results of radial pole forces with and without asymmetric inductance synthesis of DITC with S-RFMC at $T = 5\,\mathrm{Nm}$ and $n = 400\,\mathrm{rpm}$ (1$\underline{1}$0-1)

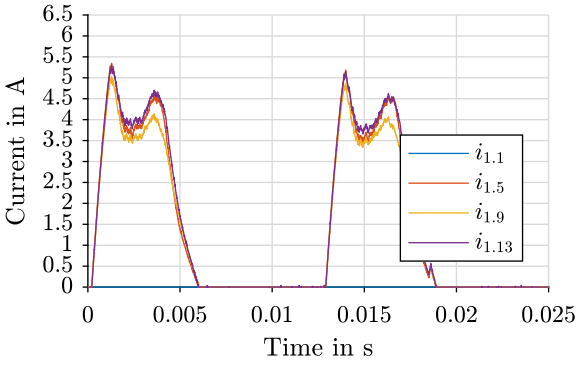

(a) Phase 1: pole currents

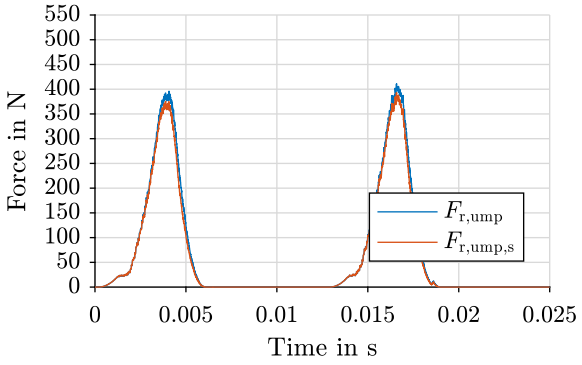

(b) Phase 1: net radial force

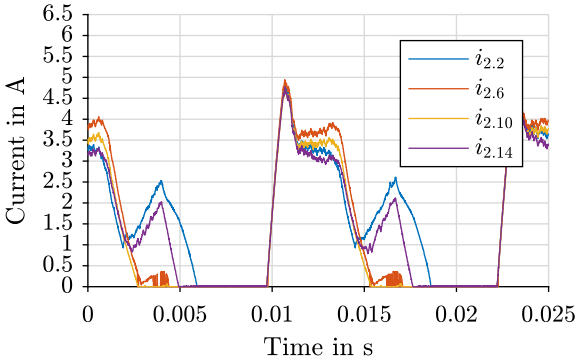

(c) Phase 2: pole currents

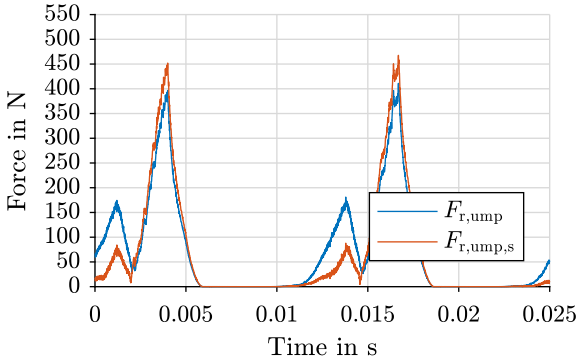

(d) Phase 2: net radial force

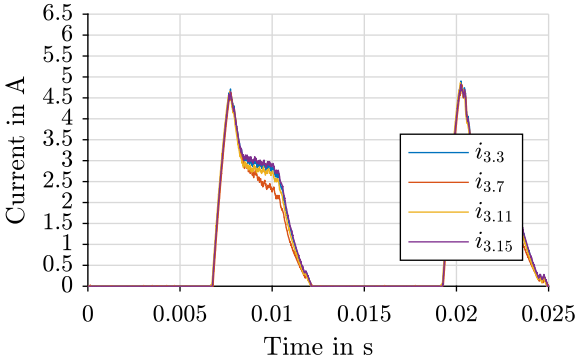

(e) Phase 3: pole currents

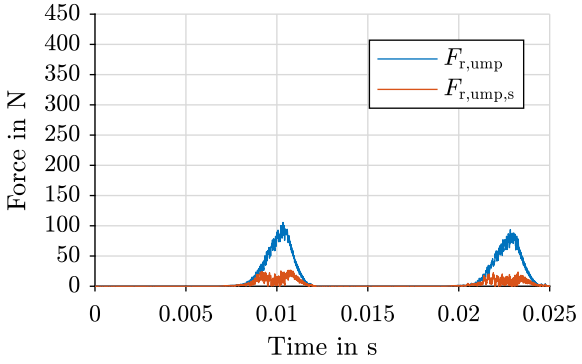

(f) Phase 3: net radial force

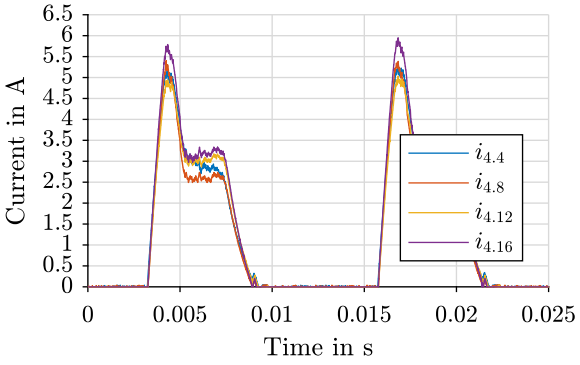

(g) Phase 4: pole currents

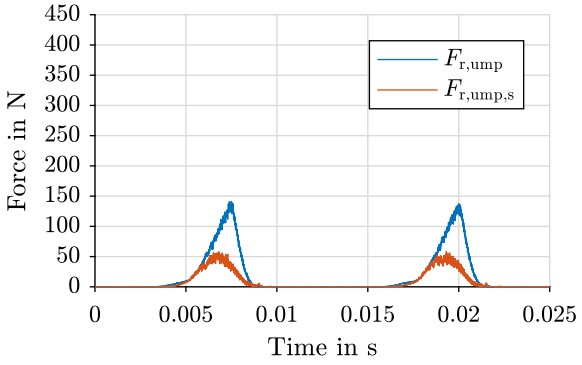

(h) Phase 4: net radial force

Figure A.14: SRM-16/12: Measurement results of pole currents and UMP with and without asymmetric inductance synthesis of DITC with S-RFMC at $T = 5\,\mathrm{Nm}$ and $n = 400\,\mathrm{rpm}$ (1$\underline{1}$0-1)

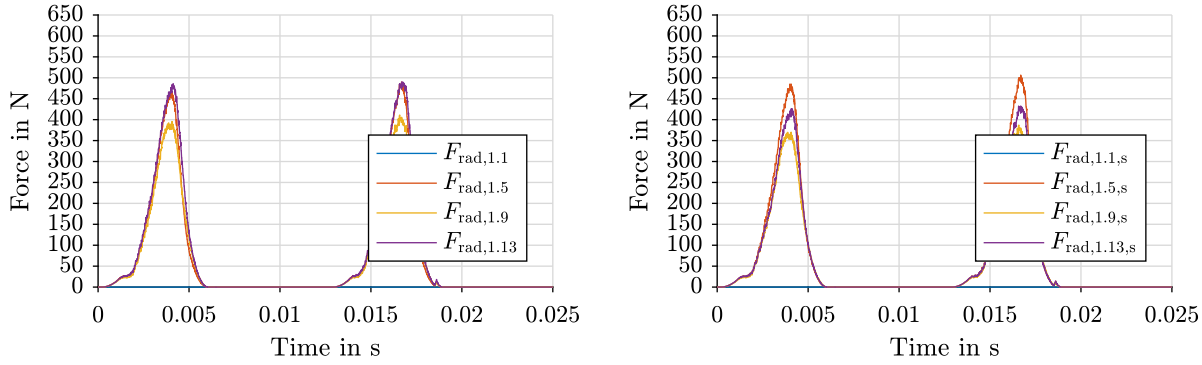

(a) Phase 1: no synthesis

(b) Phase 1: with synthesis

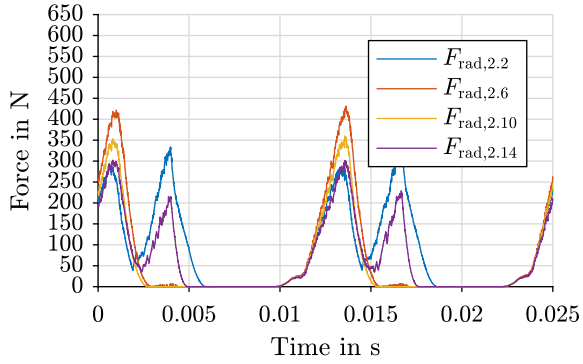

(c) Phase 2: no synthesis

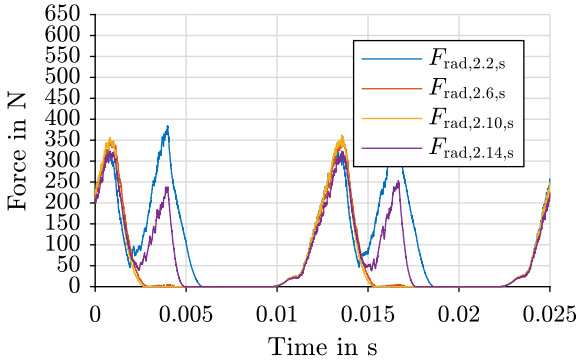

(d) Phase 2: with synthesis

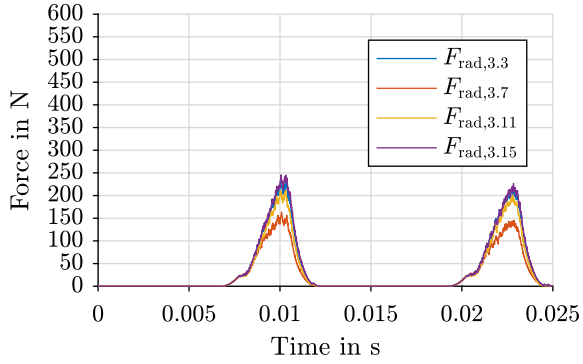

(e) Phase 3: no synthesis

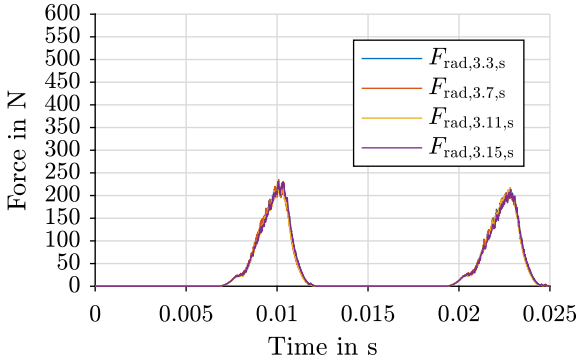

(f) Phase 3: with synthesis

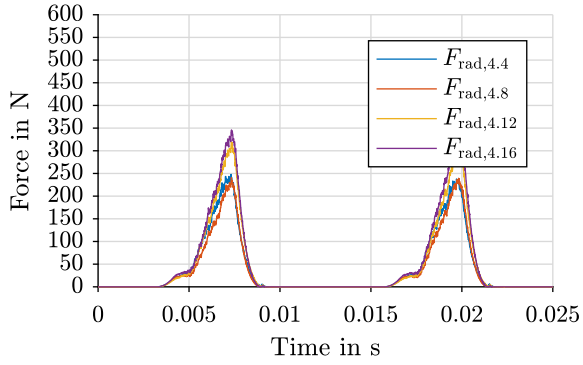

(g) Phase 4: no synthesis

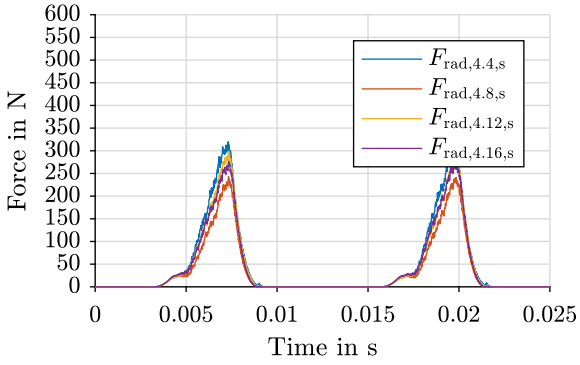

(h) Phase 4: with synthesis

Figure A.15: SRM-16/12: Measurement results of radial pole forces with and without asymmetric inductance synthesis of DITC with S-RFMC at $T = 5\,\mathrm{Nm}$ and $n = 400\,\mathrm{rpm}$ (0$\underline{1}$0-1)

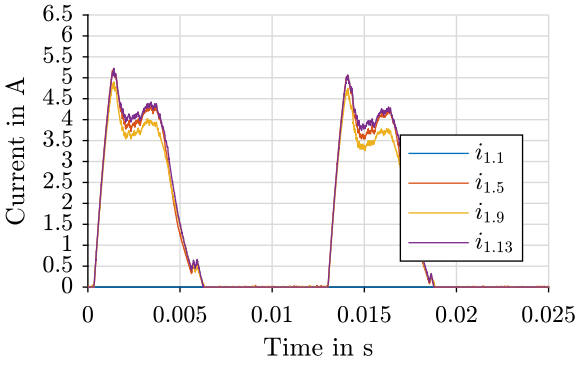

(a) Phase 1: pole currents

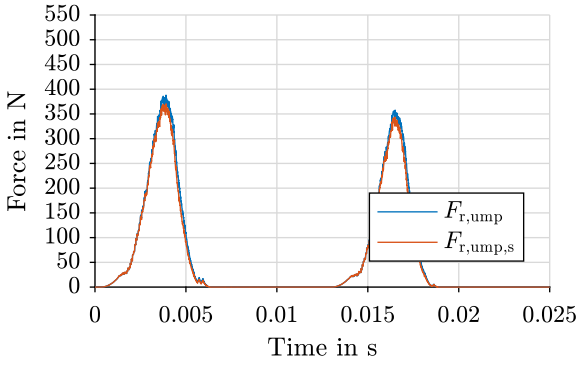

(b) Phase 1: net radial force

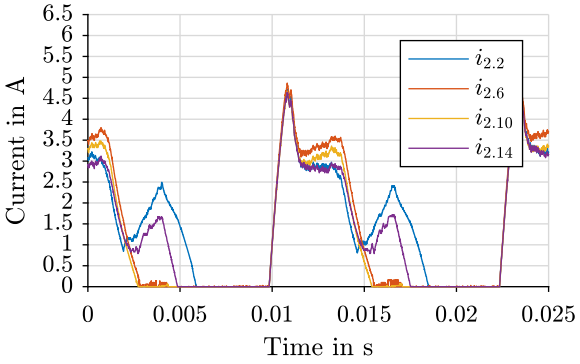

(c) Phase 2: pole currents

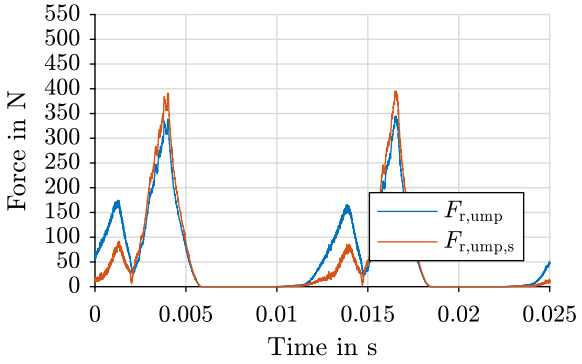

(d) Phase 2: net radial force

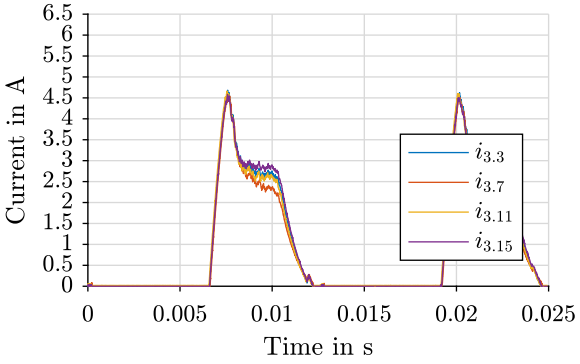

(e) Phase 3: pole currents

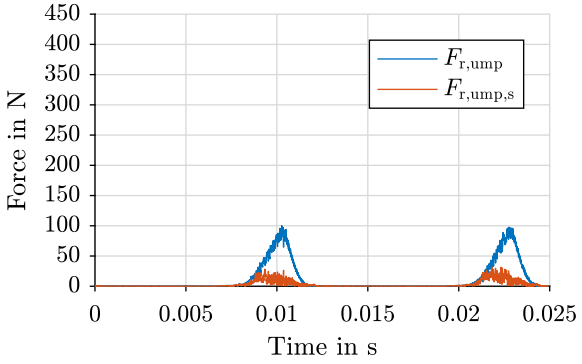

(f) Phase 3: net radial force

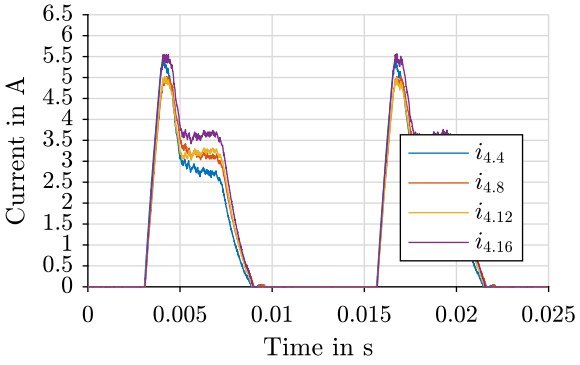

(g) Phase 4: pole currents

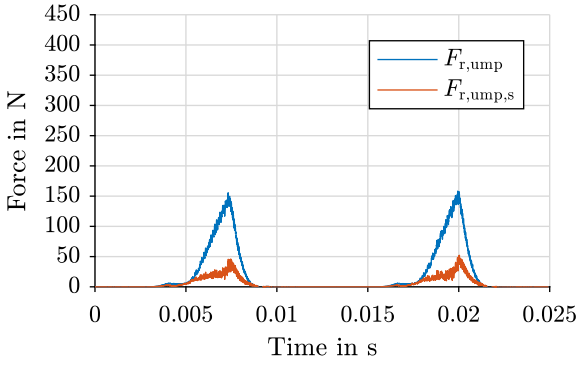

(h) Phase 4: net radial force

Figure A.16: SRM-16/12: Measurement results of pole currents and UMP with and without asymmetric inductance synthesis of DITC with S-RFMC at $T = 5\,\mathrm{Nm}$ and $n = 400\,\mathrm{rpm}$ (0$\underline{1}$1-1)

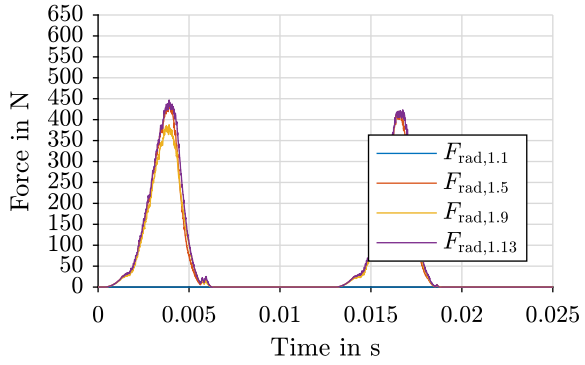

(a) Phase 1: no synthesis

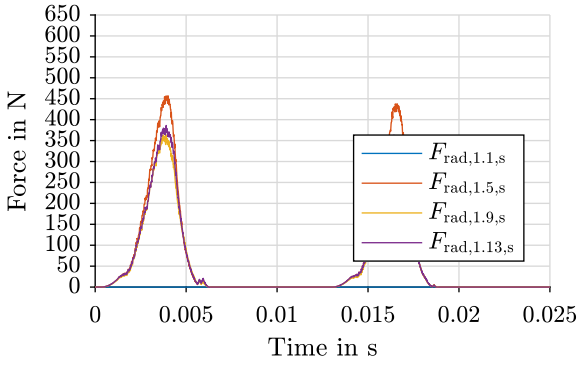

(b) Phase 1: with synthesis

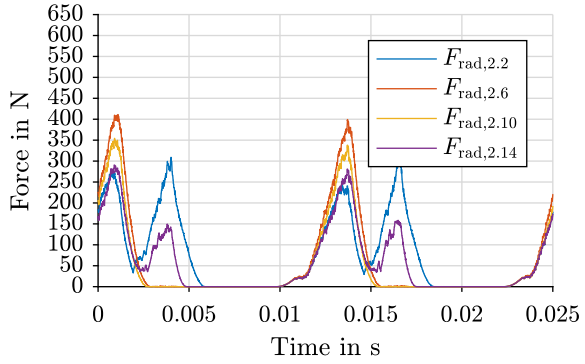

(c) Phase 2: no synthesis

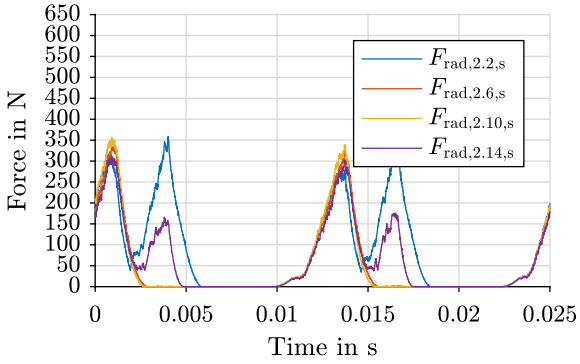

(d) Phase 2: with synthesis

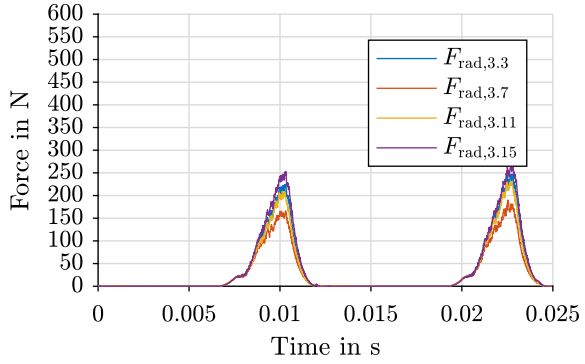

(e) Phase 3: no synthesis

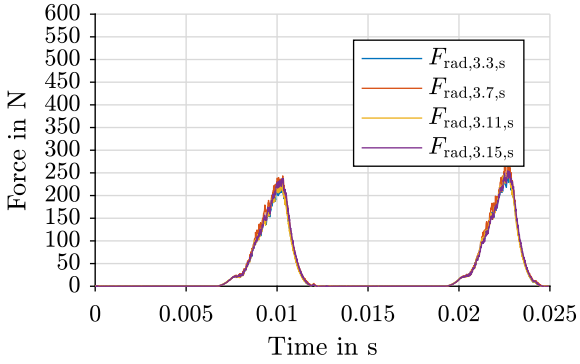

(f) Phase 3: with synthesis

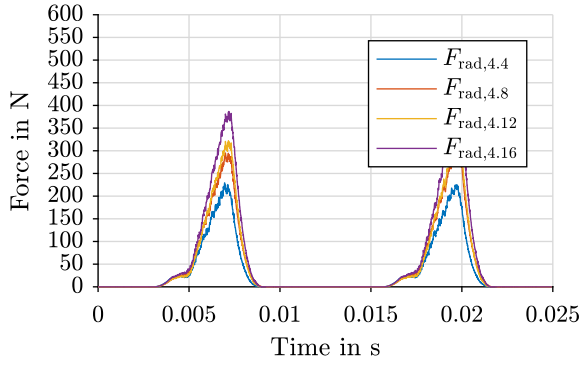

(g) Phase 4: no synthesis

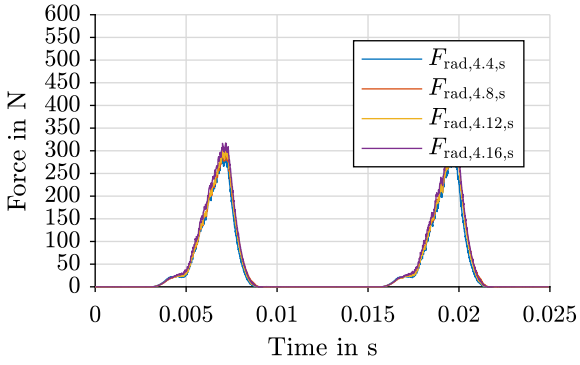

(h) Phase 4: with synthesis

Figure A.17: SRM-16/12: Measurement results of radial pole forces with and without asymmetric inductance synthesis of DITC with S-RFMC at $T = 5\,\mathrm{Nm}$ and $n = 400\,\mathrm{rpm}$ (0$\underline{1}$1-1)

A.2.2 Phase 3 Polarity in S-RFMC

The different influences the polarity of the faulty phase (phase 1) and the preceding phase (phase 2) have on the proposed S-RFMC fault tolerant control has been discussed in great detail in section 6.4. This section contains a comparison between measurements where the polarity of phase 3 is reversed. In all measurements it is visible that the influence of phase 3 for SRM-16/12 is negligible. Phase 3 is not a directly preceding or following phase to the faulty phase and thus, it is surrounded by fault-free phases. The phase commutations with phase 3 resembles normal DITC operation with only a small amount of mutual coupling influence between the phases.

The preceding phase (phase 2) is a neighboring phase of phase 3, however, its trajectory during phase commutation resembles the normal DITC shape. Only during the second half of its conduction period, where the commutation to phase 1 takes place, does S-RFMC influence the current trajectories and cause a differing behavior to fault-free DITC. The changing trajectory of phase 2 only directly influences the faulty phase 1 as should be the case due to the control algorithm.

The first comparison is between SRFMC-1$\underline{1}$0-1 and SRFMC-1$\underline{1}$0-0 in figure A.18. The second measurement is with an inverted faulty phase (phase 1), i.e. SRFMC-0$\underline{1}$0-1 versus SRFMC-0$\underline{1}$0-0 in figure A.19. The final comparison is with an inverted preceding phase (phase 2), i.e. SRFMC-0$\underline{1}$1-0 versus SRFMC-0$\underline{1}$1-1 in figure A.20.

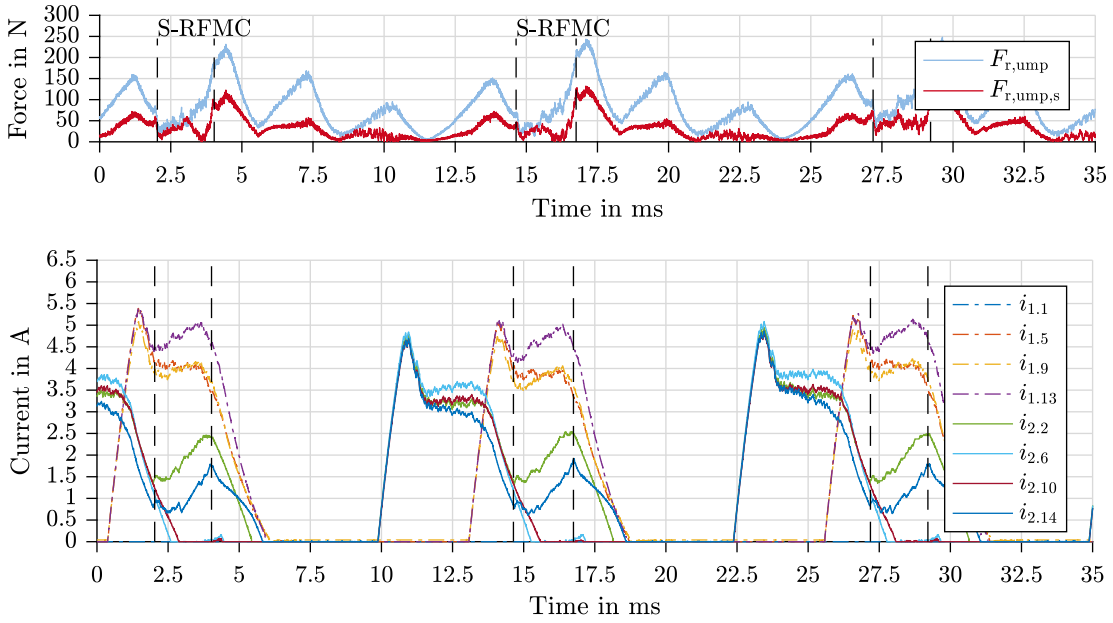

(a) S-RFMC-1$\underline{1}$0-1: UMP and pole currents of phase 1 and phase 2

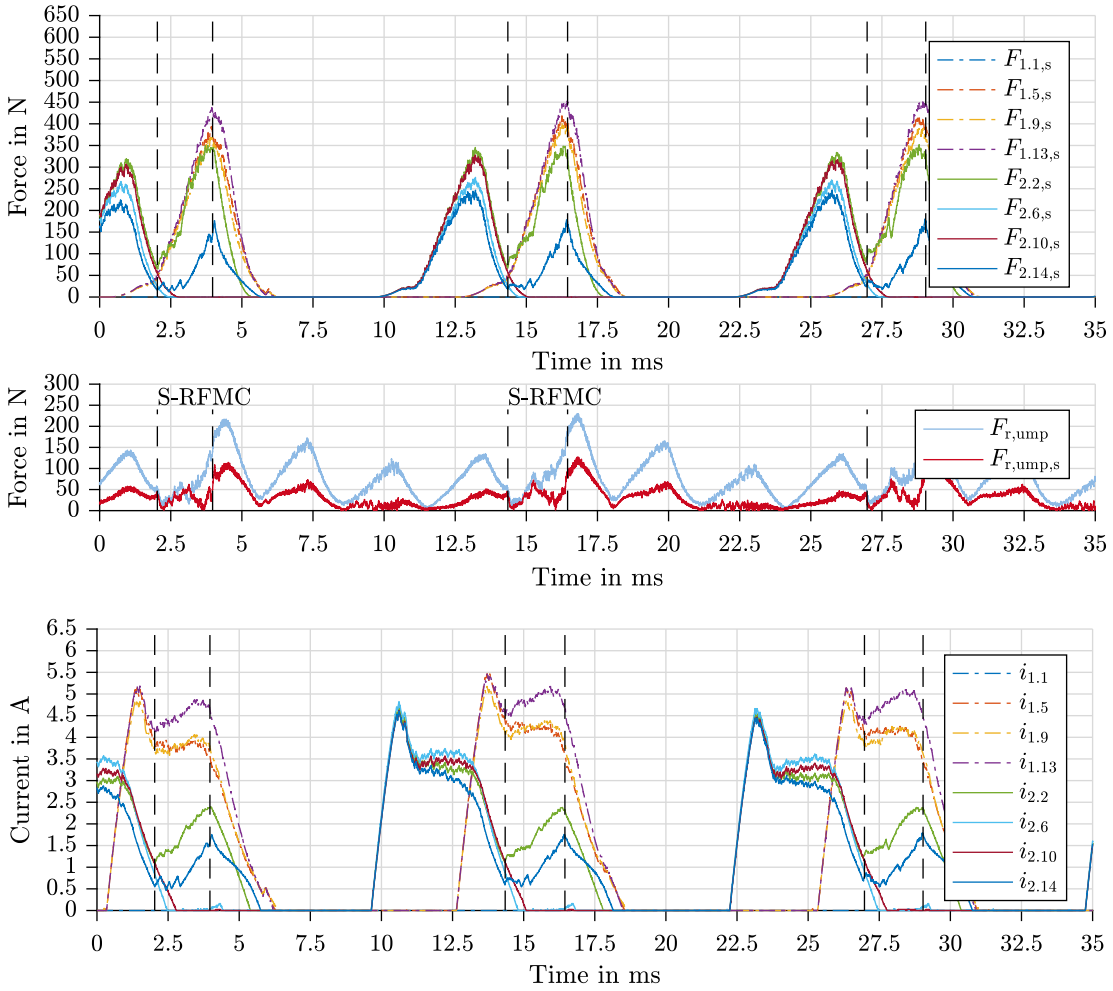

(b) S-RFMC-1$\underline{1}$0-0: Radial force, UMP and pole currents of phase 1 and phase 2

Figure A.18: SRM-16/12: S-RFMC during fault operation with 1$\underline{1}$0-1 versus 1$\underline{1}$0-0 (phase 3 polarity reversed) at 5 Nm and 400 rpm, considering coupling with a LUT representing the sine-term factor for $k_{\mathrm{mc},2.2}$ and $k_{\mathrm{mc},2.14}$

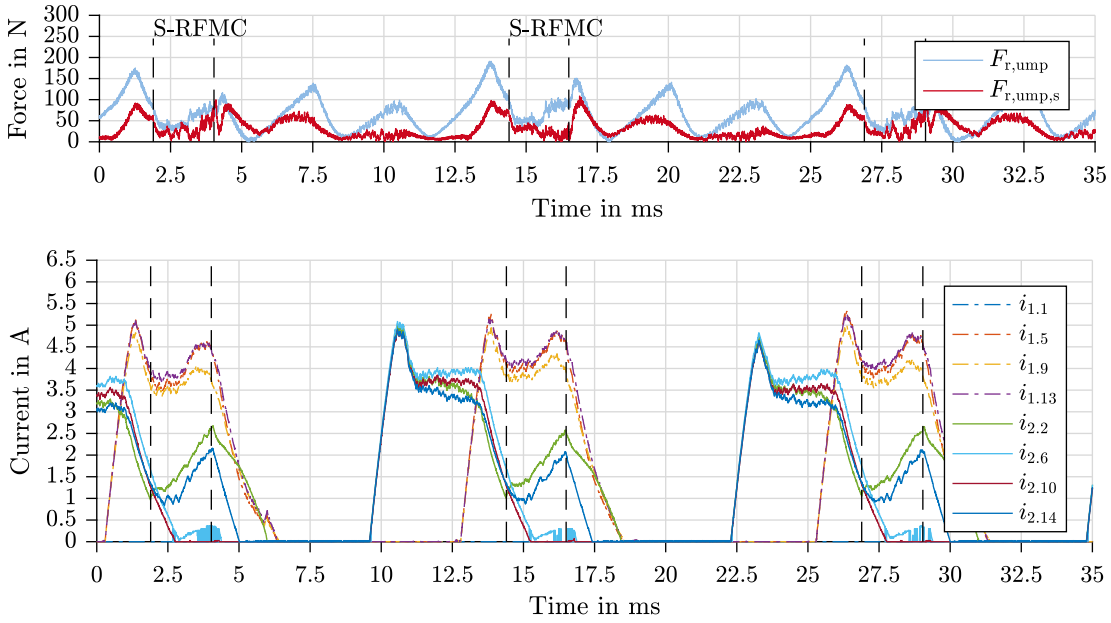

(a) S-RFMC-0$\underline{1}$0-1: UMP and pole currents of phase 1 and phase 2

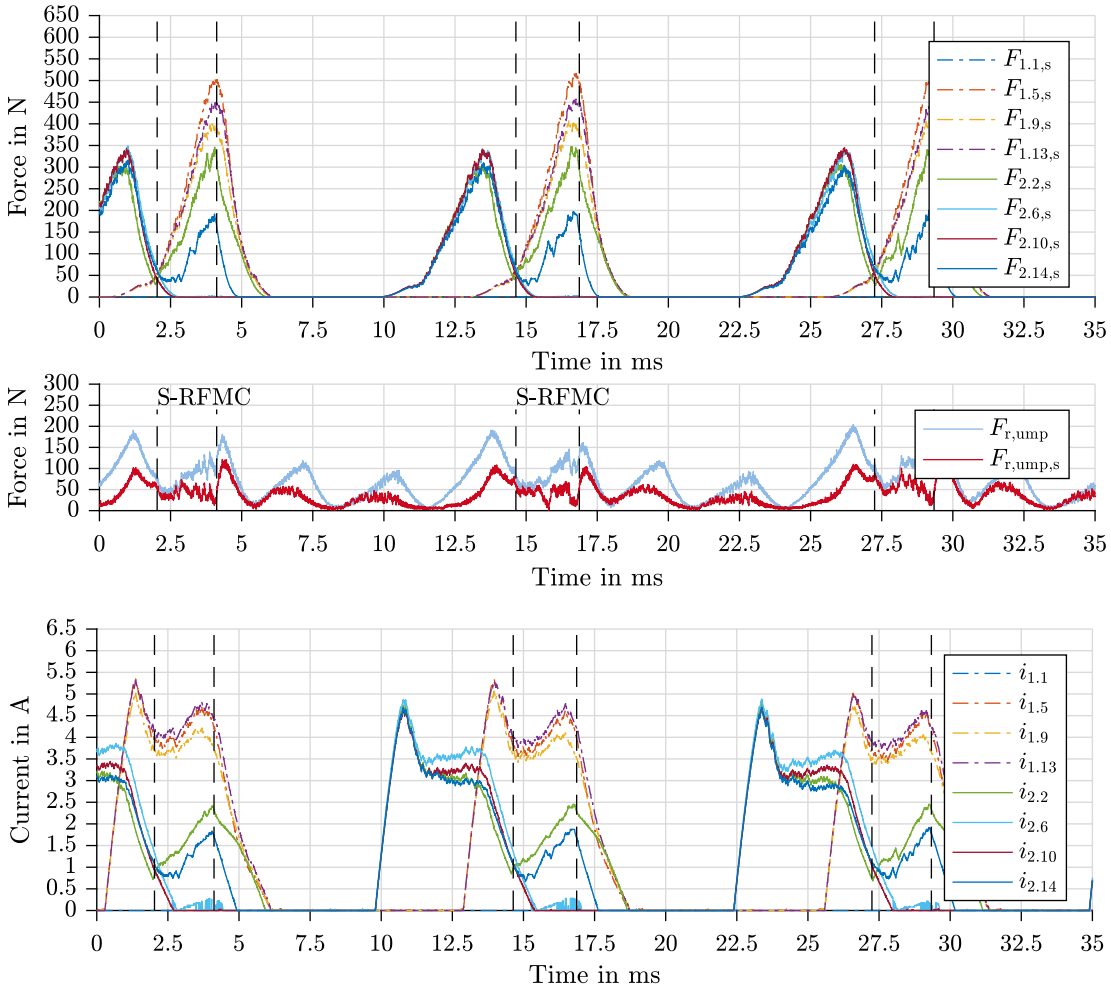

(b) S-RFMC-0$\underline{1}$0-0: Radial force, UMP and pole currents of phase 1 and phase 2

Figure A.19: SRM-16/12: S-RFMC during fault operation with 0$\underline{1}$0-1 versus 0$\underline{1}$0-0 (phase 3 polarity reversed) at 5 Nm and 400 rpm, considering mutual coupling with $k_{\mathrm{mc},2.2} = -0.02$ and $k_{\mathrm{mc},2.14} = -0.06$

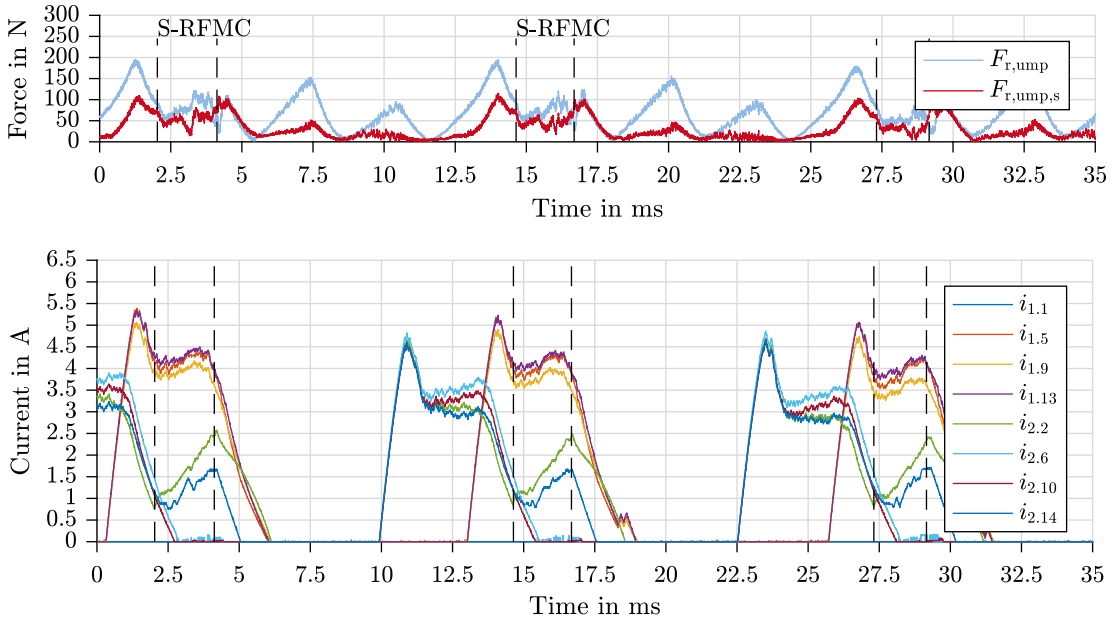

(a) S-RFMC-011-0: UMP and pole currents of phase 1 and phase 2

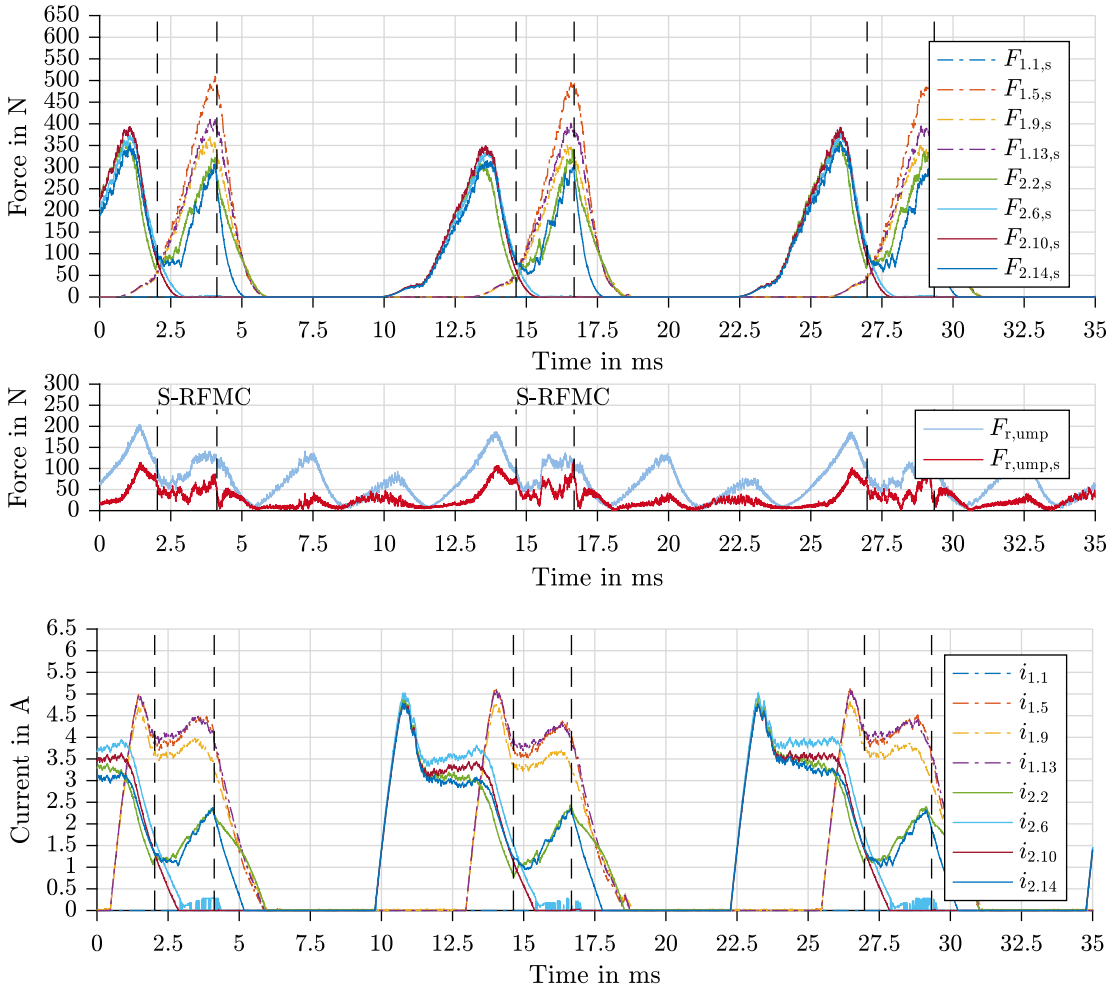

(b) S-RFMC-011-1: Radial force, UMP and pole currents of phase 1 and phase 2

Figure A.20: SRM-16/12: S-RFMC during fault operation with 011-0 versus 011-1 (phase 3 polarity reversed) at 5 Nm and 400 rpm, considering mutual coupling with $k_{mc,2.2} = -0.02$ and $k_{mc,2.14} = -0.06$

B Acronyms

1-D	1-dimensional
2-D	2-dimensional
3-D	3-dimensional
ANN	artificial neural network
DATC	direct average torque control
DIFC	direct instantaneous force control
DITC	direct instantaneous torque control
DOE	design of experiments
DSP	digital signal processor
dSPACE MicroLabBox	dSPACE, rapid prototyping hard- and software by dSPACE
EFC	elementary fault control
EMF	electromotive force
FEA	finite element analysis
FFT	fast fourier transform
FLA	flux linkage allocation
FLUX™2D	FLUX™2D, simulation software for electromagnetic design and development by CEDRAT
FPGA	field programmable gate array
FT	fault tolerant
FTC	fault tolerant control
HCC	hysteresis current control
IM	induction machine
JMAG®	JMAG®, simulation software for electromechanical design and development by JSOL
JSOL	JSOL corporation develops, among others, the computer-aided engineering (CAE) software JMAG
LPN	lumped parameter network
LPTN	lumped parameter thermal network

LUT	lookup table
MATLAB	MATLAB, simulation software by Mathworks®
MEC	magnetic equivalent circuit
Minitab®	Minitab®, simulation software for design of experiment development and statistical evaluation
MMF	magneto-motive forces
Motor-CAD	motor performance and thermal analysis software by Motor Design Limited [100]
OFAT	one factor at a time
PC	personal computer
PC-SRD	PC-SRD, simulation software for analytical design of switched reluctance machines by SPEED
PMSM	permanent magnet synchronous machine
PWM	pulse width modulation
PWM-DITC	pulse width modulation based predictive direct instantaneous torque control
RFMC	radial force minimization control
RLS	recursive least squares
RMS	root mean square
RSM	response surface method
RWTH	RWTH Aachen University, `http://www.rwth-aachen.de`
S-RFMC	simplified radial force minimization control for single pole fault
SIL	software in the loop
Simulink	Simulink, simulation software for model based design by Mathworks®
SPEED	SPEED, simulation software suite for design of electrical machines
SRM	switched reluctance machine
TSF	torque sharing function
UMP	unbalanced magnetic pull
WBG	wide-bandgap

C Symbols

$A_{\mathrm{ag,rotor}}$	rotor cross sectional area
B	flux density
$F_{\mathrm{r,ump,s}}$	unbalanced magnetic pull corrected by asymmetric pole inductances in SRM-16/12
$F_{\mathrm{rad},x,\mathrm{s}}$	radial force x corrected by asymmetric pole inductances in SRM-16/12
H	magnetic field
$J_{\mathrm{RMS}}^{\mathrm{max}}$	maximum allowed RMS current density
J_{RMS}	RMS current density
L_{LUT}	inductance from $L_{\mathrm{ph}}(\psi_{\mathrm{ph}},\theta_{\mathrm{el}})$-LUT during $T_{\mathrm{ph}}(\psi_{\mathrm{ph}},\theta_{\mathrm{el}})$ tuning
L_{est}	estimated inductance during $T_{\mathrm{ph}}(\psi_{\mathrm{ph}},\theta_{\mathrm{el}})$ tuning
L_{ph}	phase inductance
L_{pl}	pole inductance
N_{ph}	number of phases
N_{r}	number of rotor teeth
N_{s}	number of stator teeth
N_{w}	number of windings
P_{Cu}	copper loss
$P_{\mathrm{DITC}}^{\mathrm{max}}$	maximum power using DITC control
$P_{\mathrm{DITC}}^{\mathrm{nom}}$	nominal power using DITC control
P_{Fe}	iron loss
P_{design}	power rating used for SRM machine design
P^{max}	maximum power output
P^{nom}	nominal power output
$R_{\mathrm{m}}^{\mathrm{ag}}(\theta)$	magnetic reluctance: air gap
$R_{\mathrm{m}}^{\mathrm{fe}}(\phi)$	magnetic reluctance: iron steel
R_{m}	magnetic reluctance
R_{ph}	phase winding resistance
R_{pl}	pole winding resistance
S_{fill}	slot-fill factor in percent
$T_{\mathrm{DITC}}^{\mathrm{nom}}$	nominal torque using DITC
T_{amb}	ambient temperature
T_{design}	torque rating used for machine design
T_{nom}	nominal torque
T_{ref}^{*}	reference torque

T_{rem}	remaining torque to be divided amongst the phases or poles
T_{sensor}	torque measurement from torque transducer
T_{surf}	housing surface temperature
$T_{\text{w,avg}}$	average winding temperature
$T_{\text{w,max}}$	maximum winding temperature
T_{wdg}	winding temperature
W_{co}	co-energy
W_{mech}	mechanical energy
$\Delta\theta_{\text{el}}$	change in electrical angle of rotor position between two measurements
Δi	hysteresis current band
$\Theta_{\text{MMF,pl}}$	magnetomotive force per pole
Θ_{MMF}	magnetomotive force
β_{r}	rotor tooth arc
β_{s}	stator tooth arc
δ_{ag}	air-gap length
C_{dc}	dc-link capacitor
μ_0	permeability of vacuum
μ_{r}	relative permeability
i_{dc}	dc-load current
v_{dc}	dc-link voltage
η_{eff}	machine efficiency
$\overline{T}_{\text{avg,ph}}$	average phase torque
$\overline{T}_{\text{avg}}$	average torque of all phases combined
ϕ	magnetic flux
$\psi_{\text{alternating}}$	flux linkage from alternating coil arrangement
$\psi_{\text{non-alt.}}$	flux linkage from non-alternating coil arrangement
ψ_{ph}	phase flux linkage
ψ_{pl}	pole flux linkage
ψ_{self}	self flux linkage
ψ_{n+2}^{max}	maximum phase flux linkage predicted for period n+2
$\psi_{\text{lim}}^{\text{max}}$	maximum allowed flux linkage when using DITC
ψ_{n+2}^{min}	minimum phase flux linkage predicted for period n+2
σ	thrust factor
SRM_{DITC}	DITC optimized SRM design
SRM_{eff}	efficiency optimized SRM design
SRM_{ini}	initial DOE SRM design
SRM_{mas}	maximum torque per mass optimized SRM design
SRM_{rpl}	minimum torque ripple optimized SRM design
θ_{el}	electrical angle of rotor position
θ_{m}	mechanical angle of rotor position
$\theta_{\text{off}}^{\text{RFMC}}$	turn-off angle: θ_{el} at which control switches from radial force control back to DITC

$\theta_{\text{off}}^{\text{S-RFMC}}$	turn-off angle: θ_{el} at which control switches from S-RFMC back to DITC
θ_{off}	turn-off angle: θ_{el} at which negative voltage is applied to machine phase
$\theta_{\text{on}}^{\text{RFMC}}$	turn-on angle: θ_{el} at which control switches to radial force control
$\theta_{\text{on}}^{\text{S-RFMC}}$	turn-on angle: θ_{el} at which control switches to S-RFMC
θ_{on}	turn-on angle: θ_{el} at which positive voltage is applied to machine phase
d_{cu}	copper wire diameter
$d_{\text{gap,rs}}$	distance between rotor- and stator tooth tips at unaligned rotor position
d_{n}	duty cycle applied during period n
f_{PWM}	pulse width modulation frequency
$h_{\text{tooth,r}}$	rotor-tooth height
i_{RMS}	RMS current
$i_{\text{inv}}^{\text{max}}$	maximum inverter current
i_{max}	maximum current
i_{ph}	phase current
i_{pk}	peak phase current
i_{pl}	pole current of one stator tooth
i_{ref}^{*}	reference current
$i_{\text{RFMC}}^{\text{max}}$	maximum current allowed in RFMC to limit the machine current density
$k_{\text{arc,r}}$	rotor tooth arc adjustment factor
$k_{\text{arc,s}}$	stator tooth arc adjustment factor
$k_{\text{mc,2.14}}$	factor considering the mutual coupling of the faulty phase (phase 1) on the preceding phase (pole 2.14) during S-RFMC
$k_{\text{mc,2.2}}$	factor considering the mutual coupling of the faulty phase (phase 1) on the preceding phase (pole 2.2) during S-RFMC
$k_{\text{w,sy}}$	stator yoke overdimensioning factor in regard to stator tooth width
l_{stk}	active stack length
lb	lower boundary condition
m_{Cu}	mass of overall winding copper
m_{Fe}	mass of overall active iron
m_{active}	mass of active machine components
m_{rotor}	mass of machine rotor
m_{stator}	mass of machine stator
$n_{\text{DITC}}^{\text{nom}}$	nominal speed using DITC
n_{design}	speed rating used for machine design
n^{max}	maximum speed

n^{nom}	nominal speed
r_0	radius rotor yoke
r_1	radius air gap
r_2	radius stator yoke
r_3	radius outer stator
r_{ag}	radius air gap
r_{sh}	radius rotor shaft
ub	upper boundary condition
v_{design}	voltage rating used for machine design
v_{ph}	phase voltage
v_{pl}	pole voltage at one stator tooth
$w_{\mathrm{s,tooth}}$	width of stator tooth
$w_{\mathrm{s,yoke}}$	width of stator yoke
$F_{\mathrm{r},i}$	radial force belonging to pole i
$F_{\mathrm{r,max}}$	maximum reference radial force for radial force minimization control
$F_{\mathrm{r,ump}}$	radial force due to unbalanced magnetic pull
$F_{\mathrm{t},i}$	tangential force belonging to pole i
θ_{free}	freewheeling angle: θ_{el} at which zero voltage is applied to machine phase

List of Figures

List of Tables

Bibliography

[1] L. Szabo, M. Ruba, and Kovacs, E. Füvesi, V. "Fault Tolerant Modular Linear Motor for Safe-Critical Automated Industrial Applications, Journal of Computer Science and Control Systems." In: *Journal of Computer Science and Control Systems* (2009).

[2] L. Szabo. "Modular Switched Reluctance Machines to be Used in Automotive Applications." In: *Workshop on SRM drives an alternative for E-traction* (2018).

[3] W. Ding, Y. Liu, and Y. Hu. "Performance Evaluation of a Fault-Tolerant Decoupled Dual-Channel Switched Reluctance Motor Drive Under Open-Circuits." In: *Electric Power Applications, IET* 8.4 (2014), pp. 117–130.

[4] E. Bostanci, M. Moallem, A. Parsapour, and B. Fahimi. "Opportunities and Challenges of Switched Reluctance Motor Drives for Electric Propulsion: A Comparative Study." In: *IEEE Transactions on Transportation Electrification* 3.1 (2017), pp. 58–75.

[5] SaFAD-Whitepaper, ed. *Safety First for Automated Driving*. 2019.

[6] Komatsu, ed. *LeTourneau Wheel loader P&H L-2350*. 2020.

[7] W. H. Taylor. "Improvements in Obtaining Power by Means of Electro-Magnetism." Mechanics' Magazine and Journal of Science, Arts, and Manufactures, pg. 158. 1840.

[8] P. J. Lawrenson, J. M. Stephenson, N. N. Fulton, P. T. Blenkinsop, and J. Corda. "Variable-Speed Switched Reluctance Motors." In: *IEE Proceedings Electric Power Applications* 127.4 (1980), p. 253.

[9] B. Burkhart, A. Klein-Hessling, and I. Ralev, C. P. Weiss, R. W. De Doncker. "Technology, Research and Applications of Switched Reluctance Drives." In: *CPSS Transactions on Power Electronics and Applications* 2.1 (2017), pp. 12–27.

[10] T. J. E. Miller. *Brushless Permanent-Magnet and Reluctance Motor Drives: Monographs in Electrical and Electronic Engineering No. 21*. Oxford: Oxford University Press, 1989.

[11] C. M. Stephens. "Fault Detection and Management System for Fault-Tolerant Switched Reluctance Motor Drives." In: *IEEE Transactions on Industry Applications* 27.6 (1991), pp. 1098–1102.

[12] A. A. Arkadan and B. W. Kielgas. "Switched Reluctance Motor Drive Systems Dynamic Performance Prediction Under Internal and External Fault Conditions." In: *IEEE Transactions on Energy Conversion* 9.1 (1994), pp. 45–52.

[13] A. Klein-Hessling, A. Hofmann, and R. W. De Doncker. "Direct Instantaneous Torque and Force Control: A Control Approach for Switched Reluctance Machines." In: *IET Electric Power Applications* 11.5 (2017), pp. 935–943.

[14] M. D. Hennen, M. Niessen, C. Heyers, H. J. Brauer, and R. W. De Doncker. "Development and Control of an Integrated and Distributed Inverter for a Fault Tolerant Five-Phase Switched Reluctance Traction Drive." In: *IEEE Transactions on Power Electronics* 27.2 (2012), pp. 547–554.

[15] T. J. E. Miller. "Converter Volt-Ampere Requirements of the Switched Reluctance Motor Drive." In: *IEEE Transactions on Industry Applications* IA-21.5 (1985), pp. 1136–1144.

[16] S. Vukosavic and V. R. Stefanovic. "SRM Inverter Topologies: A Comparative Evaluation." In: *IEEE Transactions on Industry Applications* 27.6 (1991), pp. 1034–1047.

[17] M. Barnes and C. Pollock. "Power Electronic Converters for Switched Reluctance Drives." In: *IEEE Transactions on Power Electronics* 13.6 (1998), pp. 1100–1111.

[18] M. Ehsani, J. T. Bass, T. J. E. Miller, and R. L. Steigerwald. "Development of a Unipolar Converter for Variable Reluctance Motor Drives." In: *IEEE Transactions on Industry Applications* IA-23.3 (1987), pp. 545–553.

[19] T. J. E. Miller, P. G. Bower, R. Becerra, and M. Ehsani. "Four-Quadrant Brushless Reluctance Motor Drive." In: *Power Electronics and Variable-Speed Drives* (1988).

[20] W. Ding, Y. Hu, and L. Wu. "Investigation and Experimental Test of Fault-tolerant Operation of a Mutually Coupled Dual Three-Phase SRM Drive under Faulty Conditions." In: *IEEE Transactions on Power Electronics* PP.99 (2015), p. 1.

[21] F. C. Lin and S. M. Yang. "Instantaneous Shaft Radial Force Control with Sinusoidal Excitations for Switched Reluctance Motors." In: *IEEE Transactions on Energy Conversion* 22.3 (2007), pp. 629–636.

[22] S. Koschik, F. Adler, D. Szepanski, and R. W. De Doncker. "Scalable FPGA and DSP Based Control for Multiphase Concentrated Winding Permanent Magnet Machines with Single Coil Integrated Inverters." In: *IEEE International Electric Machines & Drives Conference (IEMDC)* (2015), pp. 1515–1521.

[23] S. Koschik. "Permanenterregte Synchronmaschinen mit Einzelzahnsteuerung - Regelkonzepte und Betriebsstrategien für hochintegrierte Antriebssysteme." dissertation. RWTH Aachen University, 2018.

[24] Y. Burkhardt, A. Spagnolo, P. Lucas, M. Zavesky, and P. Brockerhoff. "Design and Analysis of a Highly Integrated 9-Phase Drivetrain for EV Applications." In: *International Conference on Electrical Machines (ICEM), 2014*. Piscataway, NJ: IEEE, 2014, pp. 450–456.

[25] G. Engelmann, M. Kowal, and R. W. De Doncker. "A Highly Integrated Drive Inverter Using DirectFETs and Ceramic dc-link Capacitors for Open-End Winding Machines in Electric Vehicles." In: *APEC 2015*. Piscataway, NJ: IEEE, 2015, pp. 290–296.

[26] M. Marz, A. Schletz, B. Eckardt, S. Egelkraut, and H. Rauh. “Power Electronics System Integration for Electric and Hybrid Vehicles.” In: *International Conference on Integrated Power Electronics Systems* (2010).

[27] T. M. Jahns and H. Dai. “The Past, Present, and Future of Power Electronics Integration Technology in Motor Drives.” In: *CPSS Transactions on Power Electronics and Applications* 2.3 (2017), pp. 197–216.

[28] Public relations division Mitsubishi Electric Corporation. “Mitsubishi Electric Develops EV Motor System with Built-in Silicon Carbide Inverter.” In: *Press release* (2012).

[29] P. Brockerhoff, Y. Burkhardt, K. Egger, and H. Rauh. “Highly Integrated Drivetrain Solution: Integration of Motor, Inverter and Gearing.” In: *4th International Electric Drives Production Conference (EDPC 2014)*. Piscataway, NJ: IEEE, 2014, pp. 1–6.

[30] N. R. Brown and T. M. Jahns and R. D. Lorenz. “Power Converter Design for an Integrated Modular Motor Drive.” In: *IEEE Industry Applications Conference* (2007), pp. 1322–1328.

[31] S. Gopalakrishnan, A. M. Omekanda, and B. Lequesne. “Classification and Remediation of Electrical Faults in the Switched Reluctance Drive.” In: *IEEE Transactions on Industry Applications* 42.2 (2006), pp. 479–486.

[32] M. D. Hennen. “Switched Reluctance Direct Drive with Integrated Distributed Inverter.” dissertation. Aachen: RWTH Aachen University, 2012.

[33] A. Lahyani, P. Venet, G. Grellet, and P.-J. Viverge. “Failure Prediction of Electrolytic Capacitors During Operation of a Switchmode Power Supply.” In: *IEEE Transactions on Power Electronics* 13.6 (1998), pp. 1199–1207.

[34] A. H. Bonnett and C. Yung. “A Construction, Performance and Reliability Comparison for Pre-EPAct, EPAct and Premium-Efficient Motors.” In: *IEEE Industry Applications Society 53rd Annual Petroleum and Chemical Industry Conference* (2006), pp. 1–7.

[35] O. V. Thorsen and M. Dalva. “A Survey of Faults on Induction Motors in Offshore Oil Industry, Petrochemical Industry, Gas Terminals, and Oil Refineries.” In: *IEEE Transactions on Industry Applications* 31.5 (1995), pp. 1186–1196.

[36] S. Nandi, H. A. Toliyat, and X. Li. “Condition Monitoring and Fault Diagnosis of Electrical Motors—A Review.” In: *IEEE Transactions on Energy Conversion* 20.4 (2005), pp. 719–729.

[37] B. Lequesne, S. Gopalakrishnan, and A. M. Omekanda. “Winding Short Circuits in the Switched Reluctance Drive.” In: *IEEE Transactions on Industry Applications* 41.5 (2005), pp. 1178–1184.

[38] J. P. Lyons and M. Preston. “Fault Tolerant Active Magnetic Bearing Electric System.” US05578880. 26. November 1996.

[39] J. Reinert. “Optimierung der Betriebseigenschaften von Antrieben mit geschalteter Reluktanzmaschine.” dissertation. RWTH Aachen University, 1998.

[40] J. Fiedler. "Design of Low-Noise Switched Reluctance Drives." dissertation. RWTH Aachen University, 2006.

[41] K. Kasper. "Analysis and Control of the Acoustic Behavior of Switched Reluctance Drives." dissertation. RWTH Aachen University, 2011.

[42] R. B. Inderka. "Direkte Drehmomentregelung Geschalteter Reluktanzantriebe." dissertation. RWTH Aachen University, 2003.

[43] R. B. Inderka and R. W. De Doncker. "High-Dynamic Direct Average Torque Control for Switched Reluctance Drives." In: *IEEE Transactions on Industry Applications* 39.4 (2003), pp. 1040–1045.

[44] R. B. Inderka and R. W. De Doncker. "DITC-Direct Instantaneous Torque Control of Switched Reluctance Drives." In: *IEEE Transactions on Industry Applications* 39.4 (2003), pp. 1046–1051.

[45] C. R. Neuhaus, N. H. Fuengwarodsakul, and R. W. De Doncker. "Predictive PWM-based Direct Instantaneous Torque Control of Switched Reluctance Drives." In: *Power Electronics Specialists Conference, 2006. PESC '06. 37th IEEE.* 2006, pp. 1–7.

[46] N. H. Fuengwarodsakul. "Predictive PWM based Direct Instantaneous Torque Control for Switched Reluctance Machines." dissertation. RWTH Aachen University, 2007.

[47] I. Ralev. "Accurate Torque Control of Position Sensorless Switched Reluctance Drives." dissertation. RWTH Aachen University, 2018.

[48] D. van Treek. "Position Sensorless Torque Control of Switched Reluctance Machines." dissertation. RWTH Aachen University, 2012.

[49] H. J. Brauer, M. D. Hennen, and R. W. De Doncker. "Multiphase Torque-Sharing Concepts of Predictive PWM-DITC for SRM." In: *7th International Conference on Power Electronics and Drive Systems* (2007), pp. 511–516.

[50] A. Hofmann, F. Qi, and R. W. De Doncker. "Developing the Concept for an Automotive High-Speed SRM Drive with Focus on Acoustics." In: *International Conference on Power Electronics and Electrical Machines* (2014), pp. 1–5.

[51] Z. Liu, T. Winter, and M. Schier. "Direct Coil Cooling of a High Performance Switched Reluctance Machine (SRM) for EV/HEV Applications." In: *SAE International* (2014).

[52] M. Farshad, J. Faiz, and C. Lucas. "Development of Analytical Models of Switched Reluctance Motor in Two-Phase Excitation Mode: Extended Miller Model." In: *IEEE Transactions on Magnetics* 41.6 (2005), pp. 2145–2155.

[53] S. W. Zhao, N. C. Cheung, C. K. Lee, X. Y. Yang, and Z. G. Sun. "Survey of Modeling Methods for Flux Linkage of Switched Reluctance Motor." In: *International Conference on Power Electronics Systems and Applications* (2011).

[54] A. Radun. "Analytical Calculation of the Switched Reluctance Motor's Unaligned Inductance." In: *IEEE Transactions on Magnetics* 35.6 (1999), pp. 4473–4481.

[55] A. Radun. “Analytically Computing the Flux Linked by a Switched Reluctance Motor Phase when the Stator and Rotor Poles Overlap.” In: *IEEE Transactions on Magnetics* 36.4 (2000), pp. 1996–2003.

[56] R. Krishnan. *Switched Reluctance Motor Drives: Modeling, Simulation, Analysis, Design, and Applications*. CRC Press, Taylor & Francis Group, 2001.

[57] C. S. Edrington, B. Fahimi, and M. Krishnamurthy. “An Autocalibrating Inductance Model for Switched Reluctance Motor Drives.” In: *IEEE Transactions on Industrial Electronics* 54.4 (2007), pp. 2165–2173.

[58] T. Miller and M. McGilp. “Nonlinear Theory of the Switched Reluctance Motor for Rapid Computer-Aided Design.” In: *IEE Proceeding Electric Power Applications* 137 (1990).

[59] T. Kojima. “Efficiency Optimized Control of Switched Reluctance Motors.” dissertation. Aachen: RWTH Aachen University, 2018.

[60] S. A. Hossain and I. Husain. “A Geometry Based Simplified Analytical Model of Switched Reluctance Machines for Real-Time Controller Implementation.” In: *IEEE Transactions on Power Electronics* 18.6 (2003), pp. 1384–1389.

[61] X. D. Xue, K. W. E. Cheng, and S. L. Ho. “Optimization and Evaluation of Torque-Sharing Functions for Torque Ripple Minimization in Switched Reluctance Motor Drives.” In: *IEEE Transactions on Power Electronics* 24.9 (2009), pp. 2076–2090.

[62] K. Flasskamp, S. Ober-Blobaum, T. Schneider, and J. Bocker. “Optimal Control of a Switched Reluctance Drive by a Direct Method Using a Discrete Variational Principle.” In: *IEEE Conference on Decision and Control* (2013), pp. 7467–7473.

[63] R. Mikail, I. Husain, Y. Sozer, M. S. Islam, and T. Sebastian. “Torque-Ripple Minimization of Switched Reluctance Machines Through Current Profiling.” In: *IEEE Transactions on Industry Applications* 49.3 (2013), pp. 1258–1267.

[64] V. P. Vujičić. “Minimization of Torque Ripple and Copper Losses in Switched Reluctance Drive.” In: *IEEE Transactions on Power Electronics* 27.1 (2012), pp. 388–399.

[65] A. C. Pop, V. Petrus, C. S. Martis, V. Iancu, and J. Gyselinck. “Comparative Study of Different Torque Sharing Functions for Losses Minimization in Switched Reluctance Motors Used in Electric Vehicles Propulsion.” In: *International Conference on Optimization of Electrical and Electronic Equipment (OPTIM)* (2012), pp. 356–365.

[66] C. E. Carstensen, N. H. Fuengwarodsakul, and R. W. De Doncker. “Flux Linkage Determination for Correct Modeling of Switched Reluctance Machines - Dynamic Measurement versus Static Computation.” In: *Electric Machines & Drives Conference, 2007. IEMDC ’07. IEEE International*. Vol. 2. 2007, pp. 1317–1323.

[67] T. J. E. Miller, M. Glinka, M. McGilp, C. Cossar, G. Gallegos Lopez, D. Ionel, and M. Olaru. “Ultra-Fast Model of the Switched Reluctance Motor.” In: *Industry Applications Conference, 1998. Thirty-Third IAS Annual Meeting. The 1998 IEEE*. Vol. 1. 1998, pp. 319–326.

[68] C. Carstensen. "Eddy Currents in Windings of Switched Reluctance Machines." dissertation. Aachen: RWTH Aachen University, 2008.

[69] A. K. Jain and N. Mohan. "Dynamic Modeling, Experimental Characterization, and Verification for SRM Operation With Simultaneous Two-Phase Excitation." In: *IEEE Transactions on Industrial Electronics* 53.4 (2006), pp. 1238–1249.

[70] A. Hofmann, A. Klein-Hessling, I. Ralev, and R. W. De Doncker. "Measuring SRM Profiles Including Radial Force on a Standard Drives Test Bench." In: *IEEE International Electric Machines & Drives Conference (IEMDC)* (2015), pp. 383–390.

[71] L. Ge, I. Ralev, A. Klein-Hesling, S. Song, and R. W. De Doncker. "A Simple Reluctance Calibration Strategy to Obtain the Flux-linkage Characteristics of Switched Reluctance Machines." In: *IEEE Transactions on Power Electronics* (2019), p. 1.

[72] W. Ding, D. Liang, and R. Tang. "A Fast Nonlinear Variable Structure Equivalent Magnetic Circuit Modeling for Dual-Channel Switched Reluctance Machine." In: *Energy Conversion and Management* 52.1 (2011), pp. 308–320.

[73] J. M. Kokernak and D. A. Torrey. "Magnetic Circuit Model for the Mutually Coupled Switched-Reluctance Machine." In: *IEEE Transactions on Magnetics* 36.2 (2000), pp. 500–507.

[74] H. W. Derbas, J. M. Williams, A. C. Koenig, and S. D. Pekarek. "A Comparison of Nodal- and Mesh-Based Magnetic Equivalent Circuit Models." In: *IEEE Transactions on Energy Conversion* 24.2 (2009), pp. 388–396.

[75] C. P. Weiss, M. Huebner, M. D. Hennen, and R. W. De Doncker. "Switched Reluctance Machine Model Considering Asymmetries and Enabling Dynamic Fault Simulation." In: *IEEE International Electric Machines & Drives Conference (IEMDC), 2013*. 2013, pp. 979–985.

[76] F. Fleming. "Real-Time Switched Reluctance Machine Emulation via Magnetic Equivalent Circuits." dissertation. Florida State University, 2014.

[77] H. Sahraoui, H. Zeroug, and H. A. Toliyat. "Switched Reluctance Motor Design Using Neural-Network Method With Static Finite-Element Simulation." In: *IEEE Transactions on Magnetics* 43.12 (2007), pp. 4089–4095.

[78] T. Lachman, T. R. Mohamad, and C. H. Fong. "Nonlinear Modelling of Switched Reluctance Motors Using Artificial Intelligence Techniques." In: *IEE Proceedings Electric Power Applications* 151.1 (2004), p. 53.

[79] S. Mir, I. Husain, and M. E. Elbuluk. "Switched Reluctance Motor Modeling with On-Line Parameter Identification." In: *IEEE Transactions on Industry Applications* 34.4 (1998), pp. 776–783.

[80] A. Hofmann, F. Qi, C. P. Weiss, T. Kojima, and R. W. De Doncker. "The Acoustic Impact of Rotor Eccentricity in Switched Reluctance Machines." In: *EPE Journal* 26.2 (2016), pp. 47–57.

[81] C. P. Weiss, A. Hofmann, F. Qi, and R. W. De Doncker. “Analysis and Modelling of Rotor Eccentricity for Switched Reluctance Machines.” In: *7th IET International Conference on Power Electronics, Machines and Drives (PEMD 2014), Manchester* (2014).

[82] A. Hofmann, F. Qi, C. P. Weiss, and R. W. De Doncker. “Efficiently Modeling Rotor Eccentricity in Switched Relcutance Machines.” In: *2014 16th European Conference on Power Electronics and Applications*. IEEE, 2014, pp. 1–10.

[83] C. P. Weiss, S. Schoeler, and R. W. De Doncker. “Direct Instantaneous Torque Control for Switched Reluctance Machines Considering Mutual Coupling.” In: *The Journal of Engineering* 2019.17 (2019), pp. 3701–3704.

[84] D. Panda and V. Ramanarayanan. “Mutual Coupling and Its Effect on Steady-State Performance and Position Estimation of Even and Odd Number Phase Switched Reluctance Motor Drive.” In: *IEEE Transactions on Magnetics* 43.8 (2007), pp. 3445–3456.

[85] W. Ding, Liang Deliang, and H. Sui. “Dynamic Modeling and Performance Prediction for Dual-Channel Switched Reluctance Machine Considering Mutual Coupling.” In: *IEEE Transactions on Magnetics* 46.9 (2010), pp. 3652–3663.

[86] A. Klein-Hessling. “Active DC-Power Filters for Switched Reluctance Drives during Single-Pulse Operation.” dissertation. RWTH Aachen University, 2018.

[87] M. Schenk. “Simulative Untersuchung der Wicklungsverluste in Geschalteten Reluktanzmaschinen.” dissertation. RWTH Aachen University, 2015.

[88] A. Hofmann, A. Al-Dajani, M. Bösing, and R. W. De Doncker. “Direct Instantaneous Force Control: A Method to Eliminate Mode-0-Borne Noise in Switched Reluctance Machines.” In: *IEEE International Electric Machines & Drives Conference (IEMDC), 2013*. Piscataway, NJ: IEEE, 2013, pp. 1009–1016.

[89] A. Hofmann. “Direct Instantaneous Force Control – Key to Low Noise Switched Reluctance Traction Drives.” dissertation. RWTH Aachen University, 2016.

[90] C. P. Weiss and A. Klein-Hessling and R. W. De Doncker. “Discussion on Control Structure Modifications Using an FPGA for Predictive DITC in Switched Reluctance Machines Regarding LUT Resolution.” In: *19th International Conference on Electrical Machines and Systems (ICEMS), Chiba* (2016), pp. 1–6.

[91] Z. Lin, D. S. Reay, B. W. Williams, and X. He. “High Performance Current Control for Switched Reluctance Motors With On-Line Modeling.” In: *Power Electronics Specialists Conference, 2004. PESC 04. 2004 IEEE 35th Annual*. Vol. 2. 2004, pp. 1246–1251.

[92] X. Li and P. Shamsi. “Inductance Surface Learning for Model Predictive Current Control of Switched Reluctance Motors.” In: *IEEE Transactions on Transportation Electrification* PP.99 (2015), p. 1.

[93] G. Lei, J. Zhu, Y. Guo, C. Liu, and B. Ma. “A Review of Design Optimization Methods for Electrical Machines.” In: *Energies* 10.12 (2017), p. 1962.

[94] C. Ma and L. Qu. "Multiobjective Optimization of Switched Reluctance Motors Based on Design of Experiments and Particle Swarm Optimization." In: *IEEE Transactions on Energy Conversion* 30.3 (2015), pp. 1144–1153.

[95] T. J. E. Miller. *Switched Reluctance Motors and Their Control*. Oxford: Clarendon Press, 1993.

[96] M. J. Anderson and P. J. Whitcomb. *DOE Simplified: Practical Tools for Effective Experimentation / Practical Tools for Effective Experimentation*. Third edition. Boca Raton: CRC Press, Taylor and Francis Group and CRC Press, Taylor & Francis Group, 2015.

[97] T. Lange, C. P. Weiss, and R. W. De Doncker. "Design of Experiments Based Optimization of Synchronous and Switched Reluctance Machines." In: *IEEE Conference on Power Electronics and Drive Systems*.

[98] V. Rallabandi, J. Wu, P. Zhou, D. G. Dorrell, and D. M. Ionel. "Optimal Design of a Switched Reluctance Motor With Magnetically Disconnected Rotor Modules Using a Design of Experiments Differential Evolution FEA-Based Method." In: *IEEE Transactions on Magnetics* 54.11 (2018), pp. 1–5.

[99] *Minitab*. 2019.

[100] Motor Design Limited. *Motor-CAD*.

[101] B. Burkhart, A. Mittelstedt, and R. W. De Doncker. "Solution Space Based Pre-Design Approach to Compare and Select Configurations of Switched Reluctance Machines." In: *8th IET International Conference on Power Electronics, Machines and Drives (PEMD 2016)*. 2016, pp. 1–6.

[102] H. J. Brauer. "Schnelldrehender Geschalteter Reluktanzantrieb mit extremem Längendurchmesserverhältnis." dissertation. RWTH Aachen University, 2013.

[103] M. C. Costa, J. R. Cardoso, S. I. Nabeta, Y. Maréchal, A. B. Dietrich, and J.-L. Coulomb. "Optimisation of a Switched Reluctance Motor Using Experimental Design Method and Diffuse Elements Response Surface." In: *IEE Proceedings - Science, Measurement and Technology* 151.6 (2004), pp. 411–413.

[104] B. Burkhart. "Switched Reluctance Generator for Range Extender Applications: Design, Control and Evaluation." dissertation. RWTH Aachen University, 2018.

[105] H. J. Brauer, B. Burkhart, and R. W. De Doncker. "Comprehensive Electromagnetic Design Procedure for Switched Reluctance Machines." In: *Conference on Power Electronics, Machines and Drives* (2012).

[106] M. N. Anwar, I. Husain, and A. V. Radun. "A Comprehensive Design Methodology for Switched Reluctance Machines." In: *IEEE Transactions on Industry Applications* (2001).

[107] A. V. Radun. "Design Considerations for the Switched Reluctance Motor." In: *IEEE Transactions on Industry Applications* 5 (1995).

[108] M. E. Zaim, K. Dakhouche, and M. Bounekhla. "Design for Torque Ripple Reduction of a Three-Phase Switched-Reluctance Machine." In: *IEEE Transactions on Magnetics* 38.2 (2002), pp. 1189–1192.

[109] R. Mikail. “High Performance Control of a Switched Reluctance Machine.” dissertation. North Carolina State University, 2013.

[110] S. Boyd and L. Vandenberghe. *Convex Optimization*. 7th ed. Cambridge University Press, 2009.

[111] *LEONI cables*. 2020.

[112] Y. Dou, S. Vassiliadis, G. K. Kuzmanov, and G. N. Gaydadjiev. “64-bit Floating-Point FPGA Matrix Multiplication.” In: *International Symposium on Field Programmable Gate Arrays* (2005).

[113] dSPACE. *dSPACE*. 2020.

[114] N. K. Sheth and K. R. Rajagopal. “Effects of Nonuniform Airgap on the Torque Characteristics of a Switched Reluctance Motor.” In: *IEEE Transactions on Magnetics* 40 (2004).

[115] N. R. Garrigan, W. L. Soong, C. M. Stephens, A. Storace, and T. A. Lipo. “Radial Force Characteristics of a Switched Reluctance Machine.” In: *IEEE Industry Applications Conference, 1999. Thirty-Fourth IAS Annual Meeting.* 1999, pp. 2250–2258.

ABISEA Band 1
Eßer, Albert
Berührungslose, kombinierte Energie- und Informationsübertragung für bewegliche Systeme
1. Aufl. 1992, 129 S.
ISBN 3-86073-046-0

ABISEA Band 2
Vogel, Ulrich
Entwurf und Beurteilung von Verfahren zur Hochausnutzung des Rad-Schiene-Kraftschlusses durch Triebfahrzeuge
1. Aufl. 1992, 131 S.
ISBN 3-86073-060-6

ABISEA Band 3
Reckhorn, Thomas
Stromeinprägendes Antriebssystem mit fremderregter Synchronmaschine
1. Aufl. 1992, 128 S.
ISBN 3-86073-061-4

ABISEA Band 4
Ackva, Ansgar
Spannungseinprägendes Antriebssystem mit Synchronmaschine und direkter Stromregelung
1. Aufl. 1992, 137 S.
ISBN 3-86073-062-2

ABISEA Band 5
Mertens, Axel
Analyse des Oberschwingungsverhaltens von taktsynchronen Delta - Modulationsverfahren zur Steuerung von Pulsstromrichtern bei hoher Taktzahl
1. Aufl. 1992, 178 S.
ISBN 3-86073-069-X

ABISEA Band 6
Geuer, Wolfgang
Untersuchungen über das Alterungsverhalten von Blei-Akkumulatoren
1. Aufl. 1993, 97 S.
ISBN 3-86073-097-5

ABISEA Band 7
Langheim, Jochen
Einzelradantrieb für Elektrostraßenfahrzeuge
1. Aufl. 1993, 213 S.
ISBN 3-86073-123-8
(vergriffen)

ABISEA Band 8
Fetz, Joachim
Fehlertolerante Regelung eines Asynchron-Doppelantriebes für ein Elektrospeicherfahrzeug
1. Aufl. 1993, 136 S.
ISBN 3-86073-124-6
(vergriffen)

ABISEA Band 9
Schülting, Ludger
Optimierte Auslegung induktiver Bauelemente für den Mittelfrequenzbereich
1. Aufl. 1993, 126 S.
ISBN 3-86073-174-2
(vergriffen)

ABISEA Band 10
Skudelny, H.-Ch.
Stromrichtertechnik
4. Aufl. 1997, 259 S.
ISBN 3-86073-189-0

ABISEA Band 11
Skudelny, H.-Ch.
Elektrische Antriebe
3. Aufl. 1997, 124 S.
ISBN 3-86073-231-5

ABISEA Band 12
Schöpe, Friedhelm
Batterie-Management für Nickel-Cadmium Akkumulatoren
1. Aufl. 1994, 148 S.
ISBN 3-86073-232-3
(vergriffen)

ABISEA Band 13
v. d. Weem, Jürgen
Schmalbandige aktive Filter für Schienentriebfahrzeuge am Gleichspannungsfahrdraht
1. Aufl. 1995, 126 S.
ISBN 3-86073-233-1

ABISEA Band 14
Backhaus, Klaus
Spannungseinprägendes Direktantriebssystem mit schnelllaufender geschalteter Reluktanzmaschine
1. Aufl. 1995, 146 S.
ISBN 3-86073-234-X
(vergriffen)

ABISEA Band 15
Reinold, Harry
Optimierung dreiphasiger Pulsdauermodulationsverfahren
1. Aufl. 1996, 107 S.
ISBN 3-86073-235-8

ABISEA Band 16
Köpken, Hans-Georg
Regelverfahren für Parallelschwingkreisumrichter
1. Aufl. 1996, 125 S.
ISBN 3-86073-236-6

ABISEA Band 17
Mauracher, Peter
Modellbildung und Verbundoptimierung bei Elektrostraßenfahrzeugen
1. Aufl. 1996, 192 S.
ISBN 3-86073-237-4

ABISEA Band 18
Protiwa, Franz-Ferdinand
Vergleich dreiphasiger Resonanz-Wechselrichter in Simulation und Messung
1. Aufl. 1997, 178 S.
ISBN 3-86073-238-2

ABISEA Band 19
Brockmeyer, Ansgar
Dimensionierungswerkzeug für magnetische Bauelemente in Stromrichteranwendungen
1. Aufl. 1997, 175 S.
ISBN 3-86073-239-0

ABISEA Band 20
Apeldoorn, Oscar
Simulationsgestützte Bewertung von Steuerverfahren für netzgeführte Stromrichter mit verringerter Netzrückwirkung
1. Aufl. 1997, 134 S.
ISBN 3-86073-680-9

ABISEA Band 21
Lohner, Andreas
Batteriemanagement für verschlossene Blei-Batterien am Beispiel von Unterbrechungsfreien Stromversorgungen
1. Aufl. 1998, 126 S.
ISBN 3-86073-681-7

ABISEA Band 22
Reinert, Jürgen
Optimierung der Betriebseigenschaften von Antrieben mit geschalteter Reluktanzmaschine
1. Aufl. 1998, 153 S.
ISBN 3-86073-682-5

ABISEA Band 23
Nagel, Andreas
Leitungsgebundene Störungen in der Leistungselektronik: Entstehung, Ausbreitung und Filterung
1. Aufl. 1999, 140 S.
ISBN 3-86073-683-3

ABISEA Band 24
Menne, Marcus
Drehschwingungen im Antriebsstrang von Elektrostraßenfahrzeugen - Analyse und aktive Dämpfung
1. Aufl. 2001, 169 S.
ISBN 3-86073-684-1

ABISEA Band 25
von Bloh, Jochen
Multilevel-Umrichter zum Einsatz in Mittelspannungs-Gleichspannungs-Übertragungen
1. Aufl. 2001, 137 S.
ISBN 3-86073-685-X

ABISEA Band 26
Karden, Eckhard
Using low-frequency impedance spectroscopy for characterization, monitoring, and modeling of industrial batteries
1. Aufl. 2002, 137 S.
ISBN 3-8265-9766-4

ABISEA Band 27
Karipidis, Claus-Ulrich
A Versatile DSP/ FPGA Structure optimized for Rapid Prototyping and Digital Real-Time Simulation of Power Electronic and Electrical Drive Systems
1. Aufl. 2001, 164 S.
ISBN 3-8265-9738-9

ABISEA Band 28
Kahlen, Klemens
Regelungsstrategien für permanentmagnetische Direktantriebe mit mehreren Freiheitsgraden
1. Aufl. 2002, 154 S.
ISBN 3-8322-1222-1

ABISEA Band 29
Inderka, Robert B.
Direkte Drehmomentregelung Geschalteter Reluktanzantriebe
1. Aufl. 2003, 182 S.
ISBN 3-8322-1175-6

ABISEA Band 30
Schröder, Stefan
Circuit-Simulation Models of High-Power Devices Based on Semiconductor Physics
1. Aufl. 2003, 123 S.
ISBN 3-8322-1250-7

ABISEA Band 31
Buller, Stephan
Impedance-Based Simulation Models for Energy Storage Devices in Advanced Automotive Power Systems
1. Aufl. 2003, 138 S.
ISBN 3-8322-1225-6

ABISEA Band 32
Schönknecht, Andreas
Topologien und Regelungsstrategien für das induktive Erwärmen mit hohen Frequenz-Leistungsprodukten
1. Aufl. 2004, 157 S.
ISBN 3-8322-2408-4

ABISEA Band 33
Tolle, Tobias
Konvertertopologien für ein aufwandsarmes, zweistufiges Schaltnetzteil zum Laden von Batterien aus dem Netz
1. Aufl. 2004, 148 S.
ISBN 3-8322-2676-1

ABISEA Band 34
Götting, Gunther
Dynamische Antriebsregelung von Elektrostraßenfahrzeugen unter Berücksichtigung eines schwingungsfähigen Antriebsstrangs
1. Aufl. 2004, 157 S.
ISBN 3-8322-2804-7

ABISEA Band 35
Dieckerhoff, Sibylle
Transformatorlose Stromrichterschaltungen für Bahnfahrzeuge am 16 2/3Hz Netz
1. Aufl. 2004, 147 S.
ISBN 3-8322-3094-7

ABISEA Band 36
Hu, Jing
Bewertung von DC-DC-Topologien und Optimierung eines DC-DC-Leistungsmoduls für das 42-V-Kfz-Bordnetz
1. Aufl. 2004, 148 S.
ISBN 3-8322-3201-X

ABISEA Band 37
Detjen, Dirk-Oliver
Characterization and Modeling of Si-Si Bonded Hydrophobie Interfaces for Novel High-Power BIMOS Devices
1. Aufl. 2004, 135 S.
ISBN 3-8322-2963-9

ABISEA Band 38
Walter, Jörg
Simulationsbasierte Zuverlässigkeitsanalyse in der modernen Leistungselektronik
1. Aufl. 2004, 121 S.
ISBN 3-8322-3481-0

ABISEA Band 39
Schwarzer, Ulrich
IGBT versus GCT in der Mittelspannungsanwendung - ein experimenteller und simulativer Vergleich
1. Aufl. 2005, 170 S.
ISBN 3-8322-4489-1

ABISEA Band 40
Bartram, Markus
IGBT-Umrichtersysteme für Windkraftanlagen: Analyse der Zyklenbelastung, Modellbildung, Optimierung und Lebensdauervorhersage
1. Aufl. 2006, 185 S.
ISBN 3-8322-5039-5

ABISEA Band 41
Ponnaluri, Srinivas
Generalized Design, Analysis and Control of Grid side converters with integrated UPS or Islanding functionality
1. Aufl. 2006, 163 S.
ISBN 3-8322-5281-9

ABISEA Band 42
Jacobs, Joseph
Multi-Phase Series Resonant DC-to-DC Converters
1. Aufl. 2006, 185 S.
ISBN 3-8322-5532-X

ABISEA Band 43
Linzen, Dirk
Impedance-Based Loss Calculation and Thermal Modeling of Electrochemical Energy Storage Devices for Design Considerations of Automotive Power Systems
1. Aufl. 2006, 185 S.
ISBN 3-8322-5706-3

ABISEA Band 44
Fiedler, Jens
Design of Low-Noise Switched Reluctance Drives
1. Aufl. 2007, 176 S.
ISBN 978-3-8322-5864-1

ABISEA Band 45
Fuengwarodsakul, Nisai
Predictive PWM-based Direct Instantaneous Torque Control for Switched Reluctance Machines
1. Aufl. 2007, 141 S.
ISBN 978-3-8322-6210-5

ABISEA Band 46
Meyer, Christoph
Key Components for Future Offshore DC Grids
1. Aufl. 2007, 187 S.
ISBN 978-3-8322-6571-7

ABISEA Band 47
Fujii, Kansuke
Characterization and Optimization of Soft-Switched Multi-Level Converters for STATCOMs
1. Aufl. 2008, 199 S.
ISBN 978-3-8322-6981-4

ABISEA Band 48
Carstensen, Christian
Eddy Currents in Windings of Switched Reluctance Machines
1. Aufl. 2008, 179 S.
ISBN 978-3-8322-7118-3

ABISEA Band 49
Bohlen, Oliver
Impedance-based battery monitoring
1. Aufl. 2008, 190 S.
ISBN 978-3-8322-7606-5

ABISEA Band 50
Thele, Marc
A contribution to the modelling of the charge acceptance of lead-acid batteries - using frequency and time domain based concepts
1. Aufl. 2008, 165 S.
ISBN 978-3-8322-7659-1

ABISEA Band 51
König, Andreas
High Temperature DC-to-DC Converters for Downhole Applications
1. Aufl. 2009, 154 S.
ISBN 978-3-8322-8489-3

ABISEA Band 52
Dick, Christian Peter
Multi-Resonant Converters as Photovoltaic Module-Integrated Maximum Power Point Tracker
1. Aufl. 2010, 182 S.
ISBN 978-3-8322-9199-0

ABISEA Band 53
Kowal, Julia
Spatially resolved impedance of nonlinear inhomogeneous devices: using the example of lead-acid batteries
1. Aufl. 2010, 203 S.
ISBN 978-3-8322-9483-0

ABISEA Band 54
Roscher, Michael Andreas
Zustandserkennung von LiFeP04-Batterien für Hybrid- und Elektrofahrzeuge
1. Aufl. 2011, 186 S.
ISBN 978-3-8322-9738-1

ABISEA Band 55
Hirschmann, Dirk
Highly Dynamic Piezoelectric Positioning
1. Aufl. 2011, 146 S.
ISBN 978-3-8322-9746-6

ABISEA Band 56
Rigbers, Klaus
Highly Efficient Inverter Architectures for Three-Phase Grid Connection of Photovoltaic Generators
1. Aufl. 2011, 244 S.
ISBN 978-3-8322-9816-9

ABISEA Band 57
Kasper, Knut
Analysis and Control of the Acoustic Behavior of Switched Reluctance Drives
1. Aufl. 2011, 205 S.
ISBN 978-3-8322-9869-2

ABISEA Band 58
Köllensperger, Peter
The Internally Commutated Thyristor - Concept, Design and Application
1. Aufl. 2011, 214 S.
ISBN 978-3-8322-9909-5

ABISEA Band 59
Schoenen, Timo
Einsatz eines DC/DC-Wandlers zur Spannungsanpassung zwischen Antrieb und Energiespeicher in Elektro-und Hybridfahrzeugen
1. Aufl. 2011, 128 S.
ISBN 978-3-8440-0622-3

ABISEA Band 60
Hennen, Martin
Switched Reluctance Direct Drive with Integrated Distributed Inverter
1. Aufl. 2012, 141 S.
ISBN 978-3-8440-0731-2

ABISEA Band 61
van Treek, Daniel
Position Sensorless Torque Control of Switched Reluctance Machines
1. Aufl. 2012, 144 S.
ISBN 978-3-8440-1014-5

ABISEA Band 62
Bragard, Michael
The Integrated Emitter Turn-Off Thyristor. An Innovative MOS-Gated High-Power Device
1. Aufl. 2012, 164 S.
ISBN 978-3-8440-1152-4

ABISEA Band 63
Gerschler, Jochen B.
Ortsaufgelöste Modellbildung von Lithium-Ionen-Systemen unter spezieller Berücksichtigung der Batteriealterung
1. Aufl. 2012, 334 S.
ISBN 978-3-8440-1307-8

ABISEA Band 64
Neuhaus, Christoph R.
Schaltstrategien für Geschaltete Reluktanzantriebe mit kleinem Zwischenkreis
1. Aufl. 2012, 133 S.
ISBN 978-3-8440-1487-7

ABISEA Band 65
Butschen, Thomas
Dual-ICT- A Clever Way to Unite Conduction and Switching Optimized Properties in a Single Wafer
1. Aufl. 2012, 168 S.
ISBN 978-3-8440-1771-7

ABISEA Band 66
Plum, Thomas
Design and Realization of High-Power MOS Turn-Off Thyristors
1. Aufl. 2013, 113 S.
ISBN 978-3-8440-1884-4

ABISEA Band 67
Kiel, Martin
Impedanzspektroskopie an Batterien unter besonderer Berücksichtigung von Batteriesensoren für den Feldeinsatz
1. Aufl. 2013, 226 S.
ISBN 978-3-8440-1973-5

ABISEA Band 68
Brauer, Helge
Schnelldrehender Geschalteter Reluktanzantrieb mit extremem Längendurchmesserverhältnis
1. Aufl. 2013, 192 S.
ISBN 978-3-8440-2345-9

ABISEA Band 69
Thomas, Stephan
A Medium-Voltage Multi-Level DC/DC Converter with High Voltage Transformation Ratio
1. Aufl. 2014, 226 S.
ISBN 978-3-8440-2605-4

ABISEA Band 70
Richter, Sebastian
Digitale Regelung von PWM Wechselrichtern mit niedrigen Trägerfrequenzen
1. Aufl. 2014, 126 S.
ISBN 978-3-8440-2641-2

ABISEA Band 71
Bösing, Matthias
Acoustic Modeling of Electrical Drives - Noise and Vibration Synthesis based on Force Response Superposition
1. Aufl. 2014, 188 S.
ISBN 978-3-8440-2752-5

ABISEA Band 72
Waag, Wladislaw
Adaptive algorithms for monitoring of lithium-ion batteries in electric vehicles
1. Aufl. 2014, 232 S.
ISBN 978-3-8440-2976-5

ABISEA Band 73
Sanders, Tilman
Spatially Resolved Electrical In-Situ Measurement Techniques for Fuel Cells
1. Aufl. 2014, 126 S.
ISBN 978-3-8440-3121-8

ABISEA Band 74
Baumhöfer, Thorsten
Statistische Betrachtung experimenteller Alterungsuntersuchungen an Lithium-Ionen Batterien
1. Aufl. 2015, 157 S.
ISBN 978-3-8440-3423-3

ABISEA Band 75
Andre, Dave
Systematic Characterization of Ageing Factors for High-Energy Lithium-Ion Cells and Approaches for Lifetime Modelling Regarding an Optimized Operating Strategy in Automotive Applications
1. Aufl. 2015, 196 S.
ISBN 978-3-8440-3587-2

ABISEA Band 76
Merei, Ghada
Optimization of off-grid hybrid PV-wind-diesel power supplies with multi-technology battery systems taking into account battery aging
1. Aufl. 2015, 184 S.
ISBN 978-3-8440-4148-4

ABISEA Band 77
Schulte, Dominik
Modellierung und experimentelle Validierung der Alterung von Blei-Säure Batterien durch inhomogene Stromverteilung und Säureschichtung
1. Aufl. 2016, 165 S.
ISBN 978-3-8440-4216-0

ABISEA Band 78
Schenk, Mareike
Simulative Untersuchung der Wicklungsverluste in Geschalteten Reluktanzmaschinen
1. Aufl. 2016, 126 S.
ISBN 978-3-8440-4282-5

ABISEA Band 79
Wang, Yu
Development of Dynamic Models with Spatial Resolution for Electrochemical Energy Converters as Basis for Control and Management Strategies
1. Aufl. 2016, 188 S.
ISBN 978-3-8440-4303-7

ABISEA Band 80
Ecker, Madeleine
Lithium Plating in Lithium-Ion Batteries:
An Experimental and Simulation Approach
1. Aufl. 2016, 154 S.
ISBN 978-3-8440-4525-3

ABISEA Band 81
Zhou, Wei
Modellbasierte Auslegungsmethode von Temperierungssystemen für Hochvolt-Batterien in Personenkraftfahrzeugen
1. Aufl. 2016, 175 S.
ISBN 978-3-8440-4589-5

ABISEA Band 82
Lunz, Benedikt
Deutschlands Stromversorgung im Jahr 2050
Ein szenariobasiertes Verfahren zur vergleichenden Bewertung von Systemvarianten und Flexibilitätsoptionen
1. Aufl. 2016, 187 S.
ISBN 978-3-8440-4627-4

ABISEA Band 83
Hofmann, Andreas G.
Direct Instantaneous Force Control: Key to Low-Noise Switched Reluctance Traction Drives
1. Aufl. 2016, 228 S.
ISBN 978-3-8440-4715-8

ABISEA Band 84
Budde-Meiwes, Heide
Dynamic Charge Acceptance of Lead-Acid Batteries for Micro-Hybrid Automotive Applications
1. Aufl. 2016, 157 S.
ISBN 978-3-8440-4733-2

ABISEA Band 85
Engel, Stefan P.
Thyristor-Based High-Power On-Load Tap Changers Control under Harsh Load Conditions
1. Aufl. 2016, 156 S.
ISBN 978-3-8440-4986-2

ABISEA Band 86
Van Hoek, Hauke
Design and Operation Considerations of Three-Phase Dual Active Bridge Converters for Low-Power Applications with Wide Voltage Ranges
1. Aufl. 2017, 231 S.
ISBN 978-3-8440-5011-0

ABISEA Band 87
Diekhans, Tobias
Wireless Charging of Electric Vehicles - a Pareto-Based Comparison of Power Electronic Topologies
1. Aufl. 2017, 151 S.
ISBN 978-3-8440-5048-6

ABISEA Band 88
Lehner, Susanne
Reliability Assessment of Lithium-Ion Battery Systems with Special Emphasis on Cell Performance Distribution
1. Aufl. 2017, 184 S.
ISBN 978-3-8440-5090-5

ABISEA Band 89
Käbitz, Stefan
Untersuchung der Alterung von Lithium-Ionen-Batterien mittels Elektroanalytik und elektrochemischer Impedanzspektroskopie
1. Aufl. 2016, 258 S.
DOI: 10.18154/RWTH-2016-12094

ABISEA Band 90
Witzenhausen, Heiko
Elektrische Batteriespeichermodelle: Modellbildung, Parameteridentifikation und Modellreduktion
1. Aufl. 2017, 266 S.
DOI: 10.18154/RWTH-2017-03437

ABISEA Band 91
Münnix, Jens
Einfluss von Stromstärke und Zyklentiefe auf graphitische Anoden
1. Aufl. 2017, 171 S.
DOI: 10.18154/RWTH-2017-01915

ABISEA Band 92
Pilatowicz, Grzegorz
Failure Detection and Battery Management Systems of Lead-Acid Batteries for Micro-Hybrid Vehicles
1. Aufl. 2017, 212 S.
DOI: 10.18154/RWTH-2017-09156

ABISEA Band 93
Drillkens, Julia
Aging in Electrochemical Double Layer Capacitors: An Experimental and Modeling Approach
1. Aufl. 2017, 179 S.
DOI: 10.18154/RWTH-2018-223434

ABISEA Band 94
Magnor, Dirk
Globale Optimierung netzgekoppelter PV-Batteriesysteme unter besonderer Berücksichtigung der Batteriealterung
1. Aufl. 2017, 210 S.
DOI: 10.18154/RWTH-2017-06592

ABISEA Band 95
Iliksu, Merve
Elucidation and Comparison of the Effects of Lithium Salts on Discharge Chemistry of Nonaqueous Li-O_2 Batteries
1. Aufl. 2018, 160 S.
DOI: 10.18154/RWTH-2018-223782

ABISEA Band 96
Schmalstieg, Johannes
Physikalisch-elektrochemische Simulation von Lithium-Ionen-Batterien: Implementierung, Parametrierung und Anwendung
1. Aufl. 2017, 168 S.
DOI: 10.18154/RWTH-2017-04693

ABISEA Band 97
Soltau, Nils
High-Power Medium-Voltage DC-DC Converters: Design, Control and Demonstration
1. Aufl. 2017, 176 S.
DOI: 10.18154/RWTH-2017-04084

ABISEA Band 98
Stieneker, Marco
Analysis of Medium-Voltage Direct-Current Collector Grids in Offshore Wind Parks
1. Aufl. 2017, 144 S.
DOI: 10.18154/RWTH-2017-04667

ABISEA Band 99
Masomtob, Manop
A New Conceptual Design of Battery Cell with an Internal Cooling Channel
1. Aufl. 2017, 167 S.
DOI: 10.18154/RWTH-2018-223281

ABISEA Band 100
Marongiu, Andrea
Performance and Aging Diagnostic on Lithium Iron Phosphate Batteries for Electric Vehicles and Vehicle-to-Grid Strategies
1. Aufl. 2017, 222 S.
DOI: 10.18154/RWTH-2017-09944

ABISEA Band 101
Gitis, Alexander
Flaw detection in the coating process of lithium-ion battery electrodes with acoustic guided waves
1. Aufl. 2017, 109 S.
DOI: 10.18154/RWTH-2017-099519

ABISEA Band 102
Neeb, Christoph
Packaging Technologies for Power Electronics in Automotive Applications
1. Aufl. 2017, 132 S.
DOI: 10.18154/RWTH-2018-224569

ABISEA Band 103
Adler, Felix
A Digital Hardware Platform for Distributed Real-Time Simulation of Power Electronic Systems
1. Aufl. 2017, 156 S.
DOI: 10.18154/RWTH-2017-10761

ABISEA Band 104
Becker, Jan
Flexible Dimensionierung und Optimierung hybrider Lithium-Ionenbatterie-speichersysteme mit verschiedenen Auslegungs-zielen
1. Aufl., 2017, 157 S.
DOI: 10.18154/RWTH-2017-09278

ABISEA Band 105
Warnecke, Alexander J.
Degradation Mechanisms in NMC Based Lithium-Ion Batteries
1. Aufl. 2017, 158 S.
DOI: 10.18154/RWTH-2017-09646

ABISEA Band 106
Taraborrelli, Silvano
Bidirectional Dual Active Bridge Converter using a Tap Changer for Extended Voltage Ranges
1. Aufl. 2017, 94 S.
DOI: 10.18154/RWTH-2018-228242

ABISEA Band 107
Sarriegi, Garikoitz
SiC and GaN Semiconductors: The Future Enablers of Compact and Efficient Converters for Electromobility
1. Aufl. 2017, 106 S.
DOI: 10.18154/RWTH-2018-227548

ABISEA Band 108
Senol, Murat
Drivetrain Integrated Dc-Dc Converters utilizing Zero Sequence Currents
1. Aufl. 2017, 134 S.
DOI: 10.18154/RWTH-2018-226170

ABISEA Band 109
Kojima, Tetsuya
Efficiency Optimized Control of Switched Reluctance Machines
1. Aufl. 2017, 142 S.
DOI: 10.18154/RWTH-2018-226697

ABISEA Band 110
Lewerenz, Meinert
Dissection and Quantitative Description of Aging of Lithium-Ion Batteries Using Non-Destructive Methods Validated by Post-Mortem-Analyses
1. Aufl. 2018, 139 S.
DOI: 10.18154/RWTH-2018-228663

ABISEA Band 111
Büngeler, Johannes
Optimierung der Verfügbarkeit und der Lebensdauer von Traktionsbatterien für den Einsatz in Flurförderfahrzeugen
1. Aufl. 2018, 171 S.
DOI: 10.18154/RWTH-2018-226569

ABISEA Band 112
Wegmann, Raphael
Betriebsstrategien und Potentialbewertung hybrider Batteriespeichersysteme in Elektrofahrzeugen
1. Auflage 2018, 184 S.
DOI: 10.18154/RWTH-2018-228833

ABISEA Band 113
Nordmann, Hannes
Batteriemanagementsysteme unter besonderer Berücksichtigung von Fehlererkennung und Peripherieanalyse
1. Aufl. 2018, 222 S.
DOI: 10.18154/RWTH-2018-228763

ABISEA Band 114
Engelmann, Georges
Reducing Device Stress and Switching Losses Using Active Gate Drivers and Improved Switching Cell Design
1. Aufl. 2018, 195 S.
DOI: 10.18154/RWTH-2018-228973

ABISEA Band 115
Klein-Heßling, Annegret
Active DC-Power Filters for Switched Reluctance Drives during Single-Pulse Operation
1. Aufl. 2018, 166 S.
DOI: 10.18154/RWTH-2018-231030

ABISEA Band 116
Burkhart, Bernhard
Switched Reluctance Generator for Range Extender Applications - Design, Control and Evaluation
1. Aufl. 2018, 194 S.
DOI: 10.18154/RWTH-2019-00025

ABISEA Band 117
Biskoping, Matthias
Discrete Modeling and Control of a versatile Power Electronic Test Bench with Special Focus on Central Photovoltaic Inverter Testing
1. Aufl. 2018, 236 S.
DOI: 10.18154/RWTH-2019-03346

ABISEA Band 118
Schubert, Michael
High-Precision Torque Control of Inverter-Fed Induction Machines with Instantaneous Phase Voltage Sensing
1. Aufl. 2019, 221 S.
DOI: 10.18154/RWTH-2018-231364

ABISEA Band 119
Van der Broeck, Christoph
Methodology for Thermal Modeling, Monitoring and Control of Power Electronic Modules
1. Aufl. 2019, 290 S.
DOI: 10.18154/RWTH-2019-01370

ABISEA Band 120
Hust, Friedrich Emanuel
Physico-chemically motivated parameterization and modelling of real-time capable lithium-ion battery models – a case study on the Tesla Model S battery
1. Aufl. 2019, 203 S.
DOI: 10.18154/RWTH-2019-00249

ABISEA Band 121
Ralev, Iliya
Accurate Torque Control of Position Sensorless Switched Reluctance Drives
1. Aufl. 2019, 154 S.
DOI: 10.18154/RWTH-2019-03071

ABISEA Band 122
Ayeng'o, Sarah Paul
Optimization of number of PV cells connected in series for a direct-coupled PV system with lead-acid and lithium-ion batteries
1. Aufl. 2019, 114 S.
DOI: 10.18154/RWTH-2019-01843

ABISEA Band 123
Koschik, Stefan Andreas
Permanenterregte Synchronmaschinen mit verteilter Einzelzahnsteuerung - Regelkonzepte und Betriebsstrategien für hochintegrierte Antriebssysteme
1. Aufl. 2019, 158 S.
DOI: 10.18154/RWTH-2019-03446

ABISEA Band 124
Farmann, Alexander
A comparative study of reduced-order equivalent circuit models for state-of-available-power prediction of lithium-ion batteries in electric vehicles
1. Aufl. 2019, 214 S.
DOI: 10.18154/RWTH-2019-04700

ABISEA Band 125
Mareev, Ivan
Analyse und Bewertung von batteriegetriebenen, oberleitungsversorgten und brennstoffzellengetriebenen Lastkraftwagen für den Einsatz im Güterfernverkehr in Deutschland
1. Aufl. 2019, 158 S.
DOI: 10.18154/RWTH-2019-04698

ABISEA Band 126
Qi, Fang
Online Model-predictive Thermal Management of Inverter-fed Electrical Machines
1. Aufl. 2019, 154 S.
DOI: 10.18154/RWTH-2019-08304

ABISEA Band 127
Kairies, Kai-Philipp
Auswirkungen dezentraler Solarstromspeicher auf Netzbetreiber und Energieversorger
1. Aufl. 2019, 140 S.
DOI: 10.18154/RWTH-2019-06706

ABISEA Band 128
Fleischer, Michael
Traction control for Railway Vehicles
1. Aufl. 2019, 162 S.
DOI: 10.18154/RWTH-2019-10570

ABISEA Band 129
Teuber, Moritz
Lifetime Assessment and Degradation Mechanisms in Electric Double-Layer Capacitors
1. Aufl. 2019, 150 S.
DOI: 10.18154/RWTH-2019-10071

ABISEA Band 130
Bußar, Christian
Investigation of Optimal Transformation Pathways towards 2050 for the Successful Implementation of a Sustainable Reduction of Carbon Emissions from Power Generation
1. Aufl. 2019, 204 S.
DOI: 10.18154/RWTH-2019-09975

ABISEA Band 131
Wienhausen, Arne Hendrik
High Integration of Power Electronic Converters enabled by 3D Printing
1. Aufl. 2019, 146 S.
DOI: 10.18154/RWTH-2019-08746

ABISEA Band 132
Kwiecien, Monika
Electrochemical Impedance Spectroscopy on Lead-Acid Cells during Aging
1. Aufl. 2019, 138 S.
DOI: 10.18154/RWTH-2019-09480

ABISEA Band 133
Titiz, Furkan Kaan
A Three-phase Low-voltage Grid-connected Current Source Inverter
1. Aufl. 2019, 128 S.
DOI: 10.18154/RWTH-2020-00458

ABISEA Band 134
Wünsch, Martin
Separation der Kathodenalterung in Lithium-Ionen-Batteriezellen mittels elektrochemischer Impedanzspektroskopie
1. Aufl. 2019, 177 S.
DOI: 10.18154/RWTH-2019-11017

ABISEA Band 135
Badeda, Julia
Modeling and Steering of Multi-Use Operation with Uninterruptible Power Supply Systems - utilizing the example of lead-acid batteries
1. Aufl. 2020, 282 S.
DOI: 10.18154/RWTH-2020-05456

ABISEA Band 136
Kleinsteinberg, Björn
Energy Efficiency Increase of a Vanadium Redox Flow Battery with a Power-Based Model
1. Aufl. 2020, 163 S.
DOI: 10.18154/RWTH-2020-06092

ABISEA Band 137
Cai, Zhuang
Optimization of dimension and operation strategy for a wind-battery energy system in German electricity market under consideration of battery ageing process
1. Aufl. 2020, 144 S.
DOI: 10.18154/RWTH-2020-06525

ABISEA Band 138
Sabet, Pouyan Shafiei
Analysis of Predominant Processes in Electrochemical Impedance Spectra and Investigation of Aging Processes of Lithium-Ion Batteries with Layered Oxide Cathodes and Graphitic Anodes
1. Aufl. 2020, 136 S.
DOI: 10.18154/RWTH-2020-07683

ABISEA Band 139
Angenendt, Georg
Operation, Optimization and Additional Market Participation of Households with PV Battery Storage System and Power-to-Heat Application
1. Aufl. 2020, 221 S.
DOI: 10.18154/RWTH-2020-05200

ABISEA Band 140
Oberdieck, Karl Friedrich
Measurement and Mitigation of Electromagnetic Emissions of Propulsion Inverters for Electric Vehicles
1. Aufl. 2020, S.
DOI: 10.18154/RWTH-2020-

ABISEA Band 141
Bubert, Andreas Martin
Optimierung des elektrischen Antriebsstrangs von Elektrofahrzeugen mit Betrachtung parasitärer Ströme innerhalb der elektrischen Maschine
1. Aufl. 2020, S.
DOI: 10.18154/RWTH-2020-09556

ABISEA Band 142
Fleischer, Christian Georg
Model-Driven Software Development and Verification Solutions for Safety Critical Battery Management Systems
1. Aufl. 2020, S.
DOI: 10.18154/RWTH-2020-

ABISEA Band 143
Arzberger, Arno
Thermografische Methoden zur zerstörungsfreien Messung der anisotropen Wärmeleitfähigkeit von Lithium-Ionen Zellen
1. Aufl. 2020, S.
DOI: 10.18154/RWTH-2020

ABISEA Band 144
Lange, Tobias
Oberwellenbasierte Modellierung, Regelung und Auslegung von Permanentmagnet- und Reluktanz-Synchronmaschinen
1. Aufl. 2020, S.
DOI: 10.18154/RWTH-2020-

High reliability and operations-critical applications demand fault tolerant drive systems. This thesis investigates the benefits of switched reluctance machines (SRMs) coupled with a distributed inverter (one inverter module per coil) for such applications. Three main SRM topics concerning fault tolerant operation are addressed.

Firstly, a streamlined implemented pulse width modulation based direct instantaneous torque control (PWM-DITC) forms the base requirement. Secondly, a machine design methodology, to enable low torque ripple and fault tolerant control strategies, is introduced. Finally, the challenge of minimizing the unbalanced magnetic pull (UMP) caused during a single pole failure, which is the most common electrical fault found in SRMs, while maintaining constant torque control is addressed.

Various radial force minimization controls (RFMCs) in conjunction with PWM-DITC are proposed, implemented and validated on the test bench. The impact of each control on torque, radial force, unbalanced magnetic pull and current loading is investigated.

In simulation and experimental measurements the presented RFMC algorithms can deliver the required output torque, while reducing the UMP significantly. Therefore, by adding a distributed inverter to a SRM and incorporating the appropriate fault tolerant control strategy enables fault-tolerant SRM operation during pole failure.

ISSN 1437-675X